Comparative analysis of biopolymer-based scaffolds for therapeutically relevant cells

Dissertation

zur Erlangung des Grades

des Doktors der Naturwissenschaften

der Naturwissenschaftlich - Technischen Fakultät

der Universität des Saarlandes

von

Benjamin Fischer

Saarbrücken

2020

Tag des Kolloquiums:	7. Dezember 2020
Dekan:	Prof. Dr. Jörn Erik Walter
Berichterstatter:	Prof. Dr. Dr. h.c. Heiko Zimmermann Prof. Dr. Jörn Erik Walter Prof. Dr. Christof Stamm
Vorsitz:	Prof. Dr. Franziska Lautenschläger
Akad. Mitarbeiter:	Dr. Jens Neunzig

TABLE OF CONTENTS

ZUSAMMENFASSUNG

Im Rahmen dieser Arbeit wurde die Generierung somatischer, kardialer Zellen aus humanen pluripotenten Stammzellen in einen dynamischen Suspensionsbioreaktor übertragen und vergleichend mit der statischen „hängenden Tropfen“ Kultur hinsichtlich der Differenzierungseffizienz und der Reife der abgeleiteten Kardiomyozyten untersucht. Darüber hinaus wurden für die Dissoziierung der Zellen drei Enzyme vergleichend analysiert. Die Wirkung von adhäsiven, kontraktilen Biopolymeren auf die Kardiomyozytenphysiologie wurde am Beispiel von ultra-hoch viskosem Alginat untersucht. So konnte festgestellt werden, dass Kardiomyozyten auf solchen Biopolymeren eine reifere Organisation des Zytoskeletts und Geneexpression aufweisen. Des Weiteren wurde ein neuartiges Verfahren entwickelt welches die simultane Quantifizierung der Kontraktionskraft und der intrazellulären Kalziumströme erlaubt. Hierzu wurden die Kardiomyozyten unterschiedlichen Konzentrationen von Isoprenalin, ein Beta-Adrenozeptoragonist, ausgesetzt. Darüber hinaus wurde eine neuartige Methode für den 3D Druck von niedrig-konzentrierten Biopolymerlösungen entwickelt und hinsichtlich ihrer Druckauflösung charakterisiert. Kardiomyozyten wurden auf diesen Gerüststrukturen kultiviert und es konnte gezeigt werden, dass die Zytoskelette eine noch höhere Organisation aufweisen und spezifische, mit der physiologischen Reifung assoziierte Proteine, in erhöhtem Maße vorkommen.

SUMMARY

In this work, a process for the production of somatic, cardiac cells from human induced pluripotent stem cells in three-dimensional micro tissues was adapted to a dynamic, suspension-based bioreactor. The differentiation efficiency and the maturation of the generated cardiomyocytes in the bioreactor and the static hanging drop culture were analyzed. To dissociate the cardiac tissues into single cells, the performances of three enzymes were comparatively evaluated. To analyze the effect of contractile biopolymers on cardiomyocyte physiology ultra-high viscosity alginates were utilized. Cardiomyocytes cultured on these matrices for a prolonged period exhibit a matured cytoskeletal organization and gene expression. In addition, a novel approach was developed, which enables the simultaneous quantification of the generated contraction force and intracellular calcium transients. To this extent, different concentrations of the beta-adrenergic agonist isoprenaline were applied. A novel 3D printing method for the three-dimensional deposition of low concentrated biopolymer formulations was devised and evaluated concerning the printing resolution and pore formation. The culture of human cardiomyocytes on such 3D printed, biopolymer-based scaffolds led to a further maturation of the cytoskeletal organization and a higher abundance of proteins, which are associated with the maturation *in vivo.*

LIST OF ABBREVIATIONS

AMI	Acute myocardial infarction
IHD	Ischaemic heart disease
BL	BioLevitator (a suspension-based bioreactor)
Calcein-Am	Calcein-acetoxymethyl ester
CFs	Cardiac fibroblasts
CMs	Cardiomyocytes
cTnT	Cardiac troponin T
cTnI	Cardiac troponin I
Cx43	Connexin 43
DMSO	Dimethylsulfide oxide
Dpi	Days post induction
EAD	Early after depolarization
ECM	Extracellular matrix
ESCs	Embryonic stem cells
FACS	Fluorescent activated cell sorting
FiTC-PLL	Fluorescein isothiocyanate labelled poly-L-lysine
FP	Freeze printing
FSC	Forward scatter
GAG	Glycosaminoglycans
HD	Hanging drop (cell culture method)
hiPSCs	Human induced pluripotent stem cells
hPSCs	Human pluripotent stem cells
HP	Heart Patch
L.n.	*Lessonia nigrescens* (algae species)
L.t.	*Lessonia trabeculata* (algae species)
LP	Liquid printing (conventional 3D printing)
LV	Left ventricle (of the human heart)
MEA	Multi electrode array
MSCs	Mesenchymal stem cells
PCA	Principle component analysis
PEG	Polyethylene glycol
PI	Propidium iodide
PS	Polystyrene
PSG	Penicillin Streptomycin Glutamine
qPCR	Reverse-transcription quantitative real-time polymerase chain reaction
SD	Standard deviation
SEM	Standard error of the mean
SR	Sarcoplasmic reticulum

SSC	Sideward scatter
ssTnI	Slow skeletal troponin I
RT	Room temperature
UHV-alginate	Ultra-high viscosity alginate
VSMCs	Vascular smooth muscle cells
WB	Western Blot

LIST OF FIGURES

LIST OF TABLES

1 INTRODUCTION

Ischaemic heart disease (abbr. IHD) represents one of the main causes of death in the world and is responsible for 20% of all deaths in Europe (Wilkins et al., 2017). Owing to the demographic shift towards an elderly society in western countries, IHD-affected patients are expected to grow in numbers. The improvements in IHD therapy have led to a significant increase of survivors of the critical acute phase. This is particularly true for acute myocardial infarction (abbr. AMI) for which the survival rate has been elevated by 50% in the last 15 years. However, due to the limited regenerative potential of the human myocardium, AMI survivors struggle with a progressively deteriorating heart.

The major cause of AMI is ischemia, a critical shortage of oxygen and nutrients caused by a clogged coronary vessel. Upon oxygen deprivation, localised cell death sets in, accompanied by a delayed inflammatory response. This leads to an irreversible loss of cardiomyocytes, the functional force-generating unit of the heart, which is followed by a migration of other cell types (*i.e.* cardiac fibroblasts) into the affected region. This repopulation with fibroblasts, which are not able to exert a fast contraction movement, is associated with scar formation and mechanical instability in the heart (Fan et al., 2012; Krenning et al., 2010; Talman et al., 2016).

Because the adverse progression leads to arrhythmias and finally end-stage heart failure, these chronic patients are treated with ablation, cardiac resynchronization therapy and ultimately heart transplantation; a demand, which cannot be met, as only approximately 50% of all patients waiting for heart transplantation received a donated organ in Europe in 2017 (Eurotransplant, 2017; Fujita et al., 2017). To compensate this imbalance, mechanical circulatory support devices are implanted, but these can cause dangerous side-effects, *e.g.* bleeding, thromboembolism, device failure, stroke and sepsis (Fujita et al., 2017; Kirklin et al., 2015). Ultimately, none of the standard therapies is able to halt or reverse the pathological progression towards end-stage heart failure, except organ transplantation, which suffers from poor donor numbers and is still associated with significantly lower life expectancy.

There is growing interest in developing novel therapeutic strategies aimed to actively reverse or at least halt the pathological progression. Since the origins of the pathological processes are rooted in the physiological and mechanical changes induced by myocardial infarction, it has been hypothesized that effective reversal of these adverse processes can be achieved by restoring cellular homeostasis in the cardiac microenvironment through cell transplantation. However, there are still profound barriers to be overcome before cell-based transplants can be utilized in the clinic. First, the ultimate cell type has not been found and there is ongoing research to identify the most effective cellular therapeutic agent. Second, the cell production must be reproducible, economical and of high quality. Third, there is a high need for novel delivery methods, which circumvent the low retention of delivered cells in affected tissues.

Potentially suitable cell types discussed in the scientific field include mesenchymal stem cells (abbr. MSCs), cardiac progenitor cells and cardiomyocytes (abbr. CMs). MSCs possess the capability to avoid the immune system of recipients and to migrate actively into affected, inflammated tissues. Although MSCs are able to differentiate into CMs *in vitro*, the main therapeutic effect is solely based on paracrine signalling (Bartulos et al., 2016; Cai et al., 2003). The long-term effects particularly are questionable, since the local stem cell population, long suspected to be located in the myocardium and activated through paracrine signalling, is presumably not existent (Li et al., 2018b). Cardiac progenitor cells are a population of $ISL1^+$ cells that replicate an intermediate stage in early heart development and are derived *in vitro* from stem cells (Weinberger et al., 2012). It is assumed that these cells can contribute to cardiomyogenesis *in vivo* during development, but there are still doubts about the identity and the differentiation potential of ISL^+ cells *in vivo* as *in vitro* (Quaranta et al., 2018). Additionally, there is sincere doubt this population is existent in adult heart. Cardiomyocytes are the most promising candidate for therapeutic agent, because they represent a direct replacement for the lost local cardiomyocytes population. Furthermore, they are able to provide contractile support, which is crucial in the heart, because mechanically weak areas in the myocardium are the focal points of degenerative processes. The limited proliferative potential of cardiomyocytes restricts the culture and consecutive application of these cells, particularly concerning the high number of cells (between $20*10^6$ and $60*10^9$) which is needed for transplantation (Chen et al., 2004; Gao et al., 2013). This is circumvented by expanding the highly proliferative stem cell population from which the cardiomyocytes are generated (Dambrot et al., 2011; Zweigerdt et al., 2011; Zwi-dantsis et al., 2011). Stem cells are defined by their ability to self-regenerate through mitosis and to generate somatic cells of all (pluripotent stem cells) or some tissues (multipotent stem cells) through differentiation.

There are two major fractions of human pluripotent stem cells (abbr. hPSCs): embryonic stem cells (abbr. ESCs) and human induced pluripotent stem cells (abbr. hiPSCs). ESCs are obtained from early stage embryos and while they can be expanded virtually limitless, their potential is hindered by the ethically and morally problematic harvest from human embryos and - if implanted - the lifelong need of the patient to take immunosuppressive medication with all its side-effects (Ghosh et al., 2016; King et al., 2014).

In 2006 Yamanaka and Takahashi discovered a method to derive human pluripotent stem cells from somatic cells through the addition of the so-called Yamanaka factors, namely OCT3/4, Sox2, Klf4, and c-Myc (Takahashi et al., 2006). The induction of pluripotency led to their name: human induced pluripotent stem cells. This method enabled scientists worldwide to produce and expand patient-specific stem cells. In concert with the enhanced differentiation protocols established in the following years, patient-specific, differentiated somatic cells are readily available nowadays for research, drug discovery and therapy. A major drawback affecting the therapeutic side however is the risk of teratoma formation after transplantation caused by residual pluripotent stem cells (Nori et al., 2015). The introduction of integration-free reprogramming strategies and a thorough selection process before transplantation have been shown to reduce this risk significantly and transplantation of iPSC-derived cells have been

successfully conducted in humans (Ando et al., 2015; Mohseni, 2014; Tohyama et al., 2017; Warren et al., 2010). In contrast to early CM differentiation protocols, which relied on co-cultures, the state of the art generation of cardiomyocytes from hiPSCs nowadays utilizes small molecules to modulate the WNT pathway in a precisely timed manner (Kadari et al., 2015; Mummery et al., 2002, 1991a; Zhang et al., 2015). The WNT pathway is an important intracellular signalling network which is involved in embryonic development, cell fate determination, cytoskeletal organisation and cardiac lineage induction (Pahnke et al., 2016).

The established protocols are commonly utilized in conventional (two-dimensional) cell culture platforms. The production of clinically relevant cell numbers with such platforms is burdensome, costly and scale-up is very limited (Kropp et al., 2017). In this work, a small molecule-based differentiation method was adapted to a suspension-based bioreactor system to evaluate the production potential in a scalable culture platform. Additionally the effect of the dynamic environment in the suspension bioreactor on the cell production and cardiac phenotype was analysed for further characterisation of the system. The generation of three-dimensional micro tissues is reported to be beneficial for many cell models, but the strong intercellular connections and the three-dimensionality of the spheroids make a reliable and robust dissociation into single cells difficult. To this extent, the dissociative performance of three enzymes was comparatively analysed. In particular, cell viability and the resulting number of individual cells were evaluated using two independent methods to enhance the robustness of the analysis.

However, the number of economically produced cells represent only one crucial factor for the utilization of these cells in drug toxicity screenings, drug discovery approaches and therapeutic applications. An equally important factor is the quality of the produced cardiomyocytes, which is represented by its phenotype and state of maturation. hiPSC-CMs in general do not recapitulate the mature phenotype found in adult humans, but resemble more fetal cardiomyocytes, hence, they are called fetal-like. There are profound differences between immature and mature CMs concerning morphology, metabolism, electrophysiological properties and gene expression (Da Rocha et al., 2017; Robertson et al., 2013; Scuderi et al., 2017; Uosaki et al., 2016; Yang et al., 2014). In contrast to therapeutic applications, the fetal-like phenotype is a high burden for drug screenings and drug development, because the translational potential of *in vitro* models is diminished by the substantial differences to the adult human myocardium. This is also reflected by the current situation in which cardiovascular side effects are one of the major reasons for the withdrawal of drugs from the market (Gwathmey et al., 2009; Sallam et al., 2015). The withdrawn drugs exhibited major, cardiotoxic side effects, ranging from arrhythmias and myocardial infarction to QT interval prolongation, all that can ultimately cause death. Although, the lack of an adult, human cardiac *in vitro* model is already significant on its own, the low translational potential of rodent (*i.e.* rat and mouse) cardiac models caused by the absence of specific ion channels (*i.e.* the rapidly activating delayed rectifier potassium channel, which is often associated with drug-induced side effects) further deteriorates this situation. Large animal models (*i.e.* dog and swine), which have a higher resemblance to the human cardiac system, still suffer from

translational failures, are expensive to maintain, and offer only limited availability for high throughput screenings.

The development of a novel drug has an estimated cost of 800 million to 2 billion dollars and to balance this high economic burden with a decreased rate of market withdrawals is only possible by the establishment of human myocardial *in vitro* models with high translational potential (DiMasi et al., 2016). While the generation of fully physiological *in vitro* models is still far away, the progress towards more significant models has already started. The use of human cardiomyocytes derived from embryonic stem cells was an important step towards a human *in vitro* model, but only the use of hiPSC-CMs allowed avoiding human embryonic tissue. The hiPSC-CMs, albeit not fully matured, already proved advantageous compared to previous transfection-based or small animal models. Additionally, they allow the derivation of disease-specific cell lines, introducing common diseases and rare mutations in regular drug assessments. The expected reduction in animal numbers is also in agreement with the "3R principles" (Reduce, Refine, Replace), minimizing the impact of medical research on animal welfare.

After human cardiac cell models were available, a lot of effort was put into the maturation of hPSC-CMs towards a more adult phenotype. To this end, contractile substrates have been shown to foster cardiomyocyte maturation, presumably due to the cells being able to perform a contractile movement, contrary to conventional cell culture plastic ware where the rigid plastic inhibits contractile movements. In this work, the effect of such contractile substrates on cardiomyocyte maturation was investigated and additionally the analysis was extended to different substrate stiffnesses. Ultra-high viscosity (UHV) alginates, produced by mixing alginates from two algae species with conserved high molecular chain length and extremely low endotoxin values were employed as contractile matrices. Crosslinking of UHV-alginates is induced by bivalent cations and both, the resulting stiffness and the stability, depend on the selected ions and the applied UHV-alginate concentrations. The lack of an alginate receptor in mammalian cells results in a highly reproducible and neutral background in *in vitro* models (Lee et al., 2012). Therefore, the employment of UHV-alginates allows control over the physicochemical characteristics of the substrate in *in vitro* models and enables the analysis of substrate-induced effects on the cells in an unbiased manner (Lee et al., 2012). Since UHV-alginates are non-adherent, a biofunctionalisation step has to be conducted that covalently couples proteins to the surface via carbodiimide chemistry (Gepp et al., 2017; Schulz et al., 2019). Consecutively, hiPSC-CMs were cultured on functionalised UHV-alginates for eight weeks to allow time for the cells to adapt to the contractile microenvironment and to enable intercellular communication and cooperation. Afterwards, the influence of UHV-alginate substrates on hiPSC-CM contractility, gene expression and sarcomeric organisation was investigated.

While hiPSC-CMs have been utilized before, only a limited amount of studies has tried to assess the contractile force, the major functional output of these cells. Analyses of the intracellular calcium dynamics or the action potential have been used not only to resolve drug

binding and changes in the cellular homeostasis, but also to draw conclusions about the force generation. These studies often were limited in throughput; particularly Patch Clamp analyses suffer from the low number of replicates due to the complicated experimental procedures. Direct measurements of force often have been conducted on single cardiomyocytes. While these are important measurements to resolve the mechanisms involved in force generation for basic research, the concerted, virtually synchronous contraction of the myocardium is essential for the pumping performance of the heart, thus representing an ideal core characteristic of cardiac *in vitro* models. Thus, a setup had to be developed, which enabled the quantification of the contractile movement of a cardiomyocyte layer and at the same time fluorescence signals. Therefore, an experimental setup was conceived, which allows for the firs time, the simultaneous quantification of the generated force through an optical-flow based analysis, while allowing fluorescence-based analysis of intracellular calcium transients. A basic validation of this experimental setup was conducted in this work by measuring both, calcium dynamics and force generation upon beta-adrenergic stimulation with isoprenaline and by comparing it to existing models.

Due to their potential for patient-specific therapy and remuscularization, hiPSC-CMs represent the cell type of choice for therapeutic applications, but the mode of delivery is still in question. From a clinical point of view, catheter-based approaches offer the possibility to deliver highly concentrated cell suspensions to specific regions of the affected heart, either into the myocardium directly (transendocardial) or into the infarct-related artery (intracoronary). Being a standard procedure with hundreds of thousands of surgeries per year worldwide, the safety of heart catheters is well documented. Several studies investigating the cell delivery by injection into the coronary vessels or the myocardium directly in swine or humans have produced mixed results with some reporting an enhanced ejection fraction and some observing cell proliferation (Hatzistergos et al., 2010; Perin et al., 2003; Shiba et al., 2012). Albeit some parameters of the treated hearts improved, the progressive deterioration of the affected myocardia was not reversed (Caspi et al., 2007; van Laake et al., 2007). Moreover, the ratio of injected cells to engrafted cells indicated not only poor engraftment efficiency of approx. 5%, but has also shown progressive cell death of the engrafted cells in the following weeks (Huang et al., 2010b; Kraitchman et al., 2005; Templin et al., 2012). Since the therapeutic success depends on the effectiveness of cell engraftment and cell survival, the presumed advantages of local injections are in doubt (Liang et al., 2013; Nguyen et al., 2016). Reasons of this shortcoming are not fully resolved, but hypoxia, anoikis (anchorage-dependent programmed cell death) and inflammation are likely to be involved, when sensible cardiomyocytes are injected into a scarred and hypoxic tissue (Laflamme et al., 2007). Furthermore, intracoronary injections are suspected to impair coronary flow and carry a serious risks of restenosis (Schächinger et al., 2004; Vulliet et al., 2004). To overcome these potential drawbacks and to enhance the engraftment efficiency, patch-based approaches have been proposed. These patches consist of a transplantable scaffold in combination with a biocompatible support structure (*e.g*. collagen, fibrin, alginate, PEG) that can be pre-loaded with cells. A production pipeline based on 3D printing would be advantageous, because it

enables the creation of patient-specific scaffold designs and allows adaption of the construct sizes to the affected area without additional costs. These bioengineered constructs are usually implanted epicardially, which requires invasive surgery, but offers the advantage of introducing a specifically localized and stable source of cells. Following transplantation, these cells induce angiogenesis and prevent apoptosis and fibrosis through paracrine signalling. Furthermore, they also supply contractile support and have the possibility to migrate out of the patch and engraft into the host myocardium hence, further distributing the therapeutic effects.

Early studies using cell-laden scaffolds have shown that this approach enhances the engraftment efficiency of ESC-derived CMs by a magnitude and additionally induces neovascularisation (Lyon et al., 2015; Tiburcy et al., 2017; Weinberger et al., 2016). The propensity to vascularization or oxygen diffusion overcomes the biggest disadvantage of the catheter-based cell delivery, which is the lack of diffusion at the injection site and the resulting immediate cell death after transplantation. However, thick cell constructs are in danger to suffer from hypoxia, as diffusion through the tightly packed cells is slow and active cardiomyocytes are very demanding in terms of oxygen and nutrient support. This demand can be met by using highly porous scaffolds with diffusion enabling characteristics. A high elasticity will also be beneficial, because the matrix can follow the contraction movement of the heart, which further supports liquid exchange within the scaffold volume, thus enhancing nutrient exchange. Ultimately, it was shown that higher cellular maturity leads to a better engraftment of such patches (Mihic et al., 2014).

To enable the production of highly elastic and porous scaffold structures, a 3D printing process has to be developed, which can produce such structures with sufficient printing resolution and a high resemblance to the physiological microenvironment. Very often conventional printing methods rely on pasty polymer formulations to stabilize the scaffolds during the printing process, which results in a high, non-physiological stiffness. Alternative methods use aggressive chemicals for light-induced crosslinking to enable a high printing resolution, but this leads to aggressive residual side- or end-products casting doubts on the use of such scaffolds in a clinical setting. The printing performance of the developed 3D printing method was compared to conventional additive layer manufacturing and the printing resolution of both methods was evaluated. The resulting pore sizes of different UHV-alginate compositions were determined and the effect of additives on the pore sizes was investigated. Consecutively, hiPSC-CMs were cultured on these patches and the effect on the contractile behaviour was assessed. To understand the different influences on cardiomyocyte physiology better, 3D printed scaffolds and fixed UHV-alginate layers were comparatively analysed, in particular the differences in cellular organization and beating behaviour. The effect of the substrate stiffness on the morphology, intracellular skeleton, beating behaviour and drug response was investigated by using immunocytochemistry, gene expression profiling via relative quantitative real-time PCR (abbr. qPCR) and calcium imaging. In addition, fixed substrates and scaffolds with differing stiffness were produced and the influence of the substrate stiffness on the hiPSC-CMs, in particular sarcomere organization, gene expression and maturation was

assessed allowing conclusions about the influence of extracellular environments on cardiomyocyte physiology. Furthermore, the stage of maturation was evaluated by gene expression profiling and the comparison of protein abundance via Western Blotting (abbr. WB). Particularly, the stoichiometric switch from the slow skeletal troponin I to the cardiac troponin I form is a highly correlative marker for hiPSC-CMs maturity.

In conclusion, the presented work focused on enabling technologies for the reproducible production of CM-based *in vitro* models and transplants. Particular attention was paid to the three core areas of hPSC technologies, namely the cardiomyocyte generation, the maturation of these cells and the development of biopolymer-based scaffolds, since these represent the current bottlenecks for a society wide availability of clinical grade cell-based transplants.

First, a protocol for hiPSC-CM differentiation was transferred to a suspension-based bioreactor system to enable the generation of clinically relevant cell numbers with a lower economic burden compared to conventional cell culture platforms. To answer the question whether the transition to such a system has an effect on the cardiomyocyte induction, the differentiation process was evaluated by comparatively analysing the number of produced cardiomyocytes, the differentiation efficacy and the maturation status of the generated hiPSC-CMs. Since hPSC-CMs possess an immature phenotype, which limits their use in *in vitro* models of the human myocardium, the possibility to induce cellular maturation by using contractile matrices was investigated in a second step. Using functionalised UHV-alginate matrices, the effect of substrates with differing stiffness on hiPSC-CMs was comparatively assessed by analysing gene expression, contractility behaviour, sarcomere organisation and the response to beta-adrenergic stimulation. Additionally, a method was conceived to enable quantification of the generated forces upon contraction in parallel to intracellular calcium measurements. The correlated analysis of intracellular calcium dynamics and force generation integrates the functional output of cardiomyocytes as an additional parameter into established screening methods and allows for an enhanced translational potential of *in vitro* cardiac models. Third, the contractile matrices were 3D printed to enable future utilization of hydrogel-based scaffolds in tissue engineering applications (*i.e.* transplantations). Since the liquid nature of such biopolymers makes them difficult to print, a 3D printing process had to be developed to allow the production of scaffolds with physiologically relevant physical parameters (*e.g.* stiffness). The maturation state, cellular organisation and gene expression of hPSC-CMs grown on these 3D printed scaffolds for two months were also comparatively analysed to the previously used fixed coatings and conventional cell culture platforms. Finally, long-term experiments were carried out to investigate the stability of these scaffolds over several months. Thus, the development and research conducted in this work, has led to new methods and advancements tackling the bottlenecks of hPSC technologies that can serve as a basis for future studies to ultimately realize iPSC-based therapies for clinical applications.

2 BACKGROUND

Since the experiments by Gurdon proved that the dynamic expression of specific genes from the otherwise stable genome is the cause for the multitude of somatic cells seen in adult organisms, the use of stem cells for clinical applications was desired (Gurdon et al., 1958). The consecutive discovery of embryonic stem cells (abbr. ESCs), which were derived from embryonal blastocysts, proved the *in vitro* culture of human pluripotent stem cells feasible (Thomson, 1998). Great potential was seen in these cell lines since they can give rise to every cell of the human body and therefore offer the possibility to recapitulate many human-specific diseases *in vitro* and in the long term would also render cell therapies feasible. To achieve these goals, the methods were expanded onto adult stem cells and additionally led to the discovery of a method to reprogram somatic cells to a pluripotent state. These stem cells systems are profoundly different from each other and thus influence their applicability strongly.

2.1 STEM CELL PROCESSES FOR THE DERIVATION OF PATIENT AND DISEASE-SPECIFIC CARDIOMYOCYTES

Currently, there are three main sources for the derivation of stem cells, the embryonic blastocyst, mesenchymal stem cells and induced pluripotent stem cells from which cardiomyocytes can be derived. ESC are the natural source of all tissues *in vivo* and they also give rise to cardiomyocytes *in vitro*. However, these ESCs possess an immunogenic potential and additionally, the harvest from human blastocysts is ethically questionable, therefore other systems are preferred particularly in the context of cell-based therapies.

Contrary to ESCs, an adult stem cell population from the mesenchyme has shown great potential in avoiding host immune reactions. These mesenchymal stem cells (abbr. MSCs) can be obtained from a diverse set of adult tissues (adipose tissue and bone marrow) and Wharton's jelly, a gelatinous matrix of the umbilical cord. These adult stem cells can be differentiated into a multitude of somatic cells, including cardiac, adipose and chondrogenic cells. In addition, they possess unique capabilities, particularly the abilities to home into inflammated tissues and immunomodulation. Nevertheless, not all somatic cells can be derived from MSCs and their characterisation is tedious, because they are a heterogeneous cell population with unclear composition.

In 2006, Yamanaka *et al*. were able to induce a pluripotent state in somatic cells. This induction was achieved by vector-based integration of four factors: OCT3/4, SOX2, KLF4 and c-MYC. These transcription factors induce a persistent pluripotent state similar to embryonic stem

cells (Takahashi et al., 2006; Yamanaka, 2009). Furthermore, the reprogrammed cells exhibited the hallmarks of stem cells, self-replication and the capability to differentiate into somatic cells. Hence, they were called induced pluripotent stem cells (abbr. iPSCs). Since then, the original work has been expanded to human cells and human induced pluripotent stem cells (abbr. hiPSCs) are readily available nowadays. Since these cells can be derived from small skin biopsies, patient specific medicine and disease modelling has made great progress. Not only have autologous stem cell transplantations been conducted, rendering such therapies

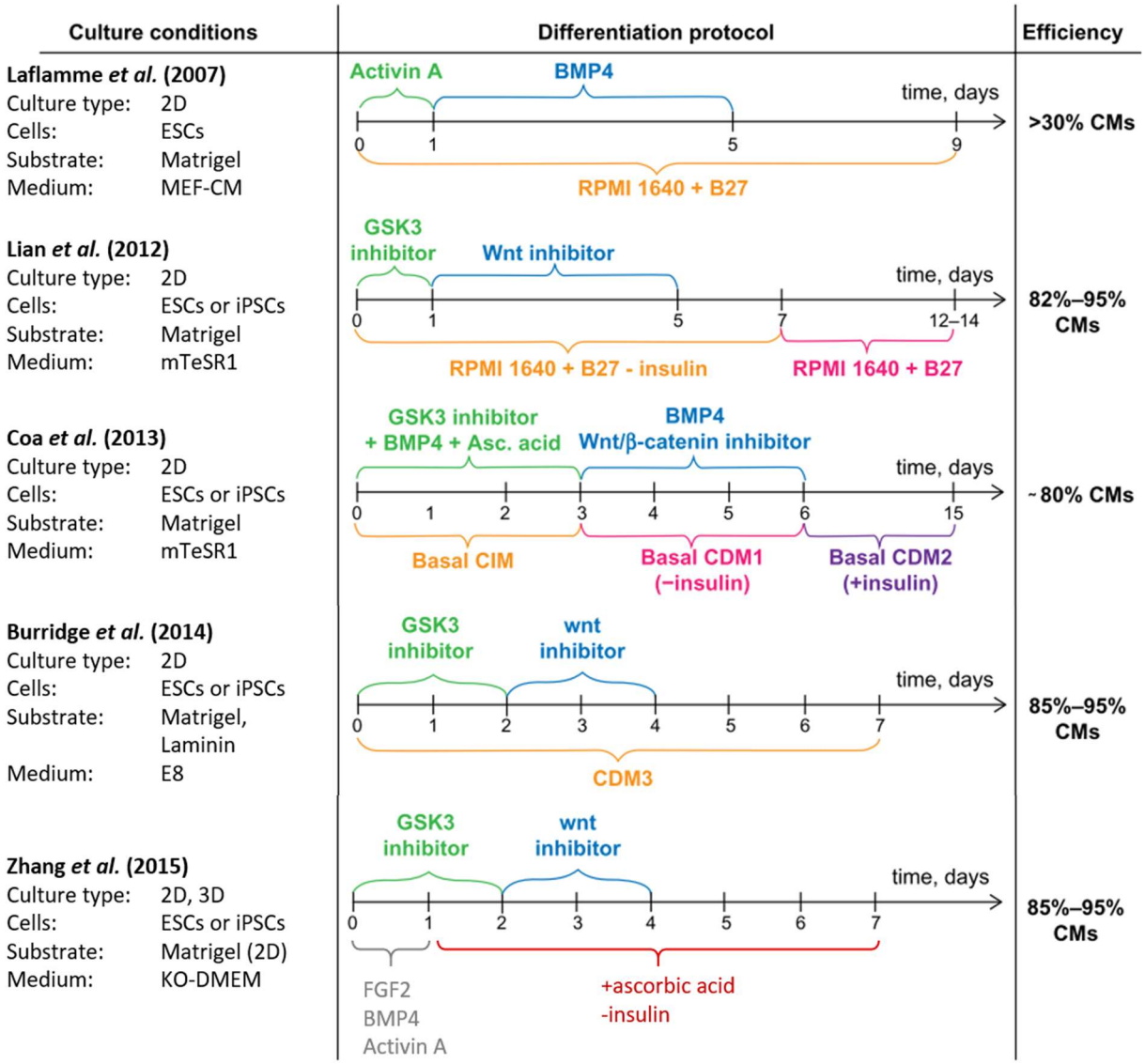

Figure 2.1 Historical view on the development of directed cardiac differentiation protocols.
Directed differentiation of pluripotent stem cells was first shown by Laflamme et al. by Activin A and BMP4 exposure. Lian et al. and Coa et al. have proven that a biphasic Wnt pathway modulation (activation followed by inhibition) produces significantly more cardiomyocytes. Additionally, Coa et al. have shown the inhibiting effect of insulin on cardiac lineage commitment. Burridge et al. established a high efficiency protocol by the use of small molecules to modulate the WNT pathway. Zhang et al established a universal protocol for two- and three-dimensional cultures with high cardiomyocyte yield. Schematic adapted from Batalov et al. 2015.

save and possible, but also many diseases have been successfully modelled *in vitro* (Brandão et al., 2017; Karantalis et al., 2012).

The reprogramming step itself, which was originally based on the use of viral vectors, has been seen as an obstacle for therapeutic applications, due to the risk of reactivation of the viral transgene and the oncogenic potential. Additionally, chromatic aberrations are detected in viral reprogrammed hiPSCs and these can lead to a modified genetic background obscuring conclusions drawn from *in vitro* modelling of physiological or pathological tissues (Chen et al., 2013; Yusa et al., 2009). This led to the development of non-integrative strategies, which include non-integrative reprogramming vectors, proteins (Kim et al., 2009; Zhou et al., 2009) and modified RNA (Warren et al., 2010). Such non-integrative vectors encompass replication-defective adenovirus (Stadtfeld et al., 2008), Sendai virus (Chen et al., 2013) and episomal non-replicative vectors (Okita et al., 2008). Even the non-integrative approaches have a much lower efficiency compared to integrative viral vectors the risk of re-establishing the pluripotent state has to be avoided to pave the road for therapeutic applications (Schlaeger et al., 2015).

The *in vitro* derivation of cardiomyocytes from PSCs was first achieved using a co-culture system with visceral-endodermal-like cells, albeit the efficiency was below 5% (Mummery et al., 1991b). It was later resolved that the visceral-endodermal-like cells contributed to the cardiac differentiation by insulin clearance. The absence of insulin during the early differentiation stages is required for cardiac fate induction. Consecutive studies have shown that, by supplying BMP4 and Activin A the cardiac fate can be actively induced (Laflamme et al., 2007). This method was further enhanced by the discovery that a biphasic WNT pathway activity is required for a physiological development of the cardiac niche *in vivo* (Ueno et al., 2007).

The WNT pathway is one of the master regulators of lineage commitment and, together with Activin/Nodal and BMP4 signalling, is responsible for fundamental developmental processes, *e.g.* embryonal axis formation, germ layer commitment and stem cell renewal (Sumi et al., 2008; Tam et al., 2007). There are two types of WNT signalling known today, the canonical and the non-canonical WNT pathway. Canonical WNT signalling relies on the presence of β catenin, which enters the nucleus and modulates gene expression. Non-canonical signalling involves WNT/JNK signalling to evoke different canonical signalling independent responses. The complex interplay of the two pathways in a concentration- and time-dependent fashion is responsible for the highly flexible, tissue-specific outcomes *in vivo* (Pahnke et al., 2016; Sumi et al., 2008). Cardiac lineage commitment requires activation of the canonical WNT pathway until mesoderm formation is achieved (Cohen et al., 2008; Mehta et al., 2014; Tian et al., 2010). Afterwards, an effective inhibition of the canonical WNT pathway fosters cardiac lineage commitment, presumably through the influence of the non-canonical WNT pathway, although the underlying mechanism have not been fully resolved (Mazzotta et al., 2016; Mehta et al., 2014; Später et al., 2014; Tian et al., 2010).

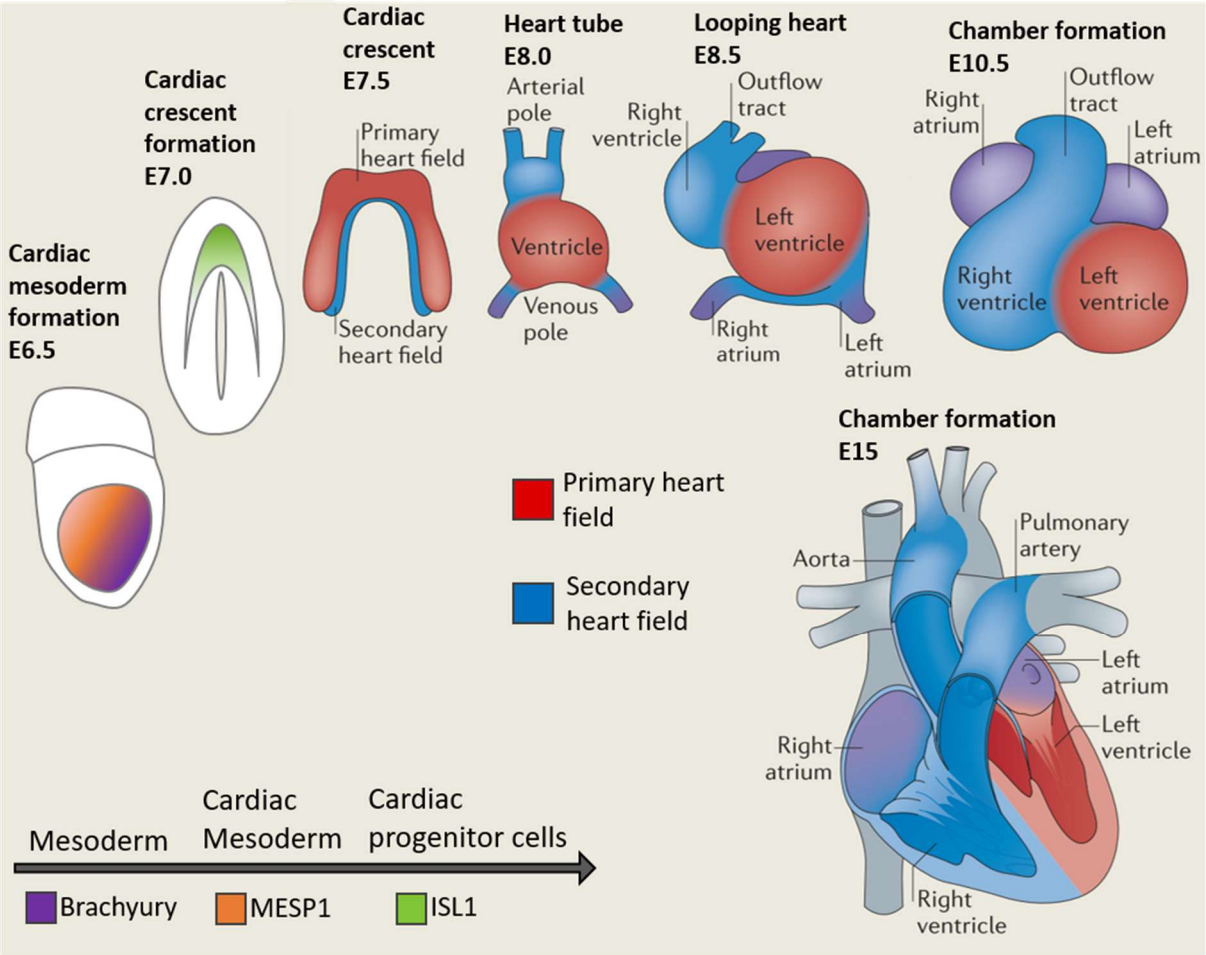

Figure 2.2 Heart development in vivo is achieved by the generation of two heart fields.
The origin of cardiac tissue is the mesoderm. Consecutive activation of Brachyury, MESP1 and ISL1 correlates with the transition from early mesoderm through the cardiac mesodermal phase to the cardiac progenitor stage. From there, the primary and secondary heart field, as structural entities of the cardiac crescent, are recognizable. After the heart tube is formed, a complex looping gives rise to the individual chambers. Adapted from Wu et al. 2008 and Xin et al. 2013.

The recapitulation of this biphasic contribution by the use of small molecules to activate and consecutively inhibit the WNT pathway *in vitro* further increased the differentiation efficiencies in two- and three-dimensional culture formats to over 75% (Burridge et al., 2014; Yang et al., 2008; Zhang et al., 2015). Additionally, small molecule based activation as well as inhibition of the WNT pathway is highly cell compatible, effective and shortens the differentiation time (Batalov et al., 2015; Mehta et al., 2014; Zhang et al., 2015). Nowadays, the *in vitro* differentiation from hiPSCs to early cardiomyocytes is performed in approximately seven days (Zhang et al., 2015). The developmental progression *in vitro* follows tightly the developmental stages *in vivo*. In the pluripotent cells, master regulators of pluripotency are active. *OCT3/4* and *SOX2* activity is maintained and required for the pluripotent state, as proven by their use in the generation of hiPSCs from somatic cells (Takahashi et al., 2006; Yoshida et al., 2010).

The formation of early mesendoderm, from which the early heart tissue originates, is initiated through, BMP4 and FGF2 signalling (Rawles, 1943). Typical genes involved in this stage are *EOMES* and *T* (Brachyury) (Izumi et al., 2007). Although these are not uniquely expressed in cardiac tissue formation, their signalling is required for mesendodermal regulation. Upon WNT inhibition, the formation of the cardiac mesoderm is initiated. Mesoderm posterior protein 1 is a key regulator of this formation and its gene, *MESP1*, is one of the earliest genes involved in cardiovascular commitment (Bondue et al., 2010) and is expressed in all cardiac progenitor cells, although it is not limited to them since it is also active in skeletal muscle as well. Thus, *MESP1*-positive cells still can give rise to all major cell types of the heart: endothelial cells (abbr. ECs), vascular smooth muscle cells (abbr. VSMCs), cardiac fibroblasts (abbr. CFs) and cardiomyocytes (abbr. CMs) (Wu et al., 2008). The further loss of potency is associated with the formation of the cardiac crescent and the transcription factors Nkx2.5 and ISL-1 (Xin et al., 2013). Cells, positive for these factors are still able to give rise to VSMCs and CMs (Saga et al., 1999). At this time, the first and second heart field can be discriminate *in vivo*. The first heart field will later give rise to the left ventricle. The second heart field is the origin of the atria and the right ventricle (Xin et al., 2013) (Figure 2.2). It is noteworthy, that the previously very common assumption that these ISL1-positive cells represent a resident stem cell population in adult hearts is presumably not reflecting the reality as a thorough study found no evidence for it (Li et al., 2018b). Current studies suggest that ISL1 takes up a supportive and enhancing role in cardiac lineage commitment during late specification (Quaranta et al., 2018). Nevertheless, ISL1 is a key marker for the transition from the cardiac mesodermal stage to cardiomyocytes (Quaranta et al., 2018; Zhang et al., 2015). The earlier described genes act mainly as transcription factors, regulating the expression of many downstream genes and directing the lineage induction. However, with the formation of the early heart tube many specific proteins are translated and functionally integrated, particularly the ones associated with ion channels and cytoskeletal arrangements. Thus, the contractile machinery of cardiomyocytes is formed and contractions are detectable in these early CMs. The further heart formation *in vivo*, from a tube to four-chambered adult organ, is achieved by looping and consecutive chamber formation. After establishment of the final organ structure, an extensive hypertrophic growth is taking place in the neonatal phase *in vivo* to supply the increasing workload demand. This is also associated with extensive cardiac maturation, in particular, the switch from a glucose-based to an oxidative metabolism, t-tubule formation, connexin 43 and sodium channel localisation at intercalated discs and the functional integration of the inward rectifying K+ channel. Contrary to the development *in vivo*, PSC-derived cardiomyocytes do not reach and recapitulate the adult phenotype found in humans, but remain in a fetal-like state *in vitro*. These discrepancies encompass all major cellular characteristics, since metabolism, electrophysiology and contractile behaviour are affected (Da Rocha et al., 2017; Robertson et al., 2013; Scuderi et al., 2017; Uosaki et al., 2016; Yang et al., 2014). Hence, the immaturity of hiPSC-CM limits accurate drug effect predictions, disease modelling and clinical applications. The *in vitro* approaches to achieve a higher physiological resemblance and the functional assays associated with these studies are described in the following chapter 2.2.

2.2 CLINICALLY RELEVANT HIPSC-CM-BASED MODELS IN THE CONTEXT OF TISSUE ENGINEERING

The Langendorff ex-vivo preparation of a fully functional heart was the first proof that a complete functional cardiac *in vitro* model can be achieved (Langendorff, 1895). Although this model was very useful in the early characterization of physiological mechanisms, particularly when imaging methods were not so advanced, it is too time consuming and costly for high throughput pharmacological screenings. Additionally, this method can not be easily expanded on human hearts, when high numbers of samples are needed.

A model system for the correct prediction of cardiovascular side effects is urgently needed, due to the often drastic nature of the side effects and the relatively low translational potential of existing model systems (Gwathmey et al., 2009) (Figure 2.3). This is also reflected in the high number of post market withdrawals of drugs with previously undetected cardiovascular side effects (Sallam et al., 2015). The stark discrepancy between the human physiology and small animal models, in concert with the high cost of large animal models makes the development of human *in vitro* models necessary.

There is great hope that hiPSC-CM-based models will be able to recapitulate the human cardiac physiology fully *in vitro*. However, the immaturity of PSC-derived cardiomyocytes obstructs this vision and significantly limits the translational potential of *in vitro* models.

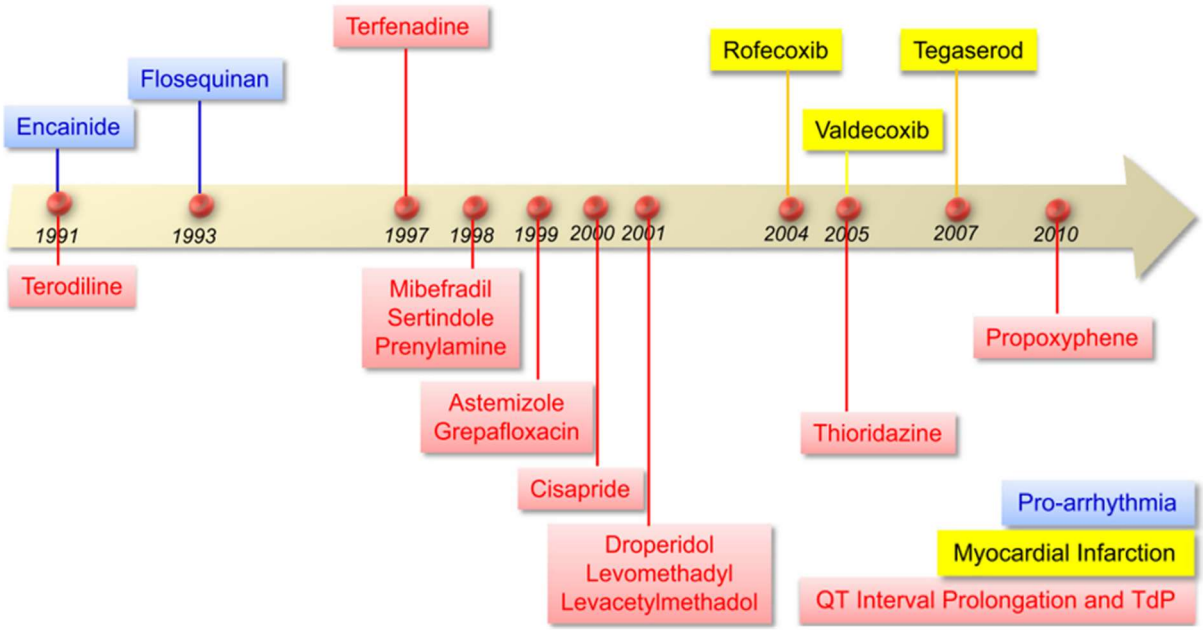

Figure 2.3 Post market withdrawals due to cardiotoxic side effects.
Since 1991, two pro arrhythmic (blue) and thirteen QT-interval affecting drugs with the potential for torsades des pointes (TdP) have been withdrawn from the market. Additionally, three compounds have been withdrawn due to their potential to induce myocardial infarction. Figure modified taken from Sallam et al. 2015.

Nevertheless, the fundamental usability of hiPSC-CMs to derive relevant clinical predictions has been shown in several studies (Guo et al., 2011; Harris et al., 2013).

A hallmark study has proven that PSC-CMs can be matured *in vivo* and therefore has proven that these cells fundamentally possess the potential for maturation (Kadota et al., 2017). Since the immaturity includes such diverse characteristics, *e.g.* cytoskeletal arrangements, ion channel expression and localisation, and the metabolism, many different approaches have been conducted to achieve a higher maturity. Although progresses have been achieved, they were always limited to specific parameters and a fully mature phenotype has not yet been derived from hiPSC-CMs (Kadota et al., 2017; Robertson et al., 2013). The different strategies to induce maturation *in vitro* can be roughly separated into four groups: electrical stimulation, extracellular matrix engineering, mechanical stimulation and cellular composition (Karbassi et al., 2020).

Approaches based on electrical stimulation rely on the positive feedback loops of the conductive apparatus in CMs and have been realised via the integration of electrodes in two- and three-dimensional cell cultures (Chan et al., 2013; Eng et al., 2016). It was shown that the expression of Cx43, sarcomere organisation and gene expression patterns benefited from a constant stimulation. Furthermore, the initially immature action potential shape was enhanced to a more adult shape (Chan et al., 2013; Eng et al., 2016).

Since primary cardiomyocytes progress towards immaturity in polystyrene-based cell cultures, it was hypothesized that the extracellular matrix composition and its mechanical characteristics influence PSC-CM maturation. Several studies using fibronectin or laminins have been show to generate PSC-CMs with enhanced sarcomeric organisation and a more mature gene expression pattern. Although conducted with neonatal rat ventricular cardiomyocytes, an early work by Zimmermann et al. has shown that these cell exhibited a highly matured sarcomere organisation when cultured in a three-dimensional collagen matrix (Zimmermann et al., 2002). The use of aligned elliptical posts in a fibrin-based hydrogel as a culture substrate has led to the fastest conduction velocities ever measured in an *in vitro* model (Liau et al., 2011).

Mechanical stimulation was also shown to significantly induce maturation of iPSC-CMs. Using a gelatinous sponge exposed to uniaxial cyclic stretch (1Hz, 12%) for 3 days, sarcomere organisation and Cx43 expression was enhanced, as well as an upregulation of the clinical relevant ion channel KCNJ2. These cellular constructs were later transplanted into a AMI model and it was observed that they fused better with the host myocardium and reduced the progressive wall thinning more than control groups (Mihic et al., 2014). Tulloch et al. have proven that, hiPSC-CMs culture in a three-dimensional collagen matrix under uniaxial mechanical stress leads to a significant upregulation of the hypertrophy and proliferation (Tulloch et al., 2011).

The physiological development of the myocardium is dependent on the presence of non-myocyte cells. This knowledge was translated into in-vitro models and it was shown that,

micro tissues consisting of cardiomyocytes, cardiac fibroblasts and endothelial cells, exhibited an enhanced gene expression and sarcomere assembly (Ravenscroft et al., 2016).

Several studies have proven the feasibility and the translational potential of toxicological screening using iPSC-CMs (Ando et al., 2017; Tertoolen et al., 2018). Since the immaturity of the human *in vitro* models still fails to predict specific pharmacologically relevant parameters in toxicological studies, the advancement and development of such models could lead an even higher translational potential. Furthermore, combinatorial approaches of the aforementioned methods have been used to achieve an even higher physiological relevance with the possibility to derive pharmacological data. The main parameters are still electrophysiological characterisation of the action potential durations, the conduction velocity and the upslope and downslope characteristics. The Biowire platform utilizes a three-dimensional biological matrix wrapped around a wire, which serves as an electrode. The assessment proved the enhanced maturation by caffeine responsiveness of hiPSC-CMs, which were stimulated and cultured in the Biowire system simultaneously (Nunes et al., 2013). The multicellular microtissues created by Ravenscroft et al. were also stimulated and pharmacologically assessed. Using this setup prediction of inotropic effects upon beta-adrenergic stimulation was superiorly detected, highlighting the higher translational potential (Ravenscroft et al., 2016).

The generation of contractile force is the major functional output of cardiomyocytes *in vivo* and there are efforts to create robust *in vitro* models, which allow the assessment of these contractile forces. Engineered heart tissues have been grown in a fibrin matrix, which is stretched between two silicone posts. Not only did the cardiomyocytes express an mature genetic pattern, but also possessed matured sarcomeric structures. Based on the optical assessment of the silicone post deflection, this setup enables the quantification of the exerted forces. Utilizing this model system, contractile work was shown to induce a metabolism-maturating effect in hiPSC-CMs (Ulmer et al., 2018). Additionally, the antagonistic effect of carbachol exposure to beta-adrenergic stimulation on force generation and calcium handling was detected with this setup (Stoehr et al., 2014). Similar to this setup was the derivation of a defined engineered human myocardium based on a collagen matrix (Tiburcy et al., 2017). A heart failure *in vitro* model was established by chronic exposure to catecholamines. The observed beta-adrenergic desensitisation and the concentration-dependent release of the clinically relevant biomarker N-terminal pro B-type natriuretic peptide was observed. Although, this model represents one of the most advanced iPSC-CM based *in vitro* models, the authors of this study concluded: “In fact, unbiased global transcriptome profiling suggested that EHMs are, at large, similar to fetal human heart at 13 weeks of gestation…” (Tiburcy et al., 2017). Thus, there is still a lot of progress and research needed until a fully physiological hiPSC-CM *in vitro* model is available.

2.3 STATE OF THE ART 3D PRINTING OF CLINICALLY RELEVANT MATERIALS AND CELLS

Both, the need for complex *in vitro* models and the limited retention of transplanted single cells in affected hearts, fostered the development of three-dimensional functional tissue equivalents, which enable a robust engraftment as well as high physiological relevance. With 3D printing techniques leading to innovations many in other fields, *e.g.* engineering, manufacturing and medicine, the adaption of this technique to the field of tissue engineering is connected with great hopes. Contrary to the engineering field, where high temperatures and pressures are normally not a burden, 3D printing of relevant materials and cells needs specific requirements to be fulfilled to allow a gentle production process. Although the cells themselves represent the most sensitive part, biopolymers are also sensitive for high temperatures and are often difficult to handle. Currently, several methods are used to structure relevant materials in a three-dimensional manner. The major focus is set on additive manufacturing, the layer-by-layer deposition of artificial substrates, biological materials and cells, ultimately producing three-dimensional structures. Additive layer manufacturing can be further divided into inkjet, laser-assisted and microextrusion-based bioprinters (Figure 2.4).

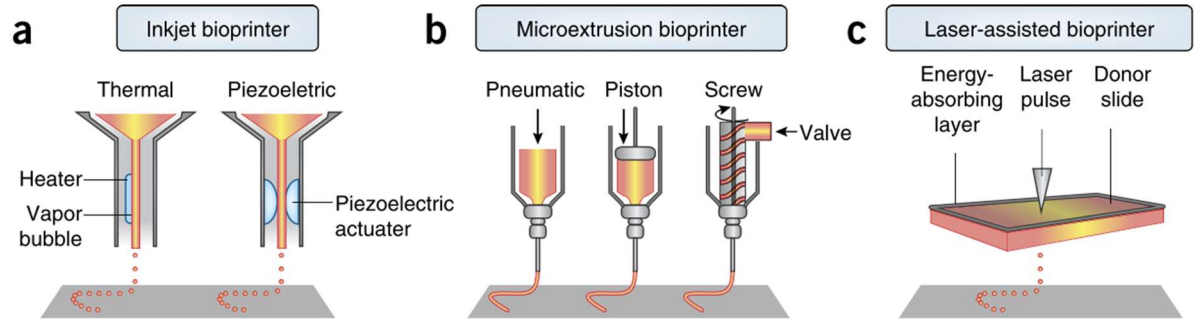

Figure 2.4 Common 3D bioprinting techniques for the deposition of biological relevant materials, cells and chemical compounds.
Inkjet based protrusion systems rely on a thermal- or acoustic-induced droplet formation (A). Microextrusion printers use mechanical or pneumatic pressures to create a constant material outflow (B). Laser-assisted printers release cells or materials from a donor slide through a laser-induced evaporation of an energy absorbing substrate (C). Figure taken from Murphy et al. 2014.

Inkjet bioprinters rely on the thermal- or acoustic-induced deposition of droplets. This method allows a precise control over the structuring process and enables the creation of small, separated compartments in the printed structures. Several studies have proven the feasibility of printing mammalian cells with this approach and have shown that the thermal-induced droplet production does not affect the viability of cells substantially (Xu et al., 2006, 2005). Skin, cartilage and neural cells have been readily structured with this method and, particularly, the production of layered, epithelial tissues (*i.e.* skin) benefits from the high resolution and the fast printing speed (Cui et al., 2012b; Skardal et al., 2012; Xu et al., 2012). The low cost, the high speed and the high printing resolution are the major advantages of this method.

However, the high printing speed and sheer stress in the nozzle has been observed to induce cell membrane disruption and lysis (Cui et al., 2012a). The ink has to fulfil specific requirements; particularly the viscosity has to be very low to avoid clogging of the nozzle. For the same reason, cell concentrations are also low. Since the viscosity is very low, crosslinking reactions have to be performed and conducted simultaneously to the printing (Murphy et al., 2014). The crosslinking has been induced with UV-light, pH and radical polymerization and is suspected to have a toxic effect on cells (Hennink et al., 2002).

Laser assisted printing relies on a laser beam that releases the donor material from a glass surface, which is coated with a photosensitive material (Murphy et al., 2014). This method allows to print single cells into high concentration structures (50 million cells/ml) (Guillotin et al., 2010). Nevertheless, this method requires the preparation of the donor material and high voluminous structures need a constant change and feed with these carrier plates. The forces applied on the cells upon disruption of the energy absorbing material have been shown to adversely affect sensitive cells, particularly stem cells (Koch et al., 2013).

Microextrusion-based systems use pneumatic or screw driven extrusion mechanics. A wide range of biological materials with different viscoelastic properties can be processed with these 3D printers. The affordability, low preparation requirements and the capability to print high cell concentration are presumably the reason why this is the most common printing method in the biological sciences. Since the first translation of this method was published, modifications of the original setup led to the possibility to print an ionic crosslinking solution simultaneously or to print hollow strands. Additionally, endothelial cells have been printed with this technique, enabling the production of engineered endothelialised myocardia (Zhang et al., 2016). Vascular geometries have also been created with this approach to allow endothelial cells to move into such structures (Lee et al., 2014; Miller et al., 2012). Furthermore, this approach allows to include different materials and cell combinations in the same scaffold since 3D printers with multi cartridge systems are already commercially available (Jia et al., 2016). Independent of the printing method, there are two main strategies to create biological engineered tissues and their distinction is the inclusion of cells into the ink. Although omitting cells from the ink enables to perform aggressive printing methods, which leads to better printing performances, it can be detrimental for the formation of highly organized structural components like vessels (Lee et al., 2014; Miller et al., 2012).

A major influence on the printing performance and the biological resemblance of the engineered constructs are due to the chosen material or the ink composition. Many different artificial and biological polymers have been utilized in 3D printing. Artificial polymers (*e.g.* polyethylene glycol, poly-caprolactone and pluronic) have superior printing performances but often have diminished biological compatibility and lack the mechanical properties of biological tissues (Müller et al., 2015; Park et al., 2009; Urrios et al., 2016). Cells often cannot penetrate into these materials and they represent single, separated compartments in the matrix. Natural polymers and hydrogels (*e.g.* cellulose, alginate, chitosan and gelatine) have been commonly utilized in bioprinting studies and have shown superior biological compatibility and

functionality (Li et al., 2005; Luo et al., 2018, 2017; Markstedt et al., 2015). However, the viscoelastic properties and the crosslinking mechanisms often limit the printing accuracies. Based on the knowledge from heart decellularisations, that biological matrices are still biologically active and accessible for cells after the harsh decellularisation process, 3D printing inks derived from primary heart, adipose or cartilage tissue were produced and were still biologically active after the printing process, thus, proving the versatility of this approach (Pati et al., 2014). Albeit this approach was successful *in vitro*, it still carries the risk for host immune reactions *in vivo* when xenogeneic biological material is used. Furthermore, the availability of human decellularized specialised tissue is limited and it can be anticipated the batch to batch variations will occur. Albeit it's critical role in the 3D printing process, the optimal bioink has not been found and there is ongoing research in this field to develop enhanced formulations and printing techniques to enable the availability of 3D printed human tissues.

3 MATERIALS AND METHODS

The material and method section was separated into three chapters, following the core areas of iPSC technologies this work was focused on. The generation of hiPSC-derived CMs was performed using two hiPSC-lines, which were generated with differing reprogramming strategies. To analyze the effect of elastic biopolymer-based substrates on hiPSC-CMs for in-vitro modelling, UHV-alginates were used. Finally, these hydrogels were 3D printed and combined with pharmaceutical-grade cardiomyocytes to enable future clinical applications.

3.1 SCALABLE CARDIOMYOCYTE GENERATION FROM HIPSCS IN A SUSPENSION BIOREACTOR

Two human induced pluripotent stem cell lines, UKBI005 and IBMT1, were used in this work. UKBi005 is a cell line reprogrammed with an integrative, but silenced retrovirus and was acquired from the European Bank for induced pluripotent Stem Cells (EBISC). The IBMT1 cell line was in-house reprogrammed with non-integrative mRNAs (Reprocell, USA) from BJ fibroblasts (ATCC, USA). Cell lines were cultured in mTeSR1 medium (Stem Cell Technologies, Canada) on 60mm petri dishes coated with growth factor reduced Matrigel (Corning, USA). 100µl of a 10mg/ml Matrigel solution was diluted in 12ml DMEM/F12. 2 ml of this solution was applied per plate and incubated overnight in the incubator at 37°C and 5% CO_2. Cell detachment for passaging was achieved with 5min incubation 0.5mM EDTA (Invitrogen, USA) exposure for in Dulbecco's phosphate buffered saline without Ca^{2+} and Mg^{2+} (DPBS(-/-)) (Gibco, USA).

Differentiation of iPSCs to cardiomyocytes in the suspension bioreactor and the hanging drop culture

Cardiac differentiation was based on the protocol devised by Zhang et al. (Zhang et al., 2015). Single hiPSCs were produced by aspirating the medium and two washing steps with DPBS(-/-), followed by TrypLE Select (Gibco, USA) treatment. After the reaction was stopped by addition of 3ml mTeSR1 (Stem Cell Technologies, Canada) with 10µM ROCK inhibitor Y27632 (Abcam, UK). Single cells from small cell clusters were produced by gentle resuspension using a 1ml pipette with a wide bore. Cell counting was performed with the NucleoCounter NC-200 (ChemoMetec, Denmark) and the cell concentration was set accordingly.

For the suspension culture in the bioreactor, the cell concentration was set to 7.5 * 10^5 cells/ml in D0 media (Table 3.1). Not less than 10ml, and up to 40ml, of the cell suspension

were gently transferred into a Levitube (OMNI Life Sciences, Germany) and, without further delay, inserted into a Levitube slot of the bioreactor (BioLevitator; OMNI Life Sciences, Germany) to culture the cells under stirring conditions at 37°C and 5% CO_2. Continuous rotations at 60rpm were performed in an alternating pattern, with two seconds per rotational direction. Medium change was performed every 24h. Sedimentation of the cells was achieved by transferring the Levitube to a sterile bench and let it rest there for up to 15 min depending on the spheroid size. Successful sedimentation was verified by optical control. The consumed medium was replaced with an equal volume of fresh medium every 24 hours.

Table 3.1 Composition of the different media used during directed cardiomyocyte differentiation (adapted from (Zhang et al.*, 2015).*

	Additive	**Additive concentration in KO-DMEM**
Day 0 medium	Penicillin-Streptomycin-Glutamine Mix	1:100 dilution
	Y27632	10 µM
	ITS (insulin, transferrin, selenium) premix	1:1000 dilution
	Activin A	10 ng/ml
	BMP4	1 ng/ml
	FGF2	10 ng/ml
	CHIR99021	1 µM
Day 1 medium	Penicillin-Streptomycin- Glutamine Mix	1:100 dilution
	TS (transferrin, selenium)	T: 5.5 mg/l, S: 6,75 µg/l
	Ascorbid acid	250 µM
Day 2 medium	Penicillin-Streptomycin-Glutamine Mix	1:100 dilution
	TS (transferrin, selenium)	T: 5.5 mg/l, S: 6,75 µg/l
	Ascorbid acid	250 µM
	Wnt inhibitor C-59	2 µM
Day 3 medium	Penicillin-Streptomycin-Glutamine Mix	1:100 dilution
	TS (transferrin, selenium)	T: 5.5 mg/l, S: 6,75 µg/l
	Ascorbid acid	250 µM
	Wnt inhibitor C-59	4 µM
Maintenance medium	Penicillin-Streptomycin-Glutamine Mix	1:100 dilution
	TS (transferrin, selenium)	T: 5.5 mg/l, S: 6,75 µg/l
	Ascorbid acid	250 µM

Concerning the HD culture, 7500 hiPSCs were seeded per d0 media drop (40µl) in Perfecta3D hanging drop plates with 96 wells (Sigma, Germany). Culture media was changed every 24h by replacing half of the consumed media twice. The media composition is shown in table 3.1. In short, KO-DMEM served as the basic medium for every medium composition used during cardiomyocyte differentiation. Penicillin-streptomycin-glutamine (abbr. PSG) (Gibco, USA) was added in a 1:100 dilution according to producer instructions to prevent microbial contamination. The D0 medium contained a ROCK inhibitor (Y27632, Abcam, UK) to prevent apoptosis and an insulin-transferrin-selenium mix (Corning, USA), which was added in a 1:1000 dilution following the producers' instructions. Activin A (eBioscience, USA), BMP4 (R&D systems, USA), FGF2 (Peprotech, USA) and CHIR99021 (Axon Medchem, Netherlands) were added to achieve the specific concentrations given in table 1. D1 medium consisted of KO-DMEM with added PSG and ascorbic acid. On day 2, the D1 medium was replaced by D2 medium, which contained PSG, ascorbic acid and the WNT inhibitor C59 (Tocris, USA). The following day, the medium was replaced with D3 medium containing an increase concentration of the WNT inhibitor C59. Afterwards, the cells were kept in maintenance medium until the dissociation was performed.

Dissociation of cardiac spheroids with three different enzymes

To dissociate the cardiac spheroids Accutase (Sigma-Aldrich, USA), Papain (Worthington Biochemical, USA) and TrypLE Select (Gibco, USA) were used in this work. Papain was activated with L-Cysteine before being used for cell dissociation. To achieve this, a dissociation solution with 40U/ml Papain and 2mM L-Cysteine in PBS(-/-) was incubated for 10min at 37°C. The spheroids were transferred into 15ml centrifugation tubes and washed twice with 4mM EDTA in PBS(-/-). The cells were centrifuged for 2min at 250g and the washing solution was replaced with 1ml of either Accutase and TrypLE. For the papain dissociation the spheroids were transferred into 0.5ml PBS(-/-) and 0.5ml of the activated papain solution was added. The cells were then incubated for 15min (Accutase and TrypLE) or 30 min (papain) at 37°C. The papain reaction was stopped with addition of 1ml stopping solution containing 1mg/ml trypsin inhibitor (Sigma-Aldrich, USA) and 40µg/ml DNAse I (Sigma-Aldrich, USA). The cell concentrations were either assessed with the Nucleocounter, following

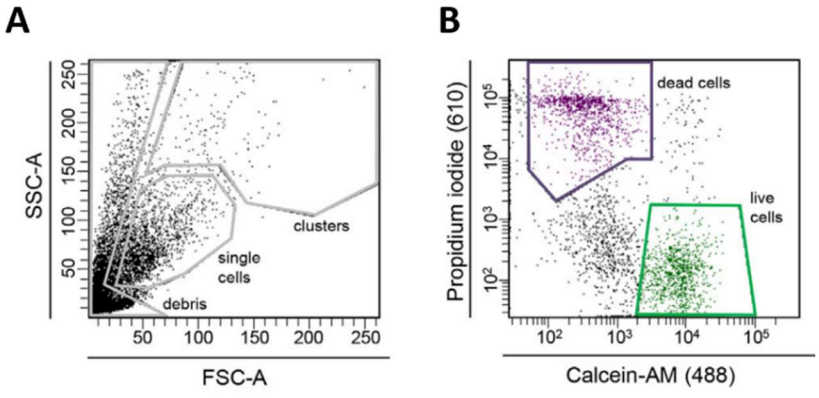

Figure 3.1 Depicted is the gating strategy, which was used to discriminate between cell clusters, cell debris and single cells.
Viable and dead single cells were quantified by fluoresce dependent separation of the single cell gate in A, based on a propidium iodide and calcein staining (B).

strictly the manufacturer instructions, or sieved with a 40µm cell strainer (Thermo Fisher Scientific, USA) and measured via flow cytometry. For the flow cytometry-based analysis, the sieved cell suspension was not stained (control group) or stained with either calcein acetoxymethyl (abbr. calcein AM) (Fisher Scientific, USA), propidium iodide (abbr. PI) (Fisher Scientific, USA) or both. To achieve a sufficient calcein AM staining, 10^6 freshly dissociated cells were in incubated in 1ml PBS(-/-) with 5ng calcein AM for 25min at 37°C. The cell suspension was then centrifuged and the calcein containing supernatant was replaced with 0.5ml PBS(-/-). 1µl PI solution was added to each sample directly before flow cytometry analysis with a FACSAria III (BD Biosciences, USA). Discrimination of cell clusters, single cells and debris was achieved by plotting the forward scatter against the sideward scatter in combination with the gating strategy shown in Figure 3.1.

3.2 GENERATION OF BIOPOLYMER-BASED SUBSTRATES FOR *IN VITRO* MODELLING OF THE CARDIAC NICHE

To enable the analysis of biopolymer-based substrates, UHV-alginates were used in this study. To achieve the desired concentration of the UHV-alginate solutions, weighed amounts of solid UHV-alginates (Alginatec, Germany), either from *L.t.* and *L.n.*, were transferred into 50ml centrifugation tubes under sterile conditions and filled with according volumes of sterile 0.9% NaCl solution to achieve 0.3%, 0.7%, 1.0% and 1.5% (w/v %) solutions. To ensure homogenous solutions, the tubes were incubated on an orbital rotator for a minimum of 48 hours. Additionally, the 1.5% solution was homogenized by gentle manual stirring with a sterile laboratory glass rod. Afterwards, equal amounts of *L.t.* and *L.n.* alginates were transferred to a new centrifugation tube and mixed on a laboratory orbital rotator for a minimum of 48h. To ensure homogeneity of this mixing step as well, the 1.5% solution was again stirred manually under sterile conditions.

Analysis of UHV-alginate viscosity

The viscosity measurements of the UHV-alginate solutions were carried out on a rheometer (Physica MCR 101, Anton Paar, Germany). The used probe was "Messplatte PP25" (Anton Paar, Germany) with a diameter of 25mm. Of each UHV alginate solution (1:1 mixture of *L.t.* and *L.n.*) 500µl were applied onto the measurement platform. The distance between the probe and the base was set to 0.3mm during the measurements. A dynamic shear rate measurement was conducted with a rotational velocity of $1s^{-1}$. A measurement period of 2 minutes was set and the data acquisition was conducted with the Rheoplus software (Anton Paar, Germany). The first 10 sec of each measurement were excluded for the analysis due to the high noise. The remaining data points were analysed, averaged and the standard error of the mean was calculated.

Measurement of the Young's modulus

The Young's modulus of the fixed UHV-alginate layers and the HP was derived using the Piuma Nanoindenter (OPTICS11 B.V., Netherlands). To this extent, for each stiffness (0.7%, 1.0%, 1.5%) nine measurements were conducted per UHV-alginate concentration using a probe with 48µm tip size and 4.0N/m stiffness. For the measurement of the 0.3% UHV-alginate layers and the HP, a different probe with a 3.5µm tip and 0.017N/m stiffness was used. The soft 0.3% UHV-alginate layers were measured 18 times and the HP equal to or more than six times. The calculation of the Young's modulus was performed automatically by the Piuma software including the standard error of the mean.

UHV-alginate layer production and functionalisation

Poly-L-lysine (abbr. PLL) (Sigma-Aldrich Chemie GmbH, Germany) was diluted 1:5 in PBS(-/-). Per well of a 48 multiwell plate, 200µl of the PLL solution was applied and incubated for 1h at 37°C. The solution was aspirated and the plate was dried overnight under a sterile hood at room temperature (abbr. RT). 220µl of UHV-alginate solution was gently transferred into each well without air bubbles. To achieve a homogenous layer height, the plates were put to rest for 20 min followed by addition of the crosslinker (20mM $BaCl_2$, 0.5ml/well) solution. The crosslinker solution was incubated overnight at room temperature (20°C). Consecutively, the crosslinker solution was aspirated and a washing step with 1ml 0.9% NaCl was conducted. Functionalisation of the inert layers was based on a previously published method to achieve a carbodiimide-mediated coupling of proteins to the alginate surface (Gepp et al., 2017). Briefly, the crosslinker solution was aspirated and 600µl of a 300mM N-(3-Dimethylaminopropyl)-N'-ethylcarbodiimide hydrochloride (abbr. EDC) (Sigma-Aldrich, USA) and 75mM N-Hydroxysuccinimide (abbr. NHS) (Sigma-Aldrich, USA) solution (in ddH_2O) was applied. The EDC/ NHS solution was incubated for 1h at RT and then aspirated. 500µl of a 0.1g/L Tyramine-HCl (Sigma-Aldrich, USA) solution was added to each well and incubated overnight. Serial washing steps were conducted afterwards. First, the layers were washed twice with 0.9% NaCl (0.5ml/well) and then three times with 0.5ml/well DMEM/F12 (Gibco, USA). 20µg/cm^2 of Matrigel, a heterogeneous protein mix derived from Engelbreth-Holm-Swarm mouse sarcoma cells, was applied in 500µl ice cold DMEM/F12. The plates were incubated on an orbital shaker for 1h at RT, then transferred to the incubator (5%CO_2, 37°C) and incubated overnight. The Matrigel solution was aspirated and the layers were washed once with medium (1h incubation at 37°C and 5% CO_2) and then the cells were seeded on the layers (for details refer to "Human PSC-derived cardiomyocyte culture and maintenance" below).

Human PSC-derived cardiomyocyte culture and maintenance

Human PSC-derived cardiomyocytes (COR.4U) were acquired from Ncardia (Germany). The COR.4U cells were initially sold as derived from induced pluripotent stem cells, but during this work, an embryonic fingerprint was detected in the COR.4U cell line (personal communication with Ncardia, 2019). While this cell line has been discontinued since then, it still represents a well-characterized human cardiomyocyte cell line. Additionally, it was shown that this cell line shares many characteristics with iPSC-derived cardiomyocytes, thus the results and conclusions are represent valid contributions in the field of cardiac maturation (Blinova et al., 2017; Yamazaki et al., 2018).

The cells were delivered as live shipment and all handling was performed following the suppliers' instructions. For detachment, the cells were washed once with 15ml PBS(-/-) with 2mM EDTA and afterwards incubated for 7min in 15ml PBS(-/-) with 2mM EDTA at 37°C, 5% CO_2. The solution was aspirated and 6ml of a warm Trypsin/ EDTA solution was applied. After a two-minute incubation at 37°C and 5% CO_2, the reaction was stopped with an equal

volume of COR.4U medium and the cells were detached by gentle tapping. The cell suspension was centrifuged for 3min at 200g. The supernatant was aspirated, the cell concentration was adjusted with warm medium and 100 000 cells in 0.5ml medium were transferred in each well of a 48 well plate. The next day the medium was changed. The following media changes were performed every other day.

3.3 PRODUCTION OF A 3D PRINTED, TRANSPLANTABLE HEART PATCH FOR TISSUE ENGINEERING APPLICATIONS

To enable the production of a 3D printed scaffold carrying human cardiac cells, the biopolymer inks had to be 3D printed and functionalized before COR.4U cardiomyocytes (Ncardia, Germany) were cultured on the contractile matries.

Fabrication of UHV-alginate scaffolds using conventional 3D printing and freeze printing

3D Printing was conducted with the Bioscaffolder 2.1 (GeSim, Germany) and a costum-built insulating box made out of an epoxy material with low thermal expansion (RENshape, OBO-Werke GmbH, Germany). 0.3%, 0.7%, 1.0%, and 1.5% UHV-alginate solutions were printed on microscopic glass slides with dispensing needles of 0.2mm diameter (Vieweg, Germany). The freeze printing was conducted after the insulating box was filled with dry ice and the temperature reached values below -20°C. During printing, a probe-based and an infrared thermometer were used to control the temperature. After the printing process was finished, a drop of a 20mM $BaCl_2$ solution was dropped onto the frozen scaffold. When the drop was frozen, the whole scaffold was transferred to 10ml of $BaCl_2$ (20mM) solution. After a 1h incubation at RT the scaffolds were transferred into a 0.9% NaCl solution until further use. Then, the scaffolds were either directly stained to assess the structural details with a confocal scanning microscope or biofunctionalised to create an adhesive surface for the culture of hiPSC-CMs.

Fluorescence labelling of the UHV-alginate scaffolds was performed with Fluorescein-5-Isothiocyanate-labelled Poly-L-Lysine (abbr. FITC-PLL) (Sigma-Aldrich, USA). 10mg FITC-PLL was diluted in 1ml ddH_2O. Before staining, the solution was diluted 1:100 in 0.9% NaCl and 1ml was applied to each scaffold. The scaffolds were incubated on an orbital shaker for 24h at RT in the dark. Afterwards, the scaffolds were transferred to an isotonic 0.9% NaCl solution and images were acquired using a confocal laser-scanning microscope (TCS SP8, Leica, Germany). To prevent drying of the scaffolds, they were visually inspected and, if needed, more 0.9% NaCl solution was applied. Analysis of the scaffold pores was carried out by hand with the software FIJI ImageJ (version 1.5f).

Biofunctionalisation of the scaffolds followed the protocol used for the biofunctionalisation of the UHV-alginate layers. Briefly, the scaffolds were transferred from the 0.9% NaCl storage solution to a functionalisation solution, containing 200mM EDC/ 50mM NHS in water. After 1h at RT under constant, gentle agitation the functionalisation solution was replaced with a 0.1g/ml Tyramine-HCl solution. After overnight incubation (RT, constant agitation), the scaffolds were washed twice with 0.9% NaCl solution and then transferred into DMEM/F12. Matrigel was added to ice cold DMEM/F12 to a final concentration of 20µg protein per cm^2 scaffold growth area. The scaffolds were incubated overnight at RT under constant agitation

and then washed with COR.4U medium. 500 000 COR.4U cells per scaffold were seeded in COR.4U medium. The medium was then changed every other day.

Scanning electron microscopy

To prepare the scaffolds for scanning electron microscopy, the UHV-alginate matrices were fixed in sterile filtered 0.075M cacodylate buffer containing 6.25% glutaraldehyde (pH7.2-7.4; 300-360mOsmol) and stored in the dark at 4°C. Next, each UHV-alginate scaffold was washed three times with 0.15M cacodylate buffer and then incubated for 1h at RT in sterile filtered 0.15M cacodylate buffer containing 1% tannic acid. Afterwards, the scaffolds were washed once in 0.15M cacodylate buffer and the dehydrated. First, the scaffolds were exposed to increasing ethanol concentrations (50%, 70%, 80%, 90%, 96%, 100%). Second, the scaffolds were incubated in a solution containing 50% hexamethyldisiloxane and 50% ethanol. This buffer was replaced with a 100% hexamethyldisiloxane solution, which was replaced twice. Then the scaffolds were dried for 3 days under a chemical fume hood. The scaffolds were placed on SEM sample carriers and sputtered with carbon before imaging them on the scanning electron microscope EVO MA (Zeiss, Germany)

Loss and storage modulus calculation

The loss and storage modulus analysis of the UHV-alginate solutions and the crosslinked UHV-alginate scaffolds were carried out on the Physica MCR 101 (Anton Paar, Germany) as well. For the non-crosslinked UHV-alginate solutions 500µl were applied to the measurement area. To measure the scaffolds, per measurement a 1cm scaffold was placed in the centre of the measurement. Here, an oscillatory sweep measurement was conducted ranging from 0.1 rad per sec to 10 rad per sec. Using the Rheoplus software (Anton Paar, Germany) the corresponding G’ and G’’ values were calculated from the measurements and plotted accordingly.

Staining of cellular structures with immunocytochemistry

The samples were fixed for 15min at RT with BD Cytofix fixation buffer (BD Biosciences, USA). Afterwards, samples were washed for three times with PBS(-/-) and then, the permeabilisation step was performed by incubating the samples in a solution of 0.2% Triton X in PBS(-/-) for 20min at RT. Again, the samples were washed three times with PBS(-/-). Consecutively, the samples were blocked with a blocking buffer containing 4% bovine serum albumin (abbr. BSA) (Sigma-Aldrich, USA) and 0.2% Tween solution in PBS(-/-). The blocking solution was aspirated and the samples were washed twice in blocking buffer. After this step, the samples were kept in the blocking buffer. Primary antibodies were diluted in the blocking buffer according to their specific concentrations. Antibodies against α- Actinin (1:200, clone EA-53, Sigma-Aldrich,

USA), desmin (1:500, #ab15200, Abcam, UK) and connexin 43 (1:400, #ab11370, Abcam, UK) were employed. When alginate layers or HPs were stained, then the same dilutions have been used except the anti-connexin 43 antibody, which has been used in a 1:800 dilution. Samples were incubated overnight at 4°C in the primary antibody solutions. Afterwards, they were aspirated and anti-rabbit or anti-mouse IgG secondary antibodies (A11034 or A21422, Life Technologies), labelled with either Alexa-488 or Alex-555, were employed in a 1:1000 dilution. The samples were incubated in the secondary antibody solution for 1h at RT in the dark. The secondary antibody solution was aspirated and transferred into blocking solution with DAPI staining (Thermo Fisher Scientific, USA). Image acquisition was conducted via a confocal laser-scanning microscope (TCS SP8, Leica, Germany).

Gene expression profiling with RT-qPCR

RNA extraction was conducted with the RNeasy Micro Kit (Qiagen, USA). The spheroids were transferred into a 1ml microcentrifuge tube and the medium was aspirated. After a washing step with PBS(-/-), the lysis buffer was added and profoundly resuspended to disrupt the cell membranes. Two-dimensional cell cultures were similarly treated; the medium was aspirated and the cells were washed once with PBS(-/-). Afterwards, the lysis buffer was added to the wells and resuspended. Cells grown on UHV-alginate scaffolds, were gently lifted from the growth substrate and immediately transferred to a 1ml microcentrifuge tube containing 300µl lysis buffer. Following strictly the manufacturer's instructions, the RNA was isolated with consecutive isolation and washing step via a column-based isolation. The RNA concentration was measured with a NanoDrop microvolume spectrophotometer (Thermo Fisher Scientific, USA). Reverse transcription was conducted with the high capacity reverse transcription kit (Applied Biosystems, USA) following strictly the manufacturer's instructions. A maximum of 500ng RNA were used for each reaction, which was performed with a thermocycler for 2h at 37°C. The DNA was then stored at 4°C or analysed via quantitative real time PCR.

Assessment of gene expression has been performed with the $2^{-\Delta\Delta Ct}$ method and normalization was conducted against the geometric average of three endogenous control genes (*GUSB, GAPDH* and *HPRT1*). The plotted values are given as fold changes compared to day 0 hPSCs. Cardiac induction efficiency was analysed by the means of gene expression profiling and quantification of α-actinin and Cx43-positive cells. Gene expression analysis was conducted via reverse transcription quantitative polymerase reaction (abbr. RT-qPCR) and is based on the normalization to the geometric average of reference genes and the sequential application of the $2^{-\Delta\Delta Ct}$ method (Bustin et al., 2009). *GAPDH*, *GUSB* and *HPRT1* were selected as control genes in this work when cardiac differentiation and the effect of dissociation enzymes was assessed. Otherwise, *GAPDH* and *HPRT1* were used as reference genes. These reference genes must fulfil certain criteria so they can be used as reference genes in a gene expression analysis. First, they must be expressed at a constant level in all cell types. Second, the expression should be high enough so a robust analysis can be carried out and third, it should not be affected by the experimental design.

Table 3.2 TaqMan assay IDs used in this work for gene expression profiling via RT-qPCR.

Gene name	TaqMan Assay ID	Gene name	TaqMan Assay ID
ACTN2	Hs00153809_m1	*MYL7*	Hs01085598_g1
CACNA1C	Hs00167681_m1	*OCT3/4*	Hs00742896_s1
DES	Hs00157258_m1	*RYR2*	Hs00181461_m1
EOMES	Hs00172872_m1	*S100A1*	Hs00984741_m1
GAPDH	Hs99999905_m1	*SCN5A*	Hs00165693_m1
GUSB	Hs99999908_m1	*SOX2*	Hs00602736_s1
HPRT1	Hs99999909_m1	*T*	Hs00610080_m1
ISL1	Hs00158126_m1	*TCAP*	Hs00366220_m1
KCNH2	Hs04234270_g1	*TNNI1*	Hs00913333_m1
KCNQ1	Hs00923522_m1	*TNNI3*	Hs00165957_m1
MESP1	Hs01001283_g1	*TNNT2*	Hs00943911_m1
MYH7	Hs01110632_m1	*TTN*	Hs00399225_m1
MYL2	Hs00166405_m1		

Additionally, the use of multiple reference genes minimizes drastically the influence of variability in a single reference. *GAPDH* encodes for glyceraldehyde 3-phosphate dehydrogenase, a tetrameric enzyme involved in glycolysis (Tan et al., 2012). *GUSB* encodes for glucuronidase beta, a glycosaminoglycan degrading hydrolase (Molina et al., 2018). *HPRT1* encodes for hypoxanthine phosphoribosyltransferase 1, an enzyme needed for the production of purine nucleotides (Duan et al., 2004; Eyre et al., 1971; Vandesompele et al., 2002a). All three reference genes are commonly used and have been shown to fulfil these criteria (Anderson et al., 2007; Burridge et al., 2007; Bustin et al., 2009; Tan et al., 2012; Vandesompele et al., 2002b). The real-time quantification was assessed by using hydrolysis probes (TaqMan™, Applied Biosystems, USA). For each reaction, at least two technical replicates were performed and in case of a divergent result (with a discrepancy over 1 cycle), this reaction was repeated. The assay id numbers are given in Table 3.2.

Analysis of intracellular calcium transients

The fixed UHV-scaffolds and PS controls were washed in sterile Tyrode's buffer containing 130mM NaCl, 4.2mM KCl, 10mM HEPES, 2mM $CaCl_2$, 2mM $MgCl_2$ and 6g/l glucose. The osmotic concentration was adjusted to 290mOsmol and the pH was set to 7.4. Calbryte 520 (AAT Bioquest, USA) served as the calcium dye in this work. First, 50µg Calbryte 520 were solubilized in 9.7µl DMSO and then diluted (1:1000) in Tyrode's buffer with 0.04% Pluronic F127 (Sigma-Aldrich, USA). 1mM isoprenaline solution was diluted in Tyrode's to a final concentration of 10µM, this is referred to as the isoprenaline stock solution. Tyrode's buffer was applied to each well and incubated for 1h at 37°C and 5% CO_2. The buffer was aspirated and 300µl of Tyrode's buffer with Calbryte 520 was added to each well and incubated for

another hour at 37°C and 5% CO_2. While the cells were incubating, the heating plate of the microscope was set to 38.7°C and kept at this temperature throughout the experiment.

The Tyrode's buffer containing Calbryte 520 was replaced by Tyrode's buffer without Calbryte 520. The samples were incubated for another 20 minutes at 37°C and 5% CO_2. Using a fluorescent microscope (Zeiss, Germany), through light and fluorescence-based videos (30s) of the well centres were acquired at 10*x* magnification. Either 3µl or 30µl of the isoprenaline stock solution was added to each well to achieve 100nM and 1µM isoprenaline concentrations. After another incubation time of 10 min in the incubator, videos were acquired. Although a heating plate was used, only six wells of each multiwell plate were assessed at a time; then, the plate was transferred back to the incubator to prevent cooling of the samples and equilibration of the pH.

Assessment of the fluorescence was conducted with the software NiS elements 4.0 AR (Nikon, Japan) and the function "time measurement". The assessment of the peak width duration at 90 percent repolarisation (abbr. PWD90), falling slope, and beat rate was conducted with a custom-made script using RStudio (Version 1.1.456; RStudio, Inc., USA). To achieve a robust readout concerning the displacement analysis, images of the resting state before each contraction and the contraction maximum were manually selected. These images were pairwise analysed using jPIV (version 17.02.21) (Vennemann et al., 2006).

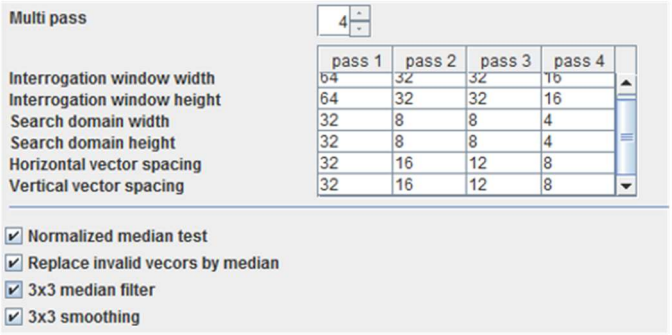

Figure 3.2 Settings used for the analysis of displacement using jPIV.
Using the jPIV software, a multi pass analysis was conducted with decreasing interrogation windows, search domains and was decrease from 32px to 4px and the vector spacing was decreased from 32px to 8px. Additionally, median filtering and smoothing was conducted.

The settings used in jPIV for the analysis of each image pair is given in Figure 3.2. A multi pass analysis was conducted with smaller interrogation windows each time. The square interrogation window sizes were 64px, 32px and 16px, respectively. The search domain was decreased from 32px to 4px and the vector spacing was decreased from 32px to 8px. Additionally, median filtering was based on a normalized median test. Vectors were only seen as valid when three valid neighbour vectors were found. The vector lengths of each contraction were averaged and calculated into micrometres.

Protein quantification using western blotting

Cells were transferred to a 1ml microcentrifuge tube containing 300µl RIPA buffer. The RIPA buffer contained 150mM NaCl, 1%NP-40, 0.5% Sodium deoxycholate, 0.1% SDS, 50mM Tris (pH 8.0) and Proteinase inhibitor (cOmplete™, Mini, EDTA-free Protease Inhibitor Cocktail; Roche, Switzerland). After sonication (5-10s) the cell lysate was put on ice for 45min and then centrifuged (13000rpm) for 25min at 4°C. Samples containing UHV-alginate were centrifuged for another 20min at 4°C. The supernatant was transferred into a new tube, the protein concentration was measured using the NanoDrop microvolume spectrophotometer (Thermo Fisher Scientific, USA) and the samples were stored at -80°C until further use.

Before gel electrophoresis, the 20µg protein of each sample was transferred into a new 100µl microcentrifuge tube and a 4x sample buffer was added 1:4. The sample buffer contained 4ml 100% glycerol, 2.4ml Tris HCl (pH 8.0), 0.8g SDS, 4mg Bromophenol blue and 0.5ml mercaptoethanol. The samples were vortexed, shortly spun down and then incubated at 95°C or 10min. Mini-PROTEAN® TGX™ Precast Gels (Bio-Rad, USA) were loaded with 20µl per sample and the gel was run with 15-20mA for approx. 1:45h on a Mini-PROTEAN® Tetra Vertical Electrophoresis Cell (Bio-Rad, USA). Afterwards, the proteins were transferred with a TransBlot® Turbo™ Transfer System (Bio-Rad, USA) to nitrocellulose membranes. The membranes were blocked in 10ml 5% skimmed milk in 20mM Tris-buffered saline with 0.1% Tween 20 (abbr. TBST) for 2h under constant agitation at RT. The primary antibodies were diluted 1:1000 in 1% skim milk in TBST and incubated overnight at 4%. Primary antibodies against GAPDH and against both, the skeletal and the cardiac form of Troponin I (MAB1691, Clone C5, Merck, Germany) were used. The next day, the membranes were washed four times with 10ml 1% skimmed milk in TBST. Secondary antibody against mouse IgG were diluted 1:1000 and incubated for 1h at RT in the dark. Afterwards the membranes were washed five times with 10ml TBST. Then, the membranes were imaged with the ChemiDoc System (Bio-Rad, USA). The following analysis of the acquired images was conducted with the Image Lab software (version 6.0.1) (BioRad, USA). To calculate the Tnni1/Tnni3 ratio, the respective bands were analysed and the ratio was calculated. Three independent biological replicates were performed and averaged.

Electrophysiological characterisation of the Heart Patch

Electrophysiological characterisation was conducted with the MEA 2100 system (Multi Channel Systems GmbH, Germany). The multi electrode arrays (abbr. MEA) were rinsed with 70% ethanol and dried afterwards. The perforated MEA for the HP measurements was not further processed. The standard MEA used for the two-dimensional cell culture control was coated with Matrigel. 160µg protein in 2ml ice-cold DMEM/F12 were applied to the MEA and incubated for 2h at 37°C. 40000 COR.4U were seeded on the MEA and cultured for 5 days. On the day of the recording, the HP was transferred to the MEA and kept in contact with the electrodes through a suction system. The HP sample and the monolayer culture control were

each measured. Afterwards isoprenaline was added and, after an incubation of 10 minutes, the samples were again recorded. Analysis has been conducted with the Cardio2D+ software (version 2.6.2; Multi Channel Systems, Germany).

4 RESULTS

4.1 ESTABLISHMENT OF A WORKFLOW FOR THE GENERATION OF CLINICALLY RELEVANT NUMBERS OF HIPSC-CMS IN A SUSPENSION BIOREACTOR

The generation of cardiomyocytes from human induced pluripotent stem cells for therapeutic applications and disease modelling requires large numbers of cells. The reason for this is rooted in the creation of patient-specific cell lines and every single one needs to be expanded and differentiated. Furthermore, drug discovery screenings encompass hundreds of compounds and each of these compounds needs biological as well as technical replicates to allow robust conclusions. Because the reprogramming step still suffers from low efficiencies, it is mandatory to multiply the cell numbers downstream, either at the pluripotent stage or after differentiation. Furthermore, the differentiation method and the cultivation type must be carefully chosen, because both have significant influence on the cost, workload and the number of produced cells. Two-dimensional cell culture vessels offer a reproducible environment, but possess a low cell number to media volume ratio and take up a lot of lab space. Furthermore, three-dimensional, cellular spheroids represent a system with significant advantages, especially the favourable microenvironment and the closer resemblance to the *in vivo* situation. The hanging drop method, a three-dimensional cell culture method based on the culture of cells in hanging drops leads to such spheroids due to the absence of a culture surface. To overcome the laborious creation of high cell numbers in hanging drops, a complete workflow for the production of hiPSC-CMs using a newly developed differentiation protocol in concert with a small-scale bioreactor was established. The differentiation procedure was comparatively analysed in both systems by the means of induction efficiency and the progress of lineage commitment.

4.1.1 Comparative evaluation of hiPSC-CM derivation in a bioreactor and the hanging drop system

Derivation of cardiomyocytes from hiPSCs is achieved by a precisely timed modulation of the WNT pathway. To generate the high numbers needed, a differentiation protocol from Zhang et al. was adopted for the use with a small scale bioreactor (Biolevitator; OLS, Germany) (Zhang et al., 2015). The bioreactor uses a suspension-based culturing method. In this work, the dynamic environment of the suspension bioreactor was compared with a static spheroid-based culture method, the hanging drop (abbr. HD). With the HD method, cells are cultured in hanging drops of 40µl volume without a growth surface presented to them, leading to the

formation of spheroids. Two cell lines, IBMT1 and UKBi005, were utilized to test for cell line differences. In the first 24h after cell seeding, the cells clustered together in spheroids and their size increased over the course of the following seven days from 110.0 ± 7.0µm (day 1) to 215.4 ± 10.7µm (day 7) for the IBMT1 cell line and from 156.1 ± 9.6µm to 262.1 ± 17.3µm for the UKBi005 cell line (Figure 4.1, A and B). The successful induction of the cardiac fate was determined by gene expression analysis via RT-qPCR (Figure 4.1, C). The analysis focused on pairs of genes that are uniquely expressed in specific developmental stages, recapitulating the differentiation *in vivo*. The plotted values are given as fold changes compared to day 0 hiPSCs. The gene expression profile was comparable between both cell lines and is depicted for UKBi005 in Figure 4.1, C. The pluripotency markers *OCT3/4* and *SOX2* were downregulated after 24h in both systems (HD: 0.68-fold and 0.27-fold, BL: 0.27-fold and 0.12-fold) correlating with the upregulated expression of early primitive mesendodermal markers (*T* and *EOMES*) from day 1 to day 3. *EOMES* peak expression on day 2 was 857-fold (BL) and 528-fold (HD) higher compared to day 0. Noteworthy, the day 1 expression was significantly higher in the BL (733-fold) compared to HD (189-fold). The peak expression of *T* was observed on day 1 in the BL (2175-fold) and in the HD (1740-fold) on day 2. Cardiac mesodermal genes were expressed afterwards, the maximum expression of *MESP1* was observed on day 2 in both culturing methods with a twofold higher mRNA abundance in the BL (771-fold) compared to the HD (359-fold). *ISL-1*, a late cardiac mesodermal marker was transiently expressed from day 3 on and the maximum expression was observed on day 4 in the BL (319-fold) and HD (218-fold). *TNNT2* and *MYH7* are responsible for two major constituents of the intracellular cytoskeleton of cardiomyocytes and were expressed from day 5 on. In the HD system, *TNNT2* (392-fold) and *MYH7* (3601-fold) maxima were detected on day 6 and the expression of these genes remained at that level on day 7 (3429-fold (*MYH7*) and 318-fold (*TNNT2*)). In the BL the genes responsible for structural components of the cardiac sarcomeres experienced a steady up regulation, thus the maximum expression of *MYH7* (11524-fold) and *TNNT2* (668-fold) were observed on day 7. Differences between the two culture systems could not be seen concerning the dynamics of the pluripotency markers, but got more prominent during the course of the experiment. While Brachyury (*T*) reached its maximum a day later in the HD, the consecutive downstream markers (*EOMES, MESP1, ISL1, TNNT2 and MYH7)* reached higher expression levels in the bioreactor. To assess the efficiency of cardiac induction, immunocytochemistry directed against α-actinin, desmin and connexin43 (abbr. Cx43) was utilized and comparatively analysed in qualitative and quantitative manners (Figure 4.1, D and E). As depicted in Figure 4.1 (D), protein organization was comparable among the different conditions with spheroids from the bioreactor exhibiting a more equally distributed α-actinin pattern. Cx43 and desmin did not show any qualitative differences. 3D projection of the spheroid images highlights the higher concentration of α-actinin on the outer layers of the spheroids Figure 4.1, E). Cardiomyocyte generation (versus other cells) was very efficient with over 80% of the derived cells displaying cardiomyocyte-specific α-actinin. In the BioLevitator, differentiation gave rise to slightly more cardiomyocytes (95.30 ± 0.02%) compared to the HD culture (83.46 ± 0.11%).

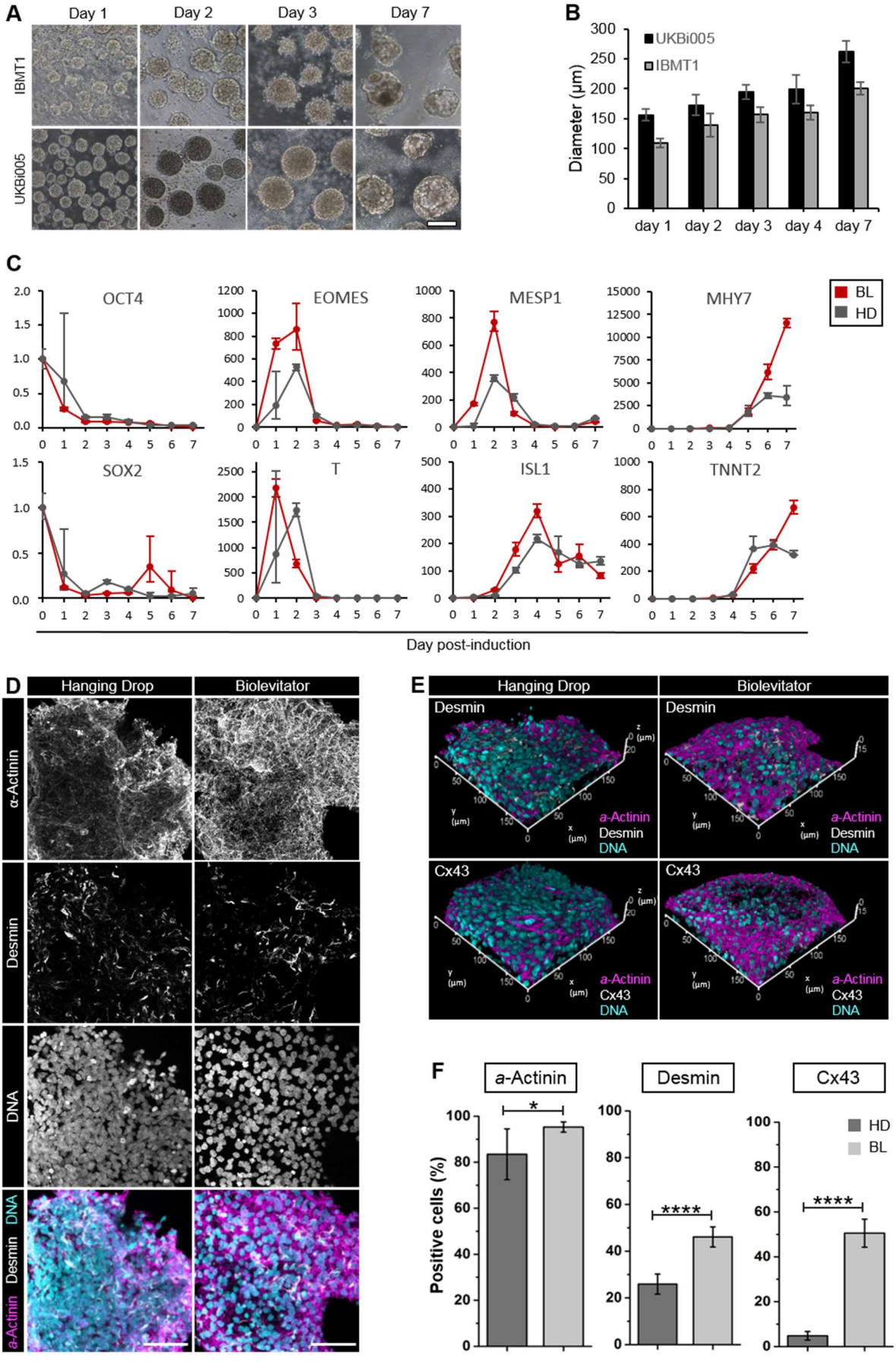

The figure description can be found on the following page.

Figure 4.1 Cardiac induction in static and dynamic three-dimensional cell culture systems by precise modulation of the WNT pathway.
Two cell lines (IBMT1 and UKBi005) were differentiated in the BioLevitator and the measured spheroid diameter is plotted as mean ± SD (n=20 per day, Scale bar in A = 200µm). Gene expression analysis was conducted every day until day 7 (A). Pluripotency (OCT3/4; SOX2), mesoderm (T, EOMES), cardiovascular progenitor (MESP1, ISL-1) and cardiomyocyte specific markers (TNNT2, MYH7) were analysed by qPCR and the 2-ΔΔCt method. Plots are given in fold change compared to day 0. All samples have been normalized to the geometric average of three endogenous control genes (C; n ≥ 3 for each condition and day). Error bars indicate the 95% confidence interval. Representatives maximum projections of 7 days old cardiac spheroids stained with immunocytochemistry against α-actinin, Cx43 and DNA are given in D (scale bar = 50µm). 3D projection of the spheroid images from D are given E. Quantitative analysis of α-actinin, desmin or Cx43 positive cells in cardiac spheroids at day 7 (F; mean ± SD; n=3-6; 200 nuclei / replicate). Figure taken from Fischer et al. 2018.

In contrast to the relatively comparable α-actinin distribution, the number of desmin- and Cx43-positive cells was significantly elevated in the bioreactor with 46.08 ± 0.04% desmin- and 50.53 ± 0.06% Cx43-positive cells compared to 25.91 ± 0.04% and 4.80 ± 0.02% in HD (Figure 4.1, F).

A major obstacle concerning the usage of bioreactors is the dissociation process at the end of the hiPSC-CM differentiation. Dissociation of the complex, multicellular, cardiac spheroids into single cells is needed for the calculation of exact cell numbers and the following use of harmonized doses thereof. Potential applications range from therapy to single cell gene expression analysis and include many sensitive *in vitro* measurements (*e.g.* patch clamp, electric field stimulation, multi electrode arrays, FACS), which rely on viable, single cells with an intact membrane. Thus, a gentle separation process is preferably chosen. Force generating cells, *i.e.* myocytes, possess strong intercellular connections (*e.g.* desmosomes and connexins), which develop very early during differentiation and mature over time. The dissociation is also needed to passage cells avoiding cell necrosis in cores of spheroid exceeding the diffusion limit. A comparative analysis was conducted to evaluate the dissociative performance of selected enzymes downstream of the hiPSC-CM generation.

4.1.2 Comparative analysis of the dissociation of cardiac spheroids

An efficient but gentle digestion is needed to acquire single cell suspension from the three-dimensional, multicellular aggregates after the culture in the dynamic environment of the BL. Accutase, Papain and TrypLE were utilized to comparatively analyse spheroid dissociation. TrypLE and Accutase are two commonly used and commercially available reagents for cell cultures. The number of single cells, small clumps and bigger aggregates (>40µm diameter), as well as cell vitality after separation was evaluated. For a robust assessment of the number of viable cells, two independent methods were employed: an analysis based on a hybrid calcein-AM and propidium iodide staining and the Nucleocounter, a commercially available cell-counting machine. Before estimating the number of viable cells, small clumps and single cells were separated from leftover aggregates by sieving the samples through a 40µm cell

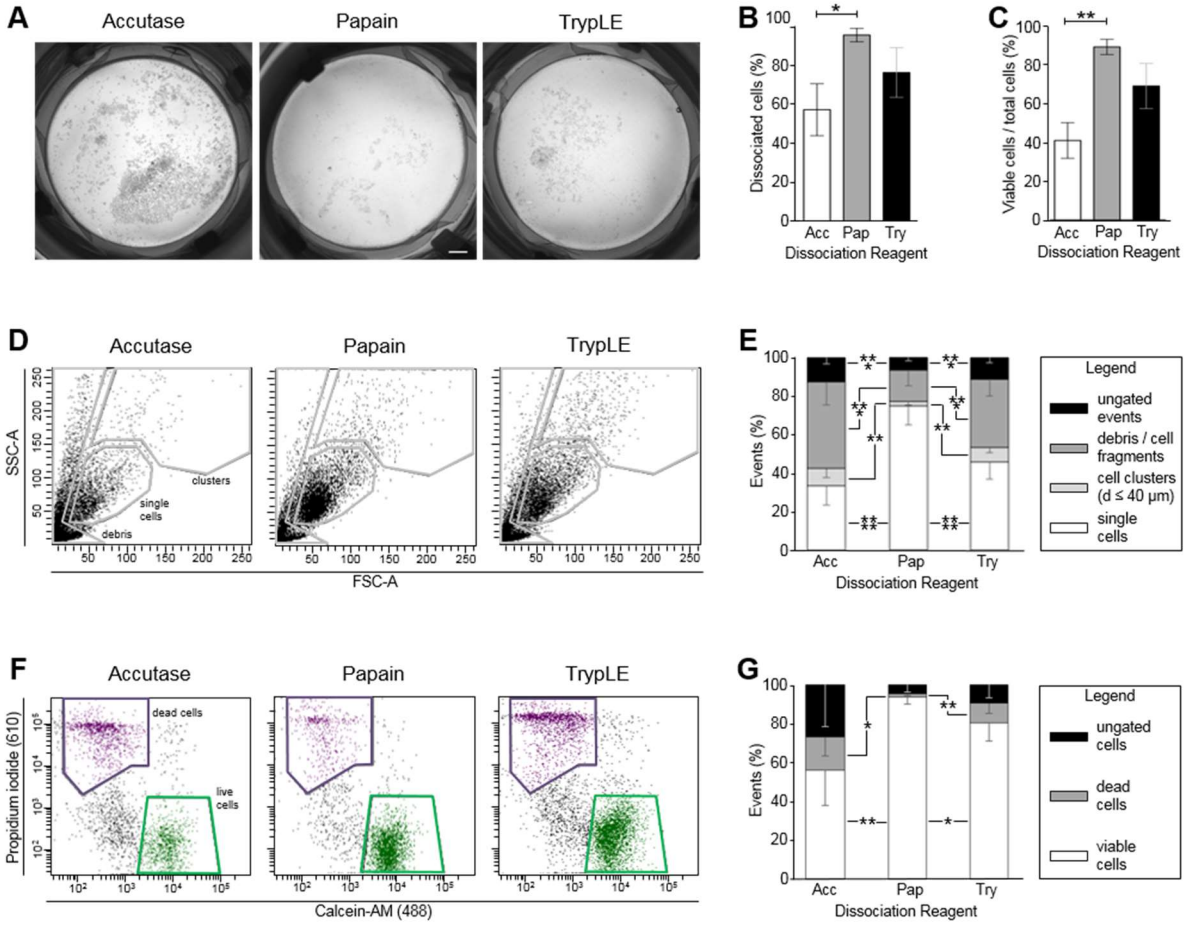

*Figure 4.2 Analysis of dissociation performance and cell viability of Accutase, TrypLE or Papain digestion. Un-dissociated aggregates with diameters over 40µm were sieved out with 40µm cell strainers (A). The number of dissociated cells (B) and viable cells (C) assessed with the Nucleocounter is dependent on the dissociation enzyme (B) (n=6–7/condition); *: $p < 0.05$; ***: $p \leq 0.005$). Representative FSC/SSC scatter plots from an alternative assessment of single and viable cells are given in D. Quantified data based on the gating strategy (D) is shown in E. Based on the gating given in F, single cells were discriminated in live, dead and ungated events and represented as mean ± SD (G). Figure taken from Fischer et al. 2018.*

strainer and collection of the residual clumps (Figure 4.2, A). The remaining cells in the flow-through, as well as the sieved clumps, were analysed with the Nucleocounter for singlets (<40µm) and cell viability (Figure 4.2, A, B and C). While Accutase led to 57.0 ± 12.1% single cells, TrypLE resulted in 76.1 ± 11.6% and Papain in 95.3 ± 3.7% (Figure 4.2, B). In combination with the viability measurement, the proportion of viable single cells for Accutase, Papain and TrypLE was calculated to be 41.5 ± 8.5%, 90.3 ± 3.7% and 70.1 ± 10.8% respectively (Figure 4.2, C). Afterwards, the flow-through was analysed using FACS to quantify the proportion of cell debris, single cells and small clusters. Size discrimination was achieved using forward and sideward scatter pattern of the cells and the gates as indicated in Figure 4.2, D. Accutase, Papain and TrypLE treatment led to 33.5 ± 10.0%, 74.8 ± 9.8% and 45.9 ± 9% single cells respectively. Small clusters (8.9 ± 4.7%) and cell debris (45 ± 12.1%) were detected in all Accutase samples, while TrypLE yielded 7.4 ± 2.6% clusters and 35.3 ± 8.6% debris. Papain resulted in fewer clusters (2.3 ± 2.0%) and debris (16.2 ± 8.0%), indicating a gentler, but at the same time, more efficient dissociation. To reproduce the viability measurement, a dual staining, employing propidium iodide (PI) and calcein-AM (CA) in combination with the gating shown in D, was used to discriminate between viable, calcein-AM stained cells and dead cells, positive for PI. Papain (93.6 ± 3.7%) resulted in a significantly higher proportion of single cells compared to Accutase (56.0 ± 18.1%; p=0.0018) and TrypLE (80.4 ± 9.3%; p=0.016.). It is known from the dissociation of primary biological material, that more mature tissue is often more difficult to dissociation. To experimentally assess the effect of culture duration on the dissociation procedure, cardiac spheroids were cultured for one or two weeks and cell viability was assessed along with the quantitative analysis of single cell, aggregate and debris proportions applying the same methods used in Figure 4.2 (D and F). Additionally, differences between two and three-dimensional cell cultures were evaluated. Maturation of cardiac spheroids is suspected to lead to a higher dissociation resilience. Therefore, it was hypothesized that the three enzymes would not digest older spheroids (15 days post induction (abbr. dpi)) with the same efficiency as younger ones (8 dpi) (Figure 4.3, A). The longer culture time did indeed lead to a significantly lower dissociation efficiency of papain (54.4 ± 2.7%; p=0.0101) and TrypLE (17.1 ± 1.7%; p=0.0008), but not of Accutase, although a clear trend is visible in this condition (Figure 4.3, A). The overall picture however, was consistent with previous experiments, resulting in the highest proportion of single cells ($p \leq 0.00001$) and the lowest proportion of debris ($p \leq 0.00001$) upon papain treatment. Papain is known for its potential to dissociate primary tissue and is rarely used in conventional *in vitro* processes. Thus, papain performance on cardiomyocyte monolayers was assessed. The results from the monolayer experiments did not differ, for any of the analysed parameters, from the previous experiments concerning three-dimensional spheroids. Papain digestion resulted in 53.4 ± 7.9% single cells, a significant higher amount than 29.3 ± 3.8% (p=0.0144) and 30.7 ± 3.2% (p=0.0171) for TrypLE and Accutase, respectively (Figure 4.3). This is also reflected in the proportion of debris, which was lowest for Papain (26.1 ± 4.7%) compared to TrypLE (48.5 ± 5.0%; p=0.0048) and Accutase (45.7 ± 3.2%; p=0.0033).

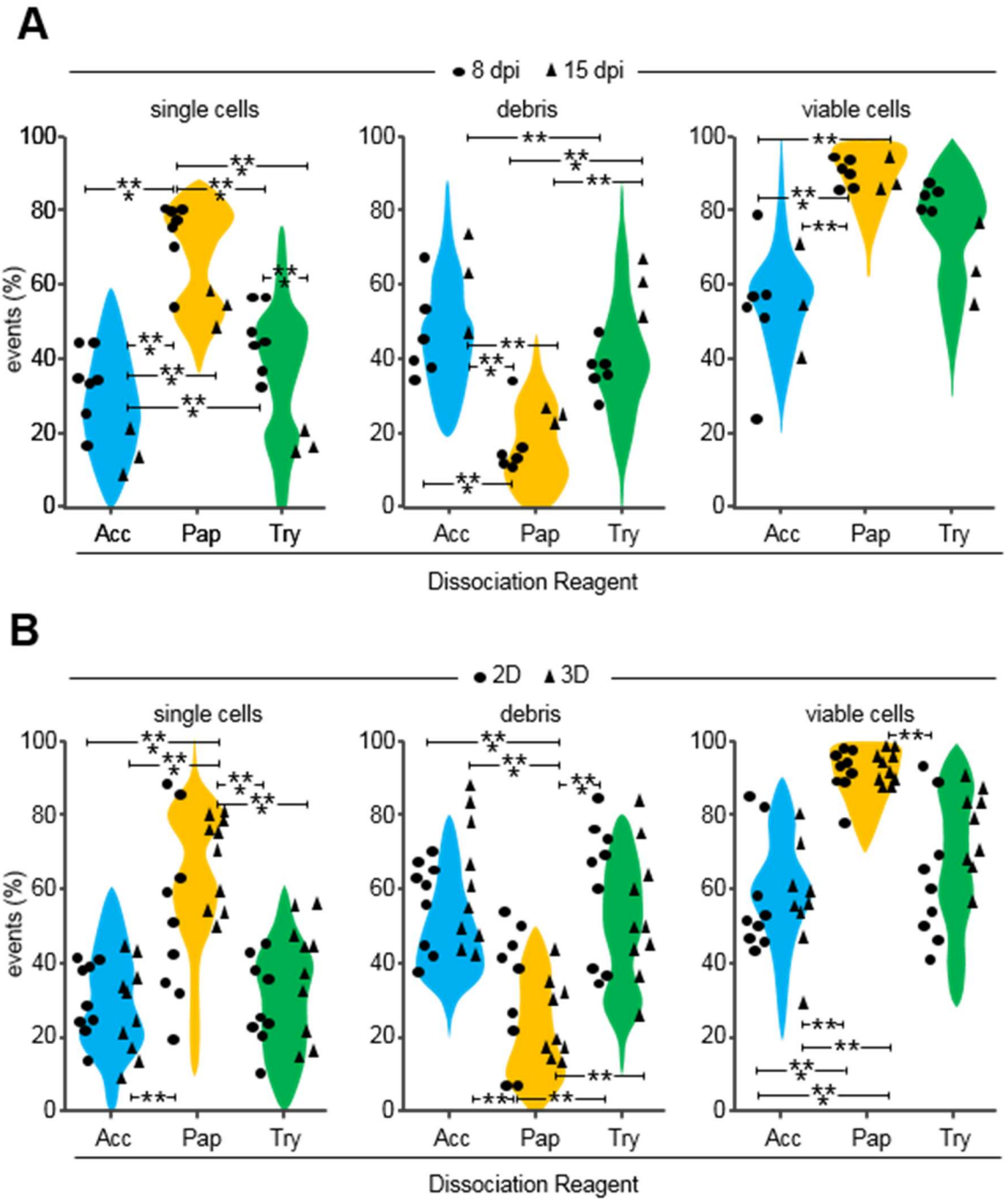

Figure 4.3 Effect of culture duration and culture condition on the dissociation process.
Using either Accutase, Papain or TrypLE, a comparative analysis of the influence of culture condition (2D or 3D) or culture duration on the dissociation is presented in hybrid scatter/ violin plots showing individual data points (black circles and triangles), representing different culture conditions (culture duration in A, culture format in B) and the distribution (colour coded background) of the merged population of each enzyme. Each point represents the average of one biological replicate (for p≤0.05; ** for p≤0.01; *** for p≤0.005). Figure taken from Fischer et al. 2018.*

Cell viability measurement showed that Papain digestion was not only efficient in dissociating the spheroids, but resulted in the highest amount of viable cells (92.2 ± 2.0%) compared to TrypLE (63.3 ± 6.0%; p=0.0003) and Accutase (57.5 ± 5.2%; p=0.0001). Cardiomyocytes rely on an intact membrane integrity with functional proteins presented on the cell surface enabling intercellular communication and connexin fusion, the biological foundation for simultaneous contractions. The influence of the dissociation agent on this functionality was investigated in the following experiments.

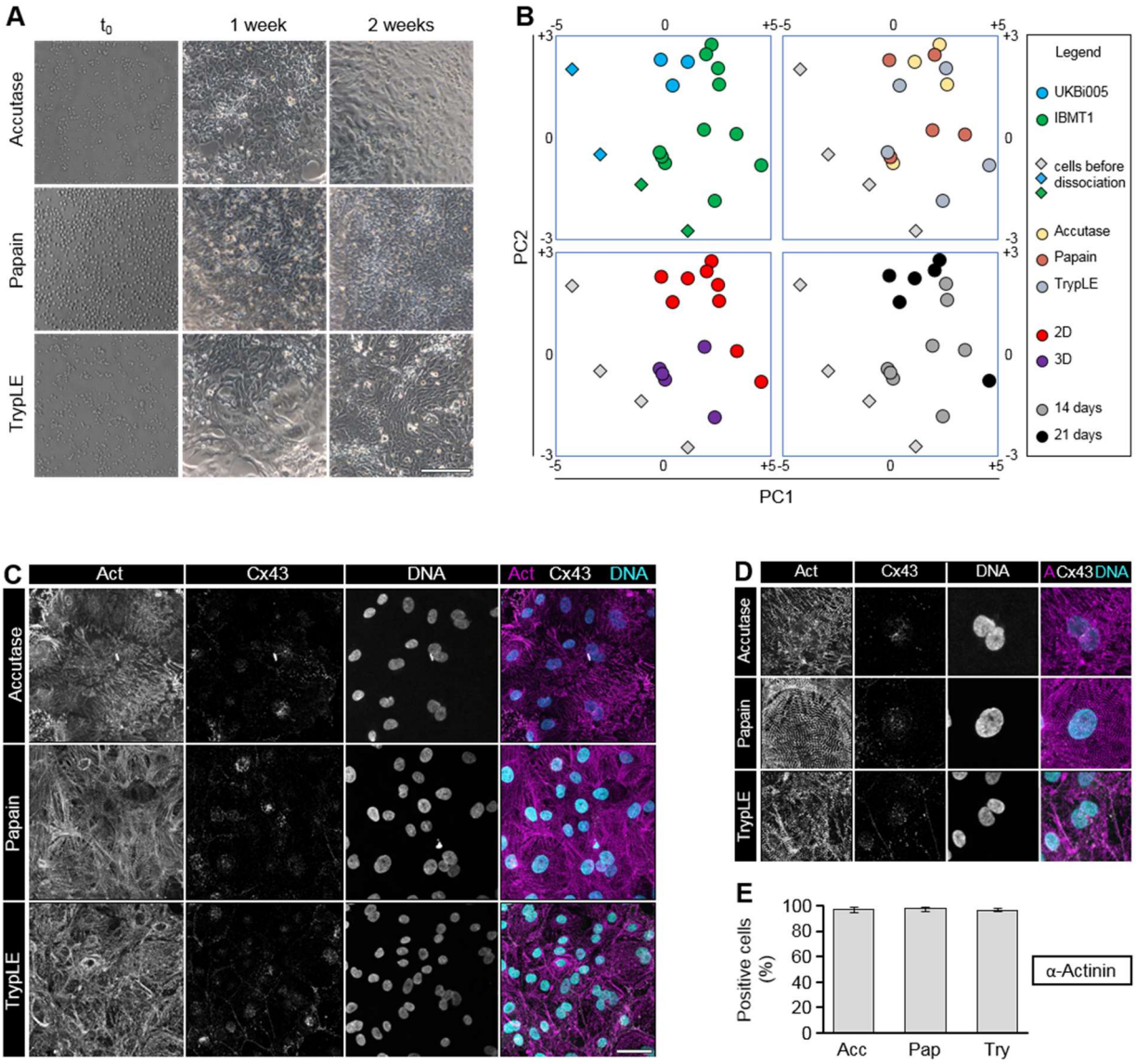

Figure 4.4 Comparative analysis of enzyme induced effects on sarcomere organization and gene expression. After dissociation, iPSC-CMs are seeded onto conventional cell culture plastic ware and kept in culture over several weeks. Representative images of the cell layers at specific time points (1h, 1week and 2 weeks after seeding) are given in A. Gene expression of cells at 2 and 3 weeks in culture was analysed via qPCR and integrated into a principle component analysis (B). The same data set has been plotted four times, but each time with a different factor discrimination: cell line (top left), culture conditions (2D vs. 3D; bottom left), time in culture (bottom right) and the choice of enzyme (top right). Representative images of double immunocytochemistry against α-actinin and Cx43 in cardiomyocytes 2 weeks after reseeding are shown in C. Detailed images of the white boxed areas (C) are given in D. Scale bars for A, C and D represent 50µm. The proportion of α-actinin positive cells is given in E (n=3; 200 nuclei per biological replicate). Figure taken from Fischer et al. 2018.

Functionality of cells after dissociation is maintained when membrane integrity is not affected and the presentation of proteins on the cell membrane is only temporarily affected. This represents a fundamental requirement for downstream applications, which rely on an intact membrane physiology to allow meaningful conclusions (*e.g.* multi electrode arrays, calcium transient measurements, patch clamp). After dissociation, the cardiomyocytes were either plated on Matrigel-coated petri dishes or reseeded in the bioreactor, followed by an assessment of digestion induced delayed effects on hiPSC-CM functionality. One additional observation was made in regard to the Papain condition, here the digested cells seemed perfectly sphere-shaped and needed slightly longer for attachment compared to the other two conditions. A small discrepancy between the counted and the observed cell numbers after attachment was observed within the Accutase and TrypLE conditions, leading to less confluent layers compared to the papain condition. Nevertheless, cardiomyocytes were able to form a functional synchronous beating monolayer in all conditions. To detect more subtle effects on the phenotype and to reveal dedifferentiation or deterioration of the genetic integrity, gene expression profiling of the samples taken at two and three weeks after reseeding was conducted.

The analysed set encompassed desmin (*DES*), myosin heavy chain (*MYH7*), myosin light chain 2 (*MYL2*), myosin light chain 7 (*MYL7*), cardiac troponin (*TNNT2*) and titin (*TTN*), genes encoding for sarcomere associated proteins. Furthermore, two genes responsible for subunits of the ion channels Kv7.1 *(KCNQ1*) and Nav1.5 (*SCN5A)* were assessed. Subsequent principle component analysis (PCA) of the qPCR data revealed a clustering according to the used cell line, culture time, and culture type (2D/ 3D), but not between any of the enzymes (Figure 4.4; B). To exclude potentially selective digestion mechanisms, the proportion of α-actinin and Cx43-positive cells was assessed (Figure 4.4, C and D). The amount of positive cells was above 97% in all conditions (Papain (98.2 ± 1.3%), Accutase (97.73 ± 1.5%) and TrypLE (97.32 ± 1.6%)) and no significant differences between the different digestions could be observed (Figure 4.4; C, D and E). In conclusion, Papain digestion was more effective to dissociate cells from cardiac spheroids and at the same time gentler with higher cell viability compared to TrypLE and Accutase.

The presented workflow represents an efficient method for the derivation hiPSC-CM spheroids in a dynamic suspension-based, small-scale bioreactor. The dissociation analysis suggests that papain, while not commonly used in conventional cell cultures, is a valuable dissociation reagent particularly with the prospect for more three-dimensional cell models. *In vitro* models using cardiomyocytes often rely on the use of polystyrene-based plastic ware (abbr. PS). The extremely high stiffness of such substrates limits any contractile movement and ultimately the major functionality of hiPSC-CMs. To enable and foster contractile movements, elastic substrates can be utilized. Furthermore, such systems can be used to simulate physiological as well as pathological microenvironments, because the transition between the two states is often accompanied with a change in tissue stiffness. Following the aforementioned hiPSC-CM production, this work investigated the effects of contractile UHV-alginate substrates on hPSC-CM functionality and maturity.

4.2 COMPARATIVE ANALYSIS OF CARDIAC CONTRACTILITY ON SUBSTRATES WITH DIFFERING STIFFNESS

The adverse effects of polystyrene-based cell cultures include intracellular stress, induction of immaturity and the inhibition of physiological mechanisms that control, modify and adapt the contraction pattern to extracellular stimuli (*e.g.* stretch, resistance, directionality). The use of polymer-based substrates enables the CMs to contract against a resistance and fosters the development of sarcomeric structures. Although many polymers have been used in this context, UHV-alginates possess a unique combination of characteristics, which make them particularly useful in *in vitro* models. The mild crosslinking can be conducted in the presence of cells and can be controlled by the crosslinker choice and concentration. They are highly biocompatible and are structural stable *in vivo* and *in vitro* for long periods. Contrary to many biological polymers, *i.e.* collagens, mammalian cells do not possess alginate receptors; hence, they represent an exceptionally neutral microenvironment that enables the investigation of specific effects on the cells (Ruvinov et al., 2016). These effects can be mediated by the substrate itself, as it is the case for the tuneable substrate stiffness, or can be induced by substrate-independent factors (*e.g.* compound exposure or co-cultures). Additionally, the high biocompatibility enables a direct transition from *in vitro* to *in vivo* models (Li et al., 2012).

Therefore, UHV-alginate was used to investigate the effects of contractile substrates on hPSC-CMs beating behaviour and contractility. In the first experiments, the beating behaviour was analysed, after a two-month culture duration, which should surface potentially adverse effects on hPSC-CM adhesion and viability. Additionally, it was hypothesized that the physical transformations in the heart from an early, soft tissue to a sturdier, adult myocardium and the transition into pathological states, which are accompanied by further hardening of the tissue, could be simulated by the use of four different concentrations. These different concentrations result in different elasticities after crosslinking without directly affecting the growth surface proteins.

4.2.1 Evaluation of hPSC-CM beating behaviour on fixed UHV-alginate scaffolds with differing elasticity

During hPSC-CM maturation, the beating frequency of single cardiomyocytes is subject to change according to the maturation status. Additionally, it is known that the contraction frequency is modulated by substrate stiffness. To assess the influence of substrate stiffness on hPSC-CMs, the cells were grown on functionalized UHV-alginate layers and polystyrene and their beating frequency was comparatively analysed over time. To enable a correlation with the situation *in vivo* the Young's modulus of the crosslinked UHV-alginates was investigated

first. The four used alginate concentrations exhibited elasticities of 388.0 ± 104.9kPa (1.5%), 178.3 ± 11.1kPa (1.0%), 138.9 ± 5.2kPa (0.7%) and 19.7 ± 4.0kPa (0.3%) (Figure 4.5, A). The beating frequency of hPSC-CMs correlated with substrate stiffness, but also exhibited substrate-independent patterns. Looking at the overall frequency changes over time, it is clearly visible that all conditions experienced similar modulations.

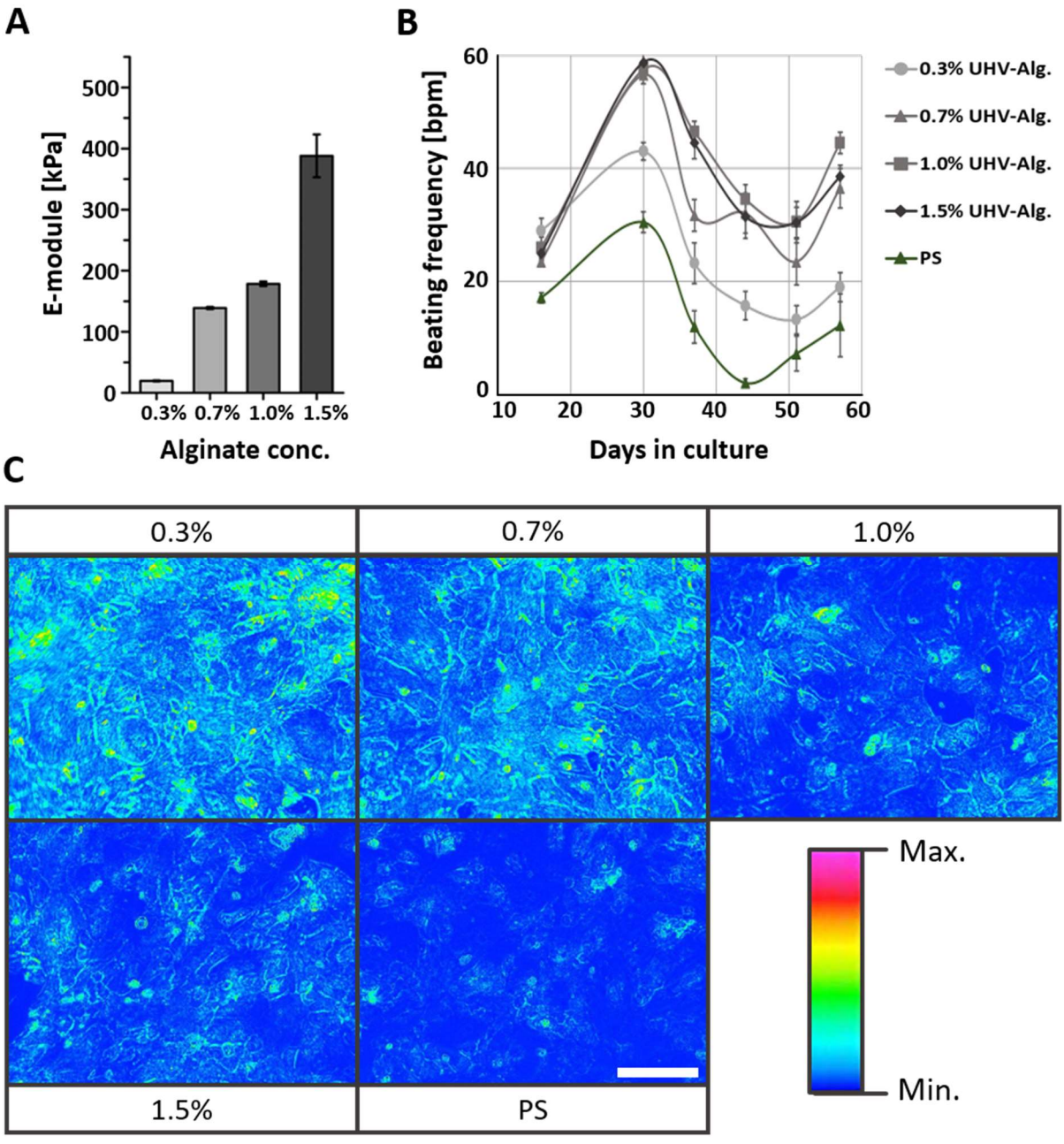

Figure 4.5 Analysis of hPSC-CM beating behaviour on fixed UHV-alginate scaffolds with differing elasticity. E-modules of fixed UHV-alginate scaffolds are plotted against the concentration of the UHV-alginate solutions before gelling (i.e. 0.3%, 0.7%, 1.0% and 1.5%) (A). Data is presented as mean ± SEM (n=9 for all samples, except 0.3% n=18). The beating frequency is dependent on matrix elasticity and culture duration, but additionally exhibits a conserved pattern over all groups (B) (mean ± SEM; n=12 from three biological replicates). Representative images of maximum projected movement ranges (based on intesity changes) during a 30s intervall are shown in C (white scale bar represents 200µm).

All groups progressed to a higher beating rate in the first month, reaching a maximum at day 30. Afterwards, they experienced a decrease of the beating rate, reaching a minimum at day 44 for the PS group and at day 51 for the other conditions. Consecutively, an elevation of the beating frequency was observable in all groups. The PS condition showed the lowest spontaneous beating rate of all samples at day 0 (17.1 ± 0.9bpm) and throughout the whole experiment. After reaching a beating rate maximum of 30.5 ± 1.8bpm at day 30 the following decrease led to a minimum average beating frequency of 2.1 ± 0.8bpm at day 44. Afterwards, a slight rise from day 51 (7.25 ± 3.1bpm) until day 57 (12.3 ± 5.5bpm) was observed. The 0.3%, 0.7%, 1.0% and 1.5% UHV-alginate conditions showed similar beating frequencies on day 0, with 29.0 ± 2.1bpm, 23.5 ± 0.9bpm, 26.0 ± 1.8bpm and 25.0 ± 1.3bpm respectively. On day 30, they also reached their respective maximum in beating frequency with 43.0 ± 1.5bpm (0.3%), 56.5 ± 1.6bpm (0.7%), 57.5 ± 0.8bpm (1.0%) and 58.8 ± 2.2bpm (1.5%). Similar to PS, the hPSC-CMs on alginate experienced a decrease in spontaneous beating rate, when 23.3 ± 3.6bpm (0.3%) 31.8 ± 2.8bpm (0.7%), 46.5 ± 1.8bpm (1.0%) and 44.5 ± 2.9bpm (1.5%) were observed at day 37. Although, the minimum in the 0.7% condition was reached on day 37, the beating frequency stayed relatively constant in this group with 32.1 ± 3.5bpm on day 44. However, the beat rate in the 0.3%, 1.0% and 1.5% groups were further decreased to 15.75 ± 2.5 bpm, 34.6 ± 2.5bpm and 31.5 ± 3.8bpm, respectively. On day 57, the beat rate of the 0.3% (19.0 ± 2.5bpm), 0.7% (36.5 ± 3.5bpm), 1.0% (44.5 ± 2.0bpm) and 1.5% (38.6 ± 5.5bpm) conditions was higher than on day 44 and day 51.

While the overall pattern was very similar, a distinction between the stiffer alginate conditions (0.7%, 1.0% and 1.5%) and the other two conditions (0.3% alginate and PS) can be made based upon the dynamic changes they experienced. First, 0.7%, 1.0% and 1.5% UHV-alginate scaffolds experienced a greater change (absolutely and relatively) in beat rate. Especially in comparison with the 0.3% alginate condition, which started at a higher beating frequency at day 16, but progressed towards a maximum at day 30 of only two-fold, the difference is visible with the stiffer alginate groups almost triplicating their beat rate from day 16. Additionally, the softer substrates allowed for a higher contractile movement range as shown in the representative images of an optical analysis based on intensity changes (Figure 4.5, C). After each contraction, the substrate's elasticity caused a passive return motion to the original resting state before contraction, thus, resulting in a robust workload cycle. A correlation of the stiffness with the beating range can be observed with lower effective e-modules leading to higher observed movement ranges. While all UHV-alginate conditions enabled contractile action, the PS group showed virtually no movement. There, the cells exhibited only partial contraction motions, resulting in only a few isolated contraction centres (Figure 4.5).

Contraction behaviour of cardiomyocytes is a relevant parameter of cellular fidelity, because it reflects the complex interplay of sarcomeric structures and the SR. Furthermore, it is modulated *in vivo* and *in vitro* by hormones and drugs. To investigate the usability of UHV-alginate scaffolds for *in vitro* modelling, a fluorescence-based quantification of intracellular calcium was conducted. In addition, a method to quantify the generated force by hPSC-CMs was experimentally evaluated. The parallel execution of the two methods opens up the

possibility to compare the two approaches directly. This strategy also enables correlation of the calcium dynamics on UHV-alginate with common PS-based approaches and additionally explores the potential to assess force generation simultaneously. To evoke a specific cellular reaction and to foster correlation with previous reports, the cellular response to isoprenaline, a widely used beta-adrenergic agonist, was investigated.

4.2.2 Optical-based analysis of cardiac calcium dynamics and force generation on different substrates

In vitro modelling of the cardiac niche with high resemblance to the adult myocardium is an important advancement for drug discovery and toxicity screenings, which still possess limited translational potential. Additionally, *in vitro* reproduction of the complex cardiac muscle would allow the transition of mechanistic studies that are only conductible *in vivo* in humans, to an *in vitro* environment. Particularly, the cellular effects of aging, sport and the long-term exposure to drugs are difficult to access in small animal models and humans. The pumping motion of the heart is generated through the collective work of cardiomyocytes. This contractile action is mediated by the extensive intracellular release of calcium ions from the SR caused by an initial influx of extracellular calcium. As shown in the previous experiment, UHV-alginate matrices supported cell adhesion and repetitive contractions. However, drug screenings have higher requirements on the growth substrates, because they rely on the visualisation of the calcium dynamics with fluorescent calcium probes, thus high transparency and low autofluorescence are required.

The transition from PS-based cultures to UHV-alginate conditions was seamless and no further adjustments (*e.g.* cell seeding density, adhesion times and medium volume) were required. Representative images of the resting state and the contraction maximum of hPSC-CMs grown on PS or UHV-alginate are given in Figure 4.6, A, as well as the corresponding, representative calcium waves are depicted in Figure 4.6, B and show that the UHV-alginates used in this study enable a fluorescence-based analysis. Upon exposure to 100nM isoprenaline, a noradrenaline derivate known for its inotropic (force) and chronotropic (beat rate) effect in cardiomyocytes, the observed calcium waves reflected the higher beating rate (Figure 4.6). The analysis of the inotropic response, a higher force generation seen *in vivo*, cannot be directly derived from the calcium transient data. Therefore, an algorithm was applied to assess the force generation by recognizing and quantifying the displacement of contracting cardiomyocytes. In agreement with the previous experiment (Figure 4.5), the results reflect the cells' ability to contract more on softer substrates and allows additional information about the directionality to be obtained (Figure 4.6, B). Furthermore, the vector-based approach (Figure 4.6, C) also allows for the acquisition of quantitative data concerning the average displacement upon exposure to drugs (Figure 4.7).

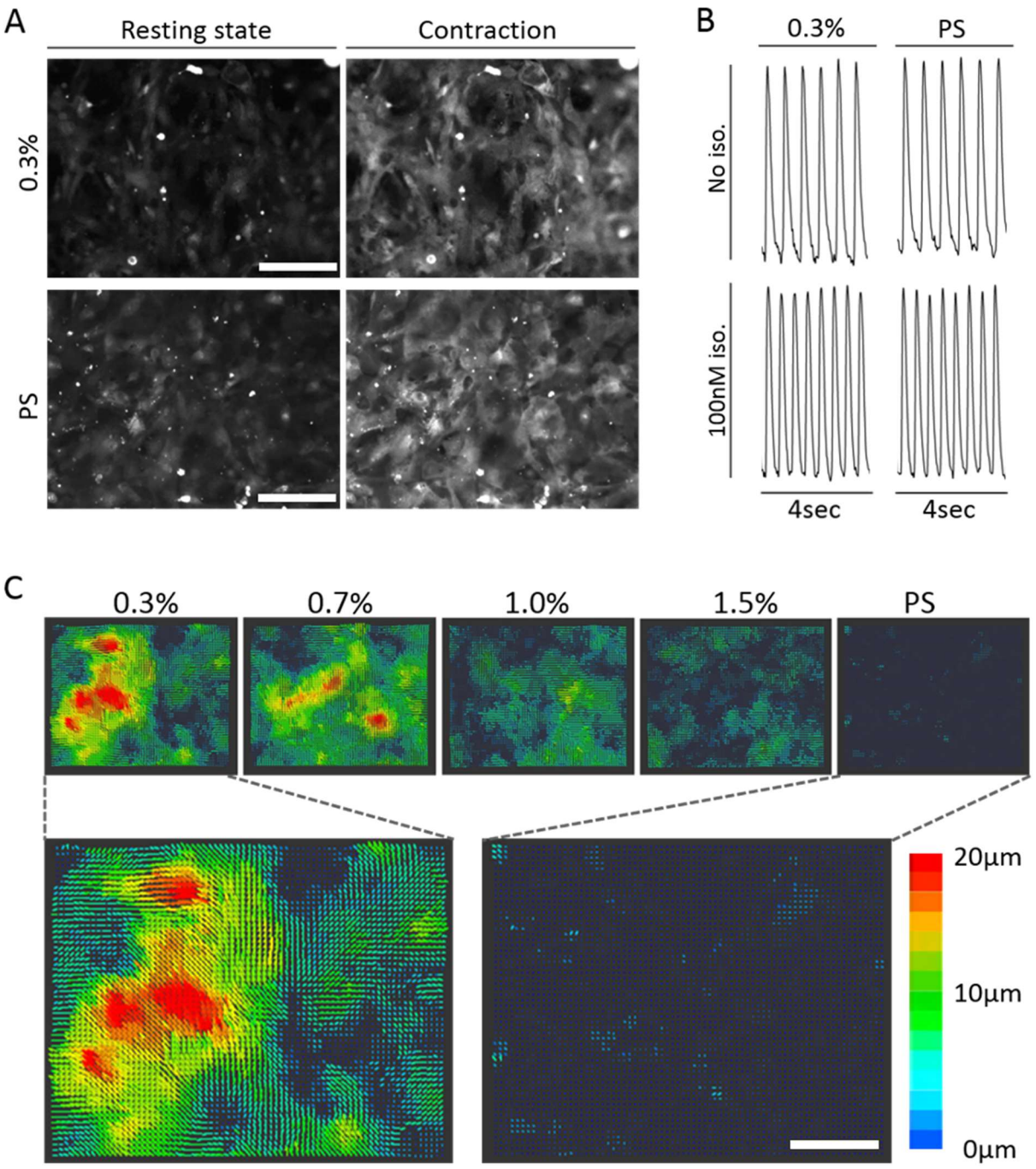

Figure 4.6 Characteristics of cardiac calcium dynamics and feasibility of optical twitch behaviour analysis. Cardiac contractions correlate with an intracellular release of free calcium ions. Molecular calcium sensor CAL520 exhibits high fluorescence upon the presence of free calcium (A). Representative calcium waves of hPSC-CMs exposed to isoprenaline are shown in B. Optical analysis of cardiac contractions based on cross correlation of resting states and contraction maxima are given in C. The analysis uses cross correlation of search windows to create a vector map indicating the direction and strength of the contractile displacement. White scale bar represents 200µm (A, C).

The quantitative analysis of calcium dynamics and contraction displacement were both carried out on the same location (in the wells); enabling a robust correlation of the calcium waves with the force generation data. Without isoprenaline exposure, the cells' beat rate was comparable among the different conditions with 14.1 ± 1.6bpm (0.7%), 10.6 ± 4.9bpm (1.0%), 14.3 ± 1.3bpm (1.5%) and 8.7 ± 1.2bpm (PS) (Figure 4.7, B and B*). Only the 0.3% condition produced a higher beat rate (23.8 ± 3.7bpm). The recorded values for the peak width duration at 90% repolarization (abbr. PWD90) were 0.59 ± 0.09s (0.3%), 0.68 ± 0.03s (0.7%), 0.64 ± 0.02s (1.0%), 0.72 ± 0.04s (1.5%) and 0.83 ± 0.04s (PS) (Figure 4.7, A and A*). No significant discrimination concerning the falling slope could be observed between the different substrates in the no isoprenaline condition with -5.74 ± 0.33 (0.3%), -5.53 ± 0.32 (0.7%), -5.19 ± 0.34 (1.0%), -4.91 ± 0.40 (1.5%) and -4.4 ± 0.31 (PS). Although, a trend of the softer substrates to produce steeper slopes can be seen. Exposure to 100nM isoprenaline led to shorter calcium peaks accompanied with higher beating rates and steeper slopes during repolarisation in all groups. The PWD90 values showed a shortening to 0.38 ± 0.02s (0.3%), 0.42 ± 0.02s (0.7%), 0.42 ± 0.01s (1.0%), 0.45 ± 0.03s (1.5%) and 0.49 ± 0.03s (PS). The no isoprenaline exposure control group (no Iso Ctrl) experienced no such shortening (0.66 ± 0.07s). Moreover, the PWD90 variation among all conditions shrunk from 0.59 - 0.83 to values ranging from 0.38s to 0.49s. The relative pattern of the beating frequencies was preserved; in all groups an increase leading to 62.0 ± 6.3bpm (0.3%), 36.0 ± 4.3bpm (0.7), 42.0 ± 2.4bpm (1.0%), 41.8 ± 3.1bpm (1.5%) and 39.7 ± 6.0bpm (PS) can be observed, while the no Iso Ctrl maintained a relatively low beat rate with 12.3 ± 2.3bpm. Moreover, the PWD90 variation among all conditions shrunk from 0.59 to 0.83 to values ranging from 0.38s to 0.49s, whereas the relative difference in beating rate was preserved, especially the higher frequency of the 0.3% group. Accordingly, the falling slopes were steeper with -11.07 ± 1.12 (0.3%), -11.01 ± 0.96 (0.7%), -11.84 ± 1.00 (1.0%), -11.24 ± 0.95 (1.5%), -12.30 ± 0.77 (PS) in contrast to the no Iso Ctrl (-4.48 ± 0.23). Rising the isoprenaline concentration from 100nM to 1µM led to PWD90 values of 0.39 ± 0.02s (0.3%), 0.46 ± 0.02 s (0.7%), 0.43 ± 0.01s (1.0%), 0.43 ± 0.02s (1.5%) and 0.47 ± 0.02s (PS). The beat rate stayed relatively constant in each condition with 65.8 ± 6.3s (0.3%), 39.2 ± 3.0s (0.7%), 40.3 ± 3.6s (1.0%), 44.7 ± 4.8s (1.5%) and 42.4 ± 7.1s (PS). Contrary to the beat rate and the PWD90 values, the falling slopes did experience a reduction in steepness in the 0.3% (-8.04 ± 0.59), 0.7% (-8.22 ± 0.63), 1.0% (-9.61 ± 1.03), 1.5% (-9.77 ± 0.80) and the PS (-9.67 ± 0.67) condition. The contraction frequency, PWD90 and falling slope of the no Iso Ctrl were comparable with the previous measurements, with 10.3 ± 1.7bpm, 0.70 ± 0.04s and -5.38 ± 0.25 respectively. Optical assessment of cardiomyocytes contractility suggested an average displacement of 2.08 ± 0.47µm (0.3%), 1.62 ± 0.32µm (0.7%), 1.45 ± 0.51µm (1.0%), 1.10 ± 0.34µm (1.5%) and 0.56 ± 0.11µm (PS), which correlated with substrate stiffness (Figure 4.7, D and D*). The clustered no Iso Ctrl exhibited an average displacement of 0.65 ± 0.11µm. Upon exposure to 100nM isoprenaline, the displacement values were elevated to 2.78 ± 0.44µm (0.3%), 2.75 ± 0.40µm (0.7%), 2.26 ± 0.73µm (1.0%), 1.86 ± 0.47µm (1.5%) and 0.74 ± 0.04µm (PS). Whereas the no Iso Ctrl group (0.63 ± 0.15µm) did not show an increased displacement.

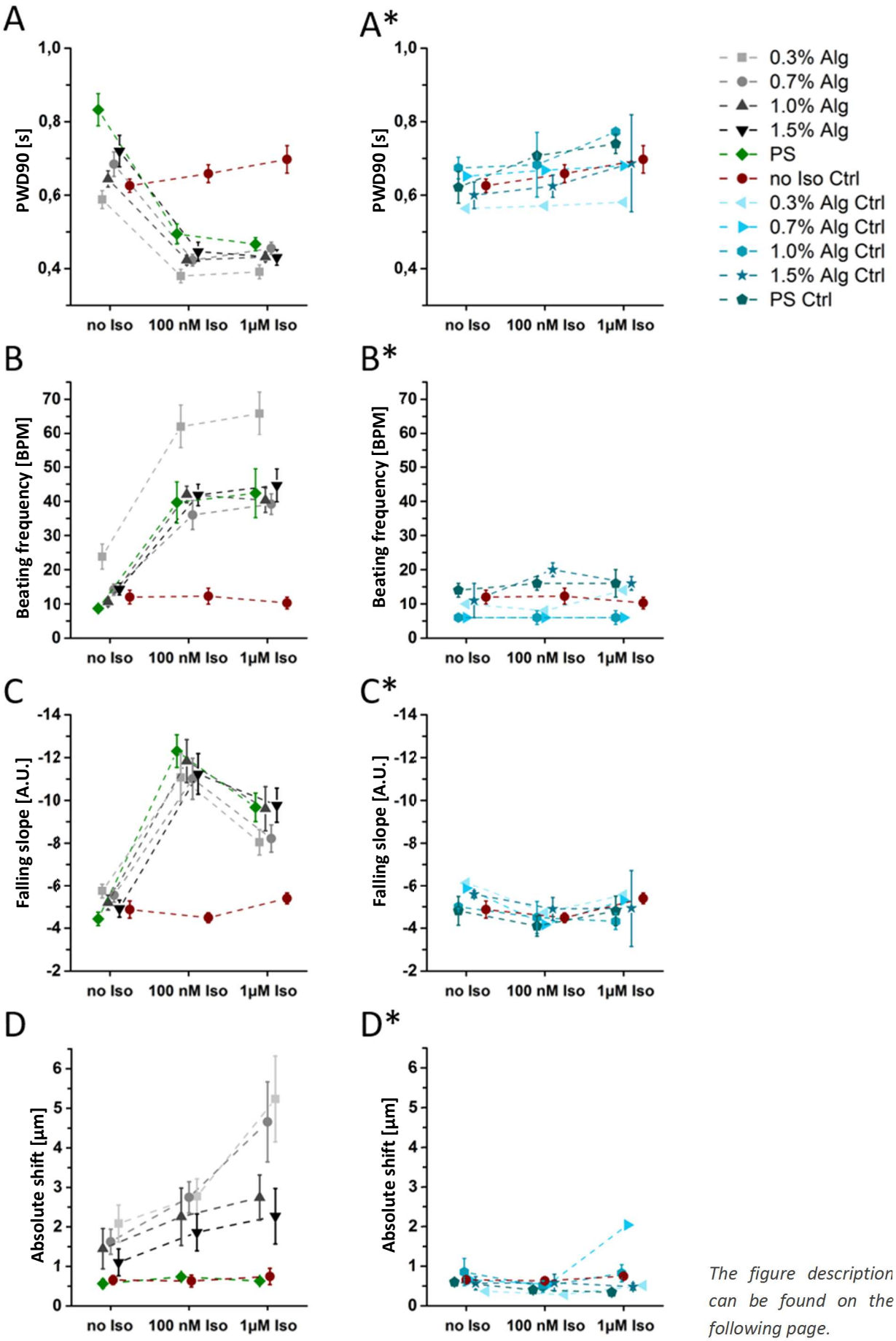

The figure description can be found on the following page.

Figure 4.7 Quantitative analysis of calcium dynamics and contraction displacement upon exposure to isoprenaline.
Analysis of calcium transients, concerning peak width duration at 90% repolarization (PWD90, A), beat rate (BPM, B) and the falling slope of repolarization (C), shows shorter peak durations (A), higher beating frequency (B) and faster repolarization dynamics (C) under isoprenaline exposure. The no isoprenaline group in A, B and C is composed of the mean value of no isoprenaline controls from each condition (0.3%, 0.7%, 1.0%, 1.5% and PS). The average values for these control groups (from each condition) as well as the merged no Iso Ctrl group is depicted in A, B* and C* accordingly. Displacement analysis reveals a stiffness-dependent contraction range and a dose-dependent rise in force generation not detectable with calcium transient analysis (D). The according control groups are depicted in D*. All data is presented as mean ± SEM. n=12 from three biological replicates.*

Contrary to the beat rate and PWD90 measurements, which produced similar results as the 100nM isoprenaline condition, an enhanced displacement was observed when the hPSC-CMs were exposed to 1µM isoprenaline. In this case, the increase translated into an average displacement of 5.23 ± 1.08µm (0.3%), 4.66 ± 1.01µm (0.7%), 2.74 ± 0.57µm (1.0%) and 2.27 ± 0.70µm (1.5%). No increase was detected in the PS (0.63 ± 0.04µm) and no Iso Ctrl group (0.75 ± 0.21µm) was measured. The previous experiments proved the feasibility of hPSC-CM culture on functionalised UHV-alginate scaffolds and the possibility to harness the advantages of UHV-alginate scaffolds for *in vitro* drug screenings, particularly in the context of force generation quantification in drug screenings. The different stiffnesses were also reflected by the results and provide a good basis for future experiments with disease lines. Using this setup, compound-induced changes of cardiomyocyte contractility were also detected and could represent a valuable addition in the workflow of drug toxicity and discovery screening.

The inotropic and chronotropic responses of hPSC-CMs on UHV-alginate substrates upon isoprenaline exposure, suggest a high degree of physiological resemblance. Thus, the possibility to use these substrates in the context of tissue engineering was investigated. To make such a transition feasible the substrates had to be produced in a different manner. First, the shape of the fixed scaffolds was defined by the well architecture and complex shapes were not easily produced. Second, the scaffolds are subjected to vertical shrinkage when gelled, which is difficult to control and modulate. Third, in the context of tissue engineering the constructs must be transplantable and adaptable. To this extent, a method was developed, which enabled structuring the biopolymers in a non-fixed, three-dimensional manner, thus offering the possibility to create individualised, transplantable constructs.

4.3 DEVELOPMENT OF A 3D PRINTING PROCESS TO STRUCTURE LOW CONCENTRATED BIOPOLYMER INKS WITH HIGH SPATIAL RESOLUTION IN A VISCOSITY INDEPENDENT MANNER

The use of UHV-alginates has great potential in tissue engineering applications due to the high biocompatibility, the flexible biofunctionalisation and the readily transition from *in vitro* models to *in vivo* applications. The chronotropic and inotropic drug responses in the previous experiments suggest that the culture on functionalised UHV-alginate is advantageous for hiPSC-CMs functionality and physiology; hence, this combination could represent a valuable *in vitro* model of the cardiac niche. *In vivo*, the myocardium experiences a greater movement range during contraction and filling compared to the fixed scaffolds used in the previous experiments. It was hypothesized that the use of free-floating scaffolds would further enhance the resemblance to the physiological situation *in vivo* due to the different hydrodynamic forces. At the same time, 3D printing enables the production more complex *in vitro* models, due to the possibility to generate diverse designs. The implementation of such a free-floating model system required the development of a production process, which combines a robust structuring process with high flexibility. 3D printing enables the creation of such application-specific structures and allows complex architectures of different artificial and biological materials without the need to redesign the whole production process. Focussing on biopolymer solutions with low concentrations the production had to be carried out with these difficult-to-handle materials. Particularly, the extremely fluid nature of the low-concentrated, non-crosslinked inks makes it difficult to create three-dimensional structures. To overcome the limitation, a 3D printing method had to be conceived and established first before downstream applications were realised.

4.3.1 3D printing of low-concentrated UHV-alginate solutions with a novel 3D printing process

3D printing of hydrogels or more specifically UHV-alginates, suffers from the liquid nature of the biopolymer solutions before crosslinking. Even a fast printing process could not compensate the fast melting of lower concentrated alginate inks; thus, the loss of shape and ultimately of the design is the consequence. The most common technique to circumvent this is the use of highly concentrated inks, which exhibit a pasty behaviour. However, these highly concentrated formulations lead to a high scaffold stiffness after crosslinking and restrict the flexibility of the whole production process. Additionally, pasty inks still tend to lose their shape during the printing process, albeit not as fast. This becomes even more relevant when the printing process is conducted over a longer period, *i.e*. when printing large structures.

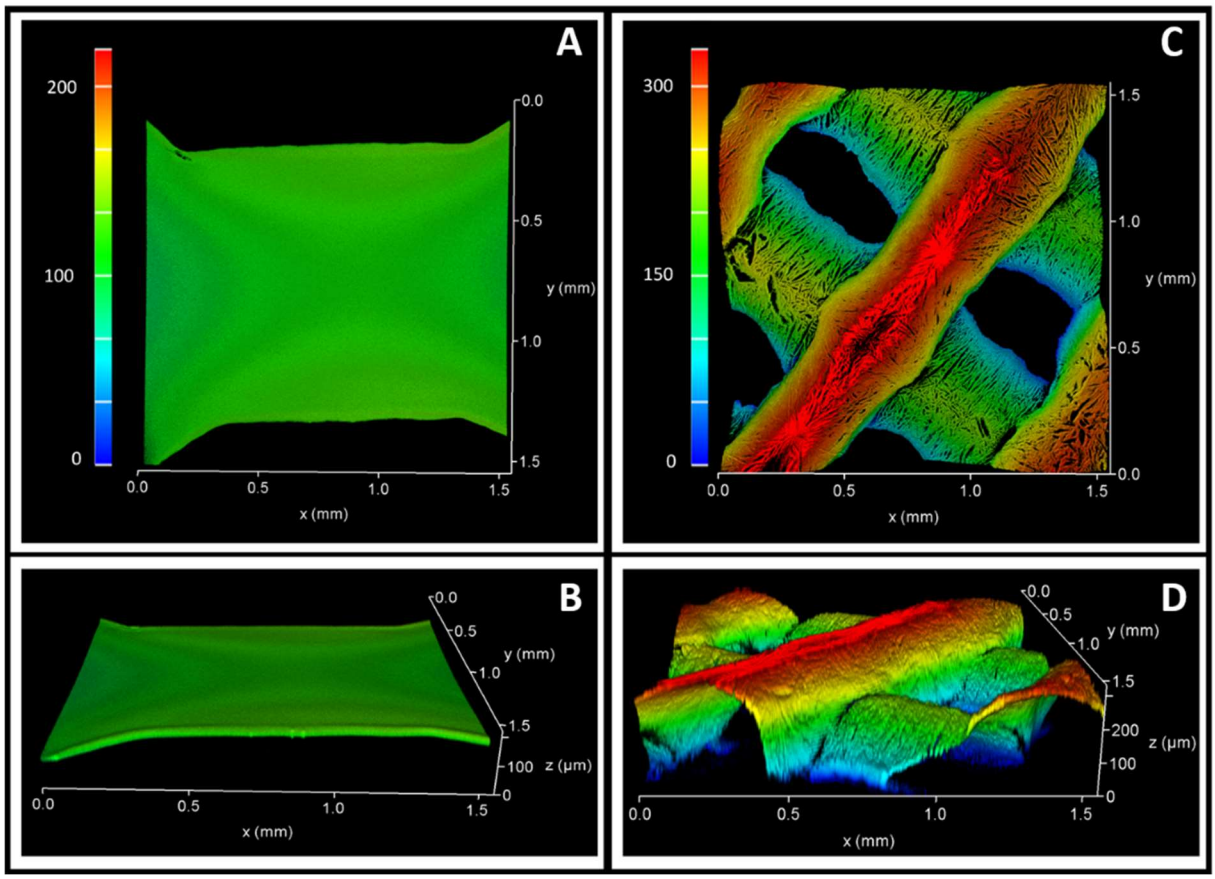

Figure 4.8 Freeze printing allows for three-dimensional deposition of fluidic, hydrogel-based inks. Depicted is the stained scaffolds after liquid (A, B) and freeze (C, D) printing. Staining has been achieved with FITC-labelled PLL. The scaffolds differ significantly in height due to the shape loss under liquid printing and the shape-preserving freezing step in the freeze printing method. Printing pressure was 50kPa. Image taken from Fischer et al. 2016.

A novel printing method was conceived, which utilizes a cooled surface to freeze the 3D printed UHV-alginate inks immediately upon deposition. This method kept the printed UHV-alginate solidified during the whole printing process, thus, decoupling the duration of the printing process from the loss of shape caused by the liquid nature of non-gelled UHV-alginate (Figure 4.8). A proof of concept study was conducted and the differences between conventional 3D printing, named liquid printing (abbr. LP), and freeze printing (abbr. FP), the presented method, were assessed.

3D printing a 0.7% UHV-alginate solution with a viscosity of 2.890 ± 0.037Pa*s (20°C) with either the liquid printing method or the novel freeze printing method resulted in significantly different outcomes. The freeze printing process preserved structure in much higher detail and in a three-dimensional manner (Figure 4.8, C and D), while LP suffered from the strong sideward flow of the ink (Figure 4.8, A and B). This resulted in an extremely flat deposition under LP. Using FP, the deposited lines of hydrogels maintained a height of 300µm and a width of 400µm. Although initially frozen, the simultaneous thawing and crosslinking step preserved

the printed three-dimensional structure. Furthermore, the scaffold side facing the cooled printing surface was found to be covered with pores in the micrometre range (Figure 4.9Figure 4.9, A and B). These pores were aligned in the z-axis and projected over 70µm into the scaffold volume (Figure 4.9, C).

To further gain insight into the pore architecture and to test the biocompatibility of these scaffolds, a proof of concept study was conducted. Investigation, if cell adhesion on the scaffolds was still feasible, the scaffolds were biofunctionalised and MSCs were cultured on them. After a week of culture, the samples were analysed with scanning electron microscopy (Figure 4.10, C).

An array of parallel pores at the cutting interface was observed, revealing a high porosity in the bulk volume (Figure 4.10, B). Additionally, folds, wrinkles and grooves covered the scaffold surface (Figure 4.10, C). Mesenchymal stem cells penetrated into these grooves and showed sustained viability as proven by the display of microvilli on the cell membrane. This study could not clarify if the cell location in the grooves was temporally limited or permanent.

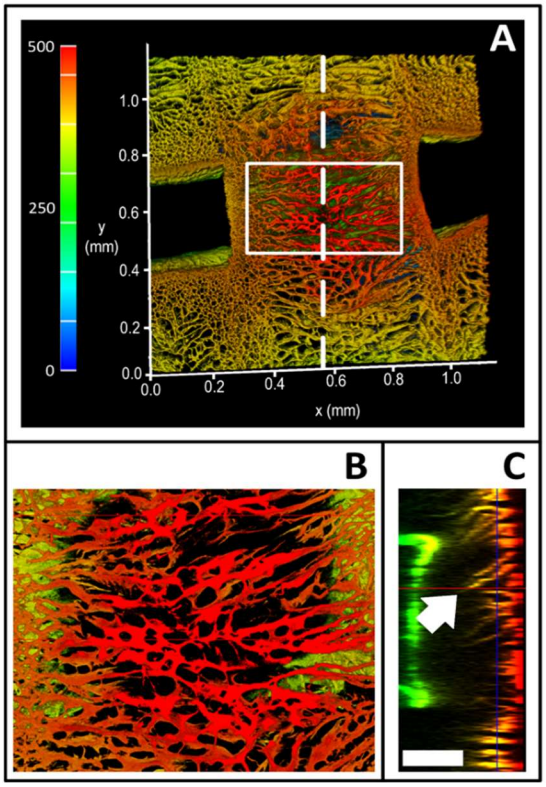

Figure 4.9 Freeze printing leads to a highly porous scaffold surface.
Fluorescent labelling of alginate reveals a highly porous surface of freeze printed scaffolds (A and B). The randomized pores project up to 70µm into the scaffold as indicated by the white arrow (C). White scale bar represents 100µm. Image taken from Fischer et al. 2016.

These early results led to the development of a more advanced experimental setup, which allowed a continuous printing process. 3D printing of biomaterials often suffers from a low printing resolution. A high resolution is important, when the production of biological tissues with relevant structural details in the submillimetre range are envisioned.

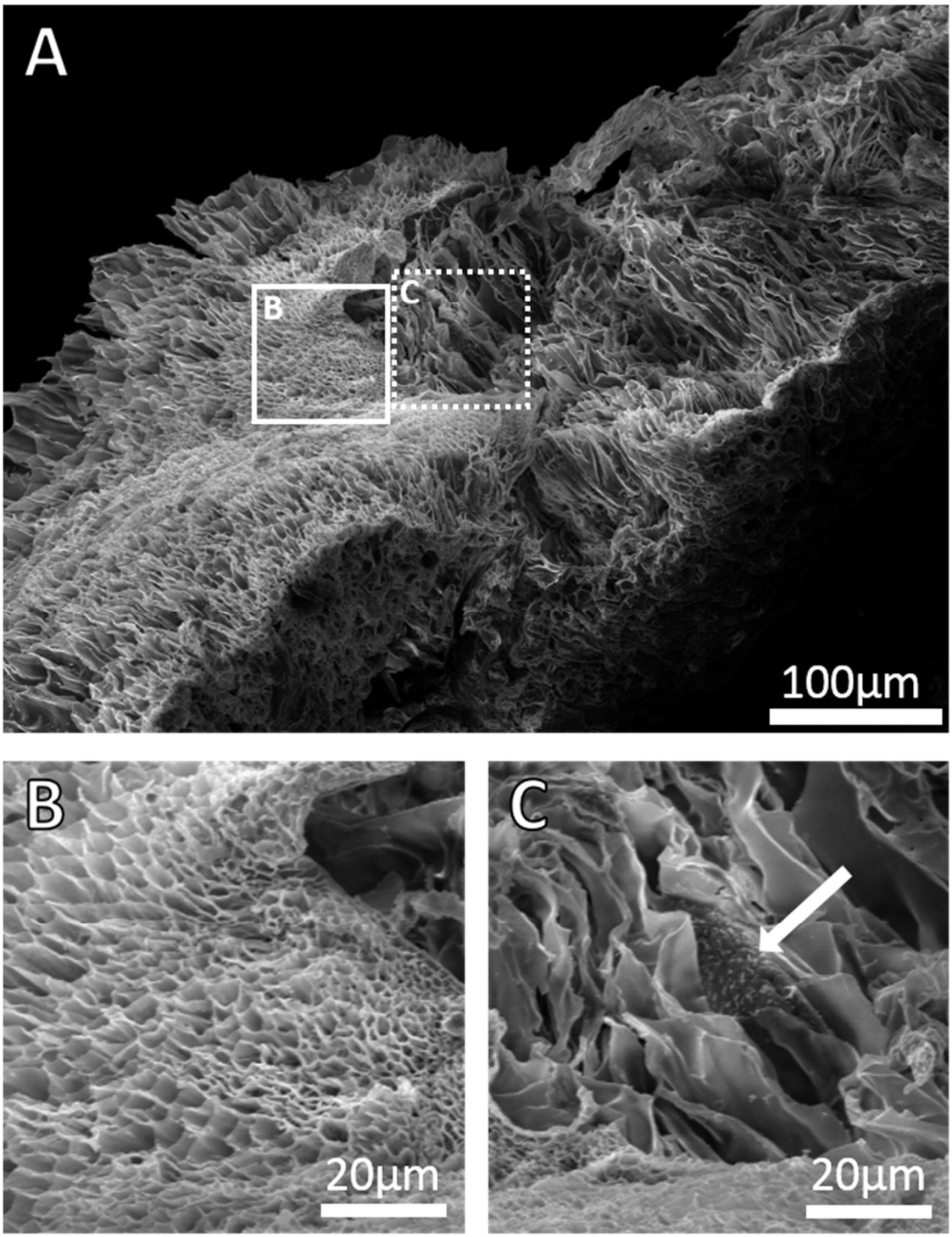

Figure 4.10 Scanning electron microscopy highlights the structural characteristics of freeze printed scaffolds.

The interface of a scaffold, cut-open by hand and imaged using scanning electron microscopy (SEM) is depicted in A. The brighter surface on the left side in A represents the interface where the scaffolds has been sectioned and offers a glimpse into the bulk volume with many parallel pores running vertically through the scaffold (solid white box, B). The right side represents the surface harbouring many folds, vertically aligned pores cannot be seen, but discrimination between pores, folds or potential pores at the bottom of the horizontal folds is difficult. As seen in C, (white arrow) mesenchymal stem cells penetrate and tightly squeeze themselves into those folds. The sustained presentation of microvilli on the cell surface (white arrow, C) is associated with preservation of the multipotent stem cell potential and high cellular viability.

4.3.2 Evaluation of printing resolution and pore sizes of freeze printing method using different UHV-alginate compositions

The printing resolution is crucial for any downstream application; because it sets the limitations of how detailed the printed designs can be structured. Furthermore, the possibility to adapt the printing process precisely to the needs of the application is a major advantage of 3D printing in general. A lack of resolution and control would translate into a diminished usability. The previous experiments showed that three-dimensional structures could be readily produced using a non-modified, 0.7% UHV-alginate solution and a standard 3D printer (BioScaffolder 2.1; GeSiM, Germany). However, the printing resolution has not been compared to conventional 3D printing.

Therefore, the evaluation of the printing resolution was conducted under different printing pressures by means of strut diameter measurement (Figure 4.11). As seen in Figure 4.11, the deposition volume correlates positively with the pressure. Strut diameters under liquid printing started from 495 ± 50µm under 20kPa pressure to 690 ± 63µm and 703 ± 260µm in the 30kPa and 40kPa condition and increased to 1013 ± 234µm, 1385 ± 251µm and 2193 ± 371µm for 50kPa, 60kPa and 70kPa respectively. The smallest printing pressure (20kPa, Figure 4.11) could not be applied in the freeze printing method, because the printing nozzle could not be placed close enough to the printing area without freezing the ink in the nozzle. The resulting diameters were 288 ± 163µm, 447 ± 70µm and 538 ± 76µm for 30kPa, 40kPa and 50kPa respectively, while the higher pressures produced struts with diameters of 609 ± 103µm (60kPa) and 620 ± 57µm (70kPa). In contrast to the exponential diameter increase in liquid printing, the diameters in freeze printing showed smaller increases with higher printing pressures. After observing the pores, seen in Figure 4.9, it was hypothesized that a change of the ink formula would translate into different pore sizes. To that extent, different concentrations of UHV-alginates were comparatively analysed. Furthermore, the influence of different UHV-alginate composition on pore formation was assessed as well.

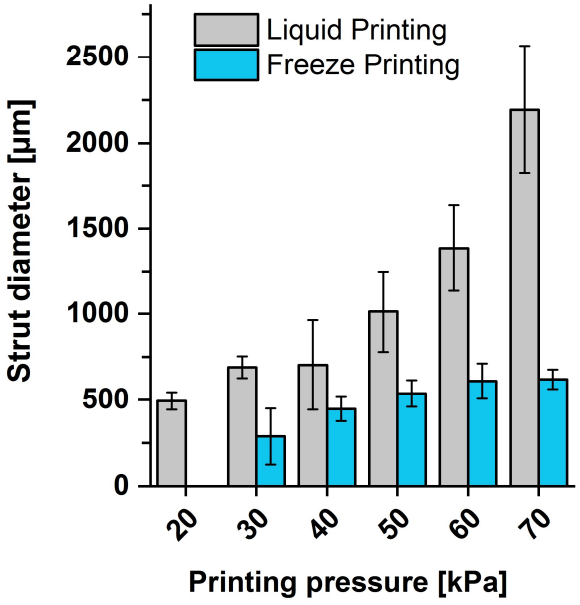

Figure 4.11 Printing resolution is dependent on the printing method and pressure
The strut diameter is plotted against the printing pressure as a measure of printing resolution (A; data is depicted as mean ± SD; n= 145 (20, 30 and 40 kPa) and n=100 (50, 60 and 70kPa) diameters). Higher deposition volumes correlate with strut diameters in a non-linear fashion.

Therefore, UHV-alginates from either Lessonia nigrescens or Lessonia trabeculata or a 1:1 mixture of both were used (Figure 4.12, A). The pore area for 0.3% UHV alginate formulations were 63.4 ± 4.7µm² (LN), 56.8 ± 10.7µm² (LT) and 31.8 ± 3.3µm² (LT/LN). 0.7% UHV-alginate inks with average pore areas of 55.6 ± 5.1µm² (LN), 102.5 ± 9.7µm² (LT) and 84.7 ± 7.6µm² (LN/LT) had the biggest pores in this experiment. 1.0% and 1.5% UHV-alginate reached similar sizes with 22.5 ± 1.7µm² (LN), 53.7 ± 3.6µm² (LT), 39.4 ± 3.2µm² (LT/LN) and 12.8 ± 0.7µm² (LN), 50.7 ± 4.7µm² (LT), 25.3 ± 2.0µm² (LT/LN), respectively. The biggest pores were found in the 0.7% LT and LT/LN conditions, where as 0.3% LN produced the third biggest pores and the biggest ones when compared to LN conditions only. A pattern is visible in 0.7%, 1.0% and 1.5% with LN having the smallest and LT producing the biggest pores. The combination of both gave an intermediate pore size. This is not true for the 0.3% condition, in which LN produced the biggest pores.

In conclusion, LT based alginates harboured the biggest pores after freeze printing, but the still relatively small diameter of approximately 10µm led to the use of additives that potentially further enlarge these pores. The used additives were pluronic F68, trehalose, dimethyl sulphide oxide (abbr. DMSO) and polyethylene glycol (abbr. PEG6000). All additives were dissolved in 0.7% UHV-alginate solutions to a concentration of either 0.1%, 1% or 10% (w/vol. %). As a control, native 0.7% UHV-alginate without additives was chosen. With an

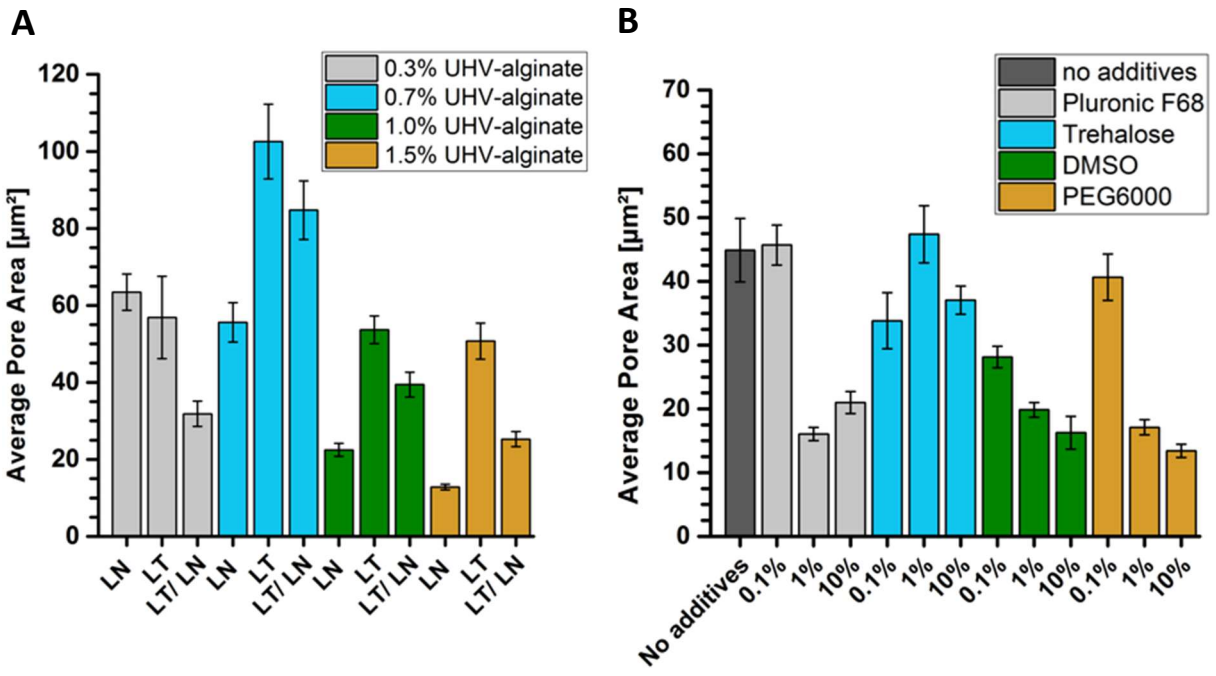

Figure 4.12 Influence of UHV-alginate composition and additives on pore formation.
Depicted is the average pore area of different concentrated UHV-alginate solutions from either Lessonia nigrescens or Lessonia trabeculata or a 1:1 mixture of both (LT/LN). The pore area is given in mean ± SEM (A; n = 90 pores from three scaffolds). The effects of different porogens, namely Pluronic F68, Trehalose, DMSO and PEG600, on pore formation were assessed. A 0.7% UHV-alginate solution was taken as a basis and the compounds added to a final concentration of 0.1%, 1.0% or 10% (B; data given as mean ± SEM; n= 270 pores from three different scaffolds).

average pore size of 45.7 ± 3.1µm² Pluronic F68 did not reduce or enhance crystal size in the 0.1% condition, but robustly lowered pore size down to 16.0 ± 1.1µm² (1.0%) and 20.9 ± 1.7µm² (10%) in higher concentrations. Trehalose showed no effect on pore size with a pore area of 47.4 ± 4.5µm² in the 1% condition. For 0.1% and 10%, an average pore size of 33.8 ± 4.4µm² and 37.1 ± 2.2µm² was measured. DMSO, a known inhibitor of water ice crystallization, already reduced pore size in the 0.1% condition (28.2 ± 1.7µm²) and progressively did so with higher DMSO concentrations, reaching values of 29.8 ± 1.1µm² (1%) and 16.2 ± 2.6µm² (10%). PEG6000 behaved very similar to Pluronic F68 producing values of 40.7 ± 3.6µm², 17.1 ± 1.2µm² and 13.4 ± 1.0µm² for 0.1%, 1% and 10%, respectively. In summary, no additive in this experiment was able to enlarge the pore size compared to the no additive control, but smaller pores were produced by using Pluronic F68, DMSO and PEG6000. The pore size was robustly decreased by additive concentrations of 1% and higher, only DMSO was able to robustly influence pore size in the 0.1% concentration. Trehalose showed smaller pores in 0.1% and 10% concentrations, but not in the 1% condition.

In conclusion, the modification of pore size was achievable with the use of different UHV-alginate formulations, but the observed differences were relatively small in regard to their projected biological function. Although a robust decrease of pore size was achieved by the use of additives, a robust enlargement was not observed. Following this analysis, the consecutive experiments investigated the use and influence of the elastic UHV-alginate scaffolds on hiPSC-CM culture. To that extent, a novel design was chosen, which fostered self-organisation of the cells and enabled a greater movement range during contractions.

4.4 INVESTIGATION ON THE SUITABILITY OF 3D PRINTED, UHV-ALGINATE-BASED SCAFFOLDS FOR IN VITRO MODELLING OF THE CARDIAC NICHE

In vitro modelling of the myocardium is the foundation for drug screenings, toxicological evaluations and the understanding of fundamental mechanisms involved in cardiac maturation and the pathological disruption of the finely tuned electrophysiological homeostasis. Conventional cultures of cardiac cells are performed on two-dimensional PS-based surfaces or on contractile substrates. However, the freeze printing method enables a robust production of non-fixed UHV-alginate scaffolds. These constructs could offer hPSC-CMs more freedom in terms of contractile movement range. Additionally the observed inotropic and chronotropic reactions suggested a high resemblance to physiological systems, hence, these scaffolds could translate into valuable additions in drug screenings. Furthermore, the free-floating nature of such scaffolds allows for additional future therapeutic applications, particularly transplantation procedures could be readily conducted. Ultimately, this setup offers a high flexibility concerning the usable biopolymer concentrations and the scaffold design.

4.4.1 Viscoelastic evaluation of the Heart Patch, a 3D printed, biopolymer-based scaffold for tissue engineering applications

For the culture of cardiomyocytes on UHV-alginate scaffolds, several points have to be considered. The four UHV-alginate concentrations (0.3%, 0.7%, 1.0% and 1.5%) used to form fixed layers were chosen again. Mainly because the previous experiments have shown, that these concentrations recapitulate relevant physiological elasticities after crosslinking. Contrary to the use as two-dimensional culture substrates, the viscosity is now an important parameter, due to its influence on the melting behaviour during 3D printing. The measured viscosities of the non-crosslinked UHV-alginate solutions were 0.16 ± 0.02Pa*s (0.3%), 3.84 ± 0.04Pa*s (0.7%), 12.29 ± 0.03Pa*s (1.0%) and 43.66 ± 0.04Pa*s (1.5%) (Figure 4.13). Using the freeze printing method, all four concentrations were printed in a robust manner and produced three-dimensional scaffolds. The design was changed to a disc and was used throughout the following experiments.

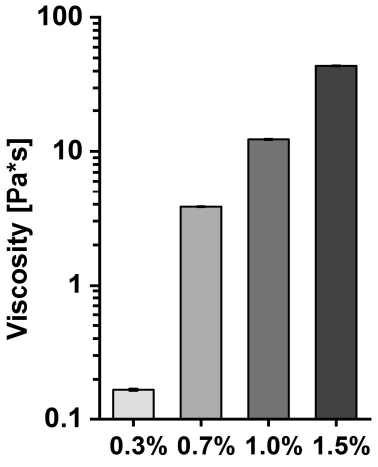

Figure 4.13 Correlation of UHV-alginate ink concentration and their viscosity.
The viscosity of different concentrated UHV-alginate solutions (w/v %) in the sol state is shown (Mean ± SEM; n=3).

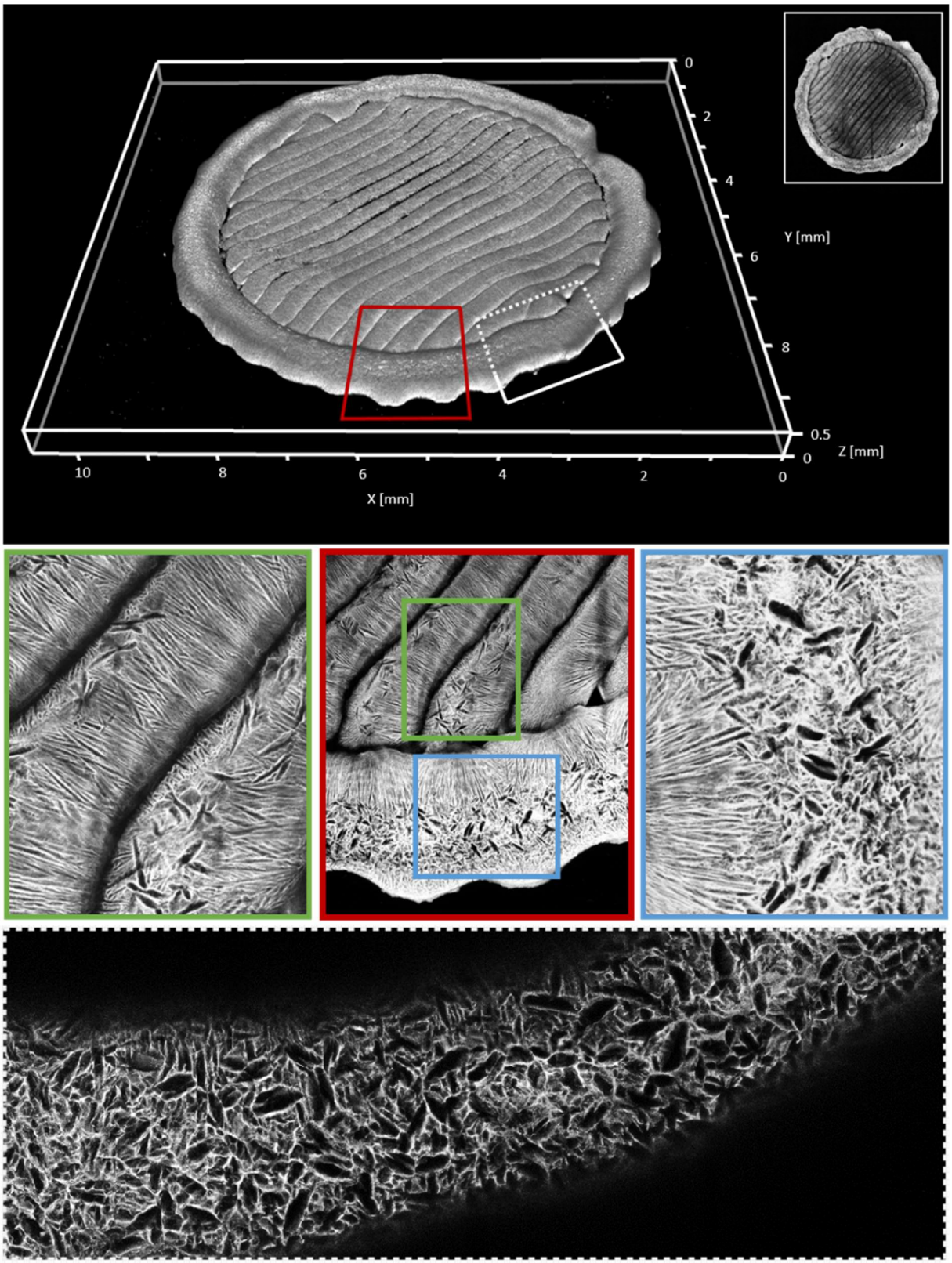

Figure 4.14 Representative fluorescence image of an UHV-alginate scaffold with uniform stiffness (single ink) for in vitro modelling of the cardiac niche.

Depicted is a UHV-alginate scaffold stained with FITC-PLL and imaged with a Leica SP8 confocal laser microscope. The disc-shaped scaffold consist of nineteen struts framed by an outline (red insert). The diameter was 0.8cm and the height approx. 300µm. The scaffold offered two differently structured surfaces: highly parallelized grooves (green insert) and pores (blue insert). The pores projected into the scaffold volume as seen in a section from the outline (white dashed inlet).

A representative, 3D printed scaffold, made of 0.7% UHV-alginate is depicted in Figure 4.14, consisting of nineteen parallel strands and an outline. The printed diameter of 0.8cm was maintained through the crosslinking process. This design has been chosen for all following experiments, due to several key characteristics. First, it offers a highly structured surface with bigger grooves, in between the printed struts and smaller structures in the range of single cells (Figure 4.14). Second, it harbours no recesses or windows, which prevents cells loss, when these are seeded on the scaffold at a later stage. Third, it offers the cells no preferential beating direction (apart from the grooves), as it would be the case for rectangular designs, fostering self-organization. Fourth, it can be scaled in size without being limited by the 3D printing method and serves as a good first approximation for a potential therapeutic plaster.

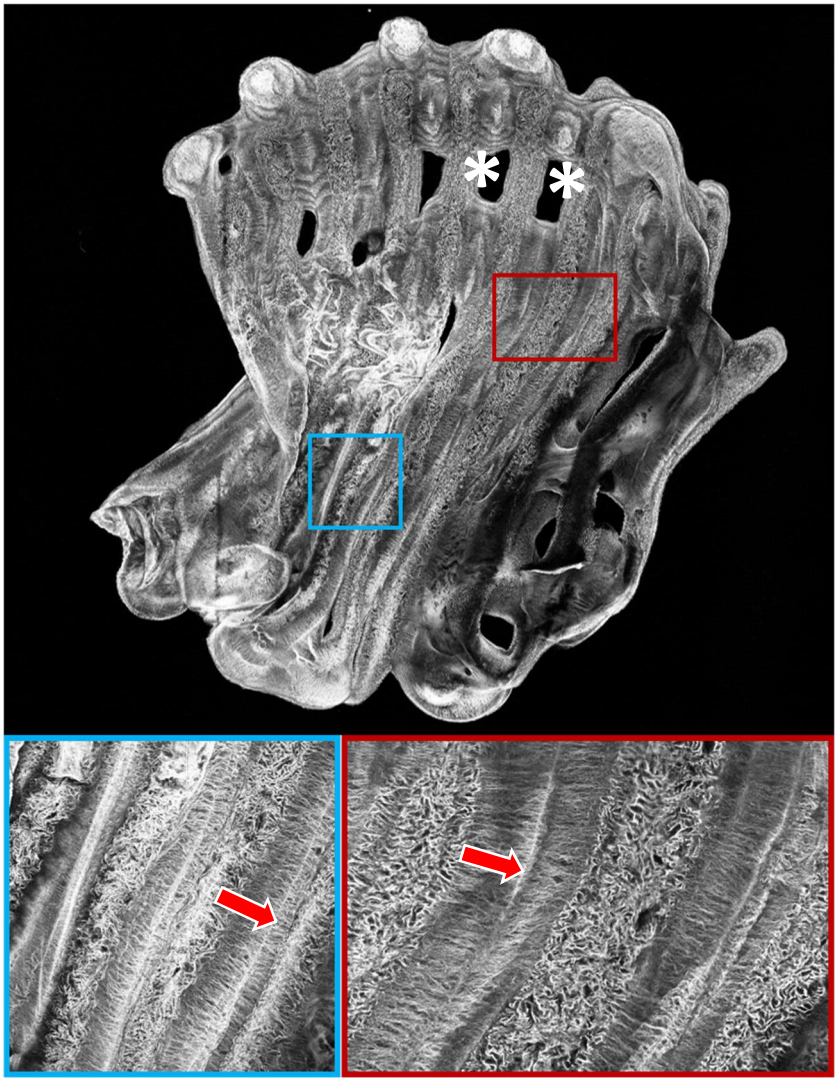

Figure 4.15 Representative fluorescence image of an UHV-alginate scaffold, printed with two differently concentrated inks. The pores in the higher concentrated ink (1.5%), which was printed first, have a vertical orientation, whereas the lower concentrated ink (0.3%) produced horizontally aligned pores. Even an interface area, where horizontal pores from both sides met each other can be seen as a white line (indicated by red arrows). Small printing artefacts are visible as holes in the construct (indicated by white asterisks).

Additionally, the printing process also enabled to include UHV-alginate solutions with different concentrations and viscosities simultaneously in one scaffold. The resulting scaffold is depicted in Figure 4.15 and although the shape is distorted due to some shrinkage caused by the crosslinking step, the printing process was successfully conducted. Contrary to single ink scaffolds, the pores orientation varied between the higher and the lower concentrated

alginates (Figure 4.15, blue and red box). They were vertically aligned in the high concentrated ink, which was printed first, and horizontally aligned in the second-printed, lower concentrated ink. The interface between the two, opposing crystallisation fronts is visible as a faint white line (red arrows).

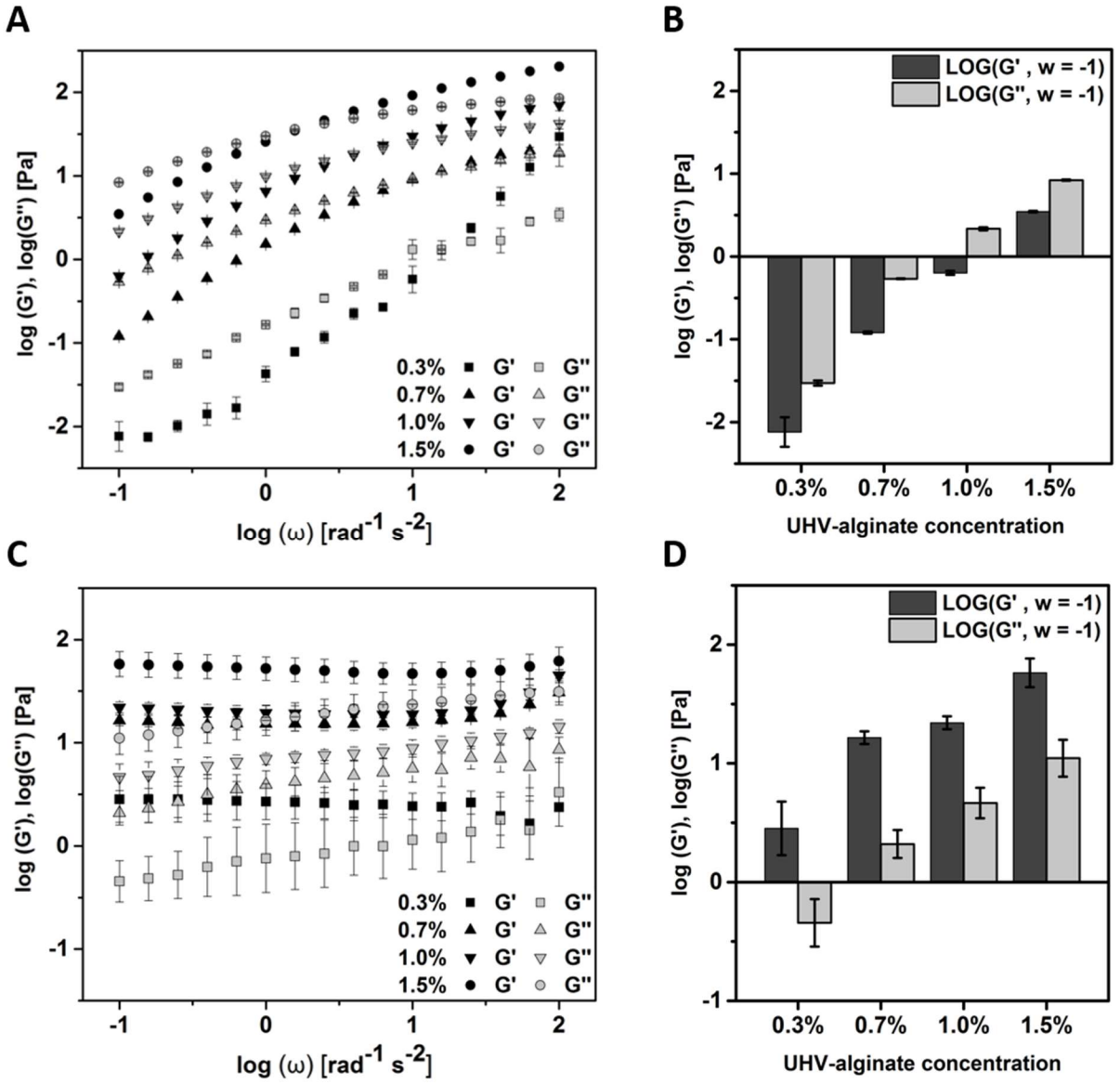

Figure 4.16 Assessment of viscoelastic properties of UHV-alginates in sol and gel states.
Sol states of UHV-alginates are characterized by viscous behaviour, when shear loss moduli dominate (G') over shear storage moduli (G'') (A). Robust measurement of G' and G'' at lower frequencies (0.1 rad/s) highlight the correlation of shear storage and loss moduli with alginate concentration (B, D). After crosslinking, elastic behaviour is dominantly exhibited with constantly lower G'' than G' and a robust plateau in the elastic proportion (C). The gelled hydrogels exhibited concentration dependent G' and G'' (D).

The novel 3D printing method of low concentrated UHV-alginates enables the production of three-dimensional scaffolds, but the freezing and subsequent structure preserving crosslinking steps could adversely affect the elastic properties of the molecular hydrogel network. Thus, potentially inhibiting its capacity to store and release deformation energy, and

the ability to return to its original state after contraction. To allow discrimination between the sol and gel states of UHV-alginate the sol was included in the analysis. As shown (Figure 4.16, A), the shear loss modulus (G') dominates over the storage modulus (G'') in UHV-alginate solutions of 0.3%, 0.7%, 1.0% and 1.5%. The rise of both, G' and G'', correlates with increasing angular frequency in all samples. Additionally, G'' can be observed to overcome G' in a frequency depending manner.

Quantitative analysis in the linear range at low frequencies showed a concentration dependency of both loss (G') and storage moduli (G'') for 0.3% (G'=0.-2.12 ± 0.18rad^{-1} s^{-2} and G''=-1.53 ± 0.03rad^{-1} s^{-2}), 0.7% (G'=-0.92 ± 0.01rad^{-1} s^{-2} and G''=-0.27 ± 0.04rad^{-1} s^{-2}), 1.0% (G'=-0.20 ± 0.02rad^{-1} s^{-2} and G''=0.33 ± 0.02rad^{-1} s^{-2}) and 1.5% (G'=0.54 ± 0.01rad^{-1} s^{-2} and G''=0.92 ± 0.01rad^{-1} s^{-2}) (Figure 4.16, B). After freeze printing and subsequent crosslinking, the elastic proportion dominates the viscous proportion in all samples and under all frequencies (Figure 4.16, C). A crossover point as seen in the sol states has not been observed, except for the 0.3% condition at the two highest oscillations. While a frequency dependent rise in the loss modulus can be seen, the storage modulus is constant in all samples. At low frequencies, the measurements reveal a correlation of loss and storage modulus with increasing alginate concentration. The values were G'=0.45 ± 0.22rad^{-1} s^{-2} and G''=-0.34 ± 0.20rad^{-1} s^{-2} (0.3%), G'=1.22 ± 0.05rad^{-1} s^{-2} and G''=0.32 ± 0.12rad^{-1} s^{-2} (0.7%), G'=1.34 ± 0.05rad^{-1} s^{-2} and G''=0.67 ± 0.13rad^{-1} s^{-2} for 1.0% and G'=1.76 ± 0.12rad^{-1} s^{-2} and G''=-1.04 ± 0.16rad^{-1} s^{-2} for 1.5% (Figure 4.16, D). The difference in storage modulus between 0.7% and 1.0% UHV-alginate scaffolds was smaller than the discrepancy in loss modulus (Figure 4.16, D).

The results suggested that the crosslinking procedure was sufficient to form a molecular hydrogel network. Furthermore, the elastic behaviour was not inhibited by the freezing step and the different concentrations did not inhibit the elastic behaviour of the scaffolds after crosslinking. The ability to store energy and then dissipate it in kinetic energy is crucial for the scaffolds to achieve a return movement to the original shape after contraction. The elastic behaviour was not inhibited by freeze printing and *in vitro* experiments with hPSC-CMs grown on the scaffolds were conducted next. The investigation focused on the influence of such contractile scaffolds and additional assessments of differences between the Heart Patch and the fixed layers were performed.

4.4.2 Evaluation of the influence of hydrogel-based scaffolds on hPSC-CM fidelity

After the cells were seeded on the functionalized UHV-alginate scaffolds, effective adhesion on the scaffold surface was observed. The hPSC-CMs exhibited contractions and started to synchronize, which also led to this biopolymer-hPSC-CM construct being called the Heart Patch. Between day 5 and 10 the scaffolds started to exhibit strong macro-contractions, deforming the scaffold during the concentric muscle contractions. The elasticity of the UHV-alginate scaffolds was able to pull the construct back into its original shape, thus enabling robust contractions over long culture periods. Viewed from the top view the contraction seems to decrease the scaffold area (Figure 4.17). The concentric force generation of the cells was conducted in time window of approx. 10ms, followed by a phase were the force was maintained (8-12ms in Figure 4.17). Upon relaxation, the biopolymer released the stored deformation energy in an elastic manner, essentially stretching the cell back into their original position.

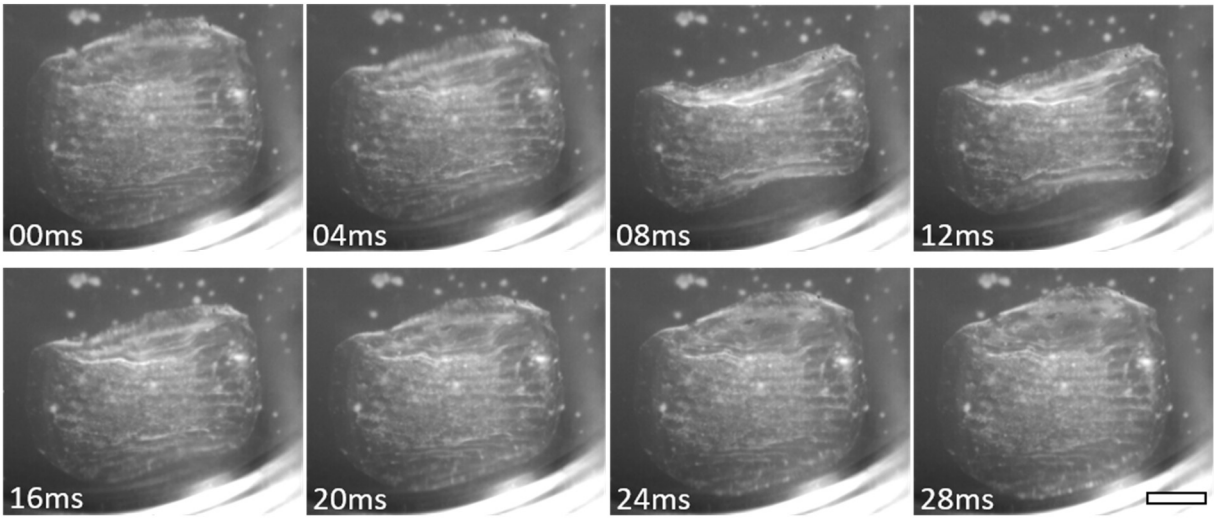

Figure 4.17 The Heart Patch exhibits synchronous macro-contractions.
After a period of approx. 7 days, the HPs exhibit powerful contractions bending the whole construct. Representative time-lapse images of a contracting HP (0.7% UHV-alginate) is given in A. White scale bar represents 200µm and the relative time in milliseconds is given in each image.

The observed macro-contractions are presumably the result of the concerted contractile action of all hPSC-CMs grown on the HP. The sarcomeric structures and their inter- and intracellular organisation are responsible for the force generation of cardiomyocytes. Furthermore, the large forces generated by the myocardium also rely on the precisely timed execution of the contractile movement, resulting in simultaneous contractions. This collective action is mediated by ion channels, which couple cardiomyocytes, thus, enabling the distribution of electrical potentials with high velocity. Immunocytochemistry directed against α-actinin and Cx43 was utilized to visualize the intracellular organization of the contractile

machinery (α-actinin) and the functional localisation of an electrophysiologically relevant ion channel at the cell boundaries (Cx43).

The functional integration of α-actinin into the cardiac sarcomere has been observed in all conditions (Figure 4.18). Cells grown on Heart Patches feature highly organized sarcomeres with a high degree of intercellular alignment. On fixed UHV-alginate scaffolds, the cells also exhibited organized sarcomeres, but with lower intra- and intercellular parallelism. Partially, the cells showed overlapping striations pointing to different directions. This was even more prominent in cells grown on PS, where virtually all cells possessed such multidirectional sarcomeric structures. Cells at the border of the cell layer on PS showed α-actinin that was not assembled in functionally organized sarcomeric structures. The majority of Cx43 clustered at the cell-cell boundaries in fixed and non-fixed alginate scaffolds, indicating a highly functional integration. Additionally, Cx43 was found in virtually all observed cells.

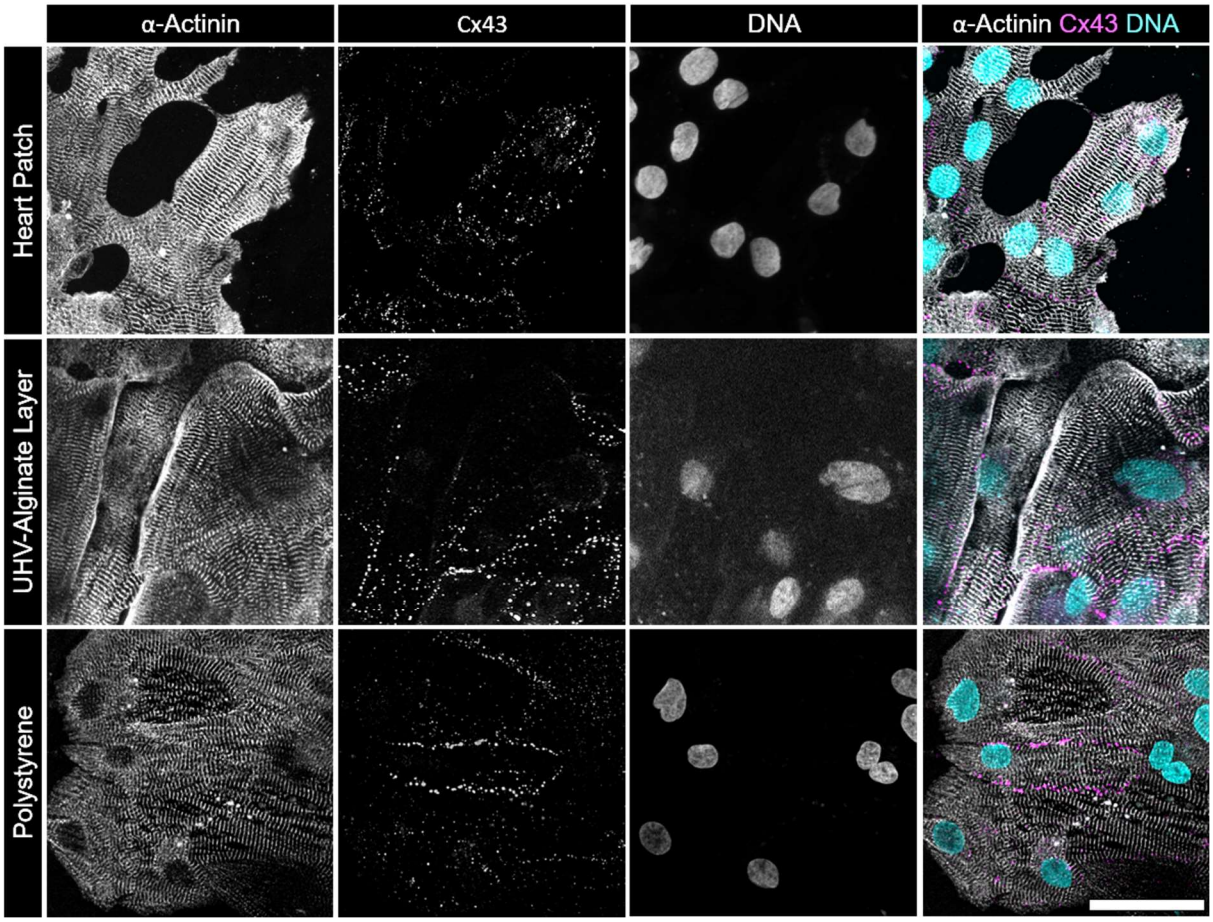

Figure 4.18 Representative images of cytoskeletal arrangements of cardiac cells grown on Heart Patches, fixed UHV-alginate scaffolds and polystyrene.
Immunocytochemistry against α-actinin (grey) and Cx43 (magenta) with labelled DNA (cyan) shows highly organized sarcomeres of cardiomyocytes grown on Heart Patches. The sarcomeric alignment is less organized in cells grown on fixed scaffolds. On PS, cells exhibit multidirectional sarcomeric structures. Connexin43 is functionally integrated in all samples at cell boundaries. White scale bar represents 50µm.

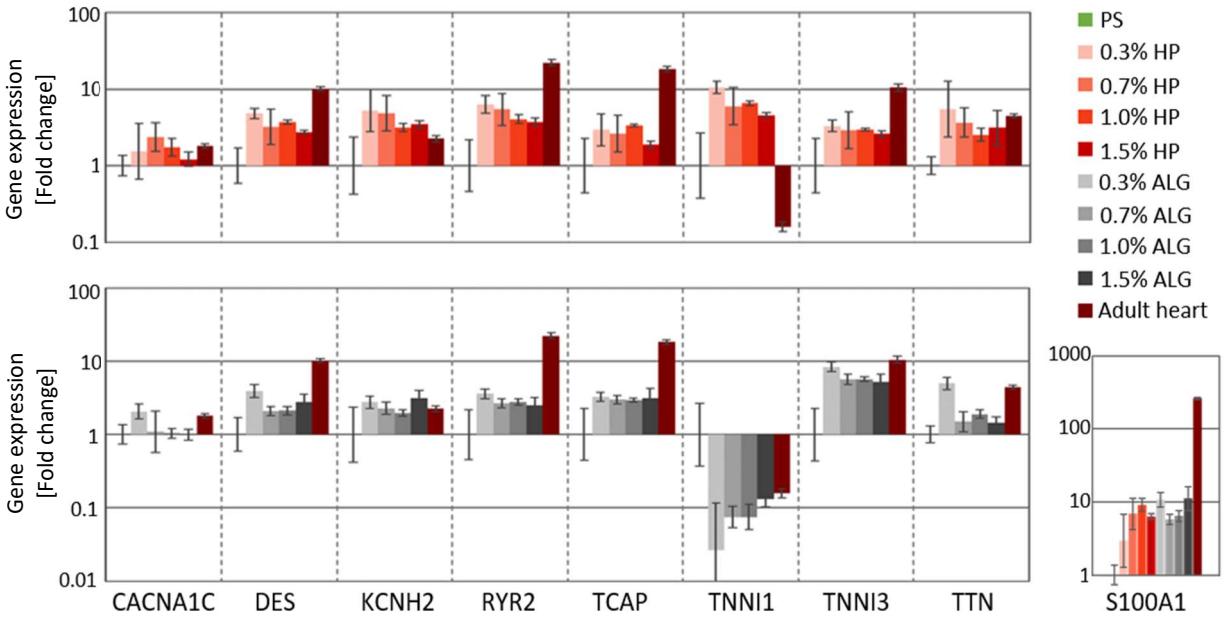

Figure 4.19 Gene expression analysis of cells cultured on Heart Patches and fixed UHV-alginate scaffolds with differing stiffness.
Gene expression analysis via qPCR of COR.4U cells grown for 8 weeks on UHV-alginate layers (ALG, grey bars), Heart Patches (HP, red bars) and PS (green) in comparison to the adult human myocardium (dark red). The data was normalized against the geometric mean of two reference genes (GAPDH and HPRT1) and the PS condition (always the first position in the bar plots). The sarcomere-associated genes Desmin (abbr. DES), Titin-cap (abbr. TCAP), Titin (abbr. TTN), slow skeletal troponin I (abbr. TNNI1) and cardiac troponin I (abbr. TNNI3) were analysed. Additionally, the calcium-handling protein S100A1 and the ion channels CACNA1C, KCNH2 and the ryanodine receptor 2 (abbr. RYR) were analysed. Data is shown as fold change (x-axis) compared to the PS condition. Error bars indicate 95% confidence interval.

In the PS group, Cx43 was not present in all cells, but when seen; it was functionally integrated at the cell boundaries as well. With no visible differences concerning its localization in the cells among all tested conditions.

To gain a better overview of the influence of contractile substrates on hPSC-CM maturity, gene expression profiling was conducted. In this work, all abbreviated genes are italicized (*e.g. TNNI3*), whereas abbreviations of proteins are not italicized (*e.g.* TNNI3). The selected genes encompassed cytoskeleton-associated genes (*DES, TCAP, TNNi1, Tnni3* and *TTN*) and genes responsible for ion channels (*CACNA1C, KCNH2, RYR2* and *S100A1*) (Figure 4.19). The clinically relevant, pore-forming, alpha-1C subunit of the voltage-gated calcium channel (abbr. *CACNA1C*) was only 1.80-fold higher expressed in the adult human myocardium compared to the PS condition. Accordingly, cell cultures on UHV-alginates did not translate into large *CACNA1C* expression differences, albeit a small, stiffness dependent trend in the HP condition was observable between 0.7% (2.06-fold), 1.0% (1.75-fold) and 1.5% (1.22-fold) concentrations. The 0.3% HP condition exhibited a 1.54-fold *CACNA1C* expression, whereas the 0.3%, 0.7%, 1.0% and 1.5% UHV-alginate layers exhibited 2.06-fold, 1.08-fold, 1.04-fold and 1.00-fold expressions, respectively. *CACNA1C* expression in the adult heart sample was 1.80-fold elevated compared to the PS group.

For the potassium voltage-gated channel subfamily H member 2 gene (abbr. *KCNH2*) an increased expression was found in 0.3% (2.75-fold), 0.7% (2.29-fold), 1.0% (1.97-fold) and 1.5% (3.15-fold) UHV-alginate layers and, with values of 5.25-fold (0.3%), 4.80-fold (0.7%), 3.15-fold (1.0%) and 3.46-fold (1.5%), an even further increase was detected in the HP conditions. Expression in the adult heart was 2.26-fold higher than in the PS group. Ryanodine receptor 2 gene (abbr. *RYR2)* and S100 calcium binding protein A1 gene (abbr. *S100A1*), both responsible for calcium handling proteins, were expressed more on UHV-alginate, although expression levels of the adult myocardium were not reached. For *RYR2*, the mRNA abundance was 6.33-fold (0.3%), 5.43-fold (0.7%), 4.04-fold (1.0%), and 3.73-fold (1.5%) elevated on the HPs and 3.60-fold (0.3%), 2.68-fold (0.7%), 2.77-fold (1.0%) and 2.51-fold (1.5%) on the UHV-alginate layers. *S100A1* expression was 2.95-fold (0.3%), 6.89-fold (0.7%), 9.18-fold (1.0%) and 6.35-fold (1.5%) elevated on the HPs and 10.68-fold (0.3%), 5.81-fold (0.7%), 6.48-fold (1.0%) and 11.11-fold (1.5%) increased on fixed UHV-alginate layers. The expression of *RYR2* and *S100A1* in the adult human heart was 22.16-fold and 261.84-fold, respectively. Cells on the HPs exhibited a 4.82-fold (0.3%), 3.22-fold (0.7%), 3.70-fold (1.0%) and 2.74-fold (1.5%) higher *DESMIN* expression, whereas values of 3.89-fold (0.3%), 2.10-fold (0.7%), 2.12-fold (1.0%) and 2.80-fold (1.5%) were estimated for the UHV-alginate layer conditions. *TCAP* expression was elevated by 2.96-fold (0.3%), 2.62-fold (0.7%), 3.35-fold (1.0%) and 1.87-fold (1.5%) on the HPs and 3.27-fold (0.3%), 2.99-fold (0.7%), 2.97-fold (1.0%) and 3.14-fold (1.5%) increased on fixed UHV-alginate layers. *TTN* expression was increased on the 0.3% (5.51-fold), 0.7% (3.67-fold), 1.0% (2.54-fold) and 1.5% (3.13) HPs and on the 0.3% (4.96-fold), 0.7% (1.50-fold), 1.0% (1.90-fold) and 1.5% (1.45-fold) layers as well. The adult heart expression of *DES, TCAP* and *TTN* was 10.15-fold, 18.26-fold and 4.43-fold higher, respectively. *TNNI1* was upregulated in the HP group compared to the PS condition and was determined to be 10.49-fold (0.3%), 5.97-fold (0.7%), 6.55-fold (1.0%) and 4.59-fold (1.5%) higher. Contrary, the relative gene expression of *TNNI1* in the 0.3% (0.03-fold), 0.7% (0.08-fold), 1.0% (0.08-fold), and 1.5% (0.15-fold) UHV-alginate layer groups was found be significantly downregulated. *TNNI3* was upregulated in both systems with estimated values of 3.30-fold (0.3%), 2.90-fold (0.7%), 2.98-fold (1.0%) and 2.60-fold (1.5%) for the HPs and 8.39-fold (0.3%),

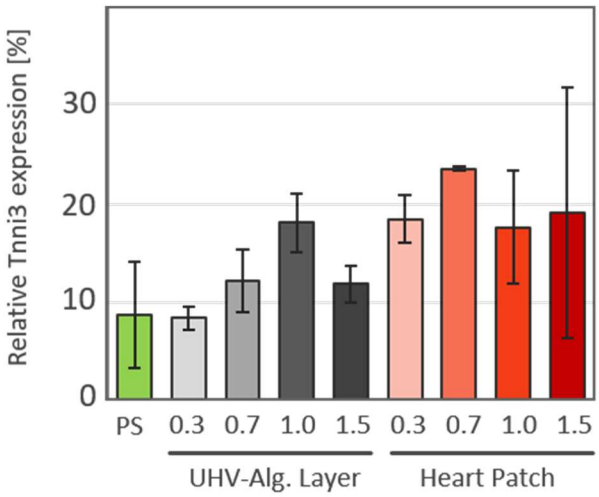

Figure 4.20 Quantitative analysis of relative Tnni3 abundance by the means of western blotting.
Analysis of relative Tnni3 content is based on the cardiac troponin I proportion of both cardiac (Tnni3) and slow skeletal troponin I (Tnni1) and reveals robust quantities of Tnni3 in hPSC-CMs grown on polystyrene (PS) or UHV-alginate layers and Heart Patches of 0.3%, 0.7%, 1.0% and 1.5% UHV-alginate solution. Results are based on two biological replicates, except PS (n=3) and 1.0% UHV-alginate layer (n=1). Data presented as mean ± SD.

5.67-fold (0.7%), 5.68-fold (1.0%) and 5.20-fold (1.5%) for the UHV-alginate layer groups. The adult heart sample showed a downregulation of *TNNI1* (0.16-fold) and *TNNI3* (10.50-fold).

A stiffness related trend is visible in both cases, but the correlation of *TNNI1* with the substrate stiffness is inverted between the two conditions. *TNNI3* expression is approximately two-fold higher in cells grown on UHV-alginate layer compared to the Heart Patch conditions. The high discrepancy concerning *TNNI1* and *TNNI3* expression led to the analysis of TNNI1 and TNNI3 protein abundance (protein abbreviations are not italicized) by the means of western blotting (Figure 4.20). The protein quantification, based on the relative ratio of cardiac troponin I (abbr. cTnI) and slow skeletal troponin I (abbr. ssTnI) reveals a robust occurrence of cTnI in all samples. On polystyrene, cTnI constituted 8.8 ± 5.4% of total troponin I. On UHV-alginate layers, cTnI proportion was lowest in the 0.3% and 1.5% conditions with 9.6 ± 0.4% and 11.9 ± 1.3% respectively. 0.7% ALG layers led to 15.2 ± 0.77% cardiac troponin I and the maximum was achieved on 1.0% layers (20.2%). The Heart Patch generally produced higher values, but also higher variances compared to layers. 0.3% and 0.7% HP resulted in 18.5 ± 1.7% and 23.6 ± 0.1% respectively, while 1.0% and 1.5% led to similar results, with 17.7 ± 4.1% and 19.1 ± 9.0% cardiac troponin I.

In conclusion, the gene expression analysis revealed a higher expression of cytoskeletal associated genes in all conditions with contractile substrates. Additionally, the gene expression pattern of calcium handling proteins resembles more the adult myocardium. The stark contrast of *TNNI1* expression between layers and HP was carried over to the protein level as suggested by western blotting, which revealed a higher cardiac troponin I contribution to the total troponin I content in Heart Patches. Drug screenings rely on the electrophysiological response of hPSC-CMs to the tested compounds. Therefore, a proof of concept experiment using multi electrode arrays was conducted to proof the feasibility of such measurements.

4.4.3 Assessment of the feasibility of electrophysiological measurements and long-term cultures of hPSC-CMs on the Heart Patch

The Heart Patch offers hPSC-CMs another grade of freedom concerning its synchronous contraction movement and the following return to its resting state. While both, calcium handling analysis and gene expression profiling, represent quantitative and robust read-outs, electrophysiological characterization is still regarded the gold standard. The design and functionality of three-dimensional scaffolds makes these analyses generally difficult to conduct particularly when it exhibits such a wide movement range. Nevertheless, a proof of concept study was conducted to evaluate the possibility to derive quantitative data using multi electrode arrays (abbr. MEA). First, it was feasible to assess the electric potential of hPSC-CMs grown on the HP as shown in Figure 4.21, C and D. Both, the spreading of the electrical wave as well as the synchronous nature of the contractions on both samples was observable using the multi electrode array chip (Figure 4.21 C, D). The measurement revealed an average electrical wave velocity of 1.47 ± 1.07cm/s for the HP compared to 3.01 ± 0.77cm/s for hPSC-CMs grown on the

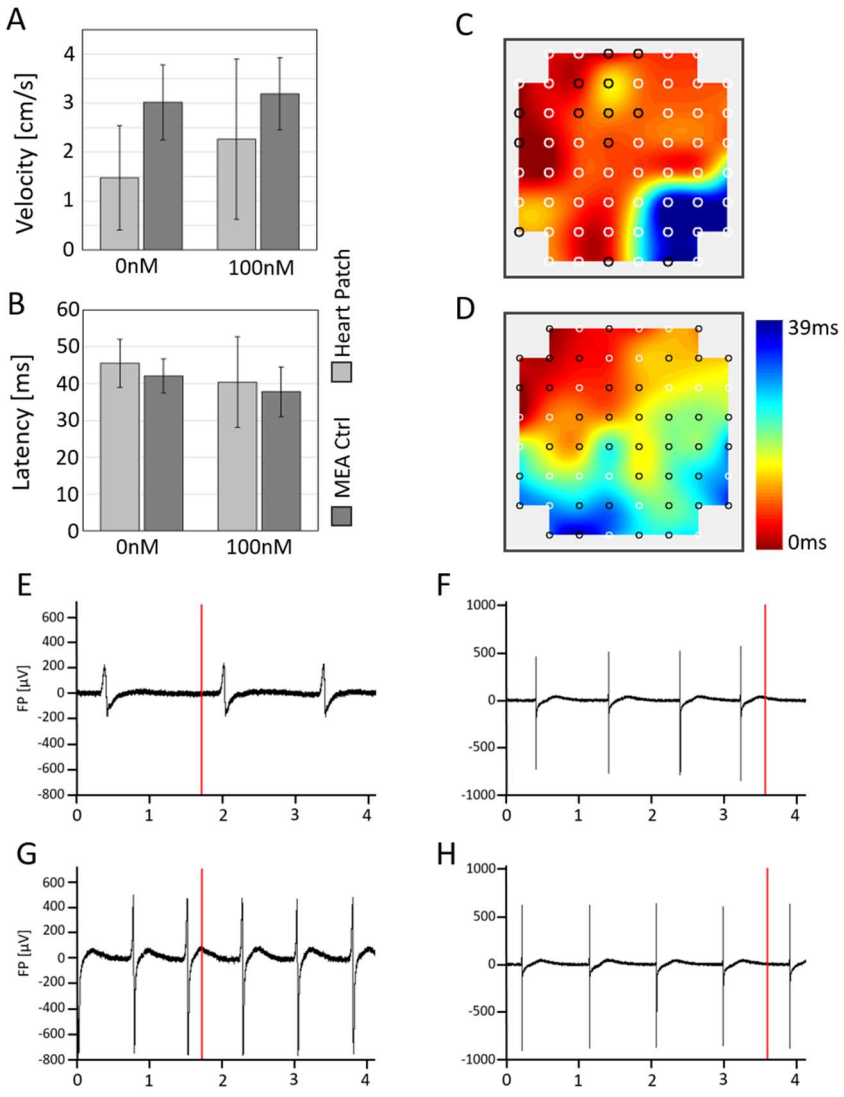

Figure 4.21 Electrophysiological characterisation of hPSC-CMs cultured on the Heart Patch.

Electrophysiological assessment of hPSC-CMs grown on the Heart Patch was possible and allowed derivation of electrophysiological data. The averaged velocity and latency of the depolarisation is given in A and B (data presented as mean±SD). n=118 (velocity; A) and n=145 (latency; B).

Respective heat maps in relation to the electrodes (based on the latency) is given for the HP (C) and the control group (D). Respective field potential waves without and with isoprenaline stimulation are given for the HP (E, F) and the control (G, H) conditions.

MEA chip directly (MEA Ctrl) (Figure 4.21, A). Upon stimulation with 100nM isoprenaline the velocity rose in the HP condition to 2.27 ± 1.64cm/s, while in the MEA Ctrl the velocity increased slightly to 3.12 ± 0.74cm/s. The latency was similar in both conditions with 45.5 ± 6.5ms and 42.1 ± 4.6ms, for HP and MEA Ctrl respectively. Both conditions experienced a shortening of the latency upon beta-adrenergic stimulation, leading to a latency of 41.4 ± 12.3ms (HP) and 37.8 ± 6.7ms (MEA Ctrl) (Figure 4.21, B). The field potential rise upon depolarization was faster on the MEA Ctrl samples (Figure 4.21, F and H), but the relative change in amplitude was higher in the HP samples (Figure 4.21, E and G). In the MEA Ctrl condition, the action potentials were also shorter compared to the HP condition.

Another important factor concerning cardiac *in vitro* models is the culture duration, which is often limited in classical polystyrene-based cultures. In this work, a long-term experiment has been conducted in concert with the first application of scaffolds with alternating stiffness to assess the feasibility of long culture times using the HP system.Long-term cultures can offer crucial insight into slow biological processes or the effect of long compound exposures. Often they are limited by the culture systems, which are themselves not stable for such long times or which cannot sustain the biological material over such long periods. In this experiment, scaffolds consisting of single (either 0.3% or 1.5%) or hybrid biopolymer formulae have been used to present stiffness gradients to the hPSC-CMs over the course of several months. The hybrid HPs consisted of alternatively printed struts of 0.3% and 1.5% UHV-alginate (0.3%/1.5% HP). The hPSC-CMs were viable over the course of 6 months until the end of the experiment, as proven by their ability to exert macro-contractions (as seen in Figure 4.17). The scaffolds were subject to deformations in their relaxing state (see Figure 4.22, 0.3% condition) and changed their contraction pattern over time. In the 0.3% condition, the HPs were rolled and the major contraction direction was along the longitudinal axis (Figure 4.22). In the 1.5% condition, the HP made one fold and was bended during the contractions along that deformation axis (see

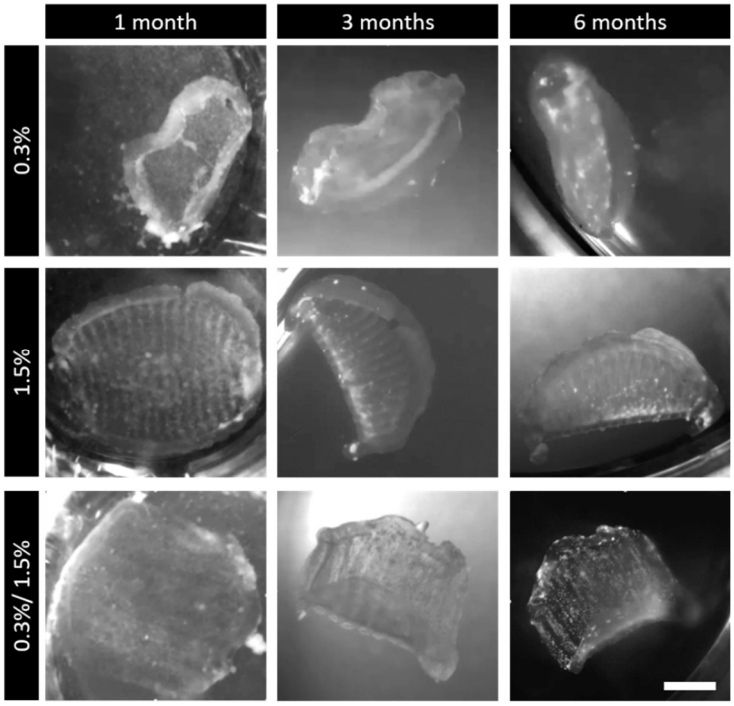

Figure 4.22 Long-term culture of hPSC-CMs is feasible on the HP. HPs, produced with either constant hydrogel concentrations or printing an alternating pattern of low and high concentrated UHV-alginate solutions were used as a long-term culture substrate for hPSC-CMs After six months the deformations correlated with substrate stiffness. White scale bar represents 200µm.

also Figure 5.11). The hybrid scaffold exhibited a complex contraction pattern, which changed over the course of the experiment. In the first month, a mainly compressive movement of the scaffold volume with no to little scaffold bending was observed. Over the course of the experiment one side started to perform a bending movement, while the other part of the scaffold sustained the compressing movement.

After four months, the macro contractions of the hybrid scaffolds broke down completely with no observable macro contractions, while the other two conditions sustained their contraction pattern. The beating frequency also changed during the experiment. While the 0.3% (25.7 ± 0 bpm), 1.5% (24.9 ± 3.2bpm) and 0.3%/1.5% (22.3 ± 0 bpm) conditions behaved similarly after 1 month, they differed significantly later on. After 3 months, the 0.3% and 1.5% HPs contracted with 15.9 ± 0.4bpm and 2.6 ± 1.1bpm respectively, while the 0.3%/1.5% condition exhibited no macro contractions. After 6 months, the 0.3% conditions contracted with 3.2 bpm, while the 1.5% condition exhibited a beating rate of 11.1 ± 2.1bpm.

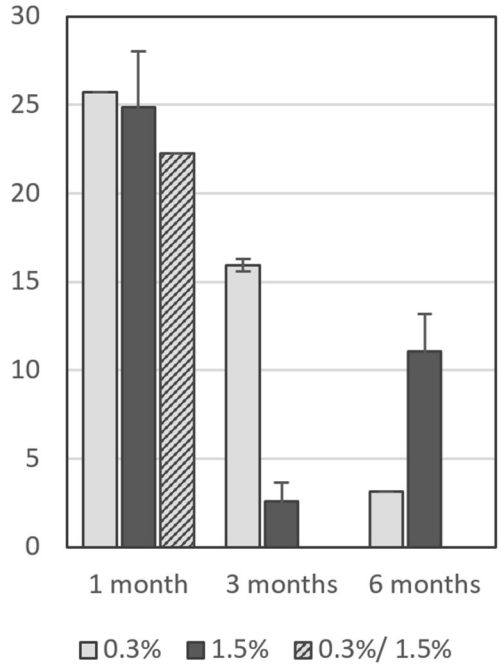

Figure 4.23 Macro contractions are longer sustained on scaffolds with uniform stiffness. Uniform stiff HPs, produced with either 0.3% or 1.5% UHV-alginate support macro contraction for a minimum of six months, whereas the HPs structured with alternating hydrogel concentrations showed no macro contractions after three months. Data shown as mean ± SEM. Data from two replicates.

The presented work investigated the generation of cardiomyocytes from human induced pluripotent stem cells in a small-scale bioreactor. It was shown that the differentiation was highly efficient and number of produced cells per vessel was in a range relevant for many applications. Furthermore, three enzymes were comparatively analysed concerning their dissociation potential of cardiac spheroids. A comparative analysis revealed that Papain, an enzyme traditionally used for the dissociation of primary neural tissue, was highly efficient in digesting cardiac spheroids with high resulting viability and functionality of the cardiac cells. The resulting workflow from this study represents a highly efficient and robust method to derive hiPSC-CMs in suspension-based bioreactors, which can be easily transferred into an application for the industrial generation of cardiac cell models.

Furthermore, an *in vitro* system using an optical-based method and fixed UHV-alginate scaffolds for the quantitative analysis of contractile behaviour of hPSC-CMs was presented. The correlation with calcium transient data showed chronotropic and inotropic behaviour in hPSC-CMs and demonstrated calcium transient independent contractile force increase upon beta-adrenergic stimulation. While the conducted characterization needs further emphasis, the presented method is, to our knowledge, the first method, which allows for the

quantification of the contractile action of cardiac tissue models in an experimental setup, that is also usable to perform standardized calcium flux measurements.

A novel 3D printing method, based on the immediate freezing of biopolymer scaffolds was developed and utilized to structure low concentrated UHV-alginate formulae in a three-dimensional manner. The major resulting advantage of this method is the possibility to 3D print inks with vastly differing viscosities and being able to integrate these in the same 3D printing process and ultimately in the same scaffold without mixing the different concentrations.

Biologically, these UHV-alginate scaffolds, due to their contractile nature, allowed for a higher movement range compared to the stiff polystyrene plastic ware used in conventional cell cultures. The assessment of the cytoskeletal arrangements, in concert with gene expression profiling revealed a higher maturity of the hPSC-CMs when grown on UHV-alginate scaffolds. Western blotting did not support the strong difference in the expression of immaturity-associated TNNI1, suggesting a higher proportion of cardiac troponin I instead. Particularly displacement analysis and the troponin I quantification showed a correlation with the substrate stiffness indicating an effect of the stiffness on cytoskeletal arrangements in cardiac cells and on the maturation thereof. Additionally, long-term cultures over the course of 8 months were conducted and showed sustained macro contractions throughout the experiment. Up to date, such long-term cultures have not been performed without passaging, suggesting an exceptional microenvironment for cardiac cells and unfolding many possibilities for the analysis of long-term processes, such as progression towards heart failure, aging and hypertrophic myopathies.

5 DISCUSSION

The generation of cardiomyocytes from human induced pluripotent stem cells for therapeutic applications and disease modelling requires large numbers of cells. The reason for this is rooted in the creation of patient-specific cell lines of which every single cell line needs to be expanded and differentiated. Furthermore, drug discovery screenings encompass hundreds of compounds and each of these compounds needs biological as well as technical replicates to allow robust conclusions. Because the reprogramming step still suffers from low efficiencies, it is mandatory to multiply the cell numbers downstream, either at the pluripotent stage or after differentiation. Furthermore, the differentiation method and the cultivation platform must be carefully chosen, because both have significant influence on the cost, workload and the number of produced cells. Two-dimensional cell culture vessels offer a reproducible environment, but possess a low cell number to medium volume ratio and take up a lot of lab space. Furthermore, three-dimensional, cellular spheroids represent a system with significant advantages, especially the favourable microenvironment and the closer resemblance to the *in vivo* situation. The hanging drop method, a three-dimensional cell culture method based on the culture of cells in hanging drops leads to such spheroids due to the absence of a culture surface. The major disadvantage for the hanging drop method is the time consuming and tedious medium changes. To overcome the laborious creation of high cell numbers in hanging drops, a complete workflow for the production of hiPSC-CMs using a highly efficient differentiation protocol in concert with a small-scale bioreactor was envisioned.

Precisely timed modulation of the WNT pathway leads to a robust induction of the cardiac lineage in a suspension-based bioreactor

Since the discovery of hiPSCs, patient-specific cellular models can be readily produced. But the laborious expansion and the consecutive cardiac differentiation still lack behind the demand and limit the deployment in daily clinical practice. In addition, drug screenings require even larger cell numbers compared to the projected 20-60 million cells per therapeutic dose. Since more efficient differentiation protocols are being developed and are readily available the major limitation for the production of high cell numbers with low cost is the production platform (Freund et al., 2009; Kadari et al., 2015; Tran et al., 2009; Zhang et al., 2015). Therefore, the workload and economic burden represents a major roadblock for a broad use of hiPSC-CMs.

Bioreactors enable the production of relevant cell numbers with decreased workload and cost. Particularly suspension-based bioreactors seem advantageous with the propensity to upscaling and homogeneous nutrient supply. Several studies proved the feasibility of hiPSC maintenance in stirred bioreactors (Kwok et al., 2018). For a broad application of hiPSCs a

robust workflow had to be designed that enabled the production of iPSC-derived cardiomyocytes with high differentiation efficiency and low workload.

In this work, the differentiation protocol by Zhang et al. was adapted to a suspension-based bioreactor, the BioLevitator (abbr. BL). To reveal cell line dependent discrepancies, two different hiPSC lines, namely IBMT1 and UKBI005, were used. As seen in Figure 4.1, A, both cell lines were able to form viable spheroids with a final diameter of 200µm (IBMT1) and 250µm (UKBi005). The spheroid diameter is an important factor, because the diffusion limit for nutrients and oxygen in tissues is approx. 300µm and it can be hypothesized that it is even lower when such active and energy demanding cells, as the cardiomyocytes are, are being cultured. Thus, the initial setting provided suitable sized cardiac spheroids. It was expected that the increase is slowed down by the end of the seven day interval, due to the lower proliferation on cardiomyocytes compared to undifferentiated iPSCs. In the cardiac spheroids, structural changes between day 3 and 7 are visible and could explain the gain in size with only limited proliferation. The onset of contractions could cause such structural reorganisation, but further studies have to be conducted to clarify the gain in size in detail. To assess the cardiac induction success gene expression profiling was conducted.

In both culture methods, the hanging drop as well as the bioreactor, an effective loss of pluripotency has been observed at day 2 as indicated by the downregulation of *OCT3/4* and *SOX2* (Figure 4.1, C). However, in the BL the loss of pluripotency was more reliable compared to the high variability in the HD. It can be assumed that in the BL the differentiation inducing factors are distributed more homogenously, particularly the transport into the spheroid volume is more efficient and thus the differentiation is induced reliably. It can be hypothesized that in the HD, the small drop volume of 40µl enables a fast distribution of the factors in the medium; therefore, the main reason for this discrepancy must be rooted in the diffusion rate into the spheroids.

Successful transition into the mesendodermal stage was indicated by expression of *EOMES* and *T*. Again, day 1 in the HD showed higher variability with some biological replicates exhibiting the maximum already in day 1 and some in day 2. This is the direct consequence of the variable loss of pluripotency in HD. The higher expression of *EOMES* and *T* suggests an intensified commitment towards the primitive mesendodermal stage, either qualitatively or quantitatively. *MESP1* as an early cardiac- specific marker was significantly higher expressed in the BL, indicating a favourable environment for the cardiac induction. Re-expression of *MESP1* was detected at day 7 in both setups, but the significance is not clear. The genetic background and the proteome at that stage is already typical for the cardiac niche with the vast majority of cells showing functional integration of α-actinin and exhibiting spontaneous contractions. From the qPCR data it cannot be concluded, that a small subset of cells with high re-expression of *MESP1* exists or if low expression of *MESP1* happens in all cells. *MESP1* is known to be expressed in cardiac progenitors and in early cardiomyocytes, thus, developmental processes inducing *MESP1* expression at different time points could be

responsible for the re-expression (Beqqali et al., 2006; Bondue et al., 2010, 2008; Liu et al., 2013; Paige et al., 2015).

It can be hypothesized that the higher variance of gene expression in the HD slightly effects expression of downstream genes as indicated by the lower expression of *EOMES* and *MESP1* and the timing of their maximum expression. Nevertheless, the effective downregulation and avoidance of transient expressions of intermediate stage genes is more supportive of a robust cardiac differentiation process than gene expression differences of two folds and smaller. ISL1 induction is comparable between the two systems and a transient, ongoing expression is established in both. This transient expression, typical for a premature, proliferative cardiomyocyte population, has been observed in previous studies and is seen as a robust indicator of cardiac differentiation (Cai et al., 2003; Lin et al., 2006; Quaranta et al., 2018). The progressive reduction in ISL1 expression can be explained by the ongoing maturation of cardiomyocytes (Quaranta et al., 2018). The expression of *MYH7* and *TNNT2*, which encode for the cardiac specific proteins myosin heavy chain 7 and cardiac troponin T, are direct indicators of a successful cardiomyocyte differentiation (Anderson et al., 1991; Colegrave et al., 2014; Sehnert et al., 2002; Witjas-Paalberends et al., 2013). The expression of *TNNT2* and *MYH7* was elevated in the BL and experienced a steady increase compared to the HD condition. This increased expression of cardiac-specific genes (*MYH7* and *TNNT2*) in the BL suggests that cells cultured in the BL showed higher commitment for cardiomyocyte differentiation. It can be excluded that the difference in loss of pluripotency timing transcendent through the whole differentiation, because the *EOMES*, *T* and *MESP1* showed comparable timings. Thus, it can be assumed that the dynamic environment in the BL leads to an enhanced commitment towards the cardiac fate. Possible factors could be the mechanical stimulus, faster diffusion rates or the availability of nutrients and oxygen. The hypothesis that diffusion into the spheroids is enhanced in the BL is also reflected by the more homogenous α-actinin distribution throughout the spheroid volume (Figure 4.1, D).

Also, Zhang *et al*. reported an approximately two-fold higher expression of cardiac specific genes in three-dimensional cell cultures compared to two-dimensional systems (Zhang et al., 2015). The two-fold difference concerning *TNNT2* and *MYH7* expression between the dynamic and static environment in this work could indicate a further enhancement of the cardiac induction in the BioLevitator™ compared to the three-dimensional static approaches used in this work and by Zhang *et al*. Nevertheless, the comparability of qPCR data between different studies is limited, particularly the use of different primer sets and RNA extraction protocols makes further experiments necessary.

Gene expression analysis via qPCR is a method designated for the detection of relative differences in gene expression and the variance thereof; it does not allow conclusions on individual cells and subpopulations, because it always represents the average gene expression. To investigate if static or dynamic culture led to different proportions of cardiomyocytes and to spot differences in cytoskeletal organization, immunocytochemistry directed against α-actinin was used to assess the ratio of cardiomyocytes to non-

cardiomyocytes and to reveal differences in cytoskeletal arrangements. α-actinin is known to be essential in sarcomere formation, where it incorporates into the z-disc and serves as a scaffold for many proteins, *e.g.* titin, desmin, vinculin and actin (Sanger et al., 2010). In the BL a higher abundance and a more homogeneous α-actinin distribution in cardiac spheroids was found (Figure 4.1, D). This qualitative difference was only mildly reflected in the number of α-actinin-positive cells, but indicates a more mature cytoskeletal machinery.

However, α-actinin, needed for sarcomere formation, is very early observed in cardiomyocytes. Desmin and Cx43 on the contrary, are observed later and are associated with cardiomyocyte maturity (Delva et al., 2009; McCain et al., 2012). They are both needed for the cooperative action of cardiomyocytes and are relevant for the formation of functional tissues (Herron et al., 2016; Scuderi et al., 2017). These later staged indicators have a clearly increased abundance in the BL, suggesting that the major advantage of this system is not the differentiation efficiency, although it is slightly increased by means of α-actinin abundance, but that it fosters collective action and tissue formation more. This could translate into shorter culture periods until physiological relevance or a robust end-point for pharmacological screenings is reached. Multicellular cardiac aggregates have been shown to enhance the translational potential and based on the presented data it can be assumed that the derivation of such micro tissues would benefit from an dynamic environment (as seen in the BL), which fosters intercellular action (Ravenscroft et al., 2016).

Noteworthy is also the difference concerning differentiation efficiency between the presented setup and the one used by Zhang et al. The efficiency of cardiomyocyte generation between two- and three-dimensional cultures, which resulted in a higher output in 2D (80-95%) compared to 3D (50-75%). The three-dimensional culture applied by Zhang et al. is also different from the method used in this work, in that not hanging drop multiwell plates were used, but 96 well V-bottom plates with 4000-8000 seeded cells per well. Additionally, a centrifugal step (400g) had been used to concentrate the cells in the wells. Therefore, the varying cardiac induction efficiencies could be caused by the different culture methods or the compression of the spheroids due to the centrifugation. This finding also supports the above -mentioned hypothesis that the more efficient differentiation in the BL is mediated through a better access to nutrients, oxygen and small molecules.

In conclusion, the adaption of the protocol devised by Zhang et al. led to a highly efficient and robust cardiac lineage commitment with the dynamic environment facilitating intercellular action and fostering sarcomere maturation. Additionally, as long as functional vessels are not readily available in three-dimensional cardiac spheroids, there is a need to develop strategies to overcome the concentration gradients between the spheroid surface and core. Therefore, culture systems minimizing the heterogeneity are will be crucial in the production

Furthermore, the BioLevitator™ offers a higher cell output for the less hands on time compared to conventional two dimensional cell culture methods. The timesaving regarding media changes is particularly crucial, when compared to HD plates, where the media of every drop has to be changed twice. Only 50% of the media in one drop can be aspirated at a time,

otherwise the spheroids would be removed as well. 20-60 million cells per cardiac induction and per Levitube were generated in the BioLevitator™. Between 50.000 and 150.000 cardiac cells were produced per 96 well hanging drop plate. Thus, cardiac induction in the BioLevitator™ produces sufficient cell numbers for small to medium sized toxicity screenings and is in the range of therapeutic doses (Schächinger et al., 2004).

The majority of assays, as well as the therapeutic doses, rely on single cell suspensions. They serve as highly comparable starting points and the suspension also make cell counting and concentration determination easier and more reliable. One disadvantage of three-dimensional cardiac spheroids is their progressive resistance to enzymatic digestion to achieve a single cell solution. The higher amount of desmin- and Cx43-positive cells in the BioLevitator adversely affects this even more. The difficulty of cardiac tissue dissociation also lies in their force generating nature, which needs robust cell-cell and cell-matrix connections. The dissociation with aggressive enzymes is diametric, as they also affect cell viability, membrane integrity and the presentation of proteins at the membrane surface through unspecific interaction sites. An effective enzyme must balance the task of acting unspecific enough to achieve a high dissociation rate, while minimizing negative effects on the cells.

Papain-based dissociation of cardiac spheroids leads to a high number of viable single cells

A robust production of cardiomyocytes and their use in highly sensitive assays or as a therapeutic compound fundamentally relies on a mild and effective dissociation to preserve cell vitality and maintain the integrity of the cell membrane. Cardiac spheroids are a complex mixture of cells interacting with each other, through connexins, cadherins and desmins, and with the extracellular matrix through integrins (Figure 5.1). The extracellular matrix of the heart consists of glycoproteins (*e.g.* collagens, elastins, fibronectin and laminins), glycosaminoglycans (hyaluronic acid and heparan sulphate) and proteoglycans (*e.g.* perlecan and aggrin) (Brown, 2005; Rienks et al., 2014).

A dissociation enzyme must digest relevant cell-cell (cadherins; Figure 5.1) and matrix-cell connections (integrins; Figure 5.1), while exhibiting high specificity to avoid damaging the cells. Due to the three-dimensional nature of the spheroids, a diffusion-based gradient will lead to longer exposure times with higher concentrations of the enzymes presented to the outer cells than cells in the inner compartment. In this work, TrypLE, Accutase and Papain were assessed in a comparative analysis and their dissociation potential and possible effects on cell viability were evaluated. TrypLE and Accutase are two commonly used commercially available dissociation mixtures of enzymes, which are widely used for the passage of different cell types in conventional two-dimensional cell cultures. Both exhibit proteolytic activity but in contrast to TrypLE, Accutase and papain additionally exhibit collagenolytic activity. Papain has been chosen due to its traditional use on primary tissue, particularly neurons with long axonal projections and heart tissue. After digestion, cell viability was assessed and papain was found to produce significantly more singlets in combination with a higher cell viability

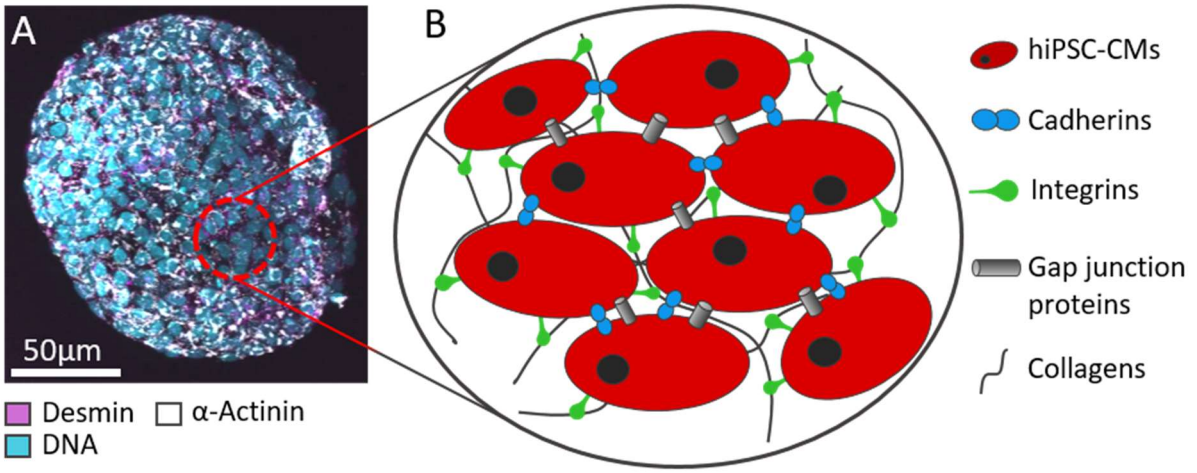

Figure 5.1 Cardiac spheroids represent a complex network of cells and extracellular matrix components Representative image of a three dimensional cardiac spheroid, stained with immunocytochemistry against desmin (magenta) and α-actinin (grey) with labelled DNA (cyan) (A). A schematic of the complex network of cell-cell interactions (based on cadherins and gap junction proteins) and cell-extracellular matrix interactions through integrins is given in B.

compared to Accutase. Although statistical testing did not show any significant difference between TrypLE and papain, a clear trend is visible under TrypLE treatment suggesting a slightly lower viability and a lower proportion of single cells compared to papain.

The Nucleocounter offers a fast and direct read-out, but flow cytometry analysis produces additional information and allows to discriminate between clumps (≤ 40µm), single cells and cell debris when gating the forward scatter (abbr. FSC) and sideward scatter (abbr. SSC) (Figure 4.2, D). Papain produced the biggest fraction of single cells and the smallest fraction of ungated events, debris and cell clusters. Calcein-AM is a cell permeant dye, which is hydrolysed to fluorescent calcein upon exposure to intracellular esterases. These esterases are pH dependent and membrane destruction leads to inhibition, thus, calcein-AM stays in its non-fluorescent form.

Using this dual staining, transitional states are also detected that could be either double positive or double negative. These intermediate stages presumably represent dead cells, which in case of the double positive findings could maintain a physiological pH in the cytoplasm or in some compartments. Double negative cells have not accumulated enough PI and were not able to hydrolyse enough calcein to produce a signal. It can be assumed that these signals represent apoptotic cells with enough membrane integrity to inhibit PI uptake, but with such a distorted homeostasis, that calcein cannot be effectively hydrolysed or cellular debris where neither of the two fluorophores can accumulate.

The viability analysis by flow cytometry verified the previous experiment in which papain application resulted in the biggest proportion of viable cells and Accutase produced the lowest amount of viable cells. Additionally, papain also led to the smallest fraction of transitional states (double negative or positive), further indicating a gentler dissociation.

As stated above enzymes must be able to diffuse efficiently into the spheroids. However, papain and trypsin are of comparable size with estimated sizes below 30kDa. Apart from the size-based diffusion, enzymes possess similar hydrophobicity and charge on their surface. Thus, the diffusion rate is assumingly not the reason for the different outcomes. A strong influence on enzyme performance is exerted by the organisation of the reactive space and the resulting specificity. The mode of action and specificity of proteolytic enzymes is defined by the composition of their active centre. While papain is a cysteine peptidase, trypsin is a serine peptidase. It is known that trypsin digestion affects membrane surface proteins, *i.e.* cadherins, and proteins of the cytoskeleton (Huang et al., 2010a). Although this was shown in cancer cells, the affected tropomyosin is essential for sarcomere formation in cardiomyocytes. TrypLE is shown to be more specific and gentler than traditional porcine trypsin. Nevertheless, it can be hypothesized that cardiac specific cell-cell complexes, *i.e.* connexins, are still inefficiently digested and adverse effects of TrypLE digestion on sarcomere integrity assumingly causes the diminished cell viability. Papain is known for its low specificity, but it maintains a high cell fidelity as it was shown in many in-vivo applications ranging from treating allergic disorders of the gut to the regeneration of sport induced injuries (Ezekiel Amri et al., 2012; Kimmel et al., 1954; Trickett, 1964). Furthermore, Papain was efficient in digesting tight junction proteins between keratinocytes, which are known for their strong intercellular connections (Stremnitzer et al., 2015). It is known that maturation also fosters dissociation resistance, due to the higher frequency of cell-cell interactions, *e.g.* Cx43, cytoskeletal anchors (desmin), and cell-matrix interactions (Burridge et al., 2015). Therefore, a comparative analysis of 8-day and 15-day-old cardiac spheroids was conducted to assess potential differences hereby. Indeed, older spheroids were more difficult to dissociate as shown in Figure 4.3. In accordance with the literature, Papain and TrypLE performed with diminished dissociation effectiveness when treating more mature spheroids (day 15). Accutase did not result in a significant reduction, but a trend for lower dissociation is observable. The specificity of Accutase presumably did exclude proteins, which were not integrated into the maturation process as the other two enzymes.

It is not clear why papain performs so effective in dissociating cardiac spheroids or thick tissue samples, but the long-term use in that specific field suggests an advantageous enzymatic process. It can be hypothesized that papain digests the multitude of cell-cell and cell matrix connections effectively while keeping the membrane of the cells intact. Thus, balancing the delicate task between too little and too much digestion. In fact it can be hypothesized that papain is specific enough to not digest the cell membranes, thus not damaging the cells on the spheroid outer layers more than in the spheroids and second, being unspecific enough to digest most of the proteins projecting out from the membrane. It must be noted that the dissociation protocol for each enzyme was not optimized specifically for this application, but was based on previous experiences with these enzymes and the literature. It can be expected that all parameters of the dissociation process can be enhanced further by a thorough optimization. Nevertheless, in a time when multicellular, three-dimensional cell constructs and organoids with complex cellular architecture are in the focus of current scientific studies,

a dissociation reagent offering reliable and robust dissociation performances with high flexibility is advantageous. The comparable performance of papain on two- and three-dimensional cell cultures and its traditional use in neurobiology with focus on long neurons harbouring long, delicate projections further highlights the advantages of this compound. It can be assumed that the higher variability in two-dimensional cultures observed in this study has been the reason for other enzymes to become the gold standard traditional cell cultures. An extensive digestion of membrane surface proteins could explain the longer lasting, spherical shape of cells dissociated with Papain. Although no delayed, adverse effects have been spotted, a papain inhibitor (E64 papain inhibitor) is already commercially available and could stop further digestion.

The presented workflow for the generation of hiPSC-derived cardiomyocytes in a small-scalable bioreactor represents a valuable basis for any downstream applications using hiPSC-CMs. The most frequent application of hiPSC-derived cells are *in vitro* cell models used for disease modelling and drug discovery. The widespread availability of human cellular models represents one of the key advances and fosters accurate predictions and conclusions as interspecies differences are avoided. Traditional cell culture plastic ware has been shown to induce stress on the force exerting cardiomyocytes. Furthermore, non-contractile substrates limit cardiac contractions and prevent the analysis of this highly functional parameter. In this study, hiPSC-CMs were cultured on biopolymer-based scaffolds to allow an evaluation of their applicability in advanced cardiac models. The effects of such contractile substrates on hiPSC -CM contractility and maturation were assessed.

In vitro modelling of the cardiac niche on fixed UHV-alginate matrices

Since the establishment of human PSCs, human disease models and pharmacological screenings using human derived cells are frequently available. Nevertheless, the drawback of current culture platforms is the two-dimensional culture on hard plastics or glass substrates. This has adverse effects on cell integrity and functionality. Concerning hPSC-CMs, force generation is the major functional output and represents the sum of all intracellular upstream processes. However, the assessment of force cannot be conducted on hard substrates and is often conducted with expensive custom-made setups using single cells. Utilizing UHV-alginate substrates, which are fixed in conventional multiwell plates, the following experiments evaluated the possibility to derive quantitative data from the force generation of hPSC-CMs.

Pharmacological gold standard hPSC-CMs (COR.4U, Ncardia, Germany) were employed, due to their mixture of ventricular and atrial cardiomyocytes, pacemaker cells and cardiac fibroblasts. Pacemaker cells possess leaky channels, which slowly depolarizes the cells, leading to a rhythmic self-depolarisation of their membrane. Through intercellular gap junctions, the depolarisation is distributed among the neighbouring cells, causing the spontaneous synchronous contraction of the cardiomyocytes. The beating frequency of hPSC-CMs is regularly assessed in pharmacological studies; because it is modulated by clinically relevant

drugs and the observed effects recapitulate the response of the myocardium *in vivo*. Apart from the spontaneous contractions analysed in this work, electric stimulation is also used in such electrophysiological assessments. This lowers the differences between different cell lines and maturation states, but masks differences in the starting conditions without drug exposure. Therefore, this study focused on the characterisation of spontaneous contractions, enabling a discrimination of substrates induced influences on the unexposed conditions. Subsequently, hPSC-CMs have been cultured on fixed UHV-alginate scaffolds and their beating rate was assessed.

The selection of the UHV-alginate concentrations was based on the comparability between this artificial setup and the natural environment, particularly the range between the early, soft embryonic cardiac niche, the stiffer adult myocardium and deteriorated, scarred cardiac tissue (Engler et al., 2008). As shown in Figure 5.1, the beating frequency changed drastically over the course of 60 days. Apart from the dynamic changes over time, which were very similar across all conditions, a conserved influence of the matrix stiffness on the beating frequency is observable. Since the beating frequency is dependent on the self-depolarizing behaviour of the pacemaker population, it can be assumed that the mechanisms enabling self-depolarisation are influenced by the substrate stiffness. A simple explanation cannot be drawn, because the lowest beating rates were found in the stiffest (PS) and the softest sample. It can be hypothesized, that the soft substrate limits the maturation process more than the stiffer biopolymer compositions, which still allow contractile movement. The extremely high mechanical resistance of PS (in the Giga Pascal range) cannot be overcome by the cells and therefore, inhibits a physiological contractile machinery development, thus resulting in a non-physiological beating behaviour. It is reported, that the culture of cardiomyocytes in general is adversely affected when cultured on extremely stiff substrates like PS (Heras-Bautista et al., 2014). The main reason is assumingly the force generation, which cannot translate into a real movement because of the fixed adhesion sites, which are firmly attached to the substrate. Therefore, the force must be absorbed by intracellular structures forcing compensatory mechanism into action, affecting mostly the cytoskeleton synthesis and its maturation, and leading to the formation of stress fibres (Heras-Bautista et al., 2014; Tojkander et al., 2012; Young et al., 2015). In this artificial environment, regulatory mechanism could modulate the ground base rate to guard the cells from damage, leading to the low base rate in the PS group. The soft biopolymers (0.3% UHV-alginate) possess viscoelastic properties similar to the early myocardium and it is reported, that this softness inhibits maturation (Happe et al., 2016; Lockhart et al., 2011; Young et al., 2015). Although, the soft scaffolds are able to return to the resting state after contractions, the matrix exerts a lower pull and this could interact with intracellular sarcomeric structures responsible for the passive tension. Titin, a macromolecule responsible for passive tension sensing and regulation, is also crucial in cardiomyocyte maturation and could represent a molecular basis for the aforementioned hypothesis, since the passive tension on it is too low on soft substrates and too high on PS (Krüger et al., 2011; Sequeira et al., 2014; Yamasaki et al., 2001). Another hypothetical influence on the beating rate on PS is a selection process: the higher the beating frequency,

the more often the force has to be compensated, resulting in a gradual elimination of cells with higher frequency.

It must be noted that the highly dynamic change of the beating rate over time, particularly the substrate-independent increase and following decrease, was not detected in rat neonatal cardiomyocytes (Forte et al., 2012). Another study using hiPSC-CMs reported a loss of spontaneous beating on PS, whereas the hydrogel conditions maintained a relatively constant frequency (Heras-Bautista et al., 2014). Because the different biological replicates produced the same pattern on different substrates over a duration of 60 days with very little variation, a cell line specific effect can be suspected. Although a systemic bias cannot be fully excluded, the sustained relative difference between the conditions, the precautious setup with short documentation times in combination with a heating plate and the consecutive execution of the biological replicates speaks against it.

In conclusion, a correlation of the beating frequency with substrate stiffness was found in accordance with the robust evidence in the scientific field. The system allowed a viable cell culture of hPSC-CMs for a minimum of two month with lower mechanical stress and the possibility to control the substrate stiffness. The high biocompatibility of UHV-alginates in combination with the lack of an alginate receptor in human cells leads to a robust and reliable *in vitro* model, which minimizes the influence of substrate-induced effects. An established *in vitro* model, based on this setup, would provide valuable insights into the incidence of drug responses.

The following experiments evaluated the response of hPSC-CMs upon drug exposure and explored the feasibility of an optical-based quantification of force generation. An early characterisation of the contraction range was conducted by calculating the maximum projections of all frame-to-frame differences of a 30s video. As depicted in Figure 4.5 C, the contraction range correlated with the substrate stiffness. The collective action of the cardiomyocytes was able to contract the substrate and the optical-based method was able to detect the contraction difference with sufficient accuracy. It can be expected that the longer the cells are grown faithfully on these substrates the more the force generation differs. Like all muscle cells, cardiac cells are prone to training effects and, accordingly, the contractions during the first days were almost not visible, while they became more prominent after the first week. Additionally, the sarcomere formation needs time to adapt to the new environmental cues after dissociation.

Although the method to produce these intensity-based contraction analyses is good to present the differences in a qualitative manner, it does not allow for a quantitative discrimination and is suspected to introduce biases (Huebsch et al., 2015). One bias for example is caused by varying contraction velocities. The presented images are averaged frame to frame differences of a 30s video, if contractions in one sample would be faster than in the other groups then the frame to frame differences would be higher on average, resulting in wrong conclusions about the contraction force. Additionally, directionality and artefacts cannot be spotted easily and could lead to misinterpretation of the data (Huebsch et al., 2015).

Therefore, this approach was abandoned and two other methods have been employed to assess the beating behaviour: calcium transient analysis and optical flow measurements. Calcium transient analysis is based on the use of molecular calcium probes, which are highly fluorescent in the presence of calcium. Cardiomyocyte contractions rely on the intracellular release of calcium ions from the sarcoplasmic reticulum. Thus, intracellular calcium dynamics correlate with the action potential and the release and uptake of calcium ions (Fearnley et al., 2011; Stoehr et al., 2014; van Meer et al., 2016). This allows a robust and quantitative analysis of the electrophysiology of cardiomyocytes. The high transparency and the extremely low autofluorescence of UHV-alginates enables the use of such techniques. In parallel to the fluorescent calcium dynamics, phase contrast microscopy videos were acquired and analysed with optical flow measurements using a software originally developed for particle image velocity (abbr. PIV) measurements (Huebsch et al., 2015; Vennemann et al., 2006). The name PIV is derived from the earliest uses when laminar flows were analysed using small fluorescent particles (Adrian, 1984; Vennemann et al., 2006). The discreet distribution of these particles allowed the analysis software to recognize the particles and quantify their displacement between two images. Earlier studies have proven the feasibility of analysing the contraction behaviour of cardiomyocytes with PIV-based software (Huebsch et al., 2015; Sala et al., 2018). When calcium imaging and PIV measurements are conducted on the same samples, the fluorescent signal from the calcium probes interferes with the fluorescent particles. The different viscosities of the UHV-alginate solutions also would interfere with the sedimentation speed of the particles and it would require complex validation and calculation steps to minimize the bias introduced by different particle distributions in the hydrogels. Thus, phase contrast microscopy videos were acquired to avoid such an interference. Afterwards, manually picked images from the resting state and the contraction maximum were analysed by cross-correlation using the software jPIV (Vennemann et al., 2006).

With this method, not only can the average displacement per vector or search window be quantified, but also directionality and indirectly the force (Figure 4.6). On substrates with different elasticities, the same vector size is not comparable, because on stiffer substrates more force is needed for the same contraction distance. Nevertheless, the method allows for a relative quantitative comparison, especially when the same substrate is used. As shown in Figure 4.6, calcium imaging as well as the PIV analysis is feasible using UHV-alginate substrates. A faithful *in vitro* model of the cardiac niche should exhibit hallmarks of cardiac drug responses including inotropy, lusitropy and chronotropy (Li et al., 2018a; Mannhardt et al., 2016; Negroni et al., 2015; Zimmermann et al., 2000). Chronotropic drugs modulate the beating frequency upon exposure to specific signalling molecules (Mummery et al., 2003; Zwi et al., 2009). Inotropic drugs increase the peak force of myocardial contractions, whereas lusitropy is the modulation of force development and relaxation (Godier-Furnémont et al., 2015; Negroni et al., 2015). To test if the matured cardiac models exhibit such behaviour, the cells have been exposed to isoprenaline.

Isoprenaline, also known as isoproterenol, is a noradrenaline derivate and a beta-adrenergic agonist (Hoffmann et al., 2004). It is widely used for the verification of faithful *in vitro* models

and is known for its inotropic, lusitropic and chronotropic effects (Cohn et al., 2000; Negroni et al., 2015; Reno et al., 2018; Zhang et al., 2013). The acquired calcium waves recapitulated the beta-adrenergic stimulation, revealing positive chronotropic effects in accordance with the literature (Figure 4.6). A quantitative analysis was conducted harnessing the advantages of such an approach. Upon isoprenaline exposure (100nM), the beat rate was increased, the PWD90 shortened and the slope of repolarisation was steeper (Figure 4.7). The slightly shorter PWD90 of the 0.3% condition correlated with the higher beating frequency. The fluorescent labelling of the calcium transient required a different medium and this could be the reason for the general discrepancies to the previous experiment in terms of beating frequency. A slight gain in contraction displacement upon drug exposure, which also correlated with substrate elasticity was observed. This translates into an increase in contractile force suggesting a positive inotropic effect (Figure 4.7, D). Elevating the isoprenaline concentration to 1µM did not induce any changes on the beat rate or ADP90. A slightly decreased repolarization slope can be spotted in the calcium transients. Further experiments are needed before solid conclusions can be drawn, but it can be speculated that an elevation of the intracellular Ca2+ is responsible for the lower repolarization slope. Thus, the relative difference between the maximum Ca2+ concentrations during contractions and the minimum concentration was smaller, resulting in the observed effect and leading to a higher propensity towards contraction. This assumption is also supported by the observation of intracellular, locally limited Ca2+ signals during these experiments. In addition a second, myofilament-based effect of isoprenaline has been suggested affecting the relaxation in work-loop contractions, but not in isometric muscle work (Layland et al., 2002). This physiological behaviour could have been recapitulated on UHV-alginate substrates and not on PS, but this requires extensive additional testing.

In contrast to the calcium transient analysis, exposure to 1µM isoprenaline led to a further increase in displacement indicating a further increase of the contraction forces. This effect was more prominent on the softer substrates. A possible mechanism for this could be an increased calcium sensitivity at force generating actomyosin complex mediated through tropomyosin (Mccubbin et al., 1987; Tobacman et al., 1986). The concerted execution of a higher contraction force without a respective change in the Ca^{2+} signals has to be verified by additional methods to enable definitive conclusions. Additionally, the recently reported interaction of the protein RAD with Calcium channels, more specifically, the release of RAD upon beta-adrenergic stimulation is responsible for the effect of isoprenaline exposure. Since only the most basic features of this pathway have been described, additional down-stream targets of RAD are thinkable and, thus, could modulate force generation by interacting with the cytoskeleton itself (via a second mode of action) (Liu et al., 2020). Nevertheless, the detection of the enhanced force generation highlights the importance of force measurement, as it represents the key functional output of the myocardium. Furthermore, calcium transient measurements cannot be used to conclude the exhibited forces. This is especially evident when processes downstream of the free intracellular calcium concentration (as measured by fluorescence) are affected, *e.g.* calcium sensitivity, sarcomere integrity or the actin-myosin

complex (Kyrychenko et al., 2017; Lanzicher et al., 2015; Montag et al., 2018). This underlines the evaluative potential of this model, which allows the early discrimination between calcium homeostasis-related effects and downstream mediated effects (*e.g.* influencing the Actin and Myosin reaction) and could provide a valuable contribution to basic research and drug screenings, particularly when disease cell lines (*i.e.* carrying myosin mutations) are analysed.

The possibility to enable concentric muscle work in a highly parallelizable system is a great advantage as it simulates the workload *in vivo*; hence, an environment with higher physiological resemblance is created. However, several other systems, which include force measurements, are being developed at the time of this work. Among the reported systems are those focusing on single cells, which often lack the physiological resemblance to the multicellular myocardium and lack the throughput (Engler et al., 2008; Hersch et al., 2013). Other rely on three-dimensional fibrin-based constructs, which are stretched between two silicone posts to allow force quantification through optical analysis of the silicone post deflection (Eder et al., 2016; Hansen et al., 2010). Although this enables the measurement of absolute force, it requires specific culture plate designs. Parallelization would require additional redevelopment, particularly the design of the silicone posts. Additional calcium measurements are conductible, but the comparability is questionable due to the three-dimensional nature of the cell models. Furthermore, the internal stiffness of the biological material cannot easily be modulated, only the posts can be made stiffer. Nevertheless, the three-dimensional cardiac environment is advantageous and absolute force analysis is very valuable. The biowire system focuses on the electrophysiological analysis of three-dimensional cardiac constructs. It utilizes a wire that serves as a structural stabilizer for the culture and serves as an electrode, but the inflexible environment inhibits force measurements (Nunes et al., 2013). Contrary to the calcium measurements in this work, the derivation of calcium transient data from the biowire system was only possible through dissociation of the three-dimensional cellular constructs and consecutive seeding on two-dimensional glass slides. However, the electrophysiological characterization of cardiomyocyte reaction upon drug exposure is essential for drug screening and toxicological analyses. At this point, the use of UHV-alginate hydrogels makes this very difficult to conduct, due to the lack of integrated, insulated electrodes. A first trial to coat MEA chips with a thin UHV-alginate layer produced no measurable signals, although the cells were viably contracting on the biopolymer surface. This indicates that the direct contact of cells and electrodes was inhibited by a thin hydrogel layer. It can be assumed that the layer's porous volume filled with media is conductive and prevents a robust readout, due to short circuiting the electrodes. It is possible that the introduction of electrode-like elements into the biopolymer volume represent a solution for this problem as it was shown before to allow the transport of electric information (Golafshan et al., 2017; Kumar et al., 2014). Furthermore, this application cannot be only limited to natural alginate polymers, but all biocompatible conductive materials.

In conclusion, the presented setup enabled a relative quantitative analysis of the force in concert with calcium flux measurements. The positive effect of the contractile environment was proven by the inotropic, chronotropic and potentially lusitropic responses of the hPSC-

CMs upon isoprenaline exposure, all which have been described *in vivo*. Utilizing this setup, it was possible to detect and quantify such physiological reactions. The great potential for parallelisation and the low economic cost make an application in the early stages of drug discovery and toxicity screenings seem feasible. Apart from the aforementioned improvement of highly parallelisable *in vitro* models, the advanced insights into the complex intercellular interactions and the capability of cells to sense and react to subtle environmental cues, makes the development of more complex cardiac models necessary. Great potential has been put into the 3D printing technique, which enables the use of one flexible production platform for the generation of three-dimensional models with differing geometries and viscoelastic properties. To replicate the microenvironment of the previous *in vitro* model in 3D printed, free-floating UHV-alginate constructs a method had to be established enabling the printability of the low concentrated UHV-alginate formulae.

Is it possible to 3D print low concentrated biopolymer inks with high resolution?

3D printing of hydrogels has been conducted since the dawn of bioprinting. It is the unique combination of characteristics, *i.e.* high biocompatibility in combination with mild crosslinking conditions, tuneable stiffness and a set of different functionalization strategies, which makes hydrogels so attractive for bioprinting. The big disadvantage lies in their liquid nature, which forced many labs to use highly concentrated and pasty inks to achieve an adequate printing resolution (Freeman et al., 2017; Luo et al., 2018, 2017; Sun et al., 2013). After crosslinking, this translates in sturdy matrices, which is only reflected *in vivo* in bone tissue. The early experiments conducted in this study focused on the replication of these methods. In contrast to many other laboratories, which rely on low viscosity alginates, ultra-high viscosity alginates (Alginatec, Germany) have been employed in this work. UHV-alginates are a blend of alginates from two algae species, *Lessonia nig*rescens (abbr. *L.n.)* and *Lessonia trabeculata* (abbr. *L.t.)* with exceptional purity and biocompatibility (Zimmermann et al., 2005). UHV-alginates allow a readily transition into *in vivo* applications and due to the lack of an alginate receptor in mammalian cells serve as an inert matrix. It is known, that the high purity in combination with the conserved, high molecular weight causes UHV-alginate inks to behave differently compared to commercially available alginates with low molecular weight (Zimmermann et al., 2005, 2007).

A method, in which the printing area was steadily flooded with gelling solution, could not be replicated in the way it was reported. Using UHV-alginates, the whole scaffold was immediately crosslinked, although only the lower levels had direct contact with the gelling solution. To avoid such a high volumes of crosslinker solution, a setup was devised to vapour the $BaCl_2$ solution onto the scaffold to achieve a mild superficial gelling, potentially stabilizing the scaffold enough for a robust printing process and to avoid crosslinking the alginate in the printing nozzle. The printed scaffold was slightly stabilized by the gelling vapour, but whenever the printed alginate had minimal contact with the crosslinked biopolymer, it inhibited future connections between the printed ink and the deposited ink. It was concluded that a freezing

step could potentially circumvent this problem, because it avoids intermediate gelling steps and makes stable connections between different layers feasible. This setup can be realised on many conventional 3D printers with minimum cost and can be readily adapted to other low viscosity materials, with can be frozen and which allow a relatively fast crosslinking.

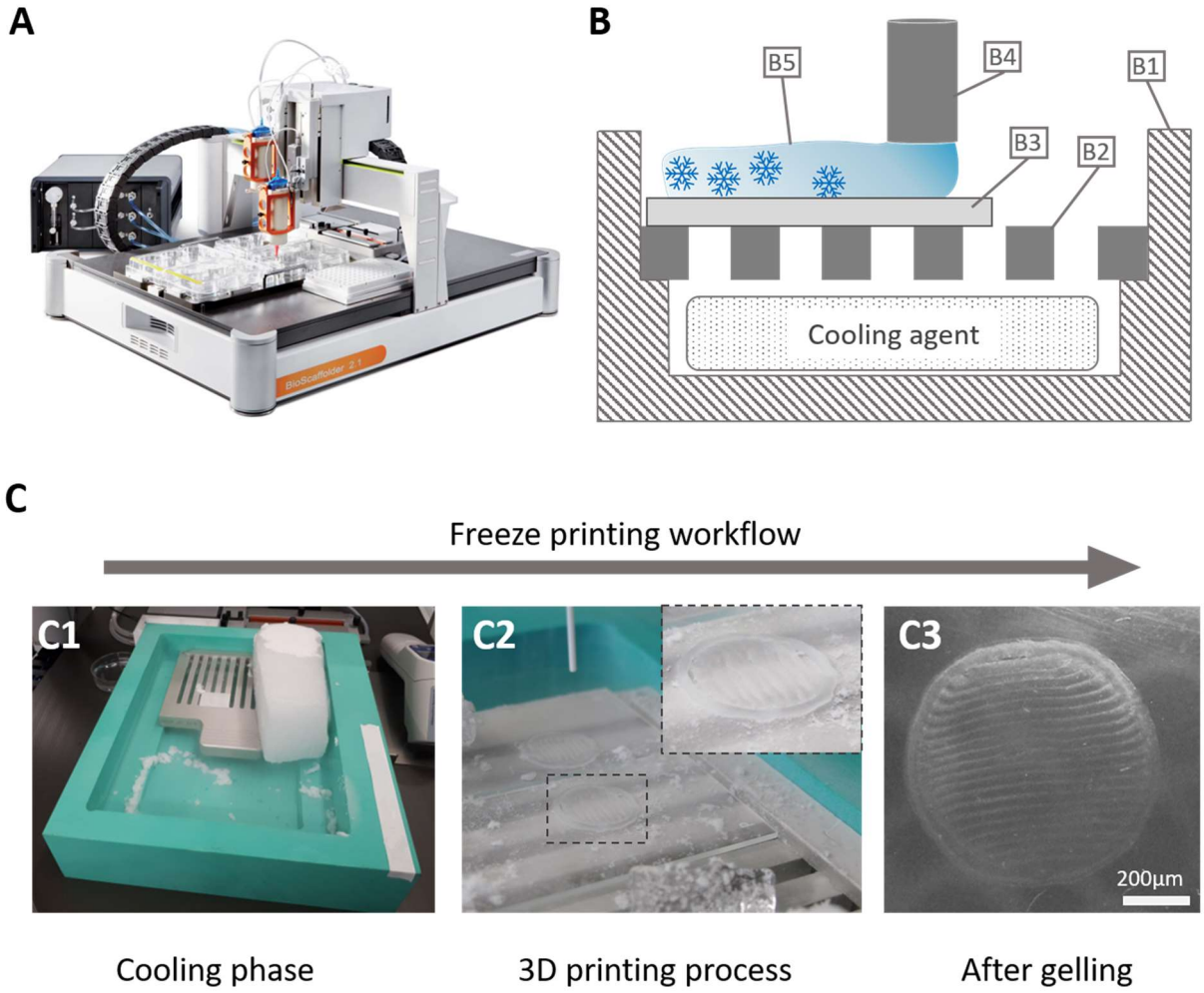

Figure 5.2 Freeze Printing enables low concentrated biopolymer solutions to be printed with additive layer manufacturing without further adaptions.
3D printing has been conducted on the BioScaffolder 2.1 (GeSiM mbH, Germany), a protrusion-based, additive manufacturing platform offering two cartridges for different inks to be printed in one scaffold (A). The novel freeze printing setup consists of an insulating box (B1; C1) shielding the 3D printer from the extreme temperature gradients in the printing chamber. The hydrogel-based ink (B5) is printed on a microscopic slide (B3), which serves as a thermal conductor and as a mobile sample holder needed for the fast transfer of frozen scaffolds into the crosslinking bath. Inside the insulating box, the microscopic slide rests on a metal lattice (C1), which is precooled and due to its bigger volume, is capable to take up and dissipate heat from the printed ink. Only before printing, dry ice is placed on top of the lattice, allowing direct contact and enabling achieving the low printing temperatures quickly (C1). Otherwise, the cooling agent is stored directly under the metal lattice. When the printing process is finished the frozen, but not crosslinked, scaffolds retain their shape and can be transferred to a crosslinker bath (C2). After crosslinking, the scaffolds preserve their shape with great fidelity (C3). Image A taken from GeSiM mbH.

Crosslinking is conducted after the whole scaffold is printed, which is advantageous, because it leads to a more homogenous crosslinking and offers the possibility for intermediate processing steps, *e.g.* heat based structuring (imprinting, laser, microwaves), mechanical modifications (scraping, pore stitching) or integration of the scaffold into other systems. Furthermore, the diffusion-based crosslinking can be conducted while the scaffold shape is maintained with high detail. This is important because the normally liquid core volume distorts the shape towards a low energy state, which can be observed when spherical microcarriers are produced by dropping alginates in a crosslinker solution. Although, the alginate immediately starts to gel, the drop, which was deformed upon impact onto the water surface, returns to the spherical shape before complete crosslinking is achieved. It can be expected that this effect is significantly influencing printing resolution, when larger construct are being produced. The devised setup consist of an insulating box that shields the expensive 3D printer from the low temperatures and mobile elements on which the constructs were printed on (Figure 5.2). This allows transition of the printed scaffolds into the crosslinker solution without interrupting the production of the next scaffold.

The difference between conventional 3D printing (called liquid printing) and the freeze printing method can be seen Figure 4.8. The depicted strut shows only little height (approx. 40µm in height) using the liquid printing method and a high degree of melting, in contrast to the approx. 300µm height in freeze printing with virtually no melting. Even the scaffold had minimal complexity (*i.e.* a two tiered grid; 1x1cm), a high degree of drying of the outer struts (crystallization was observable) was observed when printing conventionally. This could be avoided by printing in a humid atmosphere, but would requires additional redesign of the printing process, which still would not allow higher scaffold geometries.

Freeze printing led to a high degree of surface structuring with many parallel impressions on the scaffold surface and many vertical pores reaching into the scaffold. To avoid any misinterpretation based on potential staining errors or a limitation of FiTC-PLL to diffuse sufficiently into the scaffold, pore geometry was assessed by an alternative method. The imaging was conducted via scanning electron microscopy and the pores were clearly visible, especially where the scaffold had been sectioned (Figure 4.9). The vertical pores were more frequent seemed bigger where the ink had direct contact with the cold printing surface, indicating that it is caused by water ice crystallization.

How could these vertical pores form?

A hypothetical mechanism on how these pores are formed is depicted in Figure 5.3. The freezing point for water is higher than for alginate solutions and it can be assumed that a freezing process would recruit water molecules out of the alginate solution leading to a concentration of alginate at the crystallization front. This crystallization is started many folds on the cold surface and due to the higher alginate concentration between these crystallization

centres than above, where more water is still available. Thus, the main growth trajectory is upwards, vertically oriented to the printing surface (Figure 5.3).

This hypothesis can explain the basic growth direction; it cannot fully reflect the complex reality, in which the local concentration of alginates is not the same between differently concentrated alginate solutions. It can be hypothesized that the concentrating effect has enough time to enforce a specific alginate concentration level due to the recruitment of water molecules. The observed differing stiffnesses contradict this and hint to the fact that a fast freezing process conserves the different UHV-alginate concentrations.

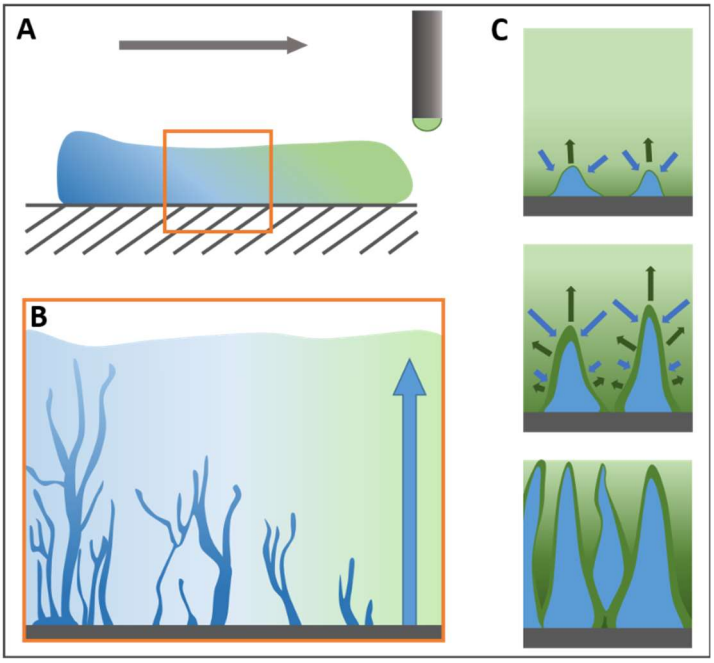

Figure 5.3 A hypothesis on pore formation during freeze printing. The freeze printing process leads to an immediate freezing of the hydrogel (green to blue transition; blue represents frozen alginate; green represents liquid alginate; grey arrow represents printing direction; A). The growth of pores (B and C) is dependent on water ice crystals, which grow bigger through recruitment of water molecules (C; blue arrows) and simultaneous aggregation of alginate chains at the crystallization front (C; green solid and arrows). The highly aligned nature of the pores is caused by this up concentration, when more water molecules are available above the nucleation centres than in between, leading to a primarily upward crystallization direction. This results in vertical growth being faster than horizontal growth, leading to vertically aligned pores after gelling (C).

The preservation of viscoelastic cues is important for the production of scaffolds bearing varying stiffness. That the freezing of differently concentrated formulae translates into different pore sizes was suspected, but was not observed in the experiment (Figure 4.12, A). The only condition to produce larger pores was 0.7% UHV-alginate, which led to a significantly increase in pore diameter. Thus, the effect of alginate concentration on pore formation was limited. Additional analyses, concerning the pore formation of alginates from either *L.t.* or *L.n.* and mixtures of both were analysed. Indeed, pore size correlated with alginate inks from different sources, suggesting a potential strategy to influence pore formation (Figure 4.12). The robust correlation of larger pores within the *L.t.* conditions, hinted at an underlying origin-dependent mechanism, which influences pore formation. This was further supported by the fact that the mixture of *L.t.* and L.n produces intermediate pore sizes, suggesting an additive mechanism and hints against a possible “either/or” mechanism. Although 1:1 mixtures were used, the mixture tended to produce slightly larger pores than one would expect if the system produced purely the average pore size. The ratio of guluronic und mannuronic acid, the polymer blocks of alginate, depends on the origin species and a high

guluronic acid content is found in alginates harvested from *L.t.*, whereas alginates from *L.n.* mostly possess mannuronic acid chains (Storz et al., 2009). The varying composition could have an impact on diffusion at the crystallization front, because the viscosity is also depended on the composition (Storz et al., 2009). However, charge, molecular chain weight, freezing point differences or combinations of them could potentially influence pore formation and further studies are needed, before this process is fully elucidated.

Freeze printing allows for a bioink deposition with high spatial resolution

Next, the relationship between printing pressure and the resulting printing resolution was assessed by measuring the strut diameter of 3D printed grids (Figure 4.11). For liquid printing, the strut diameter follows a positive exponential trend. In contrast, the freeze printing method led to a smaller raise in diameter size, which is probably rooted in the three dimensional nature of the struts. This experiment also highlights the basic nature of pressure, defined as force per area, and printing speed (the movement speed of the nozzle), which results in a certain volume to be deposited. The strut diameter, measured from above is a simplified measurement of deposited volume, because it neglects the height. A printing pressure of 30kPa led to measured diameters of 690µm (LP) or 288µm (FP). Assuming a constant volume deposition per time (based on the same printing pressure and nozzle movement speed) the height is 5.7 times higher in the FP condition. Raising the printing pressure to 70kPa led to a calculated 12.5 fold difference in height. This is caused by the liquid nature of the 0.7% UHV alginate ink, which readily flows to the sides using conventional printing and therefore has virtually no net gain in height. Freeze printing on the other hand preserves the ink deposition in z-axis almost instantaneously, thus higher printing pressures lead to higher struts (Figure 5.4). Furthermore, the smaller variance and the smaller gains in diameter size suggest a more controllable printing process

In a comparative study, Freeman et al. evaluated their printing resolution by the spreading ratio, the calculated ratio between the average strut diameter and the diameter of the printing nozzle (Freeman et al., 2017). The lowest spreading ratio they observed was 4.30 ± 0.77. Calculating the spreading ratio from the average strut diameters given in Figure 4.11, the FP method resulted in values between 1.5 (30kPa) and 2.5 (70kPa) using a 0.2mm nozzle, highlighting the high printing resolution and the ability to adapt the printing process without the need to further modify the ink. It must be noted, that the spreading ratio is, at most, an indication for the printing resolution, as it neglects crucial parameters, especially printing speed and printing pressure, which strongly affect volume deposition (Figure 4.11) (Khalil et al., 2007).

The freezing process does depend on a fast energy transfer from the warm ink to the cold surface to achieve a high shape fidelity. Limiting factors of this energy transfer are assumed to directly affect the deposition accuracy, because the slower the freezing the more time for melting is available. How much energy has to be transferred, is one of such factors, because

more time is needed for the transfer (under a constant energy transfer rate). Increasing the deposition volume directly increases the total thermal capacity and thus the energy.

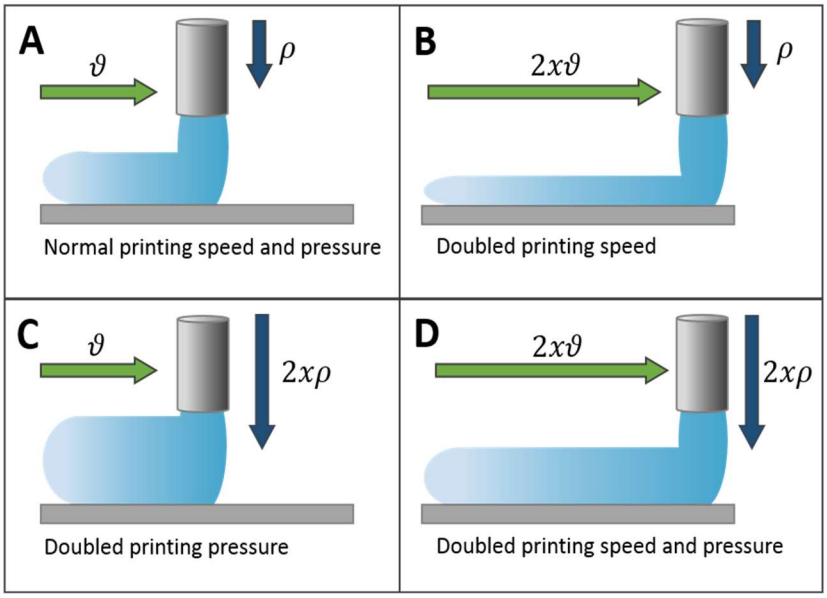

Figure 5.4 Hydrogel deposition is dependent on printing speed and pressure. A simplified model for hydrogel deposition is presented. A specific printing speed (ϑ) and printing pressure (ρ) results in a certain amount of ink volume to be deposited per length unit (A). Increasing the speed results in lower volume deposition per length unit (B), whereas a higher pressure leads to thicker struts (C). An increase of both, the speed and the pressure, balances the two factors and the same printing geometries as in A can be achieved (D).

It can be assumed, that upon reaching a certain deposition volume, the energy transfer through the ink itself is not fast enough to allow for a freezing process with high fidelity. Higher melting and loss of ink deposition in z-axis would be the consequence. Big volume deposition rates are not in the focus of tissue engineering, where a higher printing resolution is wanted. Because the freezing allows for long printing processes without the loss of structural detail, large scaffolds can be produced with additive layer manufacturing; thus, this disadvantage is rather negligible. Another important factor is the distance of the printing nozzle from the printing surface. The nozzle has to be close enough for the ink to contact the surface, but far enough away to allow a sufficient z-axis deposition. Sometimes, the ink was observed to crawl up the side of the nozzle on many occasions. This was avoided by wrapping hydrophobic Parafilm™, a paraffin-based plastic film, around the nozzle. This early setup was then changed to the use hydrophobic and flexible nozzles, which also diminished printing errors significantly. Very small structures or volumes could not be printed, because the ink in the nozzle froze and clogged upon contact with the cold printing surface. A potential solution for this problem is switching to faster printing velocities, which enables the printing of finer structures (see Figure 5.4, A and B), and the use of a heated nozzle to prevent freezing in the printing nozzle. Or the combination of freeze printing with other established methods, which enable even higher printing resolutions, *i.e.* microdrop printing (Pataky et al., 2012).

The optimal biomimetic matrix would foster the generation of vessels to supply large constructs with nutrients and oxygen. The observed pores in the inside were already a promising start into that direction, because the measured diameters (approx. 10µm) was in

the same the order of magnitude as capillary vessels (Fung, 1973). However, vessels large enough to support bigger tissue areas could not form in such pores. Therefore, the influence of different UHV-alginate ink compositions on pore formation were explored.

Can the pore formation be influenced by alginate selection or additives?

Based on the hypothesis of pore formation, it was assumed that the pore size could be influenced by using different alginate compositions or additives. First, four different concentrations were tested (0.3%, 0.7%, 1.0% and 1.5%), either the established 1:1 blend of alginates, harvested from *L. n.* and *L. t.,* or single source alginate solutions from one of the two algae species. The analysis was inconclusive concerning the used alginate concentration. 1.5% and 1.0% solutions led to a comparable size to 0.3%, whereas 0.7% solutions resulted in larger pores. This nonlinear trend could be the result of several influences masking a direct relationship between alginate concentration and pore formation. So far, no model has been found to explain the high spike in pore size in the 0.7% condition, but it could be caused by small mistakes in the data acquisition. The most important factor in this analysis was to capture the images at a constant height, because the pore size was suspected to change when reaching into the scaffold. It can be speculated, that the measuring height was erroneous here. Albeit all three replicates produced bigger pores. Further experiments will resolve if such an error was made or if the concentration/ pore relationship follows a parabolic trend with a maxima surrounded by two minima. Contrary to the concentration, a correlation between alginates from different sources was found. This trend, with larger pores in alginates from *L.t.* and smaller pores in scaffolds printed with alginate from *L.n.,* is also supported by the fact that the blend robustly produced intermediate sized pores. While the latter supports the idea that pore size is dependent on the recruitment efficiency of water molecules through diffusion, the different alginate concentrations producing comparable pore sizes hints at a mechanism independent of the intrinsic viscosity. One such cause could be the difference in molecular weight between the different alginate batches, affecting the freeze point, which solely depends on the number of solutes. Since the solutions were adjusted for weight to volume concentrations, a lower molecular chain length leads to a higher number of solutes. However, the viscosity also depends on the molecular weight and a comparative analysis has to be conducted to allow further conclusions.

Taken together, the effect on pores size in alginate selection was limited, but achievable with great potential for future applications. Alginates can be harvested from many different algae species and are not restricted to the plant kingdom, as bacteria are also a possible source. It can be assumed that alginates from such vastly differing sources harbour widely different characteristics, which could utilized to exert tailored effects on pore formation.

The hypothesis that the pore formation relies on water ice formation also implicated that this process could be influence by additives. As known from freezing biological samples, there are many substances to affect ice crystallization. Mostly, these are used to prevent intracellular

water ice formation to achieve a high cell viability after freezing and thawing of biological samples. Substances regularly used in this context include, but are not limited to, dimethyl sulphide oxide (abbr. DMSO), Trehalose, polyethylene glycol (abbr. PEG) and poloxamers (Alink et al., 1976; Ashwood-Smith et al., 1973; Buchanan et al., 2004; O'Neil et al., 1997). Based on their uses in the freezing of biological samples, these compounds were used to modify pore formation. It was hypothesized that these compounds would either lower the pore size due to slower crystal growth or reduce the number of nucleation sites, enabling the growing water ice cones to increase horizontal growth. A pore enlargement was not observed and it can be theorized that it cannot be achieved by adding a single component. If the hypothesis, that the pore diameter is limited by the distance to neighbouring pores (Figure 5.3), is correct, then a reduced number of nucleation sites could lead to an increased pore diameter. Furthermore, the smaller pores (observed when using additives) could also be caused by the lowered freezing point of the water/ additive solution, which is closer to the freezing point of alginate, then without additives. Thus, less time would be available for water ice to form until freezing of alginate sets in and the whole scaffold freezes. Therefore, the time between water ice formation and the beginning of alginate freezing has to be prolonged, which would be achieved by creating a bigger temperature gap between the freezing points. However, this demands a more complex setup, which effectively modulates the two very different dynamics. Further studies are needed to verify the hypothesis of pore formation and the resulting modification strategies. Additionally, the possibility to include compounds such as cryoprotectives could lead to further applications. Encapsulation of cells in the ink could benefit from the addition of DMSO, as it seems to have a similar effect in alginate inks as in biological samples and could serve as a promising additive for freeze printing cells in alginate hydrogels, thus offering great potential in *in vitro* modelling of tissues and in regenerative applications.

The discussed method of freeze printing offers the possibility to 3D print low concentrated UHV-alginates. A relatively high resolution is achieved and the maintained structural integrity through the crosslinking stage allows the production of scaffolds with biologically relevant sized structures. Thus, it allowed to 3D print the UHV-alginate solutions used for fixed culture substrates in the previous *in vitro* modelling approach. Contrary to this earlier approach, the scaffolds would now be completely free-floating, lying the basis for future applications in clinical settings, where transport and transplantation rely on such "free" constructs. However, it was not clear of the FP method influenced the viscoelastic properties of biopolymers processed in that way. Thus, after a design decision was made the scaffolds viscoelastic behaviour was evaluated.

Printing scaffolds with physiologically relevant viscoelastic properties is feasible

Utilizing UHV-alginate scaffolds for *in vitro* modelling of the human myocardium made a transition from a lattice to a disc shape necessary (Figure 4.14). It was assumed that this shape facilitates a more homogenous cell seeding on the scaffold surface. Cells, when applied in a

suspension solution, sediment to the bottom of culture vessels. To limit the amounts of cells missing the scaffold and thus adhering to the culture vessel, a disc-shaped geometry was chosen. Additionally, printing with the freeze printing method enables the use of inks with highly different viscosities (Figure 4.13), which allows utilizing the full range of different elasticities from the fixed scaffolds used in the drug exposure experiments (Figure 4.5). The scaffolds maintained their 3D printed shape throughout the crosslinking process (Figure 4.14).

Generally speaking, the shape of higher concentrated UHV-alginate formulae did retain their structure better through the crosslinking phase. The shrinkage experienced during crosslinking is suspected to cause this effect. If this effect can be counterbalanced by milder crosslinking agents (*e.g.* Ca^{2+}) must be seen. Since, the lower concentrations were affected more, it can be assumed that the polymer density and distribution of the polymer chains has an influence on that parameter. It is known, that concentration dependent crowding effects, affect the resulting structure and shape, when solid polymer networks are formed from solutions. This is also supported by the observation, that 0.1% UHV-alginate solutions, used as cell culture substrate, only formed extremely thin films. Thus, the polymer concentration is already very low in 0.3% solutions which are presumably at the threshold of tor preserve the shape during crosslinking. These effects could not be studied in the context of 3D printing before at future research will clarify the effects of such low concentrations on shape fidelity. Because the FP method allows printing such low concentrated solutions, they also can be used to create such thin coatings on other materials in one scaffold. This could be achieved by using two materials, where one is an ultra-low concentrated UHV-alginate solution. During the simultaneous crosslinking and thawing the alginate polymer chains will adsorb at the surface and crosslink at the same time, thus forming thin layers at specific locations in the inside of a scaffold.

Contrary to the production process of surface coatings, the FP method additionally enables the integration of inks with different viscosities in the same scaffold, as long as the freezing characteristics are comparable. A representative image of an alginate scaffold with alternating printed 1.5% and 0.3% alginate ink is depicted in Figure 4.15). Surprisingly, the pores in the lower concentrated alginate solution grew horizontally. This does not contradict the above-discussed hypothesis of pore formation (Figure 5.4). To 3D print inks with such different viscosities, the higher concentrated ink was deposited first and then the spaces were filled with the lower concentrated ink. Therefore, when the second ink was printed, the already printed and frozen 1.5% alginate ink could have served as a nucleation catalyst. It is not clear, why nucleation did not seem to start at the glass slide surface, as it was the case for the first printed ink. The general occurrence of water ice (from the first printed alginate) as the main factor for nucleation directionality can be excluded, because the glass slide, after being cooled to sub-zero temperatures always accumulated water ice from the atmosphere and a fine layer of ice crystals regularly covered the whole surface, before each print. Roughness is another known factor of ice nucleation (Conrad et al., 2005; Zhang et al., 2014). The surface of the glass slide is much smoother than the frozen alginate surface with wrinkles, folds and pores present on the surface. The roughness therefore could have led to an earlier onset of

nucleation and set the directionality at the beginning of the freezing process. Even if water ice nucleation starts mainly at the interface of already printed alginate, it was not expected that almost no vertical pore formation in the middle was observed. Furthermore, a thin interface zone, where the horizontally growing pores from both sides met was seen, indicating a relatively undisturbed nucleation process. Under a massive in-growth of vertical pores, such a fine interface is hard to imagine. Further experiments will enhance the insight into the mechanics of the pore formation especially when using materials with differing roughness or thermal conduction efficiencies. Using the FP method, uniform scaffolds were produced with different concentrated UHV-alginate solutions. It is important for the biopolymers to retain its elastic behaviour throughout the production process, so the advantages of the hiPSC-CM maturing effects, which were observed when these biopolymers were used as fixed substrates, are conserved. Therefore, the viscoelastic properties of the biopolymers were assessed before and after crosslinking.

Elastic properties of the biopolymers are conserved throughout the freeze printing process

The disc-shaped UHV-scaffolds must fulfil specific criteria for an advancement in biomedical research. For instance, it must retain its elasticity to be able to return to the resting state after each contraction, so that the cells experience an external force, essentially stretching the sarcomeric machinery and allowing the cells to repeat the contraction movement. To investigate the viscoelastic properties, the storage and the loss modulus of UHV-alginate inks and freeze printed UHV-alginate scaffolds (after crosslinking) have been assessed via an oscillatory sweep measurement (Figure 4.16). The measurement covered frequencies of 0.1 to 100 rad/s and it showed that the non-crosslinked inks exhibit a viscous behaviour with their loss modulus dominating their storage modulus at lower frequencies. Thus, the received energy is dissipated through heat without the possibility release kinetic energy in form of a return movement to its original state as would solid networks do.

Accordingly, in all, non-crosslinked samples the loss modulus was higher than the storage modulus Figure 4.16, A). This behaviour is typical for liquids. The higher loss and storage moduli at higher frequencies are caused by the higher energy input, which results in a corresponding increase. A clear correlation of the alginate concentration and increasing loss and storage moduli have been observed (Figure 4.16, B). The concentration-dependent intersection of both moduli at higher frequencies as well as the viscous behaviour was comparable to previous studies focusing on the physicochemical features of UHV-alginates as well and suggests a robust analysis (Storz et al., 2010).

It was not clear how freeze printing would affect the elastic behaviour of the alginate network, especially when such extensive pore formations took place (Figure 4.10). The analysis of gelled scaffolds indicates a solid but elastic gel, due to the dominant, constant storage modulus, which is typical for solidified polymer networks. The increasing loss modulus correlates with the higher energies introduced through higher frequencies. Intersections of G’ and G’’ as seen

at higher frequencies are caused by frequencies overcoming the relaxation time of the gel, thus not allowing enough time for the gel to fully return to its original state.

The concentration dependent increasing storage modulus also indicates that higher concentrated gels are able to handle higher deformation energies before breakage (Figure 4.16, D). Although, the absolute difference cannot be assessed with this method, it enables drawing qualitative conclusions. Concerning the use as a cardiac *in vitro* model the freeze printed patches offer a highly elastic behaviour over a wide range of introduced deformation energy. The relatively small difference in storage modulus between the 0.7% and the 1.0% condition could be caused by the porous macrostructure, which could have masked the hydrogel behaviour in this analysis. Since, this method measures the introduced and returned deformation energy; a macroscopic structural component could have influenced the read-out. It is possible that the pores led to a macroscopic honeycomb-like architecture, which behaves in a spring-like fashion, minimizing the differences in storage modulus, while the loss modulus showed linear increase with UHV-alginate concentration.

The ability of the 3D printed scaffolds to allow deformations and to return to its original shape afterwards could represent an advancement from the earlier experiments, which relied on fixed substrates. If the higher movement ranges and the higher flexibility of the scaffolds translated into a physiologically relevant self-organisation and more matured phenotypes was investigated in the following experiments.

The Heart Patch, a potential in vitro model for the human myocardium

The culture of hPSC-CMs on the disc shaped scaffolds has been conducted for 60 days to assess the cellular behaviour after a long culture time, allowing beneficial and adverse effects to fully develop. The relatively long culture time is normally not achieved on PS without passaging and very often, partial or complete detachment of the cell layer from the PS substrate was observed in this work. After a week of culture, macroscopic synchronous contractions have been observed (Figure 4.17). The delayed occurrence of this large force generation, suggests, that self-organisational processes were needed to transform the individual contractions into a simultaneous, concerted contractile action. Additionally, the macroscopic contractions indicate a maturation of the intracellular contractile machinery to exert the forces needed to overcome the resistance of the bulk UHV-alginate volume. The contraction timing was fast but also allowed a steady increase of the contraction force until the scaffold was contracted.

Noteworthy, the return movement took longer than the contraction. If this was only due to a slower hydrogel movement or if the passive tension of cardiomyocytes had an effect on that observation must be further investigated. The eccentric work exerted by the cardiomyocytes already represents a significant advancement compared to the isometric workload in

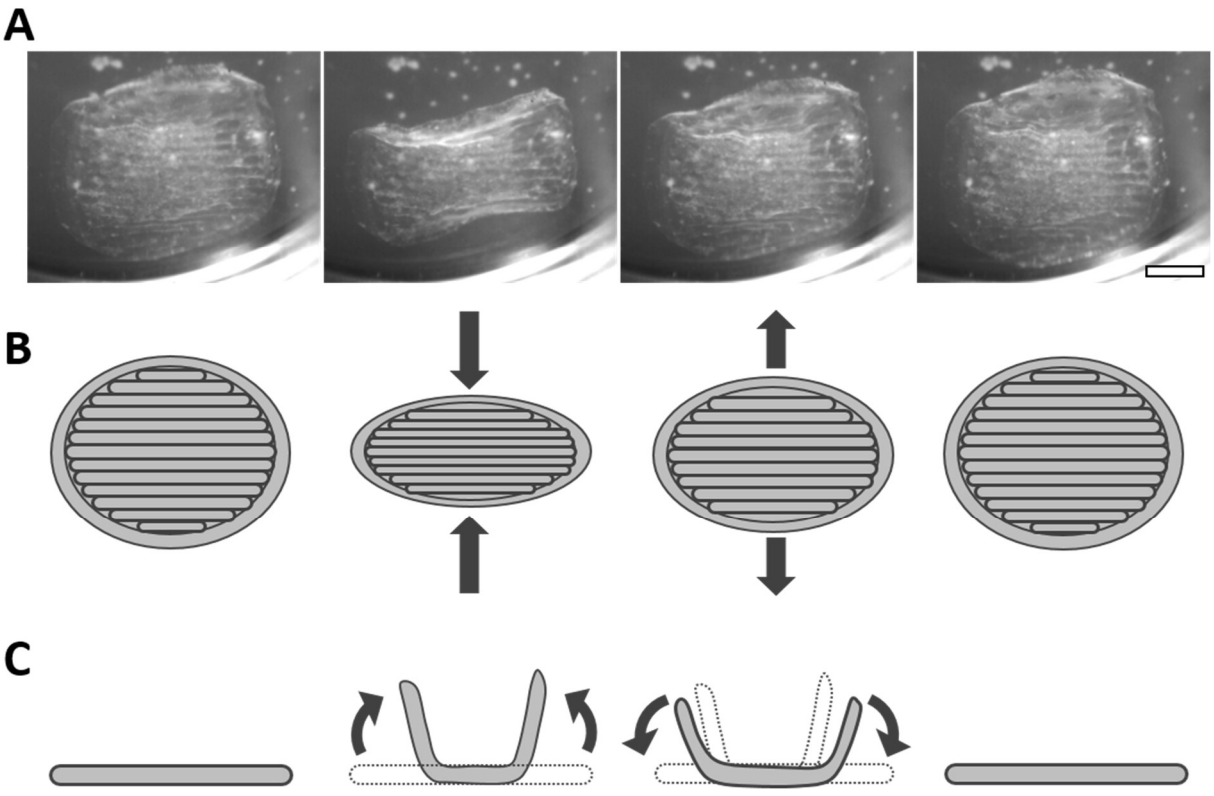

Figure 5.5 Collective force generation leads to macro contractions.
After an initial reorganisation phase, hPSC-CMs collectively generate enough force that macro contractions, visible with the bare eye are executed (A). During these contractions, the cell-UHV-alginate construct is not only horizontally compressed as the top view documentation would suggest (A and B), but is also bended (C). Thus, a complex contraction-relaxation work loop is realised. Scale bar in A represents 2mm.

conventional PS-based systems (van Meer et al., 2016). The long culture duration in concert with synchronous macro contractions and a wide contractile movement range led to the name the Heart Patch (abbr. HP) as a combination of free-floating UHV-alginate-based scaffolds with hiPSC-CMs.

In contrast to fixed substrates, the HP leads to significantly different resistances for the cells to overcome. Whereas layers only exert a force contrary to the contraction axis, the movement of the HP, additionally needs medium (indicated by "Fluid" in Figure 5.6, B) to be pushed away. The dynamic work against hemodynamic resistances (light grey arrows in Figure 5.6, B) is a relevant parameter of the human heart, especially in the context of pressure volume relationships and maturation of the conductive system (Ratshin et al., 1972; Reckova et al., 2003; Sagawa, 1981). While this work focused on the cellular reaction, particularly maturation, this setup could be used to simulate specific physiological and pathological conditions of the myocardium. Especially, the potential to simulate different resistances in the myocardium wall by adjustment of the biopolymer stiffness could provide valuable insights into effects on the cellular level. The higher movement range also translates to the cellular level, in which the cardiac cells are allowed to contract over the full range even when stiffer matrices are used.

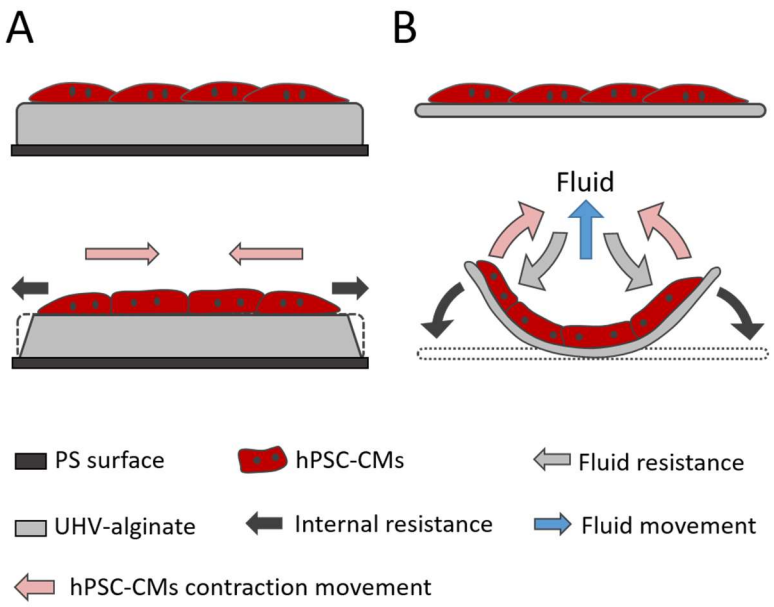

Figure 5.6 Conventional, two dimensional culture formats and the HP system differ in their dynamic resistances exposed to hPSC-CMs during contractions.
When cultured on fixed, contractile substrates, hPSC-CMs have to overcome the polymer networks' internal resistance to exert a contraction movement (grey arrows) (A). Contractile work (red arrows) on the HP has to overcome the internal resistance (dark grey arrows) as well as the hydrodynamic resistance (light grey arrows) of water (blue arrow) to enable macro contractions (B).

The investigation of the HP culture on hPSC-CMs initially focused on the sarcomeric arrangements. A high intra- and intercellular alignment of the α-actinin bands was observed in the HP condition, indicating a high degree of self-organisation (Figure 4.18). This highly matured sarcomeric structure already has a very high resemblance to the intracellular organisation of primary human cardiomyocytes. Since, the maturation of the intercellular component is presumably the reason for the macroscopic contractions (because small groups of cells cannot create enough force to induce macroscopic contractions), this enhanced

intercellular sarcomeric arrangement is assumingly induced collective alignment for a major contraction direction.

In comparison to the HPs, the fixed layers also showed a high degree of intracellular sarcomeric organization but the alignment between cells was putatively lower (Figure 4.18). A high signal for α-actinin was observed at the cell borders. It can be assumed that this was caused by compensatory mechanisms, which reacted on the strong forces exerted by neighbouring cells. When such forces are produced and the substrate allows only limited contractile movement, then the cell borders will be strengthened. The fact, that the fixed layers enabled the cells to exert a contractile movement without a dominant directionality could be the cause for the lack of uniformity.

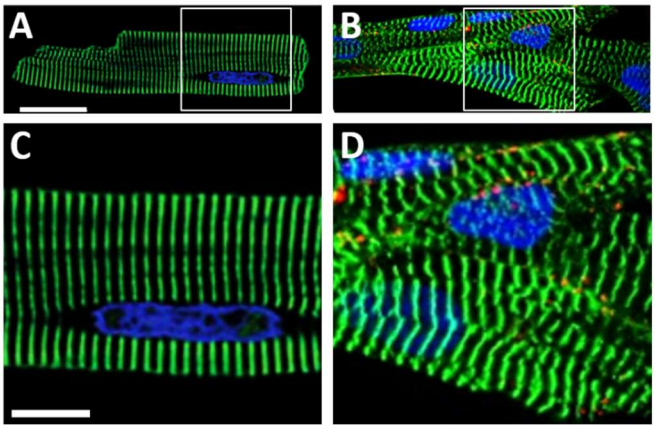

Figure 5.7 The HP leads to sarcomeric structure with high resemblance to adult human cardiomyocytes.
Fully mature, adult human cardiomyocytes possess extremely aligned sarcomeres (A and C). Human iPSC-CMs culture on the HP (B, D) induces inter- and intracellular alignment similar to primary human cardiomyocytes. (White scale bar = 25µm in A and B. White scale bar = 10µm in C and D).

On the stiff PS substrate the cells exhibit sarcomeric structures with lower intra- and intercellular alignment, due to the lack of a real contraction movement (Geach et al., 2015). Furthermore, it is suggested that the exerted force is compensated intracellularly, leading to lowering cellular integrity and cell viability over time (Heras-Bautista et al., 2014). In addition, stress fibres have been observed regularly in hiPSC-CMs on PS, due to the integration of α-actinin into these actomyosin bundles. The cellular cytoskeleton is essential in environmental mechanosensing, which influences determination of stem cell lineage determination (Discher et al., 2005; Engler et al., 2006; Happe et al., 2016). Stress fibres are a sign of a disturbed physiological homeostasis of the cytoskeletal machinery and their appearance is associated with either immaturity or disease (Bedada et al., 2016; Young et al., 2015). The stress fibres found in the PS condition were mostly located in cells at the boundary of the cell layer. A potential mechanism for their occurrence at this specific location is presumably caused by the contractile pull exerted by neighbouring cells (Figure 5.8, B and C). Thus, limiting a homogenous maturation of the sarcomeric apparatus of hPSC-CMs on extremely stiff substrates. In addition, the stress-fibre-like precursors of myofibrils in neonatal cardiomyocyte exhibit a morphologically comparable phenotype further underlining the association with immaturity (Figure 5.8, E) (Tojkander et al., 2012).

Functional integrated connexons are essential for contraction synchronisation and electrical coupling of cardiomyocytes. The staining against Cx43 did not reveal significant differences between the HP, fixed UHV-alginate layers and PS condition concerning the Cx43 localisation. Often cells on the PS condition had no detectable Cx43 (Figure 4.18 and further quantitative analysis of Cx43 frequency could reveal Cx43 promoting mechanisms or a selective pressure towards Cx43 harbouring cells on the contractile substrates.

In vivo, Cx43 distribution correlates with desmosome localization in the left ventricle, whereas in the myocardial trabeculae the expression is more disorganized (Kempen et al., 1991). Thus, it could be speculated that the HP, with more widespread integration of Cx43 in the cell membrane, reflects more the trabeculae type, but this could also point to the immature state in general and has to be substantiated further (Bedada et al., 2014). Furthermore, Cx43 is not universally expressed in the heart; the atria as well as the sinoatrial node rely on different connexins forms (Gaborit et al., 2007; Kempen et al., 1991; Kostin et al., 2004). The observed higher incidence of cells without Cx43 could represent a subpopulation of atrial cells or sinoatrial cells. However, if a selection process took place is not clear and has to be analysed extensively. The loss of Cx43 could also represent a dedifferentiation of the cardiomyocytes, which is known occur in PS cultures (Ausma et al., 2002; Dispersyn et al., 2001).

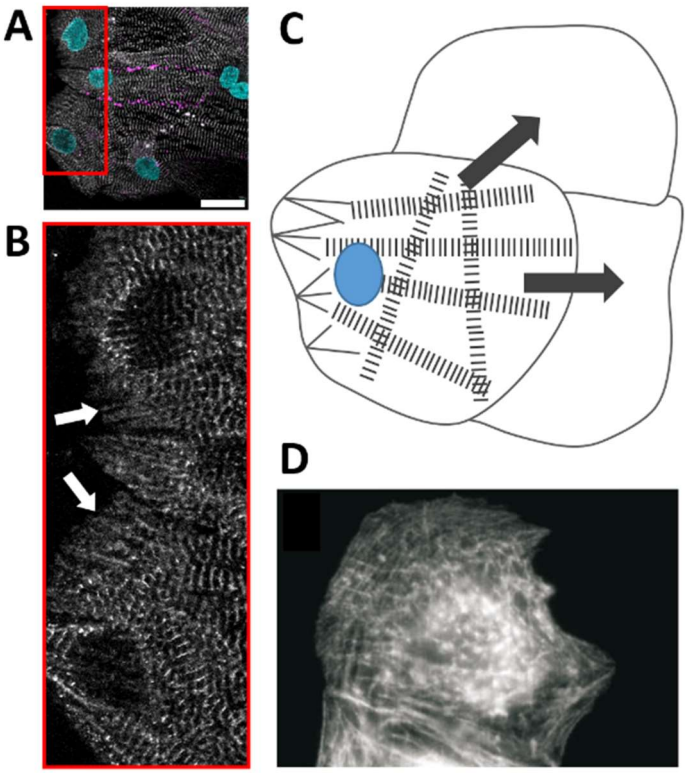

Figure 5.8 Schematic representation of late stress fibre localisation at the cell layer boundaries.
Stress fibres and non-organized α-actinin found in hiPSC-CMs grown on PS (A, B). The cell layer boundary to the left must compensate the pull (grey arrows) exerted by contracting, neighbouring cardiomyocytes to the right, inhibiting sarcomere development in the outer cells (C). The late stress fibres observed in this work have a high resemblance to stress-fibre-like precursors of myofibrils in cultured rat neonatal cardiomyocytes (D). Image D modified from Tojkander et al. 2012.

Since an immature cytoskeleton directly correlates with an immature, fetal-like phenotype it can be assumed that the structural maturation observed on the contractile substrates (Layers and HP) represents a significant progress from the disorganized structural phenotype observed on PS (Bedada et al., 2016; Young et al., 2015) (Figure 5.10). The optical assessment of the sarcomeres indicates that the higher movement range in concert with the dynamic

resistances generated during the deformation of the patch fosters the maturation of the cytoskeleton even more than on fixed, contractile surfaces. Furthermore, the need for the cells to organise and harmonize their contractile machinery to create macro contractions and the ability to maintain them over long periods suggests that the HP represents a highly relevant *in vitro* model. Since a long and gradual development from immaturity to maturity is seen *in vivo*, it can well be that a long time is also needed *in vitro* to create fully mature cardiac models (Figure 5.10). While the HP is still not fully recapitulating fully mature sarcomeric arrangements, the progress is in the right direction and it will be the sum of such small steps, which enable the future adult myocardium in a petri dish.

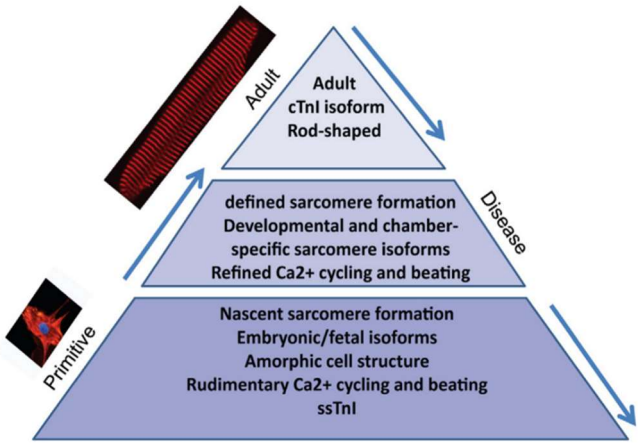

Figure 5.9 Nascent sarcomere formation is associated with cardiac immaturity.
Cardiomyocytes develop from small round cells with an early and disorganized cytoskeleton to rod shaped, elongated cells with extensively organized sarcomeres. Image modified from Bedada et al. 2016.

Cardiomyocyte immaturity is not restricted to the cytoskeleton alone and encompasses gene expression patterns, the metabolism and electrophysiology. Thus, gene expression analysis of relevant genes was conducted (Figure 4.19). RNA from an adult human myocardium served as a control for complete maturation. *CACNA1C* translates into the alpha 1 C subunit of the L-type, voltage-gated calcium channel (Cav1.2), which counterbalances the fast depolarizing sodium current upon cardiac depolarization. No significant differences regarding mRNA frequencies have been found, albeit a small trend towards higher expression was detected in the 0.7% and 1.0% HP samples. In comparison, a two-fold higher expression in the adult heart was found, but it can be disputed if that small discrepancy really translates to the protein level. *KCNH2* encodes for the alpha subunit of the potassium channel Kv11.1 and is also named hERG (human ether-a-go-go related gene) for its leg shaking phenotype in Drosophila melanogaster upon etherisation (Kaplan et al., 1969; Vandenberg et al., 2012). Point mutations in this gene are associated with long QT syndrome and the channel is regularly affected by drugs leading to drug-induced arrhythmias (Modell et al., 2006; Sanguinetti et al., 1995; Vandenberg et al., 2012). The expression pattern in fixed scaffold samples was comparable to the adult heart control, but two-fold higher in the soft (0.3% and 0.7%) HP samples. On the HP samples, a slight trend correlating with stiffness is visible, but the small differences requires further analyses to draw meaningful conclusions. Nevertheless, ion channels are regionally expressed in the human heart and it can be hypothesized that matrix elasticity or the higher contraction/ stretch movement on the HP could have an influence on the expression of those (Gaborit et al., 2007). In addition, there are two more channels in the Kv11.x family (Kv11.2 and Kv11.3).

An analysis of the expression of those in concert with protein content measurements could clarify, if the channel density is smaller on fixed scaffolds or if an alternative channel composition is favoured (Vandenberg et al., 2012). *RYR2* encodes for the cardiac ryanodine receptor type 2, responsible for the intracellular Ca^{2+} release from the SR into the cytoplasm (Bootman, 2006; Fearnley et al., 2011; Itzhaki et al., 2006). It is essential in excitation-contraction coupling and guarantees effective and homogenous distribution of intracellular Ca2+ (Fearnley et al., 2011; Louch et al., 2015). The localization and density of *RYR2* is highly associated with a mature and physiological phenotype (Louch et al., 2015). Gene expression analysis revealed a significantly higher expression of *RYR2* on both, HP and fixed scaffolds, compared to PS. The expression was slightly higher when HPs were used, which could be induced by the maintenance of the extensive sarcomeres on the HP. These findings indicate a more matured cytoskeletal arrangement, but when compared to the adult myocardium also underline that full maturity is not reached at the gene expression level. This is especially evident in the case of *S100A1*, a gene encoding for a highly conserved protein crucial for contractile performance and calcium handling (Kraus et al., 2009; Wright et al., 2009). HPSC-CMs grown on the HP and fixed scaffolds exhibit a ten-fold higher expression compared to PS, which represents a significant advancement, but it is still ten-fold lower than the expression in the adult human myocardium. The strong difference between the *S100A1* discrepancy and the other assessed genes, could hint at another factor, which limits its expression. Since the metabolism of hiPSC-CMs is still immature, the main energy input comes from the glucose rich medium and it can be speculated that the switch to a fatty acid-based metabolism as seen in adult cardiomyocytes could induce the expression. The lower values in the 0.3% HP condition cannot be simply explained, but several findings in this work suggest that the softest substrates were, in their biological outcomes, “closer” to the PS condition, at least in specific parameters. The beating frequency of 0.3% layers for instance is closer to the PS condition (Figure 4.5). Only further experiments can exclude a random correlation here, but *S100A1* is known to contribute to diastolic performance and interacts with titin, a protein with the capacity to sense passive tension intracellularly. This interaction could offer an causal explanation, because passive tension sensing is assumedly disturbed on stiff PS, where no real contractile movement can be exerted (Granzier et al., 1995, 2004; Wright et al., 2009; Yamasaki et al., 2001).

Titin is encoded by *TTN* and interacts with telethonin a protein encoded by *TCAP*. Titin expression levels of HPs were similar to the adult heart control and the 0.3% UHV-alginate layer condition. The lower expression on stiffer fixed layers supports the idea, that a sufficient contractile movement range must be available for the cells to mature their cytoskeleton. Additionally, there is a small stiffness-dependent trend in HP samples visible, indicating higher expression levels on softer substrates. This would be in accordance with the common belief, that titin is responsible for the passive stiffness of cardiomyocytes, which has to be upregulated on soft substrates. A chronical analysis of *TTN* expression could reveal the early spike in expression needed for sarcomere genesis after detachment and following attachment on the HPs. Additionally with such an experiment, discrimination between an ongoing

sarcomere synthesis and remodelling could be conducted. Telethonin is critical for myofibrillogenesis and sarcomere integrity and is similarly expressed on all contractile substrates (Gregorio et al., 1998; Mayans et al., 1998). The lower expression on PS highlights again the need for cellular *in vitro* models enabling contractile movement. Desmin expression is also elevated on both, fixed scaffolds and the HPs. Further substantiating the beneficial effect on cytoskeleton-associated proteins and structures. *TNNI1* and *TNNI3* encode for slow skeletal troponin I (abbr. ssTnI) and cardiac troponin I (abbr. cTnI).

Previous studies have suggested that a stoichiometric change from ssTnI to cTnI follows maturation from fetal to adult cardiomyocytes (Bedada et al., 2014). Bedada et al. also showed a high correlation between mRNA and protein levels and found no cTnI protein in long-term cell cultures of PSC-CMs. *TNNI3* levels on fixed scaffolds were ten-fold upregulated compared to PS and reached levels of the adult myocardium, whereas the HP samples exhibited slightly smaller expression levels (approx. two- fold downregulated). In accordance with the findings of Bedada et al., *TNN1* was significantly downregulated in UHV-alginate layers and the adult human heart. Contrary to these samples, a significant upregulation of *TNNI1* expression was detected in all HP samples. Furthermore, a clear stiffness correlation can be spotted in both the fixed scaffolds and the HPs, but with an inversed directionality. The HP samples exhibited higher *TNNI1* expression on softer substrates, while on UHV-alginate layers, the expression was lower on softer substrates. This has not been reproduced in other studies, but the robustness of the findings over all conditions and the low variances suggest that this is not an artefact. Furthermore, it indicates an overall higher amount of *TNNI1* and *TNNI3* mRNAs in HP samples, which is not substantiated by the study of Bedada et al. Since the PS group served as a reference, one could speculate that this condition leads to lower mRNA abundance of cTnI and ssTnI. However, the inversed correlation of cTnI and ssTnI in the adult heart and UHV-alginate layer samples indicated a more a unique situation in the HP group.

To investigate this effect further and to exclude posttranscriptional modifications, western blotting has been performed to assess the amount of cTnI and ssTnI proteins (Figure 4.20). The results show that, contrary to the gene expression profiling, the proportion of cTnI from the total troponin I amount is higher in the HP condition than in hPSC-CMs grown on PS and UHV-alginate layers. The stark difference between protein content and mRNA frequency in HP samples could be caused by processes, which require both troponin I forms. It can be hypothesized that the HP represents a dynamic environment, which promotes constant adaption of the sarcomeric alignment and reorganization. This process would cause the cytoskeleton to constantly resynthesize and rebuild, which needs ssTnI to be incorporated first and since the microenvironment does not change immediately, maturation induces the replacement by cTnI. Thus, sarcomere synthesis and maturation would simultaneously happen in the cardiomyocytes, in a dynamic manner (Figure 5.10). This hypothetical state of an dynamic maturation could explain the differences compared to the other conditions, which would not require a constant adaption and only need maintenance of their protein structures with little dynamic change. Additionally very early in development (fetal; Figure 5.10) and in the adult stage (adult, Figure 5.10), very little amounts of either cTnI or ssTnI are needed,

because only one isoform is abundant (Figure 5.10). When a dynamic maturation is assumed, constant supply of both, cTnI and ssTnI, would be needed and the total mRNA abundance would be higher compared to the other conditions.

The reversed correlation with the substrate stiffness could also be explained, since softer substrates are more prone to deformations that shift the prominent contraction direction. Thus, more sarcomere synthesis causes an increased *TNNI1* expression. Although the hypothesis assumes that, the abundance of cTnI and ssTnI protein and mRNA is not constant under certain circumstances, the earlier studies using hiPSC-CMs could not find proof of such an intermediate stage or a total increase of troponin I abundance. However, they mainly focused on a cell model cultured on PS that neglects the dynamic processes involved during development and training.

The use of a decellularized extracellular matrix to induce cTnI expression led to a higher sarcomeric arrangement, but could not induce or increase cTnI expression (Bedada et al., 2014). Reason for this are presumably cell line specific, since in the presented work even hPSC-CMs grown on PS expressed *TNNI3*. Noteworthy, a study conducted in mice reported such an intermediate stage with elevated total troponin I mRNA abundance, indicating that such a transitional stage is taking place during development. A quantitative analysis focusing on the immunocytochemical staining of both isoforms in the cell would enable further conclusions, particularly about the localisation, the stability and ultimately about the functionality. The culture on contractile substrates allows hPSC-CMs to contract freely, minimizing intracellular stress and adverse structural remodelling of the cytoskeleton.

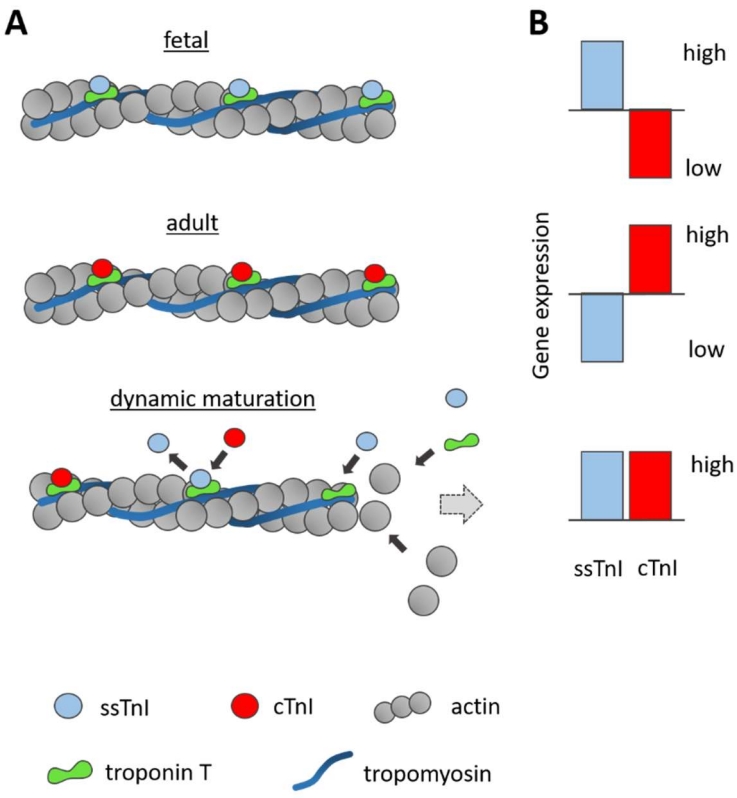

Figure 5.10 A hypothetical dynamic stage could explain the differing gene expression pattern of troponin I isoforms on the HP. During development, cardiac thin filament architecture is strictly regulated and fetal ssTnI is replaced by cTnI during maturation in the neonatal phase (A). Upon reaching adulthood, cTnI fully replaces ssTnI. Gene expression profiling and protein detection suggest a transitional state in the HP. This state could reflect an intracellular dynamic maturation, where sarcomere formation and maturation are simultaneously executed. The mRNA levels of cTnI and ssTnI correlate with the troponin I protein levels (B). The depicted hypothesis is an extended model of the ssTnI/cTnI switch suggested by Bedada et al. (2014).

Additionally, sarcomeric structures show enhanced intracellular alignment. The use of the HP platform, increases the intracellular alignment further and additionally fosters intercellular alignment and cooperative force generation. When grown on either UHV-alginate layers or the HP, hiPSC-CM exhibit a more mature gene expression pattern, particularly of cytoskeleton-associated genes. However, the HP seems to induce a highly dynamic state with simultaneous sarcomere synthesis and maturation. This represents a unique feature, which could enable future research to resolve the mechanism behind the troponin I isoform switch and the associated maturation processes. Characterisation of cardiomyocyte contractile behaviour and responses upon drug exposure are often assessed by electrophysiological methods. These allow the rapid characterization of underlying molecular mechanisms and an adequate evaluation. Since such analyses normally need close contact of the cell membrane to the electrodes, a proof of concept study was conducted to explore the feasibility of such measurements on the HP.

Electrophysiological assessment of the Heart Patch is feasible

To assess the possibility to derive electrophysiological measurements from hPSC-CMs grown on the HP, a proof of concept study was conducted using a multi-electrode-array (abbr. MEA) chip with fine pores used for characterisation of tissue slices (Figure 4.21). Thus, the HP could be hold in close contact to the electrodes. In comparison with hPSC-CMs that were cultured on the MEA chip, the conduction velocity was rather low with 1.5cm/s. The reported velocities for the primary cardiomyocytes are approx. 100cm/s and thus both the MEA Ctrl and the HP samples exhibit very immature conduction velocities (van Meer et al., 2016). Upon stimulation with 100nM isoprenaline the velocity of the HP increased by 50%, while the MEA Ctrl only showed a very small raise. The latency on the other hand decreased slightly in both conditions. It can be assumed, that the inotropic response of the cardiomyocytes to isoprenaline leaded to the Heart Patch contracting further towards the MEA, resulting in a better contact of cells and electrodes. The field potential in the unstimulated condition was also very low in the HP (Figure 4.21, E). Upon beta-adrenergic stimulation, the HP experienced a FP increase of up to three fold, whereas the FP of the MEA Ctrl increased by approx. 25%. Since only one sample per condition was studied, the measurement does not allow drawing definitive conclusions. Nevertheless, it is crucial for any *in vitro* platform to enable scientist to characterise and assess key parameters of cardiac integrity. Furthermore, the high relative gain in velocity and FP could indicate a higher sensitivity towards specific stimulations, which could be advantageous particularly in the context of drug toxicity screenings. For a robust assessment of HP electrophysiology, further experiments with more biological replicates are mandatory.

Long-term cultures of hiPSC-CMs are feasible on the Heart Patch

The present work focused on a culture period of two months. However, the ability to perform even longer cultures also enables to study processes, which are progressively exhibited *in vivo*. Particularly the research of aging and degenerative processes would benefit from such an *in vitro* model. To demonstrate the possibility to culture hiPSC-CMs for a longer culture period, HPs with either uniform stiffness (0.3% or 1.5%) or alternating stiffness were used. Such controllable gradient in matrix elasticity could serve as a basis for future *in vitro* models which recapitulate the stiffness gradients in failing, scarred hearts. That way the slow and adverse progression could be studied *in vitro* on human heart cells. Until the date of this work, the experiment was running for slightly longer than six months. Again, modulations of the beating frequency were visible overtime with all groups beating slower than 30bpm. The alternating stiffness group resulted in a breakdown of the macroscopic contractions after three months. However, the cell viability all conditions was maintain throughout the full culture duration, as seen by the small patches of contracting cells. If the disruption of the cell layer was mediated by an imbalance of the forces exerted by the cardiac cells translated by the different elasticities or if the substrate of the 0.3% alginates destabilised more must be analysed in future experiments. Nevertheless, this represents a promising setup for the development of an *in vitro* model for such heterogeneous matrix elasticities as seen in aging and myocardial scarring after AMI.

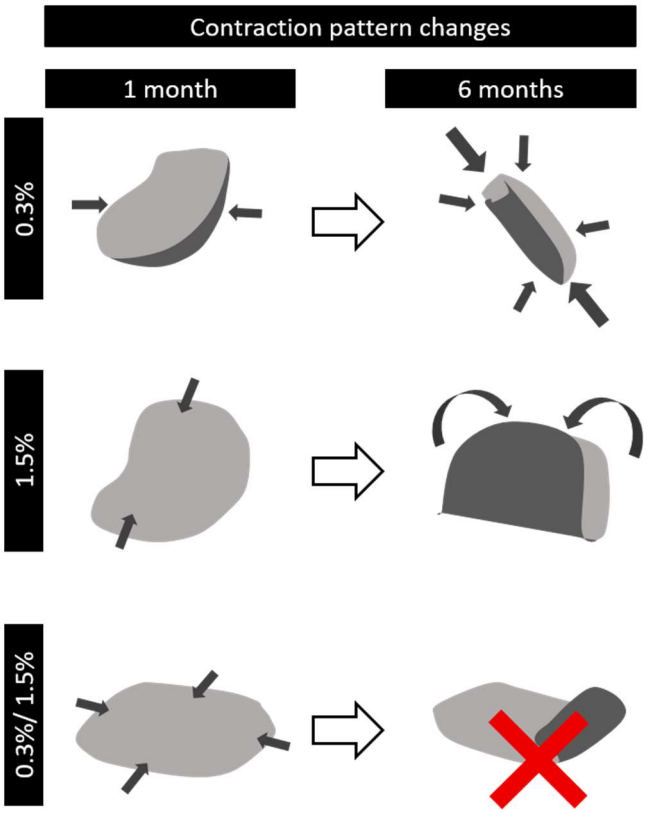

Figure 5.11 Long-term cultures of the HP lead to changes in contraction patterns and scaffold deformations.
During a six month culture period, the macro contraction are strengthened on HPs with uniform elasticities. Breakdown of the macro contractions was observed on heterogeneous scaffolds after 3 months (indicated by a red cross). After six months the scaffolds are deformed into a wrap-like structure (0.3%) or folded along a middle axis (1.5%).

Apart from the breakdown of macroscopic contractions, a stiffness dependent deformation was observed. The uniform scaffolds exhibited similar contractions, following a dominant axis (Figure 5.11). Concerning the heterogeneous scaffold, there, the contraction led to a horizontal compression of the bulk volume and on little bending was observable at the edges. This was presumably mediated by the stabilising influence of the 1.5% UHV-alginate strands,

because these strands were more rigid compared to the soft 0.3% UHV-alginate strands. After 6 months, the softest scaffolds showed a wrap like deformation along the previous contraction axis, but exhibited now an orthogonal shifted major contraction axis. The 1.5% condition did not experience such shift, contrary, the contraction along the original axis was enforced. Before the macro contractions dissipated into small microscopic contraction of the alternating scaffolds, a very heterogeneous contraction pattern was observed. One side of the scaffold folded and rolled up and the contraction direction was orthogonal to the fold, whereas the unfolded part still exhibited contraction without bending of the scaffold. Although this small-scale experiment proofed the feasibility of long-term experiments using the HP, functional conclusions about the heterogeneous elasticities have to be seen with caution, due to the small number of replicates and the unresolved variability. However, this behaviour was never observed in previous experiments with uniform HPs. Nevertheless, the breakdown of the macro contractions through loss of intercellular organisation and contacts in the alternating stiffness condition could serve as an interesting starting point for future mechanistic studies, specifically for scarred myocardia models, since this pathology is known to be accompanied by drastic matrix rigidity differences.

The use of hPSC-CMs in *in vitro* modelling of the cardiac niche or for therapy makes a parallelizable and robust workflow for the generation of high numbers of cells with limited hands on time necessary. The presented work combined highly efficient and robust differentiation protocols with small-scale bioreactors to produce relevant cell numbers per vessel and induction. Since the media volume can be adjusted from 10 to 50ml, this setup offers a high flexibility in terms of cost and labour. Thus, this workflow represents a valuable method for the production of cardiac cells in small academic laboratories and patient-specific cell therapies. The presented papain-based dissociation method focused on the widespread problem of spheroid dissociation and revealed that papain, a dissociation enzyme traditionally used in primary cell cultures, resulted in high dissociation efficiencies with high preserved cellular viability. Furthermore, it was shown that the use of contractile substrates promotes cardiomyocyte maturation, particularly the structural intracellular components of the cytoskeleton, *i.e.* sarcomere alignment and organization. In addition, the gene expression pattern of sarcomere-associated genes resembled more the situation *in vivo*. The acquisition of calcium transient data in concert with optical-based relative force measurements revealed inotropic and chronotropic responses upon beta-adrenergic stimulation with isoprenaline and demonstrated a higher force exertion not recapitulated in the calcium measurements. This could represent a valuable analysis platform for drug screenings and disease modelling in concert with a high automation and parallelization potential.

A novel method for the three-dimensional deposition of hydrogels was developed and hydrogel formulae with viscosities as low as 0.17Pa*s have been printed in a three-dimensional manner using a commercially available 3D printer. The method does not rely on the addition of additives and requires no readjustment of the equipment. The possibility to introduce different biopolymer compositions in the same scaffold enables the investigation of such heterogeneous matrices on biological systems. The transition from a

fixed culture platform with limited contractile range to the Heart Patch, which offers a wide movement range independent of the substrate stiffness, further enhanced the structural and genetic resemblance to adult human myocardia. Particularly the abundant sarcomeres with high inter-and intracellular alignment was of high morphological similarity to primary human cardiomyocytes. Although the discrepancy between *TNNI1* and *TNNI3* gene expression and ssTnI and cTnI abundance at the protein level has not been reported before, the presented dynamic maturation theory in combination with reported similar states found *in vivo* could represent a valid hypothesis for the observed effects. Furthermore, this indicates that the HP could serve as a unique *in vitro* model to study the underlying developmental processes. The possibility to acquire electrophysiological data from the HPs could expand such mechanistic studies and will provide valuable data in drug screenings or when using disease-specific cell lines. Additionally, long-term cultures, without the need for cell passaging, are feasible on the HP and highlight the high biocompatibility and the lowered physical stress on cardiomyocytes compared to cultures on stiff substrates. The long culture duration over the course of several months enables the assessment of drug or chemicals exposures in a highly controllable environment. In an aging society, such long-term *in vitro* models could lead to specific cell model systems recapitulating the processes during ageing in a petri dish.

6 OUTLOOK

The presented work focused on the production of hiPSC-CMs, their dissociation and their use in the production of an *in vitro* model of the cardiac niche. The scalable force measurements conductible in a conventional lab environment, without the need for specific equipment, could provide a valuable addition to conventional analyses, because it enables the investigation of disease states and drugs on force generation in concert with calcium transient measurements. The potential to correlate these two parameters allows for a faster localization pathological or physiological processes and fosters deeper insights into these. The freeze printing method enabled the creation of individualized scaffolds, which offers the possibility to transport and transplant such cell-hydrogel constructs in the future. Such patch-based approaches have been shown to enhance the cardiac performance after AMI *in vivo* (Ye et al., 2013). While this extensive evaluation *in vivo* would have gone past the scope of this work, the experimental exploration of the biocompatibility of the HP in an animal model is highly interesting. In addition, the ability of the host circulatory system to infiltrate and support the hiPSC-CMs on the HP through angiogenesis is crucial for clinical applications, particularly for transplantations, and should be investigated. The coupling to the circulatory system could also be enhanced by additional factors (*i.e.* VEGF), either dissolved in the hydrogel or by using carriers (*i.e.* nanoparticles). To minimize the impact and to enable live microscopic evidence the skin chamber assay in mice would represent a valuable first experimental setup. The second stage could be an ischemic mouse model to evaluate the therapeutic potential of the HP to halt the adverse processes and restore the function of IHD-affect myocardia (Figure 6.1). Using UHV-alginates could also prove as a valuable functional coating for assist devices (*i.e.* artificial pacemakers and ventricular assist devices), which are already in clinical use, to enhance the engraftment and limit fibrotic processes. The possibility to structure UHV-alginates in 3D could also be extended to other biopolymers, in particular, natural extracellular matrix components, *e.g.* collagens, laminins and hyaluronic acid. The

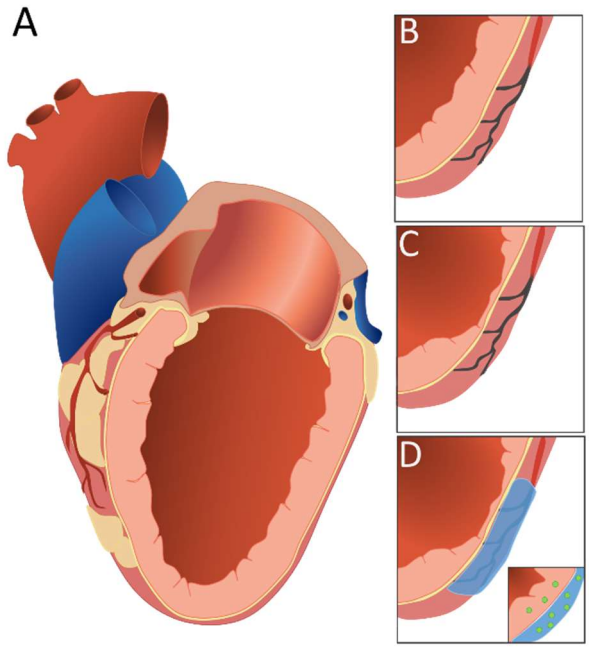

Figure 6.1 A possible application of UHV-alginate-based scaffolds is the transplantation onto an ischemic heart disease affected heart.
The healthy myocardium (A) is affected by ischemia-induced necrosis (B and C). The advantageous biocompatibility of UHV-alginates and optimized localization of matured hiPSC-CM potentially induces regenerative mechanisms through paracrine signalling and angiogenesis (D).

limiting factor herein is the crosslinking kinetics, which are generally slower than the thawing process, but specific crosslinkers with adapted thawing protocols could make such artificially freeze-printed matrices feasible. The ability to combine those polymers and to create specific three-dimensional structures using only a conventional 3D printer could allow for mechanistic experiments concerning the cellular response on varying substrates and different physicochemical cues. Furthermore, the creation of UHV-alginate-based scaffolds with tuneable stiffness can be adapted to the needs of many clinically relevant cell types, *e.g.* skeletal muscle, neuronal and chondrogenic cells. Hence, the spectrum of tissues, which could be potentially targeted, has not been fully covered yet. At last, the potential to structure the biopolymers three dimensionally could also be used in applications, which are not limited to the biological field. In particular, soft robots could be produced with the aforementioned methods and potentially utilized in a wide range of applications, from temperature and force sensors to biomimetic and magneto responsive hydrogel actuators (Banerjee et al., 2018).

7 REFERENCES

Adrian, R.J., 1984. Scattering particle characteristics and their effect on pulsed laser measurements of fluid flow: speckle velocimetry vs particle image velocimetry. Appl. Opt. 23, 1690.

Alink, G.M., Agterberg, J., Helder, A.W., Offerijns, F.G.J., 1976. The effect of cooling rate and of dimethyl sulfoxide concentration on the ultrastructure of neonatal rat heart cells after freezing and thawing. Cryobiology 13, 305–316.

Anderson, D., Self, T., Mellor, I.R., Goh, G., Hill, S.J., Denning, C., 2007. Transgenic enrichment of cardiomyocytes from human embryonic stem cells. Mol. Ther. 15, 2027–2036.

Anderson, P.A.W., Malouf, N.N., Oakeley, A.E., Pagani, E.D., Allen, P.D., 1991. Troponin T Isoform Expression in Humans. Circ. Res. 69, 1226–1233.

Ando, H., Yoshinaga, T., Yamamoto, W., Asakura, K., Uda, T., Taniguchi, T., Ojima, A., Osada, T., Hayashi, S., Kasai, C., Miyamoto, N., Tashibu, H., Yamazaki, D., Sugiyama, A., Kanda, Y., Sawada, K., Sekino, Y., Ando, H., Yoshinaga, T., Asakura, K., Osada, T., Hayashi, S., Kasai, C., Tashibu, H., Sugiyama, A., Sawada, K., Sekino, Y., Ando, H., Uda, T., Yoshinaga, T., Taniguchi, T., Ojima, A., Shinkyo, R., Kikuchi, K., Miyamoto, N., Sawada, K., Yamamoto, W., Asakura, K., Hayashi, S., Osada, T., Kasai, C., Tashibu, H., Yamazaki, D., Kanda, Y., Sekino, Y., Sugiyama, A., 2017. A new paradigm for drug-induced torsadogenic risk assessment using human iPS cell-derived cardiomyocytes. J. Pharmacol. Toxicol. Methods 84, 111–127.

Ando, M., Nishimura, T., Yamazaki, S., Yamaguchi, T., Kawana-Tachikawa, A., Hayama, T., Nakauchi, Y., Ando, J., Ota, Y., Takahashi, S., Nishimura, K., Ohtaka, M., Nakanishi, M., Miles, J.J., Burrows, S.R., Brenner, M.K., Nakauchi, H., 2015. A safeguard system for induced pluripotent stem cell-derived rejuvenated T cell therapy. Stem Cell Reports 5, 597–608.

Ashwood-Smith, M.J., Voss, W.A.G., Warby, C., 1973. Cryoprotection of mammalian cells in tissue culture with pluronic polyols. Cryobiology 10, 502–504.

Ausma, J., Borgers, M., 2002. Dedifferentiation of atrial cardiomyocytes: from in vivo to in vitro. Cardiovasc. Res. 55, 9–12.

Banerjee, H., Suhail, M., Ren, H., 2018. Hydrogel Actuators and Sensors for Biomedical Soft Robots: Brief Overview with Impending Challenges. Biomimetics 3, 15.

Bartulos, O., Zhuang, Z.W., Huang, Y., Mikush, N., Suh, C., Bregasi, A., Wang, L., Chang, W., Krause, D.S., Young, L.H., Pober, J.S., Qyang, Y., 2016. ISL1 cardiovascular progenitor cells for cardiac repair after myocardial infarction. JCI Insight 1, 1–17.

Batalov, I., Feinberg, A.W., 2015. Differentiation of Cardiomyocytes from Human Pluripotent Stem Cells Using Monolayer Culture. Biomark. Insights 10s1, BMI.S20050.

Bedada, F.B., Chan, S.S.K., Metzger, S.K., Zhang, L., Zhang, J., Garry, D.J., Kamp, T.J., Kyba, M., Metzger, J.M., 2014. Acquisition of a quantitative, stoichiometrically conserved

ratiometric marker of maturation status in stem cell-derived cardiac myocytes. Stem Cell Reports 3, 594–605.

Bedada, F.B., Wheelwright, M., Metzger, J.M., 2016. Maturation status of sarcomere structure and function in human iPSC-derived cardiac myocytes. Biochim. Biophys. Acta - Mol. Cell Res. 1863, 1829–1838.

Beqqali, A., Kloots, J., Ward-van Oostwaard, D., Mummery, C., Passier, R., 2006. Genome-Wide Transcriptional Profiling of Human Embryonic Stem Cells Differentiating to Cardiomyocytes. Stem Cells 24, 1956–1967.

Blinova, K., Stohlman, J., Vicente, J., Chan, D., Johannesen, L., Hortigon-Vinagre, M.P., Zamora, V., Smith, G., Crumb, W.J., Pang, L., Lyn-Cook, B., Ross, J., Brock, M., Chvatal, S., Millard, D., Galeotti, L., Stockbridge, N., Strauss, D.G., 2017. Comprehensive Translational Assessment of Human-Induced Pluripotent Stem Cell Derived Cardiomyocytes for Evaluating Drug-Induced Arrhythmias. Toxicol. Sci. 155, 234–247.

Bondue, A., Blanpain, C., 2010. Mesp1: A key regulator of cardiovascular lineage commitment. Circ. Res. 107, 1414–1427.

Bondue, A., Lapouge, G., Paulissen, C., Semeraro, C., Iacovino, M., Kyba, M., Blanpain, C., 2008. Mesp1 acts as a master regulator of multipotent cardiovascular progenitor specification. Cell Stem Cell 3, 69–84.

Bootman, M.D., 2006. Calcium signalling during excitation-contraction coupling in mammalian atrial myocytes. J. Cell Sci. 119, 3915–3925.

Brandão, K.O., Tabel, V.A., Atsma, D.E., Mummery, C.L., Davis, R.P., 2017. Human pluripotent stem cell models of cardiac disease: from mechanisms to therapies. Dis. Model. Mech. 10, 1039–1059.

Brown, L., 2005. Cardiac extracellular matrix: a dynamic entity. Am. J. Physiol. Circ. Physiol. 289, H973–H974.

Buchanan, S.S., Gross, S.A., Acker, J.P., Toner, M., Carpenter, J.F., Pyatt, D.W., 2004. Cryopreservation of Stem Cells Using Trehalose: Evaluation of the Method Using a Human Hematopoietic Cell Line. Stem Cells Dev. 13, 295–305.

Burridge, P.W., Anderson, D., Priddle, H., Barbadillo Muñoz, M.D., Chamberlain, S., Allegrucci, C., Young, L.E., Denning, C., 2007. Improved human embryonic stem cell embryoid body homogeneity and cardiomyocyte differentiation from a novel V-96 plate aggregation system highlights interline variability. Stem Cells 25, 929–38.

Burridge, P.W., Holmström, A., Wu, J.C., 2015. Chemically Defined Culture and Cardiomyocyte Differentiation of Human Pluripotent Stem Cells. Curr. Protoc. Hum. Genet. 87, 21.3.1-21.3.15.

Burridge, P.W., Matsa, E., Shukla, P., Lin, Z.C., Churko, J.M., Ebert, A.D., Lan, F., Diecke, S., Huber, B., Mordwinkin, N.M., Plews, J.R., Abilez, O.J., Cui, B., Gold, J.D., Wu, J.C., 2014. Chemically defined generation of human cardiomyocytes. Nat. Methods 11, 855–60.

Bustin, S.A., Benes, V., Garson, J.A., Hellemans, J., Huggett, J., Kubista, M., Mueller, R., Nolan, T., Pfaffl, M.W., Shipley, G.L., Vandesompele, J., Wittwer, C.T., 2009. The MIQE Guidelines: Minimum Information for Publication of Quantitative Real-Time PCR

Experiments. Clin. Chem. 55, 611–622.

Cai, C.-L., Liang, X., Shi, Y., Chu, P.-H., Pfaff, S.L., Chen, J., Evans, S., 2003. Isl1 identifies a cardiac progenitor population that proliferates prior to differentiation and contributes a majority of cells to the heart. Dev. Cell 5, 877–89.

Caspi, O., Huber, I., Kehat, I., Habib, M., Arbel, G., Gepstein, A., Yankelson, L., Aronson, D., Beyar, R., Gepstein, L., 2007. Transplantation of Human Embryonic Stem Cell-Derived Cardiomyocytes Improves Myocardial Performance in Infarcted Rat Hearts. J. Am. Coll. Cardiol. 50, 1884–1893.

Chan, Y.-C., Ting, S., Lee, Y.-K., Ng, K.-M., Zhang, J., Chen, Z., Siu, C.-W., Oh, S.K.W., Tse, H.-F., 2013. Electrical Stimulation Promotes Maturation of Cardiomyocytes Derived from Human Embryonic Stem Cells. J. Cardiovasc. Transl. Res. 6, 989–999.

Chen, I.-P., Fukuda, K., Fusaki, N., Iida, A., Hasegawa, M., Lichtler, A., Reichenberger, E.J., 2013. Induced Pluripotent Stem Cell Reprogramming by Integration-Free Sendai Virus Vectors from Peripheral Blood of Patients with Craniometaphyseal Dysplasia. Cell. Reprogram. 15, 503–513.

Chen, S.L., Fang, W.W., Ye, F., Liu, Y.H., Qian, J., Shan, S.J., Zhang, J.J., Chunhua, R.Z., Liao, L.M., Lin, S., Sun, J.P., 2004. Effect on left ventricular function of intracoronary transplantation of autologous bone marrow mesenchymal stem cell in patients with acute myocardial infarction. Am. J. Cardiol. 94, 92–95.

Cohen, E.D., Tian, Y., Morrisey, E.E., 2008. Wnt signaling: an essential regulator of cardiovascular differentiation, morphogenesis and progenitor self-renewal. Development 135, 789–798.

Cohn, J.N., Ferrari, R., Sharpe, N., 2000. Cardiac remodeling-concepts and clinical implications: A consensus paper from an International Forum on Cardiac Remodeling. J. Am. Coll. Cardiol. 35, 569–582.

Colegrave, M., Peckham, M., 2014. Structural Implications of β-Cardiac Myosin Heavy Chain Mutations in Human Disease. Anat. Rec. 297, 1670–1680.

Conrad, P., Ewing, G.E., Karlinsey, R.L., Sadtchenko, V., 2005. Ice nucleation on BaF2(111). J. Chem. Phys. 122, 064709.

Cui, X., Boland, T., D'Lima, D.D., Lotz, M.K., 2012a. Thermal inkjet printing in tissue engineering and regenerative medicine. Recent Pat. Drug Deliv. Formul. 6, 149–55.

Cui, X., Breitenkamp, K., Finn, M.G., Lotz, M., D'Lima, D.D., 2012b. Direct Human Cartilage Repair Using Three-Dimensional Bioprinting Technology. Tissue Eng. Part A 18, 1304–1312.

Da Rocha, A.M., Campbell, K., Mironov, S., Jiang, J., Mundada, L., Guerrero-Serna, G., Jalife, J., Herron, T.J., 2017. HiPSC-CM Monolayer Maturation State Determines Drug Responsiveness in High Throughput Pro-Arrhythmia Screen. Sci. Rep. 7, 1–12.

Dambrot, C., Passier, R., Atsma, D., Mummery, C.L., 2011. Cardiomyocyte differentiation of pluripotent stem cells and their use as cardiac disease models. Biochem. J. 434, 25–35.

Delva, E., Tucker, D.K., Kowalczyk, A.P., 2009. The Desmosome. Cold Spring Harb. Perspect.

Biol. 1, a002543–a002543.

DiMasi, J.A., Grabowski, H.G., Hansen, R.W., 2016. Innovation in the pharmaceutical industry: New estimates of R&D costs. J. Health Econ. 47, 20–33.

Discher, D.E., Janmey, P.A., Wang, Y., 2005. Tissue Cells Feel and Respond to the Stiffness of Their Substrate. Science (80-.). 310, 1139–1143.

Dispersyn, G.D., Geuens, E., Ver Donck, L., Ramaekers, F.C., Borgers, M., 2001. Adult rabbit cardiomyocytes undergo hibernation-like dedifferentiation when co-cultured with cardiac fibroblasts. Cardiovasc. Res. 51, 230–40.

Duan, J., Nilsson, L., Lambert, B., 2004. Structural and functional analysis of mutations at the human hypoxanthine phosphoribosyl transferase (HPRT1) locus. Hum. Mutat. 23, 599–611.

Eder, A., Vollert, I., Hansen, A., Eschenhagen, T., 2016. Human engineered heart tissue as a model system for drug testing. Adv. Drug Deliv. Rev. 96, 214–224.

Eng, G., Lee, B.W., Protas, L., Gagliardi, M., Brown, K., Kass, R.S., Keller, G., Robinson, R.B., Vunjak-Novakovic, G., 2016. Autonomous beating rate adaptation in human stem cell-derived cardiomyocytes. Nat. Commun. 7, 10312.

Engler, A.J., Carag-Krieger, C., Johnson, C.P., Raab, M., Tang, H.-Y., Speicher, D.W., Sanger, J.W., Sanger, J.M., Discher, D.E., 2008. Embryonic cardiomyocytes beat best on a matrix with heart-like elasticity: scar-like rigidity inhibits beating. J. Cell Sci. 121, 3794–802.

Engler, A.J., Sen, S., Sweeney, H.L., Discher, D.E., 2006. Matrix Elasticity Directs Stem Cell Lineage Specification. Cell 126, 677–689.

Eurotransplant, 2017. Annual Report 2017.

Eyre, C., Davison, A.N., Scott, J.T., 1971. Phosphoribosyl transferase activity in normal subjects, gout patients, and children with mental retardation. J. Neurol. Neurosurg. Psychiatry 34, 23–24.

Ezekiel Amri, Mamboya, F., 2012. Papain, a plant enzyme of biological importance: a review. Am. J. Biochem. Biotechnol. 8, 99–104.

Fan, D., Takawale, A., Lee, J., Kassiri, Z., 2012. Cardiac fibroblasts, fibrosis and extracellular matrix remodeling in heart disease. Fibrogenesis Tissue Repair 5, 15.

Fearnley, C.J., Roderick, H.L., Bootman, M.D., 2011. Calcium signaling in cardiac myocytes. Cold Spring Harb. Perspect. Biol. 3, a004242.

Forte, G., Pagliari, S., Ebara, M., Uto, K., Tam, J.K. Van, Romanazzo, S., Escobedo-Lucea, C., Romano, E., Di Nardo, P., Traversa, E., Aoyagi, T., 2012. Substrate Stiffness Modulates Gene Expression and Phenotype in Neonatal Cardiomyocytes In Vitro. Tissue Eng. Part A 18, 1837–1848.

Freeman, F.E., Kelly, D.J., 2017. Tuning Alginate Bioink Stiffness and Composition for Controlled Growth Factor Delivery and to Spatially Direct MSC Fate within Bioprinted Tissues. Sci. Rep. 7, 17042.

Freund, C., Mummery, C.L., 2009. Prospects for pluripotent stem cell-derived cardiomyocytes

in cardiac cell therapy and as disease models. J. Cell. Biochem. 107, 592–599.

Fujita, B., Zimmermann, W., 2017. Myocardial Tissue Engineering for Regenerative Applications. Curr. Cardiol. Rep. 19, 78.

Fung, Y., 1973. Stochastic flow in capillary blood vessels. Microvasc. Res. 5, 34–48.

Gaborit, N., Le Bouter, S., Szuts, V., Varro, A., Escande, D., Nattel, S., Demolombe, S., 2007. Regional and tissue specific transcript signatures of ion channel genes in the non-diseased human heart. J. Physiol. 582, 675–693.

Gao, L.R., Pei, X.T., Ding, Q.A., Chen, Y., Zhang, N.K., Chen, H.Y., Wang, Z.G., Wang, Y.F., Zhu, Z.M., Li, T.C., Liu, H.L., Tong, Z.C., Yang, Y., Nan, X., Guo, F., Shen, J.L., Shen, Y.H., Zhang, J.J., Fei, Y.X., Xu, H.T., Wang, L.H., Tian, H.T., Liu, D.Q., Yang, Y., 2013. A critical challenge: Dosage-related efficacy and acute complication intracoronary injection of autologous bone marrow mesenchymal stem cells in acute myocardial infarction. Int. J. Cardiol. 168, 3191–3199.

Geach, T.J., Hirst, E.M.A., Zimmerman, L.B., 2015. Contractile activity is required for Z-disc sarcomere maturation in vivo. Genesis 53, 299–307.

Gepp, M.M., Fischer, B., Schulz, A., Dobringer, J., Gentile, L., Vásquez, J.A., Neubauer, J.C., Zimmermann, H., 2017. Bioactive surfaces from seaweed-derived alginates for the cultivation of human stem cells. J. Appl. Phycol. 29, 2451–2461.

Ghosh, D., Mehta, N., Patil, A., Sengupta, J., 2016. Ethical issues in biomedical use of human embryonic stem cells (hESCs). J. Reprod. Heal. Med. 2, S37–S47.

Godier-Furnémont, A.F., Tiburcy, M., Wagner, E., Dewenter, M., Lämmle, S., El-Armouche, A., Lehnart, S.E., Vunjak-Novakovic, G., Zimmermann, W.-H., 2015. Physiologic force-frequency response in engineered heart muscle by electromechanical stimulation. Biomaterials 60, 82–91.

Golafshan, N., Kharaziha, M., Fathi, M., 2017. Tough and conductive hybrid graphene-PVA: Alginate fibrous scaffolds for engineering neural construct. Carbon N. Y. 111, 752–763.

Granzier, H.L., Irving, T.C., 1995. Passive tension in cardiac muscle: contribution of collagen, titin, microtubules, and intermediate filaments. Biophys. J. 68, 1027–1044.

Granzier, H.L., Labeit, S., 2004. The Giant Protein Titin: A Major Player in Myocardial Mechanics, Signaling, and Disease. Circ. Res. 94, 284–295.

Gregorio, C.C., Trombitás, K., Centner, T., Kolmerer, B., Stier, G., Kunke, K., Suzuki, K., Obermayr, F., Herrmann, B., Granzier, H., Sorimachi, H., Labeit, S., 1998. The NH 2 Terminus of Titin Spans the Z-Disc: Its Interaction with a Novel 19-kD Ligand (T-cap) Is Required for Sarcomeric Integrity. J. Cell Biol. 143, 1013–1027.

Guillotin, B., Souquet, A., Catros, S., Duocastella, M., Pippenger, B., Bellance, S., Bareille, R., Rémy, M., Bordenave, L., Amédée, J., Guillemot, F., 2010. Laser assisted bioprinting of engineered tissue with high cell density and microscale organization. Biomaterials 31, 7250–7256.

Guo, L., Abrams, R.M.C., Babiarz, J.E., Cohen, J.D., Kameoka, S., Sanders, M.J., Chiao, E., Kolaja, K.L., 2011. Estimating the Risk of Drug-Induced Proarrhythmia Using Human Induced

Pluripotent Stem Cell–Derived Cardiomyocytes. Toxicol. Sci. 123, 281–289.

Gurdon, J.B., Elsdale, T.R., Fischberg, M., 1958. Sexually Mature Individuals of Xenopus laevis from the Transplantation of Single Somatic Nuclei. Nature 182, 64–65.

Gwathmey, J.K., Tsaioun, K., Hajjar, R.J., 2009. Cardionomics: a new integrative approach for screening cardiotoxicity of drug candidates. Expert Opin Drug Metab Toxicol 5, 647–660.

Hansen, A., Eder, A., Bönstrup, M., Flato, M., Mewe, M., Schaaf, S., Aksehirlioglu, B., Schwörer, A., Uebeler, J., Eschenhagen, T., 2010. Development of a Drug Screening Platform Based on Engineered Heart Tissue. Circ. Res. 107, 35–44.

Happe, C.L., Engler, A.J., 2016. Mechanical Forces Reshape Differentiation Cues That Guide Cardiomyogenesis. Circ. Res. 118, 296–310.

Harris, K., Aylott, M., Cui, Y., Louttit, J.B., Mcmahon, N.C., Sridhar, A., 2013. Comparison of Electrophysiological Data From Human-Induced Pluripotent Stem Cell – Derived Cardiomyocytes to Functional Preclinical Safety Assays 134, 412–426.

Hatzistergos, K.E., Quevedo, H., Oskouei, B.N., Hu, Q., Feigenbaum, G.S., Margitich, I.S., Mazhari, R., Boyle, A.J., Zambrano, J.P., Rodriguez, J.E., Dulce, R., Pattany, P.M., Valdes, D., Revilla, C., Heldman, A.W., McNiece, I., Hare, J.M., 2010. Bone Marrow Mesenchymal Stem Cells Stimulate Cardiac Stem Cell Proliferation and Differentiation. Circ. Res. 107, 913–922.

Hennink, W.., van Nostrum, C.., 2002. Novel crosslinking methods to design hydrogels. Adv. Drug Deliv. Rev. 54, 13–36.

Heras-Bautista, C.O., Katsen-Globa, A., Schloerer, N.E., Dieluweit, S., Abd El Aziz, O.M., Peinkofer, G., Attia, W.A., Khalil, M., Brockmeier, K., Hescheler, J., Pfannkuche, K., 2014. The influence of physiological matrix conditions on permanent culture of induced pluripotent stem cell-derived cardiomyocytes. Biomaterials 35, 7374–7385.

Herron, T.J., Da Rocha, A.M., Campbell, K.F., Ponce-Balbuena, D., Willis, B.C., Guerrero-Serna, G., Liu, Q., Klos, M., Musa, H., Zarzoso, M., Bizy, A., Furness, J., Anumonwo, J., Mironov, S., Jalife, J., 2016. Extracellular matrix-mediated maturation of human pluripotent stem cell-derived cardiac monolayer structure and electrophysiological function. Circ. Arrhythmia Electrophysiol. 9, 1–12.

Hersch, N., Wolters, B., Dreissen, G., Springer, R., Kirchgessner, N., Merkel, R., Hoffmann, B., 2013. The constant beat: cardiomyocytes adapt their forces by equal contraction upon environmental stiffening. Biol. Open 2, 351–361.

Hoffmann, C., Leitz, M.R., Oberdorf-Maass, S., Lohse, M.J., Klotz, K.N., 2004. Comparative pharmacology of human β-adrenergic receptor subtypes - Characterization of stably transfected receptors in CHO cells. Naunyn. Schmiedebergs. Arch. Pharmacol. 369, 151–159.

Huang, H.-L., Hsing, H.-W., Lai, T.-C., Chen, Y.-W., Lee, T.-R., Chan, H.-T., Lyu, P.-C., Wu, C.-L., Lu, Y.-C., Lin, S.-T., Lin, C.-W., Lai, C.-H., Chang, H.-T., Chou, H.-C., Chan, H.-L., 2010a. Trypsin-induced proteome alteration during cell subculture in mammalian cells. J. Biomed. Sci. 17, 36.

Huang, N.F., Niiyama, H., Peter, C., De, A., Natkunam, Y., Fleissner, F., Li, Z., Rollins, M.D., Wu,

J.C., Gambhir, S.S., Cooke, J.P., 2010b. Embryonic stem cell-derived endothelial cells engraft into the ischemic hindlimb and restore perfusion. Arterioscler. Thromb. Vasc. Biol. 30, 984–991.

Huebsch, N., Loskill, P., Mandegar, M.A., Marks, N.C., Sheehan, A.S., Ma, Z., Mathur, A., Nguyen, T.N., Yoo, J.C., Judge, L.M., Spencer, C.I., Chukka, A.C., Russell, C.R., So, P.-L., Conklin, B.R., Healy, K.E., 2015. Automated Video-Based Analysis of Contractility and Calcium Flux in Human-Induced Pluripotent Stem Cell-Derived Cardiomyocytes Cultured over Different Spatial Scales. Tissue Eng. Part C Methods 21, 467–479.

Itzhaki, I., Schiller, J., Beyar, R., Satin, J., Gepstein, L., 2006. Calcium handling in embryonic stem cell-derived cardiac myocytes: Of mice and men. Ann. N. Y. Acad. Sci. 1080, 207–215.

Izumi, N., Era, T., Akimaru, H., Yasunaga, M., Nishikawa, S.-I., 2007. Dissecting the Molecular Hierarchy for Mesendoderm Differentiation Through a Combination of Embryonic Stem Cell Culture and RNA Interference. Stem Cells 25, 1664–1674.

Jia, W., Gungor-Ozkerim, P.S., Zhang, Y.S., Yue, K., Zhu, K., Liu, W., Pi, Q., Byambaa, B., Dokmeci, M.R., Shin, S.R., Khademhosseini, A., 2016. Direct 3D bioprinting of perfusable vascular constructs using a blend bioink. Biomaterials 106, 58–68.

Kadari, A., Mekala, S., Wagner, N., Malan, D., Köth, J., Doll, K., Stappert, L., Eckert, D., Peitz, M., Matthes, J., Sasse, P., Herzig, S., Brüstle, O., Ergün, S., Edenhofer, F., 2015. Robust generation of cardiomyocytes from human iPS cells requires precise modulation of BMP and WNT signaling. Stem Cell Rev. Reports 11, 560–569.

Kadota, S., Pabon, L., Reinecke, H., Murry, C.E.E., 2017. In Vivo Maturation of Human Induced Pluripotent Stem Cell-Derived Cardiomyocytes in Neonatal and Adult Rat Hearts. Stem Cell Reports 8, 278–289.

Kaplan, W.D., Trout, W.E., 1969. The behavior of four neurological mutants of Drosophila. Genetics 61, 399–409.

Karantalis, V., Balkan, W., Schulman, I.H., Hatzistergos, K.E., Hare, J.M., 2012. Cell-based therapy for prevention and reversal of myocardial remodeling. AJP Hear. Circ. Physiol. 303, H256–H270.

Karbassi, E., Fenix, A., Marchiano, S., Muraoka, N., Nakamura, K., Yang, X., Murry, C.E., 2020. Cardiomyocyte maturation: advances in knowledge and implications for regenerative medicine. Nat. Rev. Cardiol.

Kempen, M.J.A. Van, Fromaget, C., Gros, D., Moorman, A.F.M., Lamers, W.H., 1991. Spatial Distribution of Connexin43 , the Major Cardiac Gap Junction Protein , in the Developing and Adult Rat Heart 1638–1651.

Khalil, S., Sun, W., 2007. Biopolymer deposition for freeform fabrication of hydrogel tissue constructs. Mater. Sci. Eng. C 27, 469–478.

Kim, D., Kim, C.-H., Moon, J., Chung, Y., Chang, M., Han, B., Ko, S., Yang, E., Cha, K.Y., Lanza, R., Kim, K., 2009. Generation of Human Induced Pluripotent Stem Cells by Direct Delivery of Reprogramming Proteins. Cell Stem Cell 4, 472–476.

Kimmel, J.R., Smith, E.L., 1954. Crystalline papain. I. Preparation, specificity, and activation. J.

Biol. Chem. 207, 515–31.

King, N.M., Perrin, J., 2014. Ethical issues in stem cell research and therapy. Stem Cell Res. Ther. 5, 85.

Kirklin, J.K., Naftel, D.C., Pagani, F.D., Kormos, R.L., Stevenson, L.W., Blume, E.D., Myers, S.L., Miller, M.A., Baldwin, J.T., Young, J.B., 2015. Seventh INTERMACS annual report: 15,000 patients and counting. J. Hear. Lung Transplant. 34, 1495–1504.

Koch, L., Gruene, M., Unger, C., Chichkov, B., 2013. Laser Assisted Cell Printing. Curr. Pharm. Biotechnol. 14, 91–97.

Kostin, S., Dammer, S., Hein, S., Klovekorn, W.P., Bauer, E.P., Schaper, J., 2004. Connexin 43 expression and distribution in compensated and decompensated cardiac hypertrophy in patients with aortic stenosis. Cardiovasc. Res. 62, 426–436.

Kraitchman, D.L., Tatsumi, M., Gilson, W.D., Ishimori, T., Kedziorek, D., Walczak, P., Segars, W.P., Chen, H.H., Fritzges, D., Izbudak, I., Young, R.G., Marcelino, M., Pittenger, M.F., Solaiyappan, M., Boston, R.C., Tsui, B.M.W., Wahl, R.L., Bulte, J.W.M., 2005. Dynamic imaging of allogeneic mesenchymal stem cells trafficking to myocardial infarction. Circulation 112, 1451–1461.

Kraus, C., Rohde, D., Weidenhammer, C., Qiu, G., Pleger, S.T., Voelkers, M., Boerries, M., Remppis, A., Katus, H.A., Most, P., 2009. S100A1 in cardiovascular health and disease: Closing the gap between basic science and clinical therapy. J. Mol. Cell. Cardiol. 47, 445–455.

Krenning, G., Zeisberg, E.M., Kalluri, R., 2010. The origin of fibroblast and mechanism of cardiac fibrosis. J. cell Physiol. 225, 631–637.

Kropp, C., Massai, D., Zweigerdt, R., 2017. Progress and challenges in large-scale expansion of human pluripotent stem cells. Process Biochem. 59, 244–254.

Krüger, M., Linke, W.A., 2011. The giant protein titin: A regulatory node that integrates myocyte signaling pathways. J. Biol. Chem. 286, 9905–9912.

Kumar, P.R., Kollu, P., Santhosh, C., Eswara Varaprasada Rao, K., Kim, D.K., Grace, A.N., 2014. Enhanced properties of porous CoFe 2 O 4 –reduced graphene oxide composites with alginate binders for Li-ion battery applications. New J. Chem. 38, 3654–3661.

Kwok, C.K., Ueda, Y., Kadari, A., Günther, K., Ergün, S., Heron, A., Schnitzler, A.C., Rook, M., Edenhofer, F., 2018. Scalable stirred suspension culture for the generation of billions of human induced pluripotent stem cells using single-use bioreactors. J. Tissue Eng. Regen. Med. 12, e1076–e1087.

Kyrychenko, V., Kyrychenko, S., Tiburcy, M., Shelton, J.M., Long, C., Schneider, J.W., Zimmermann, W.-H., Bassel-Duby, R., Olson, E.N., 2017. Functional correction of dystrophin actin binding domain mutations by genome editing. JCI Insight 2.

Laflamme, M. a, Chen, K.Y., Naumova, A. V, Muskheli, V., Fugate, J. a, Dupras, S.K., Reinecke, H., Xu, C., Hassanipour, M., Police, S., O'Sullivan, C., Collins, L., Chen, Y., Minami, E., Gill, E. a, Ueno, S., Yuan, C., Gold, J., Murry, C.E., 2007. Cardiomyocytes derived from human embryonic stem cells in pro-survival factors enhance function of infarcted rat hearts. Nat. Biotechnol. 25, 1015–1024.

Langendorff, O., 1895. Untersuchungen am überlebenden Säugethierherzen. Pflüger, Arch. für die Gesammte Physiol. des Menschen und der Thiere 61, 291–332.

Lanzicher, T., Martinelli, V., Puzzi, L., Del Favero, G., Codan, B., Long, C.S., Mestroni, L., Taylor, M.R.G., Sbaizero, O., 2015. The Cardiomyopathy Lamin A/C D192G Mutation Disrupts Whole-Cell Biomechanics in Cardiomyocytes as Measured by Atomic Force Microscopy Loading-Unloading Curve Analysis. Sci. Rep. 5, 13388.

Layland, J., Kentish, J.C., 2002. Myofilament-based relaxant effect of isoprenaline revealed during work-loop contractions in rat cardiac trabeculae. J. Physiol. 544, 171–182.

Lee, K.Y., Mooney, D.J., 2012. Alginate: properties and biomedical applications. Prog. Polym. Sci. 37, 106–126.

Lee, V.K., Kim, D.Y., Ngo, H., Lee, Y., Seo, L., Yoo, S.-S., Vincent, P.A., Dai, G., 2014. Creating perfused functional vascular channels using 3D bio-printing technology. Biomaterials 35, 8092–8102.

Li, R.A., Keung, W., Cashman, T.J., Backeris, P.C., Johnson, B. V., Bardot, E.S., Wong, A.O.T., Chan, P.K.W., Chan, C.W.Y., Costa, K.D., 2018a. Bioengineering an electro-mechanically functional miniature ventricular heart chamber from human pluripotent stem cells. Biomaterials 163, 116–127.

Li, Y., He, L., Huang, X., Bhaloo, S.I., Zhao, H., Zhang, S., Pu, W., Tian, X., Li, Y., Liu, Q., Yu, W., Zhang, L., Liu, X., Liu, K., Tang, J., Zhang, H., Cai, D., Ralf, A.H., Xu, Q., Lui, K.O., Zhou, B., 2018b. Genetic Lineage Tracing of Nonmyocyte Population by Dual Recombinases. Circulation 138, 793–805.

Li, Y., Rodrigues, J., Tomás, H., 2012. Injectable and biodegradable hydrogels: gelation, biodegradation and biomedical applications. Chem. Soc. Rev. 41, 2193–2221.

Li, Z., Ramay, H.R., Hauch, K.D., Xiao, D., Zhang, M., 2005. Chitosan-alginate hybrid scaffolds for bone tissue engineering. Biomaterials 26, 3919–28.

Liang, P., Lan, F., Lee, A.S., Gong, T., Sanchez-Freire, V., Wang, Y., Diecke, S., Sallam, K., Knowles, J.W., Wang, P.J., Nguyen, P.K., Bers, D.M., Robbins, R.C., Wu, J.C., 2013. Drug screening using a library of human induced pluripotent stem cell-derived cardiomyocytes reveals disease-specific patterns of cardiotoxicity. Circulation 127, 1677–1691.

Liau, B., Christoforou, N., Leong, K.W., Bursac, N., 2011. Pluripotent stem cell-derived cardiac tissue patch with advanced structure and function. Biomaterials 32, 9180–9187.

Lin, L., Bu, L., Cai, C.-L., Zhang, X., Evans, S., 2006. Isl1 is upstream of sonic hedgehog in a pathway required for cardiac morphogenesis. Dev. Biol. 295, 756–763.

Liu, G., Papa, A., Katchman, A.N., Zakharov, S.I., Roybal, D., Hennessey, J.A., Kushner, J., Yang, L., Chen, B.-X., Kushnir, A., Dangas, K., Gygi, S.P., Pitt, G.S., Colecraft, H.M., Ben-Johny, M., Kalocsay, M., Marx, S.O., 2020. Mechanism of adrenergic Ca V 1.2 stimulation revealed by proximity proteomics. Nat. 2020 577, 1–6.

Liu, Y., Schwartz, R.J., 2013. Transient mesp1 expression: A driver of cardiac cell fate determination. Transcription 4.

Lockhart, M., Wirrig, E., Phelps, A., Wessels, A., 2011. Extracellular matrix and heart

development. Birth Defects Res. Part A Clin. Mol. Teratol. 91, 535–550.

Louch, W.E., Koivumäki, J.T., Tavi, P., 2015. Calcium signalling in developing cardiomyocytes: implications for model systems and disease. J. Physiol. 593, 1047–63.

Luo, Y., Li, Y., Qin, X., Wa, Q., 2018. 3D printing of concentrated alginate/gelatin scaffolds with homogeneous nano apatite coating for bone tissue engineering. Mater. Des. 146, 12–19.

Luo, Y., Luo, G., Gelinsky, M., Huang, P., Ruan, C., 2017. 3D bioprinting scaffold using alginate/polyvinyl alcohol bioinks. Mater. Lett. 189, 295–298.

Lyon, R.C., Zanella, F., Omens, J.H., Sheikh, F., 2015. Mechanotransduction in Cardiac Hypertrophy and Failure. Circ. Res. 116, 1462–1476.

Mannhardt, I., Breckwoldt, K., Letuffe-Brenière, D., Schaaf, S., Schulz, H., Neuber, C., Benzin, A., Werner, T., Eder, A., Schulze, T., Klampe, B., Christ, T., Hirt, M.N., Huebner, N., Moretti, A., Eschenhagen, T., Hansen, A., 2016. Human Engineered Heart Tissue: Analysis of Contractile Force. Stem Cell Reports 7, 29–42.

Markstedt, K., Mantas, A., Tournier, I., Mart??nez ??vila, H., H??gg, D., Gatenholm, P., 2015. 3D bioprinting human chondrocytes with nanocellulose-alginate bioink for cartilage tissue engineering applications. Biomacromolecules 16, 1489–1496.

Mayans, O., van der Ven, P.F.M., Wilm, M., Mues, A., Young, P., Fürst, D.O., Wilmanns, M., Gautel, M., 1998. Structural basis for activation of the titin kinase domain during myofibrillogenesis. Nature 395, 863.

Mazzotta, S., Neves, C., Bonner, R.J., Bernardo, A.S., Docherty, K., Hoppler, S., 2016. Distinctive Roles of Canonical and Noncanonical Wnt Signaling in Human Embryonic Cardiomyocyte Development. Stem Cell Reports 7, 764–776.

McCain, M.L., Lee, H., Aratyn-Schaus, Y., Kleber, A.G., Parker, K.K., 2012. Cooperative coupling of cell-matrix and cell-cell adhesions in cardiac muscle. Proc. Natl. Acad. Sci. 109, 9881–9886.

Mccubbin, W.D., Beyers, D.M., Kay, C.M., 1987. Regulation of the actin-myosin interaction by calcium; the troponin tropomyosin complex, in: Ter Keurs, H.E.D.J., Tyberg, J. V (Eds.), Mechanics of the Circulation. Springer Netherlands, Dordrecht, pp. 113–130.

Mehta, A., Ramachandra, C.J.A., Sequiera, G.L., Sudibyo, Y., Nandihalli, M., Yong, P.J.A., Koh, C.H., Shim, W., 2014. Phasic modulation of Wnt signaling enhances cardiac differentiation in human pluripotent stem cells by recapitulating developmental ontogeny. Biochim. Biophys. Acta - Mol. Cell Res. 1843, 2394–2402.

Mihic, A., Li, J., Miyagi, Y., Gagliardi, M., Li, S.-H., Zu, J., Weisel, R.D., Keller, G., Li, R.-K., 2014. The effect of cyclic stretch on maturation and 3D tissue formation of human embryonic stem cell-derived cardiomyocytes. Biomaterials 35, 2798–2808.

Miller, J.S., Stevens, K.R., Yang, M.T., Baker, B.M., Nguyen, D.H.T., Cohen, D.M., Toro, E., Chen, A.A., Galie, P.A., Yu, X., Chaturvedi, R., Bhatia, S.N., Chen, C.S., 2012. Rapid casting of patterned vascular networks for perfusable engineered three-dimensional tissues. Nat. Mater. 11, 768–774.

Modell, S.M., Lehmann, M.H., 2006. The long QT syndrome family of cardiac ion

channelopathies: A HuGE review*. Genet. Med. 8, 143–155.

Mohseni, R., 2014. Safe Transplantation Of Pluripotent Stem Cell By Preventing Teratoma Formation. J. Stem Cell Res. Ther. 04.

Molina, C.E., Jacquet, E., Ponien, P., Muñoz-Guijosa, C., Baczkó, I., Maier, L.S., Donzeau-Gouge, P., Dobrev, D., Fischmeister, R., Garnier, A., 2018. Identification of optimal reference genes for transcriptomic analyses in normal and diseased human heart. Cardiovasc. Res. 114, 247–258.

Montag, J., Kowalski, K., Makul, M., Ernstberger, P., Radocaj, A., Beck, J., Becker, E., Tripathi, S., Keyser, B., Mühlfeld, C., Wissel, K., Pich, A., van der Velden, J., dos Remedios, C.G., Perrot, A., Francino, A., Navarro-López, F., Brenner, B., Kraft, T., 2018. Burst-Like Transcription of Mutant and Wildtype MYH7-Alleles as Possible Origin of Cell-to-Cell Contractile Imbalance in Hypertrophic Cardiomyopathy. Front. Physiol. 9, 1–15.

Müller, M., Becher, J., Schnabelrauch, M., Zenobi-Wong, M., 2015. Nanostructured Pluronic hydrogels as bioinks for 3D bioprinting. Biofabrication 7.

Mummery, C., Van Achterberg, T.A.E., van den Eijnden-van Raaij, A.J.M., Van Haaster, L., Willemse, A., de Laat, S.W., Piersma, A.H., 1991a. Visceral-endoderm-like cell lines induce differentiation of murine P19 embryonal carcinoma cells. Differentiation 46, 51–60.

Mummery, C., Ward-van Oostwaard, D., Doevendans, P., Spijker, R., van den Brink, S., Hassink, R., van der Heyden, M., Opthof, T., Pera, M., de la Riviere, A.B., Passier, R., Tertoolen, L., 2003. Differentiation of human embryonic stem cells to cardiomyocytes: role of coculture with visceral endoderm-like cells. Circulation 107, 2733–40.

Mummery, C., Ward, D., van den Brink, C., Bird, S., Doevendans, P., Opthof, T., de la Riviere, a B., Tertoolen, L., van der Heyden, M., Pera, M., 2002. Cardiomyocyte differentiation of mouse and human embryonic stem cells*. J. Anat. 200, 233–242.

Mummery, C.L., Van Achterberg, T.A.E., van den Eijnden-van Raaij, A.J.M., Van Haaster, L., Willemse, A., de Laat, S.W., Piersma, A.H., 1991b. Visceral-endoderm-like cell lines induce differentiation of murine P19 embryonal carcinoma cells. Differentiation 46, 51–60.

Murphy, S. V, Atala, A., 2014. 3D bioprinting of tissues and organs. Nat. Biotechnol. 32, 773–785.

Ncardia, 2019. Detection of a embryonic fingerprint in the COR.4U cell line. Pers. Commun.

Negroni, J.A., Morotti, S., Lascano, E.C., Gomes, A. V, Grandi, E., Puglisi, J.L., Bers, D.M., 2015. β-adrenergic effects on cardiac myofilaments and contraction in an integrated rabbit ventricular myocyte model. J. Mol. Cell. Cardiol. 81, 162–175.

Nguyen, P.K., Neofytou, E., Rhee, J.-W., Wu, J.C., 2016. Potential Strategies to Address the Major Clinical Barriers Facing Stem Cell Regenerative Therapy for Cardiovascular Disease. JAMA Cardiol. 1, 953.

Nori, S., Okada, Y., Nishimura, S., Sasaki, T., Itakura, G., Kobayashi, Y., Renault-Mihara, F., Shimizu, A., Koya, I., Yoshida, R., Kudoh, J., Koike, M., Uchiyama, Y., Ikeda, E., Toyama, Y., Nakamura, M., Okano, H., 2015. Long-term safety issues of iPSC-based cell therapy in a spinal cord injury model: Oncogenic transformation with epithelial-mesenchymal transition. Stem Cell Reports 4, 360–373.

Nunes, S.S., Miklas, J.W., Liu, J., Aschar-Sobbi, R., Xiao, Y., Zhang, B., Jiang, J., Massé, S., Gagliardi, M., Hsieh, A., Thavandiran, N., Laflamme, M.A., Nanthakumar, K., Gross, G.J., Backx, P.H., Keller, G., Radisic, M., 2013. Biowire: A platform for maturation of human pluripotent stem cell-derived cardiomyocytes. Nat. Methods 10, 781–787.

O'Neil, L., Paynter, S.J., Fuller, B.J., Shaw, R.W., 1997. Vitrification of Mature Mouse Oocytes: Improved Results Following Addition of Polyethylene Glycol to a Dimethyl Sulfoxide Solution. Cryobiology 34, 295–301.

Okita, K., Nakagawa, M., Hyenjong, H., Ichisaka, T., Yamanaka, S., 2008. Generation of Mouse Induced Pluripotent Stem Cells Without Viral Vectors. Science (80-.). 322, 949–953.

Pahnke, A., Conant, G., Huyer, L.D., Zhao, Y., Feric, N., Radisic, M., 2016. The role of Wnt regulation in heart development, cardiac repair and disease: A tissue engineering perspective. Biochem. Biophys. Res. Commun. 473, 698–703.

Paige, S.L., Plonowska, K., Xu, A., Wu, S.M., 2015. Molecular Regulation of Cardiomyocyte Differentiation. Circ. Res. 116, 341–353.

Park, S., Kim, G., Jeon, Y.C., Koh, Y., Kim, W., 2009. 3D polycaprolactone scaffolds with controlled pore structure using a rapid prototyping system. J. Mater. Sci. Mater. Med. 20, 229–234.

Pataky, K., Braschler, T., Negro, A., Renaud, P., Lutolf, M.P., Brugger, J., 2012. Microdrop Printing of Hydrogel Bioinks into 3D Tissue-Like Geometries. Adv. Mater. 24, 391–396.

Pati, F., Jang, J., Ha, D.H., Won Kim, S., Rhie, J.W., Shim, J.H., Kim, D.H., Cho, D.W., 2014. Printing three-dimensional tissue analogues with decellularized extracellular matrix bioink. Nat. Commun. 5, 1–11.

Perin, E.C., Dohmann, H.F.R., Borojevic, R., Silva, S.A., Sousa, A.L.S., Mesquita, C.T., Rossi, M.I.D., Carvalho, A.C., Dutra, H.S., Dohmann, H.J.F., Silva, G. V, Belém, L., Vivacqua, R., Rangel, F.O.D., Esporcatte, R., Geng, Y.J., Vaughn, W.K., Assad, J.A.R., Mesquita, E.T., Willerson, J.T., 2003. Transendocardial, Autologous Bone Marrow Cell Transplantation for Severe, Chronic Ischemic Heart Failure. Circulation 107, 2294–2302.

Quaranta, R., Fell, J., Rühle, F., Rao, J., Piccini, I., Araúzo-Bravo, M.J., Verkerk, A.O., Stoll, M., Greber, B., 2018. Revised roles of ISL1 in a hES cell-based model of human heart chamber specification. Elife 7, e31706.

Ratshin, R.A., Rackley, C.E., Russell, R.O., 1972. Hemodynamic evaluation of left ventricular function in shock complicating myocardial infarction. Circulation 45, 127–39.

Ravenscroft, S.M., Pointon, A., Williams, A.W., Cross, M.J., Sidaway, J.E., 2016. Cardiac Non-myocyte Cells Show Enhanced Pharmacological Function Suggestive of Contractile Maturity in Stem Cell Derived Cardiomyocyte Microtissues. Toxicol. Sci. 152, kfw069.

Rawles, M.E., 1943. The heart-forming areas of the early chick blastoderm. Physiol. Zool. 16, 22–43.

Reckova, M., Rosengarten, C., DeAlmeida, A., Stanley, C.P., Wessels, A., Gourdie, R.G., Thompson, R.P., Sedmera, D., 2003. Hemodynamics is a key epigenetic factor in development of the cardiac conduction system. Circ. Res. 93, 77–85.

Reno, A., Hunter, A., Li, Y., Ye, T., Foley, A., 2018. Quantification of Cardiomyocyte Beating Frequency Using Fourier Transform Analysis. Photonics 5, 39.

Rienks, M., Papageorgiou, A.-P., Frangogiannis, N.G., Heymans, S., 2014. Myocardial Extracellular Matrix. Circ. Res. 114, 872–888.

Robertson, C., Tran, D.D., George, S.C., 2013. Concise review: Maturation phases of human pluripotent stem cell-derived cardiomyocytes. Stem Cells 31, 829–837.

Ruvinov, E., Cohen, S., 2016. Alginate biomaterial for the treatment of myocardial infarction: Progress, translational strategies, and clinical outlook. From ocean algae to patient bedside. Adv. Drug Deliv. Rev. 96, 54–76.

Saga, Y., Miyagawa-Tomita, S., Takagi, A., Kitajima, S., Miyazaki, J. i, Inoue, T., 1999. MesP1 is expressed in the heart precursor cells and required for the formation of a single heart tube. Development 126, 3437–47.

Sagawa, K., 1981. The end-systolic pressure-volume relation of the ventricle: definition, modifications and clinical use. Circulation 63, 1223–7.

Sala, L., van Meer, B.J., Tertoolen, L.G.J., Bakkers, J., Bellin, M., Davis, R.P., Denning, C., Dieben, M.A.E., Eschenhagen, T., Giacomelli, E., Grandela, C., Hansen, A., Holman, E.R., Jongbloed, M.R.M., Kamel, S.M., Koopman, C.D., Lachaud, Q., Mannhardt, I., Mol, M.P.H., Mosqueira, D., Orlova, V. V., Passier, R., Ribeiro, M.C., Saleem, U., Smith, G.L., Burton, F.L., Mummery, C.L., 2018. MUSCLEMOTION. Circ. Res. 122, e5–e16.

Sallam, K., Li, Y., Sager, P.T., Houser, S.R., Wu, J.C., 2015. Finding the Rhythm of Sudden Cardiac Death: New Opportunities Using Induced Pluripotent Stem Cell-Derived Cardiomyocytes. Circ. Res. 116, 1989–2004.

Sanger, J.W., Wang, J., Fan, Y., White, J., Sanger, J.M., 2010. Assembly and Dynamics of Myofibrils. J. Biomed. Biotechnol. 2010, 1–8.

Sanguinetti, M.C., Jiang, C., Curran, M.E., Keating, M.T., 1995. A mechanistic link between an inherited and an acquired cardiac arrhythmia: HERG encodes the IKr potassium channel. Cell 81, 299–307.

Schächinger, V., Assmus, B., Britten, M.B., Honold, J., Lehmann, R., Teupe, C., Abolmaali, N.D., Vogl, T.J., Hofmann, W.K., Martin, H., Dimmeler, S., Zeiher, A.M., 2004. Transplantation of progenitor cells and regeneration enhancement in acute myocardial infarction: Final one-year results of the TOPCARE-AMI trial. J. Am. Coll. Cardiol. 44, 1690–1699.

Schlaeger, T.M., Daheron, L., Brickler, T.R., Entwisle, S., Chan, K., Cianci, A., DeVine, A., Ettenger, A., Fitzgerald, K., Godfrey, M., Gupta, D., McPherson, J., Malwadkar, P., Gupta, M., Bell, B., Doi, A., Jung, N., Li, X., Lynes, M.S., Brookes, E., Cherry, A.B.C., Demirbas, D., Tsankov, A.M., Zon, L.I., Rubin, L.L., Feinberg, A.P., Meissner, A., Cowan, C.A., Daley, G.Q., 2015. A comparison of non-integrating reprogramming methods. Nat. Biotechnol. 33, 58–63.

Schulz, A., Gepp, M.M., Stracke, F., von Briesen, H., Neubauer, J.C., Zimmermann, H., 2019. Tyramine-conjugated alginate hydrogels as a platform for bioactive scaffolds. J. Biomed. Mater. Res. Part A 107, 114–121.

Scuderi, G.J., Butcher, J., 2017. Naturally Engineered Maturation of Cardiomyocytes. Front.

Cell Dev. Biol. 5, 50.

Sehnert, A.J., Huq, A., Weinstein, B.M., Walker, C., Fishman, M., Stainier, D.Y.R., 2002. Cardiac troponin T is essential in sarcomere assembly and cardiac contractility. Nat. Genet. 31, 106–110.

Sequeira, V., Nijenkamp, L.L.A.M., Regan, J.A., Van Der Velden, J., 2014. The physiological role of cardiac cytoskeleton and its alterations in heart failure. Biochim. Biophys. Acta - Biomembr. 1838, 700–722.

Shiba, Y., Fernandes, S., Zhu, W.-Z., Filice, D., Muskheli, V., Kim, J., Palpant, N.J., Gantz, J.A., Moyes, K.W., Reinecke, H., Van Biber, B., Dardas, T., Mignone, J.L., Izawa, A., Hanna, R., Viswanathan, M., Gold, J.D., Kotlikoff, M.I., Sarvazyan, N., Kay, M.W., Murry, C.E., Laflamme, M.A., 2012. Human ES-cell-derived cardiomyocytes electrically couple and suppress arrhythmias in injured hearts. Nature 489, 322–325.

Skardal, A., Mack, D., Kapetanovic, E., Atala, A., Jackson, J.D., Yoo, J., Soker, S., 2012. Bioprinted Amniotic Fluid-Derived Stem Cells Accelerate Healing of Large Skin Wounds. Stem Cells Transl. Med. 1, 792–802.

Später, D., Hansson, E.M., Zangi, L., Chien, K.R., 2014. How to make a cardiomyocyte. Development 141, 4418–31.

Stadtfeld, M., Nagaya, M., Utikal, J., Weir, G., Hochedlinger, K., 2008. Induced Pluripotent Stem Cells Generated Without Viral Integration. Science (80-.). 322, 945–949.

Stoehr, A., Neuber, C., Baldauf, C., Vollert, I., Friedrich, F.W., Flenner, F., Carrier, L., Eder, A., Schaaf, S., Hirt, M.N., Aksehirlioglu, B., Tong, C.W., Moretti, A., Eschenhagen, T., Hansen, A., 2014. Automated analysis of contractile force and Ca2+ transients in engineered heart tissue. Am. J. Physiol. Heart Circ. Physiol. 306, H1353-63.

Storz, H., M??ller, K.J., Ehrhart, F., G??mez, I., Shirley, S.G., Gessner, P., Zimmermann, G., Weyand, E., Sukhorukov, V.L., Forst, T., Weber, M.M., Zimmermann, H., Kulicke, W.M., Zimmermann, U., 2009. Physicochemical features of ultra-high viscosity alginates. Carbohydr. Res. 344, 985–995.

Storz, H., Zimmermann, U., Zimmermann, H., Kulicke, W.M., 2010. Viscoelastic properties of ultra-high viscosity alginates. Rheol. Acta 49, 155–167.

Stremnitzer, C., Manzano-Szalai, K., Willensdorfer, A., Starkl, P., Pieper, M., König, P., Mildner, M., Tschachler, E., Reichart, U., Jensen-Jarolim, E., 2015. Papain Degrades Tight Junction Proteins of Human Keratinocytes In Vitro and Sensitizes C57BL/6 Mice via the Skin Independent of its Enzymatic Activity or TLR4 Activation. J. Invest. Dermatol. 135, 1790–1800.

Sumi, T., Tsuneyoshi, N., Nakatsuji, N., Suemori, H., 2008. Defining early lineage specification of human embryonic stem cells by the orchestrated balance of canonical Wnt/ -catenin, Activin/Nodal and BMP signaling. Development 135, 2969–2979.

Sun, J., Tan, H., 2013. Alginate-based biomaterials for regenerative medicine applications. Materials (Basel). 6, 1285–1309.

Takahashi, K., Yamanaka, S., 2006. Induction of Pluripotent Stem Cells from Mouse Embryonic and Adult Fibroblast Cultures by Defined Factors. Cell 126, 663–676.

Talman, V., Ruskoaho, H., 2016. Cardiac fibrosis in myocardial infarction—from repair and remodeling to regeneration. Cell Tissue Res. 365, 563–581.

Tam, P.P.L., Loebel, D.A.F., 2007. Gene function in mouse embryogenesis: get set for gastrulation. Nat. Rev. Genet. 8, 368–381.

Tan, S.C., Carr, C.A., Yeoh, K.K., J. Schofield, C., Davies, K.E., Clarke, K., 2012. Identification of valid housekeeping genes for quantitative RT-PCR analysis of cardiosphere-derived cells preconditioned under hypoxia or with prolyl-4-hydroxylase inhibitors. Mol. Biol. Rep. 39, 4857–4867.

Templin, C., Zweigerdt, R., Schwanke, K., Olmer, R., Ghadri, J.-R., Emmert, M.Y., Muller, E., Kuest, S.M., Cohrs, S., Schibli, R., Kronen, P., Hilbe, M., Reinisch, A., Strunk, D., Haverich, A., Hoerstrup, S., Luscher, T.F., Kaufmann, P.A., Landmesser, U., Martin, U., 2012. Transplantation and Tracking of Human-Induced Pluripotent Stem Cells in a Pig Model of Myocardial Infarction: Assessment of Cell Survival, Engraftment, and Distribution by Hybrid Single Photon Emission Computed Tomography/Computed Tomography of Sodium Iod. Circulation 126, 430–439.

Tertoolen, L.G.J., Braam, S.R., van Meer, B.J., Passier, R., Mummery, C.L., 2018. Interpretation of field potentials measured on a multi electrode array in pharmacological toxicity screening on primary and human pluripotent stem cell-derived cardiomyocytes. Biochem. Biophys. Res. Commun. 497, 1135–1141.

Thomson, J.A., 1998. Embryonic Stem Cell Lines Derived from Human Blastocysts. Science (80-.). 282, 1145–1147.

Tian, Y., Cohen, E.D., Morrisey, E.E., 2010. The Importance of Wnt Signaling in Cardiovascular Development. Pediatr. Cardiol. 31, 342–348.

Tiburcy, M., Hudson, J.E., Balfanz, P., Schlick, S., Meyer, T., Liao, M.L.C., Levent, E., Raad, F., Zeidler, S., Wingender, E., Riegler, J., Wang, M., Gold, J.D., Kehat, I., Wettwer, E., Ravens, U., Dierickx, P., Van Laake, L.W., Goumans, M.J., Khadjeh, S., Toischer, K., Hasenfuss, G., Couture, L.A., Unger, A., Linke, W.A., Araki, T., Neel, B., Keller, G., Gepstein, L., Wu, J.C., Zimmermann, W.-H.H., Chang Liao, M.-L., Levent, E., Raad, F., Zeidler, S., Wingender, E., Riegler, J., Wang, M., Gold, J.D., Kehat, I., Wettwer, E., Ravens, U., Dierickx, P., Van Laake, L.W., Goumans, M.J., Khadjeh, S., Toischer, K., Hasenfuss, G., Couture, L.A., Unger, A., Linke, W.A., Araki, T., Neel, B., Keller, G., Gepstein, L., Wu, J.C., Zimmermann, W.-H.H., 2017. Defined Engineered Human Myocardium With Advanced Maturation for Applications in Heart Failure Modeling and Repair. Circulation 135, 1832–1847.

Tobacman, L.S., Adelstein, R.S., 1986. Mechanism of regulation of cardiac actin-myosin subfragment 1 by troponin-tropomyosin. Biochemistry 25, 798–802.

Tohyama, S., Fukuda, K., 2017. Safe and Effective Cardiac Regenerative Therapy With Human-Induced Pluripotent Stem Cells. Circ. Res. 120, 1558–1560.

Tojkander, S., Gateva, G., Lappalainen, P., 2012. Actin stress fibers - assembly, dynamics and biological roles. J. Cell Sci. 125, 1855–1864.

Tran, T.H., Wang, X., Browne, C., Zhang, Y., Schinke, M., Izumo, S., Burcin, M., 2009. Wnt3a-induced mesoderm formation and cardiomyogenesis in human embryonic stem cells. Stem Cells 27, 1869–1878.

Trickett, P., 1964. Proteolytic enzymes in treatment of athletic injuries. Appl. Ther. 6, 647–652.

Tulloch, N.L., Muskheli, V., Razumova, M. V., Korte, F.S., Regnier, M., Hauch, K.D., Pabon, L., Reinecke, H., Murry, C.E., 2011. Growth of engineered human myocardium with mechanical loading and vascular coculture. Circ. Res. 109, 47–59.

Ueno, S., Weidinger, G., Osugi, T., Kohn, A.D., Golob, J.L., Pabon, L., Reinecke, H., Moon, R.T., Murry, C.E., 2007. Biphasic role for Wnt/beta-catenin signaling in cardiac specification in zebrafish and embryonic stem cells. Proc. Natl. Acad. Sci. U. S. A. 104, 9685–90.

Ulmer, B.M., Stoehr, A., Schulze, M.L., Patel, S., Gucek, M., Mannhardt, I., Funcke, S., Murphy, E., Eschenhagen, T., Hansen, A., 2018. Contractile Work Contributes to Maturation of Energy Metabolism in hiPSC-Derived Cardiomyocytes. Stem Cell Reports 10, 834–847.

Uosaki, H., Taguchi, Y. h., 2016. Comparative Gene Expression Analysis of Mouse and Human Cardiac Maturation. Genomics, Proteomics Bioinforma. 14, 207–215.

Urrios, A., Parra-Cabrera, C., Bhattacharjee, N., Gonzalez-Suarez, A.M., Rigat-Brugarolas, L.G., Nallapatti, U., Samitier, J., DeForest, C.A., Posas, F., Garcia-Cordero, J.L., Folch, A., 2016. 3D-printing of transparent bio-microfluidic devices in PEG-DA. Lab Chip 16, 2287–2294.

van Laake, L.W., Passier, R., Monshouwer-Kloots, J., Verkleij, A.J., Lips, D.J., Freund, C., den Ouden, K., Ward-van Oostwaard, D., Korving, J., Tertoolen, L.G., van Echteld, C.J., Doevendans, P.A., Mummery, C.L., 2007. Human embryonic stem cell-derived cardiomyocytes survive and mature in the mouse heart and transiently improve function after myocardial infarction. Stem Cell Res. 1, 9–24.

van Meer, B.J., Tertoolen, L.G.J., Mummery, C.L., 2016. Concise Review: Measuring Physiological Responses of Human Pluripotent Stem Cell Derived Cardiomyocytes to Drugs and Disease. Stem Cells 34, 2008–2015.

Vandenberg, J.I., Perry, M.D., Perrin, M.J., Mann, S.A., Ke, Y., Hill, A.P., 2012. hERG K + Channels: Structure, Function, and Clinical Significance. Physiol. Rev. 92, 1393–1478.

Vandesompele, J., De Preter, K., Pattyn, F., Poppe, B., Van Roy, N., De Paepe, A., Speleman, F., 2002a. Accurate normalization of real-time quantitative RT-PCR data by geometric averaging of multiple internal control genes. Genome Biol. 3, RESEARCH0034.

Vandesompele, J., De Preter, K., Pattyn, F., Poppe, B., Van Roy, N., De Paepe, A., Speleman, F., 2002b. Accurate normalization of real-time quantitative RT-PCR data by geometric averaging of multiple internal control genes. Genome Biol. 3, research0034.1.

Vennemann, P., Kiger, K.T., Lindken, R., Groenendijk, B.C.W., Stekelenburg-de Vos, S., ten Hagen, T.L.M., Ursem, N.T.C., Poelmann, R.E., Westerweel, J., Hierck, B.P., 2006. In vivo micro particle image velocimetry measurements of blood-plasma in the embryonic avian heart. J. Biomech. 39, 1191–1200.

Vulliet, P.R., Greeley, M., Halloran, S.M., MacDonald, K.A., Kittleson, M.D., 2004. Intra-coronary arterial injection of mesenchymal stromal cells and microinfarction in dogs. Lancet 363, 783–784.

Warren, L., Manos, P.D., Ahfeldt, T., Loh, Y.H., Li, H., Lau, F., Ebina, W., Mandal, P.K., Smith, Z.D., Meissner, A., Daley, G.Q., Brack, A.S., Collins, J.J., Cowan, C., Schlaeger, T.M., Rossi, D.J., 2010. Highly efficient reprogramming to pluripotency and directed differentiation of

human cells with synthetic modified mRNA. Cell Stem Cell 7, 618–630.

Weinberger, F., Breckwoldt, K., Pecha, S., Kelly, A., Geertz, B., Starbatty, J., Yorgan, T., Cheng, K.-H., Lessmann, K., Stolen, T., Scherrer-Crosbie, M., Smith, G., Reichenspurner, H., Hansen, A., Eschenhagen, T., 2016. Cardiac repair in guinea pigs with human engineered heart tissue from induced pluripotent stem cells. Sci. Transl. Med. 8, 363ra148-363ra148.

Weinberger, F., Mehrkens, D., Friedrich, F.W., Stubbendorff, M., Hua, X., Müller, J.C., Schrepfer, S., Evans, S.M., Carrier, L., Eschenhagen, T., 2012. Localization of Islet-1–Positive Cells in the Healthy and Infarcted Adult Murine Heart. Circ. Res. 110, 1303–1310.

Wilkins, E., Wilson, L., Wickramasinghe, K., Bhatnagar, P., Leal, J., Luengo-Fernandez, R., Burns, R., Rayner, M., Townsend, N., 2017. European cardiovascular disease statistics 2017. Eur. Hear. Netw.

Witjas-Paalberends, E.R., Piroddi, N., Stam, K., van Dijk, S.J., Oliviera, V.S., Ferrara, C., Scellini, B., Hazebroek, M., ten Cate, F.J., van Slegtenhorst, M., dos Remedios, C., Niessen, H.W.M., Tesi, C., Stienen, G.J.M., Heymans, S., Michels, M., Poggesi, C., van der Velden, J., 2013. Mutations in MYH7 reduce the force generating capacity of sarcomeres in human familial hypertrophic cardiomyopathy. Cardiovasc. Res. 99, 432–441.

Wright, N.T., Cannon, B.R., Zimmer, D.B., Weber, D.J., 2009. S100A1: Structure, Function, and Therapeutic Potential. Curr. Chem. Biol. 3, 138–145.

Wu, S.M., Chien, K.R., Mummery, C., 2008. Origins and Fates of Cardiovascular Progenitor Cells. Cell 132, 537–543.

Xin, M., Olson, E.N., Bassel-Duby, R., 2013. Mending broken hearts: cardiac development as a basis for adult heart regeneration and repair. Nat. Publ. Gr. 14, 529–541.

Xu, T., Binder, K.W., Albanna, M.Z., Dice, D., Zhao, W., Yoo, J.J., Atala, A., 2012. Hybrid printing of mechanically and biologically improved constructs for cartilage tissue engineering applications. Biofabrication 5, 015001.

Xu, T., Gregory, C.A., Molnar, P., Cui, X., Jalota, S., Bhaduri, S.B., Boland, T., 2006. Viability and electrophysiology of neural cell structures generated by the inkjet printing method. Biomaterials 27, 3580–8.

Xu, T., Jin, J., Gregory, C., Hickman, J.J., Boland, T., 2005. Inkjet printing of viable mammalian cells. Biomaterials 26, 93–99.

Yamanaka, S., 2009. Elite and stochastic models for induced pluripotent stem cell generation. Nature 460, 49–52.

Yamasaki, R., Berri, M., Wu, Y., Trombitás, K., McNabb, M., Kellermayer, M.S.Z., Witt, C., Labeit, D., Labeit, S., Greaser, M., Granzier, H., 2001. Titin–Actin Interaction in Mouse Myocardium: Passive Tension Modulation and Its Regulation by Calcium/S100A1. Biophys. J. 81, 2297–2313.

Yamazaki, D., Kitaguchi, T., Ishimura, M., Taniguchi, T., Yamanishi, A., Saji, D., Takahashi, E., Oguchi, M., Moriyama, Y., Maeda, S., Miyamoto, K., Morimura, K., Ohnaka, H., Tashibu, H., Sekino, Y., Miyamoto, N., Kanda, Y., 2018. Proarrhythmia risk prediction using human induced pluripotent stem cell-derived cardiomyocytes. J. Pharmacol. Sci. 136, 249–256.

Yang, L., Soonpaa, M.H., Adler, E.D., Roepke, T.K., Kattman, S.J., Kennedy, M., Henckaerts, E., Bonham, K., Abbott, G.W., Linden, R.M., Field, L.J., Keller, G.M., 2008. Human cardiovascular progenitor cells develop from a KDR+ embryonic-stem-cell-derived population. Nature 453, 524–528.

Yang, X., Pabon, L., Murry, C.E., 2014. Engineering adolescence: Maturation of human pluripotent stem cell-derived cardiomyocytes. Circ. Res. 114, 511–523.

Ye, L., Zimmermann, W.-H., Garry, D.J., Zhang, J., 2013. Patching the Heart. Circ. Res. 113, 922–932.

Yoshida, Y., Yamanaka, S., 2010. Recent stem cell advances: Induced pluripotent stem cells for disease modeling and stem cell-based regeneration. Circulation 122, 80–87.

Young, J.L., Kretchmer, K., Ondeck, M.G., Zambon, A.C., Engler, A.J., 2015. Mechanosensitive Kinases Regulate Stiffness-Induced Cardiomyocyte Maturation. Sci. Rep. 4, 6425.

Yusa, K., Rad, R., Takeda, J., Bradley, A., 2009. Generation of transgene-free induced pluripotent mouse stem cells by the piggyBac transposon. Nat. Methods 6, 363–369.

Zhang, D., Shadrin, I.Y., Lam, J., Xian, H.Q., Snodgrass, H.R., Bursac, N., 2013. Tissue-engineered cardiac patch for advanced functional maturation of human ESC-derived cardiomyocytes. Biomaterials 34, 5813–5820.

Zhang, M., Schulte, J.S., Heinick, A., Piccini, I., Rao, J., Quaranta, R., Zeuschner, D., Malan, D., Kim, K.-P., Röpke, A., Sasse, P., Araúzo-Bravo, M., Seebohm, G., Schöler, H., Fabritz, L., Kirchhof, P., Müller, F.U., Greber, B., 2015. Universal Cardiac Induction of Human Pluripotent Stem Cells in Two and Three-Dimensional Formats: Implications for In Vitro Maturation. Stem Cells 33, 1456–1469.

Zhang, X.-X., Chen, M., Fu, M., 2014. Impact of surface nanostructure on ice nucleation. J. Chem. Phys. 141, 124709.

Zhang, Y.S., Arneri, A., Bersini, S., Shin, S.R., Zhu, K., Goli-Malekabadi, Z., Aleman, J., Colosi, C., Busignani, F., Dell'Erba, V., Bishop, C., Shupe, T., Demarchi, D., Moretti, M., Rasponi, M., Dokmeci, M.R., Atala, A., Khademhosseini, A., 2016. Bioprinting 3D microfibrous scaffolds for engineering endothelialized myocardium and heart-on-a-chip. Biomaterials 110, 45–59.

Zhou, H., Wu, S., Joo, J.Y., Zhu, S., Han, D.W., Lin, T., Trauger, S., Bien, G., Yao, S., Zhu, Y., Siuzdak, G., Schöler, H.R., Duan, L., Ding, S., 2009. Generation of Induced Pluripotent Stem Cells Using Recombinant Proteins. Cell Stem Cell 4, 381–384.

Zimmermann, H., Shirley, S.G., Zimmermann, U., 2007. Alginate-based encapsulation of cells: Past, present, and future. Curr. Diab. Rep. 7, 314–320.

Zimmermann, H., Zimmermann, D., Reuss, R., Feilen, P.J., Manz, B., Katsen, A., Weber, M., Ihmig, F.R., Ehrhart, F., Gessner, P., Behringer, M., Steinbach, A., Wegner, L.H., Sukhorukov, V.L., Vásquez, J.A., Schneider, S., Weber, M.M., Volke, F., Wolf, R., Zimmermann, U., 2005. Towards a medically approved technology for alginate-based microcapsules allowing long-term immunoisolated transplantation. J. Mater. Sci. Mater. Med. 16, 491–501.

Zimmermann, W.H., Fink, C., Kralisch, D., Remmers, U., Weil, J., Eschenhagen, T., 2000. Three-

dimensional engineered heart tissue from neonatal rat cardiac myocytes. Biotechnol. Bioeng. 68, 106–114.

Zimmermann, W.H., Schneiderbanger, K., Schubert, P., Didié, M., Münzel, F., Heubach, J.F., Kostin, S., Neuhuber, W.L., Eschenhagen, T., 2002. Tissue engineering of a differentiated cardiac muscle construct. Circ. Res. 90, 223–230.

Zweigerdt, R., Olmer, R., Singh, H., Haverich, A., Martin, U., 2011. Scalable expansion of human pluripotent stem cells in suspension culture. Nat. Protoc. 6, 689–700.

Zwi-dantsis, L., Sc, B., Mizrahi, I., Ph, D., Arbel, G., Sc, M., Gepstein, A., Ph, D., Gepstein, L., Ph, D., 2011. Scalable Production of Cardiomyocytes Derived from c-Myc Free Induced Pluripotent Stem Cells 17, 1027–1038.

Zwi, L., Caspi, O., Arbel, G., Huber, I., Gepstein, A., Park, I.H., Gepstein, L., 2009. Cardiomyocyte differentiation of human induced pluripotent stem cells. Circulation 120, 1513–1523.

8 APPENDIX

Peer-reviewed publications

1. Fischer B., Gepp M. M., Schulz A., Danz K., Gwinner F., Dehne A., Neubauer J.C., Gentile L., Zimmermann H. Towards a universal biopolymer platform for in-vitro modelling of the cardiac niche (*in preparation*).
2. Fischer B., Meier A., Dehne A., Salhotra A., Tran T.A., Neumann S., Schmidt K., Meiser I., Neubauer J. C., Zimmermann H. A complete workflow for the differentiation and the dissociation of hiPSC-derived cardiospheres. Stem Cell Res. (2018)
3. Schulz A., Katsen-Globa A., Huber E.J., Mueller S.C., Kreiner A., Pütz N., Gepp M. M., Fischer B., Stracke F., von Briesen H., Neubauer J.C., Zimmermann H. Poly(amidoamine)-alginate hydrogels: directing the behavior of mesenchymal stem cells with charged hydrogel surfaces. J. Mater. Sci. Mater. Med. (2018)
4. Gepp M.M., Fischer B., Schulz A., Dobringer J., Gentile L., Vásquez J. A., Neubauer J. C., Zimmermann, H. Bioactive surfaces from seaweed-derived alginates for the cultivation of human stem cells. J. Appl. Phycol. (2017)
5. Fischer B., Schulz A., Gepp M. M., Neubauer J. C., Gentile L., Zimmermann H. 3D printing of hydrogels in a temperature controlled environment with high spatial resolution. Curr. Dir. Biomed. Eng. (2016)

Patents

1. German patent number: 10 2017 000 896.5 "Selektives Freisetzungssystem für Tumortherapeutika und Tumordiagnostika sowie Biosensor für Tumorgewebe"

Conference Contributions

1. Fischer B., Weber L., Gepp M.M., Schulz A., Meier A., Neubauer J. C., Gentile L., Zimmermann H.; Scaffolds for off-the-shelf regenerative medicine; DGBM 2017, Würzburg, Germany
2. Fischer B., Gepp M. M., Schulz A., Gentile L., Zimmermann H.; Towards a Novel 3D Hydrogel Printing Method for Cardiac Muscle Modelling; Bioprinting & 3D Printing in the Life Sciences 2016, Cambridge, UK
3. Fischer B., Schulz A., Gepp M. M., Neubauer J., Gentile L., Zimmermann H.; The Heartpatch, a versatile cell-alginate based scaffold for cardiac tissue engineering ISSCR annual meeting 2017, Basel, Switzerland
4. Fischer B., Gepp M.M., Schulz A., DobringerJ., Vasquez J.A., Gentile L., Zimmermann H.Towards a novel ultra-high viscosity alginate scaffold for cardiac tissue engineering 22nd International Seaweed Symposium 2016, Copenhagen, Denmark

ACKNOWLEDGEMENT

I gratefully thank Prof. Dr. Heiko Zimmermann, Head of Institute of the Fraunhofer Institute for Biomedical Engineering, Professor for Molecular and Cellular Biotechnology/ Nanotechnology at Saarland University and Professor at the Faculty of Marine Sciences at the Universidad Católica del Norte (Coquimbo, Chile), for offering me the opportunity to work at the Fraunhofer IBMT on such a fascinating subject. I am deeply thankful for the advice, guidance and the critical scientific discussions throughout this time, which rendered this work possible.

I would like to thank Prof. Dr. Jörn Walter, head of the epigenetics group at Saarland University, for taking the responsibility of the secondary supervisor and the critical advice on this project.

I am grateful for Prof. Dr. Stamm, head of the group "Cardiomyocyte Restoration and Matrix Support" at the Berlin Center for Regenerative Therapies, for critically assessing this work.

I also would like to thank Dr. Julia Neubauer, head of the Cryo- and Stem Cell Technology, department for the guidance and discussions throughout this project and for allowing me to conduct this work in her department.

I thank Dr. Luca Gentile for deeply enhancing my understanding of developmental and molecular biology and the passion for scientific discussions and coffee.

I would like to thank Anna Meier, M.Sc. for her support regarding the flow cytometry-based measurements and the many fruitful discussions circulating around all the daily problems.

I would like to thank Dr. Michael M. Gepp for the establishment of the alginate functionalisation and the critical discussions around this project.

I thank André Schulz, M.Sc. for the extraction of the UHV-alginates, the analysis of G' and G'' modules and all the interdisciplinary discussions between biology and chemistry.

I would like to thank Karin Danz, M.Sc. for the support in carrying out the western blotting experiments.

I thank Dr. Frederik Gwinner and Marcel Meyerheim, M. Sc. for making the analysis of the contraction videos and the consecutive assessment of the different calcium transient parameters possible.

I thank Dr. Young Cho Oh for the production of the isolating box used for freeze printing.

I thank Dr. Sabine Müller for the critical discussions about the image-based analysis of the cardiac contractility.

I would like to thank Susan Zöllner and Sybille Richter for the maintenance of the hiPSC culture.

I would like to thank Dr. Alba Jimeno-Romero for the scientific discussions, which ventured far into the realm of molecular biology and sometimes even further.

I would like to thank the students, who contributed to this work under my supervision: Aseem Salhotra for conducting the hanging drop and BioLevitator differentiation; Lukas Weber for the assessment of the scaffold pore size and printing resolution; Annika Dehne for performing the cardiac differentiation in the Biolevitator and the consecutive dissociation experiments.

Lastly, I am deeply grateful to my family, my parents Eva and Bernhard and my brother Nick, and to Lisa for all the loving support and encouragement throughout these years.